Structure in galaxy clusters revealed through Sunyaev-Zel'dovich observations : A multi-aperture synthesis approach

Dissertation

zur

Erlangung des Doktorgrades (Dr. rer. nat.)

der

Mathematisch-Naturwissenschaftlichen Fakultät

der

Rheinischen Friedrich-Wilhelms-Universität Bonn

vorgelegt von

Sandra Burkutean

aus

Bad Soden am Taunus

Bonn, 2014

Angefertigt mit Genehmigung der Mathematisch-Naturwissenschaftlichen Fakultät der Rheinischen Friedrich-Wilhelms-Universität Bonn.

Diese Dissertation ist auf dem Hochschulschriftenserver der ULB Bonn unter `http://hss.ulb.uni-bonn.de/diss_online` elektronisch publiziert.

1. Gutachter: Prof. Dr. Frank Bertoldi
2. Gutachter: Prof. Dr. Ulrich Klein

Tag der Promotion: 14. August 2014

Erscheinungsjahr: 2014

Summary

As the largest bound objects in the universe, galaxy clusters are unique targets to study astrophysical processes, as well as powerful probes for precision cosmology. Galaxy clusters are dynamically young and their merger history and energetic feedback from galaxies leave significant traces in the pressure or entropy distribution of the intra-cluster medium (ICM), the hot plasma that contains most of the baryonic mass in clusters. A detailed understanding of how ICM observables relate to cluster mass at different cosmic epochs is also crucial to reduce the systematic uncertainties in the measurement of cosmological parameters from cluster observations.

Through analysis of new observational data, mock observations, and modelling, I explore how current and future millimeter-wavelength interferometer observations of the Sunyaev-Zel'dovich effect (SZE) allow detailed studies of the ICM structure and physics. The SZE is a change in the emission spectrum of the Cosmic Microwave Background (CMB) caused by the scattering of CMB photons off the hot ICM free electrons. The SZE signal is proportional to the electron pressure and thus allows a measure of the thermal energy content and morphology of the ICM.

I focus on the projected triaxial cluster morphology, whose extended structure is best observed at millimeter-wavelengths with a combination of interferometer and single-dish imaging observations. Interferometric observations provide good spatial resolution but suffer from sparse spatial sampling, which may hamper non-spherical cluster pressure profile constraints. Single dish observations are naturally limited in spatial resolution and commonly do not resolve the interesting cluster core regions or shocks in the ICM.

My interferometric CARMA/SZA SZE observations of the galaxy cluster MS0451 complement our prior single-dish APEX observations. While the small-dish interferometric SZA data offer better precision in spherical pressure profile fits, they suffer from insufficient interferometric spatial sampling, which does not allow to constrain the projected elliptical shape and orientation of MS0451. APEX-SZ data thus complement the interferometric fits, as they can constrain the non-spherical projected morphology.

The ICM in the core regions of clusters retains signatures of AGN energy feedback and merger-induced disturbance. The unrivaled high resolution and sensitivity of the new Atacama Large Millimeter Array (ALMA) and its compact sub-array (ACA) offer unique capabilities to study cluster cores and merger-induced shock fronts. Through mock simulations of ALMA and SZA observations and using my Bayesian MCMC code, I show that it is possible to distinguish different morphological states of clusters through their characteristic, observable pressure profiles. In addition, I quantify how future ALMA lower frequency (Band 1) observations can strengthen the present capability to measure the cluster pressure distribution. My simulations also outline how ALMA observations provide detailed views on shock fronts in the ICM. The famous Bullet Cluster is taken as an example case, for which ALMA/ACA Cycle 2 configuration simulations illustrate how the merger-induced bow shock structure can indeed be imaged.

"Nature uses only the longest threads to weave her pattern,
so each small piece of her fabric
reveals the organization of the entire tapestry."

- Richard Feynman

Contents

Chapter 1

Outline

In order to illustrate the potential of interferometric observations of galaxy clusters across a wide redshift range, this thesis explores several approaches:

1. The comparison of interferometric and bolometer single-dish galaxy cluster observations of the galaxy cluster MS0451 and their respective suitabilities for different parametric studies. (Chapters 5,6 & 9)

2. A mock cluster evolution study aimed at assessing the feasibility of joint ALMA/ACA/SZA observations in distinguishing relaxed and morphologically disturbed galaxy clusters while exploiting the new high-resolution interferometric capabilities. (Chapter 7)

3. ALMA/ACA simulations of the 'Bullet Cluster' of galaxies, that outline the potential to image shock structures in galaxy clusters via interferometry. (Chapter 8)

Chapter 2 gives an overview of the standard cosmological model, introducing the cosmological concepts and parameters relevant for the rest of this thesis.

This is followed by an overview of the status of current galaxy cluster research, in terms of multi-wavelength observations, instrumental considerations as well as of detailed cluster astrophysics (Chapter 3).

Since topic 1 assesses the nature of interferometric CARMA/SZA and single-dish APEX-SZ measurements, these two observing techniques are outlined in chapter 4. Chapter 5 comprises a discussion on my two accepted CARMA/SZA proposals on the galaxy cluster MS0451 as well as on the subsequent interferometric data reduction and single-dish/interferometric data combination. The implemented Bayesian MCMC visibility and APEX-SZ fitting methods are described in chapter 6 and the subsequent results are compared.

Chapter 7 introduces the concept of joint ALMA/ACA/SZA mock simulations for relaxed and morphologically disturbed clusters as well as the 2D likelihood parametric model contours from the Bayesian MCMC fits for selected clusters.

High-resolution mock simulated observations are further used to assess the feasibility of ALMA/ACA Cycle 2 observations in imaging the bow shock structure in the 'Bullet

Cluster' of galaxies (Chapter 8).

Chapter 9 outlines the framework for a full triaxial multi-wavelength analysis of the MS0451 project. In light of recent publicly released archival CARMA/SZA data as well as a newly accepted collaboration proposal, a planned extension of the MS0451 cluster study to a wide cluster selection is outlined.

The detailed thesis structure is outlined in Fig. 1.1 via a pyramid structure whose breakdown mirrors the topic divisions and discussion flow.

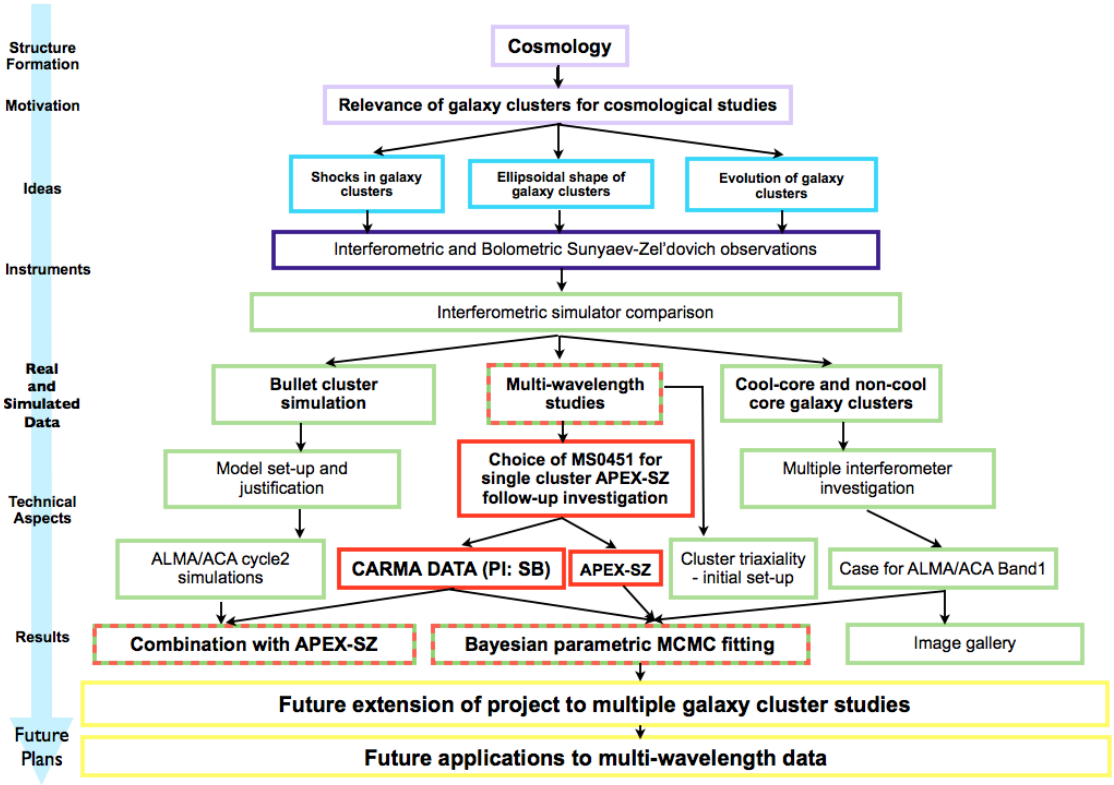

Figure 1.1: Thesis structure. The cosmological framework as well as the current status of galaxy cluster research is outlined in chapters 2 + 3 (purple). Chapter 3 further outlines the addressed science themes (turquoise). The observational techniques with an integrated discussion on my interferometric simulator code are discussed in chapter 4 (blue). In the next sections, green denotes simulations (chapter 7, chapter 8), red illustrates data reduction/analysis (chapter 5, chapter 6) and yellow stands for future projects and their subsequent preparation in terms of simulation frameworks (chapter 9). Simulations are implemented for the galaxy cluster shock project (chapter 8) as well as for the pressure profile study (chapter 7).

Chapter 2

Cosmology and structure formation

Cosmology is the study of the largest laboratory one could possibly imagine - the Universe. Rather than being investigators who design an experimental set-up and set the initial conditions of our experiments, we take the role of observers.
We test hypotheses put forward by theory, or indeed numerical simulations, through diligent comparison with what we 'see' beyond our Earth's atmosphere. Cosmology deals with the properties of our whole universe - its shape, content and evolution - spanning the concepts of quantum fluctuations and horizons.
In the simplest inflation theory scenarios, it is the quantum fluctuations of a scalar field during a period of rapid expansion of the universe, inflation, which are thought to have caused small disturbances in spacetime curvature, thus providing the seeds for structure formation.
Non-baryonic dark matter starts to form the small-scale structures that develop through hierarchical merging processes into larger scale systems, baryonic matter falling into the dark matter potential wells at a later stage. The cosmic web is made up of filaments, voids and filament intersections in which galaxy clusters reside. The study of galaxy clusters across a wide redshift range thus contributes in tracing the large-scale structure.
In order to put galaxy cluster research in a cosmological context, the cornerstones of structure evolution are outlined in this chapter.

2.1 A homogenous and isotropic picture of the universe

One may start with two postulates about the universe - the cosmological principle: "The universe is homogenous and isotropic".

Isotropy implies homogeneity but homogeneity does not imply isotropy. Before accepting the cosmological principle as given, one should test whether it provides a plausible description of reality.

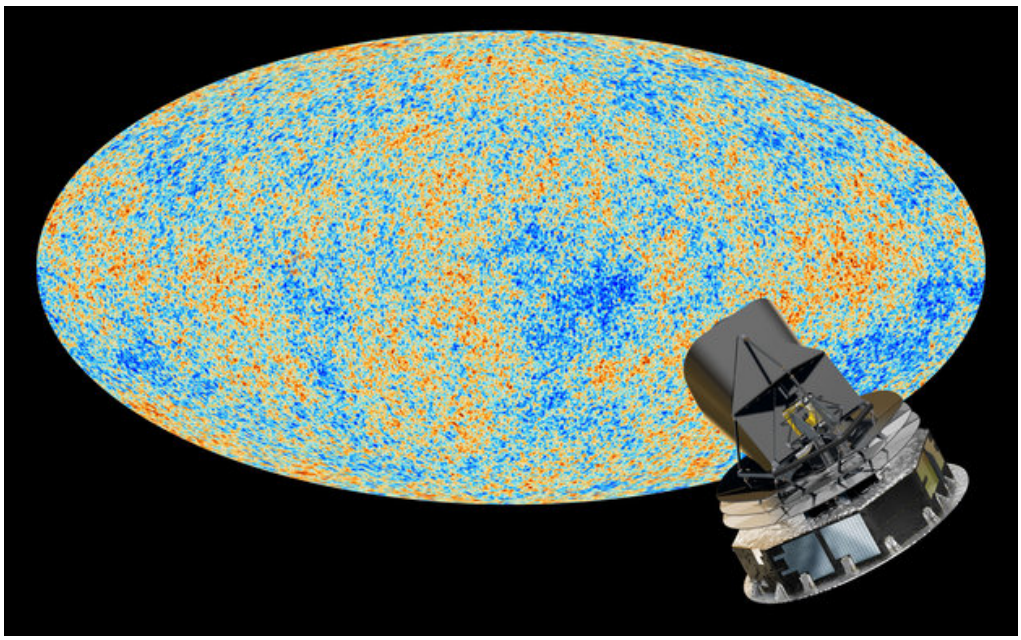

Figure 2.1: The Planck satellite view of the Cosmic Microwave Background radiation after removal of foreground, dipole moment and secondary anisotropies. The variation in this map is of the order of 1:100000. (Image credit: ESA and the Planck Collaboration - D. Ducros)

The Cosmic Microwave Background (CMB) was discovered by Penzias and Wilson in 1964. It provides us with a view of the universe at the surface of last scattering around the redshift of $z \approx 1100$ where photons and baryons decouple, allowing the CMB photons to propagate freely. The CMB has a black body spectrum at a temperature of 2.725 ± 0.002 K (Mather et al. 1999) and is almost uniform over the whole sky, showing variations only at the order of 10^{-5} (Fig. 2.1) (Planck Collaboration XVI 2013).

In the quasi-stellar object redshift survey (2dF QSO) over two $75° \times 5°$ strips in the sky, Croom et al. (2005) showed a vanishing two-point correlation beyond scales of 100 h^{-1} Mpc.[1]

[1] More recently, Clowes et al. (2013) have found a structure in the Sloan Digital Sky Survey (SDSS) data set at redshift $z \approx 1.3$ with a characteristic size of $z \approx 500$ Mpc, which may prove to challenge the homogeneity assumption. In this thesis, the homogeneity and isotropy assumption will be adopted.

In the following sections, I build up an argument for the cosmological framework based on the approaches of D'Inverno OUP (2007), Hobson CUP (2006) and the cosmology lecture notes by Prof. Schneider (2010).

Weyl's postulate states that, in a homogeneous and isotropic universe, there is an observer, the comoving observer, whose 4-velocity is orthogonal to a spacelike hypersurface defined by a constant proper time. This comoving observer thus travels along a worldline which intersects with no other along its path except for the start and possibly end point. One could hence propose the line element to be of the form [2]

$$ds^2 = g_{\mu\nu} dx^\mu dx^\nu \qquad (\mu, \nu = 0, 1, 2, 3), \tag{2.1}$$

where ds^2 describes the distance between two points in a pseudo-Riemannian manifold. The specification of a pseudo-Riemannian manifold implies that we are dealing with a continuously parameterisable set whose line element does not necessarily have to be greater than zero, thus allowing for transformations to a local frame in which special relativity applies. The latter is required by Einstein's equivalence principle, which states that " In a freely falling laboratory the laws should be those of special relativity, provided that we are considering a small region of spacetime." (Hobson CUP 2006).

On account of the isotropy assumption, this line element should also satisfy the condition that no points and directions on the hypersurface are preferred. Therefore, any change in time will affect dx^i for i=1,2,3, in the same way, such that the time variation can be described by a scale factor that solely depends on the cosmic time t - the time associated with a comoving observer. This scale factor is given by the cosmic scale factor, a(t), in Eq. 2.2 which, by definition, is normalized to 1 at the current epoch.

It now remains to find an expression for the curvature of this hypersurface. The simplest case, which satisfies homogeneity and isotropy, is a constant curvature space with curvature k. The line element can thus be expressed as

$$ds^2 = c^2 dt^2 - a^2(t) \left\{ d\chi^2 + f_k^2(\chi) \left(d\theta^2 + \sin^2\theta d\psi^2 \right) \right\} \qquad , \tag{2.2}$$

where the comoving angular diameter distance, f_k, is given by

$$f_k(\chi) = \begin{cases} k^{-\frac{1}{2}} \sin(k^{\frac{1}{2}}\chi) & (k > 0) \\ \chi & (k = 0) \\ (-k)^{-\frac{1}{2}} \sinh((-k)^{\frac{1}{2}}\chi) & (k < 0) \end{cases} \qquad . \tag{2.3}$$

The comoving radial coordinate is denoted by χ and (θ, ϕ) are the angular coordinates. This thus ensures that no positions or directions on the hypersurface are in any way special, that the scale factor applies to all points on the hypersurface and that Weyl's postulate is satisfied.

[2] Note that Einstein's summation convention is used: any repeated index is summed over.

Now that the form of the line element, and thus the Robertson-Walker (RW) metric, has been established, one may move on towards Einstein's grand idea that the energy momentum tensor is related to the curvature of the manifold.

One way to see why one would like to motivate such a tensor equation is the fact that tensor equations have the property of being coordinate independent.
Before describing the nature of the energy-momentum tensor, one might first consider how an intrinsic curvature might be assigned to a manifold - intrinsic meaning that it solely depends on the manifold under consideration. The way to describe curvature should, again, be in the form of a tensor since one would like to relate it directly to the metric without any coordinate system dependence.

With the hindsight that curvature should be linked to a second order derivative, and taking into account that, for a vector field, the second covariant derivative is not commutative (i.e. changing the order of doing the differentiation, changes the result), one can define the elements of the curvature tensor, as

$$R^a_{bcd} \equiv \partial_c \Gamma^a_{bd} - \partial_d \Gamma^a_{bc} + \Gamma^e_{bd}\Gamma^a_{ec} - \Gamma^e_{bc}\Gamma^a_{ed} \tag{2.4}$$

and the metric connection, Γ^a_{bc}, can be related to the metric for torsionless manifolds

$$\Gamma^a_{bc} = \frac{1}{2} g^{ad} \left(\partial_b g_{dc} + \partial_c g_{db} - \partial_d g_{bc}\right) \quad . \tag{2.5}$$

Via contraction of indices, one can also define the Ricci tensor $R^{ab}$and the Ricci scalar R, whose symmetry properties give

$$\nabla_a (R^{ab} - \frac{1}{2} g^{ab} R) = 0 \quad , \tag{2.6}$$

where the expression in brackets is the Einstein tensor, G^{ab}. Having established how curvature can be expressed for a manifold, it now remains to discuss the source term - the matter and energy distribution. The latter is desribed by the energy-momentum tensor, T^{ab}, of a perfect fluid, being characterized by the scalar density, ρ, and pressure, p, fields. Conservation of energy and momentum demands that

$$\nabla_a T^{ab} = 0 \quad , \tag{2.7}$$

such that the covariant form of Einstein's field equations is given by

$$G_{ab} = \frac{8\pi G}{c^4} T_{ab} - \Lambda g_{ab} \quad , \tag{2.8}$$

where Λ is a cosmological constant that can be added to the rhs of Eq. (2.8) since $\nabla_a g^{ab} = 0$. G is the gravitational constant. Hence, knowing the form of the metric for homogenous and isotropic hypersurfaces, and assuming the energy-momentum tensor to be described by a perfect fluid whose scalar fields are functions of cosmic time, one can

write the cosmological field equations, the Friedmann equations, in terms of the scale parameter as

$$\left(\frac{\dot{a}}{a}\right)^2 = \frac{8\pi G}{3}\rho - \frac{kc^2}{a^2} + \frac{\Lambda}{3} \tag{2.9}$$

$$\left(\frac{\ddot{a}}{a}\right) = -\frac{4\pi G}{3}\left(\rho + \frac{3p}{c^2}\right) + \frac{\Lambda}{3} \quad . \tag{2.10}$$

The Hubble parameter is given by

$$H(t) = \frac{\dot{a}(t)}{a(t)} \tag{2.11}$$

and is defined as H_0 at the current epoch, specified by time t_0 and denoted via the zero subscript. As will further be described in section 2.2, the universe currently seems to undergo acceleration such that $\ddot{a}>0$. Examination of Eq. (2.10) shows that, assuming the prescription of general relativity to be correct, this can only be brought about if either the cosmological constant Λ is non-zero or if we consider a field with negative pressure. For all the components of the cosmological fluid, one can write

$$\dot{\rho} = -3H\left(\rho + \frac{p}{c^2}\right) \quad , \tag{2.12}$$

by combining Eq. (2.9) and (2.10). Adopting the equation of state parameter

$$w = \frac{p}{\rho c^2} \quad , \tag{2.13}$$

one may write the solution to Eq. (2.12) for a non-evolving equation of state parameter as

$$\rho = \rho_0 a^{-3(1+w)} \quad . \tag{2.14}$$

The evolution of dust and radiation with redshift or, equivalently, the scale factor, is given by $\rho_{m,0}\ a^{-3}$ and $\rho_{r,0}\ a^{-4}$. The evolution of an arbitrary component X responsible for $\ddot{a}>0$ is given by $\rho_{X,0}\ a^{-3(1+w)}$, where $w = -1$ satisfies the condition for the cosmological constant and $w \neq -1$ suggests a dark energy model with a non-evolving equation of state parameter. Including an evolution term for the dark energy model requires

$$\rho_{DE} = \rho_{DE,0}\ e^{-3\int_1^a \frac{1+w(a')}{a'}da'} \quad . \tag{2.15}$$

Often, the evolution is parameterized as $w(a) = w_0 + w_a(1-a)$. The contribution of the cosmological fluid components can be normalized by the critical density at the current epoch

$$\rho_{cr,0} := \frac{3H_0^2}{8\pi G} \tag{2.16}$$

to give the normalized cosmological density parameters for the matter, radiation and cosmological constant: $\Omega_m \equiv \rho_{m,0}/\rho_{cr,0}$, $\Omega_r \equiv \rho_{r,0}/\rho_{cr,0}$, $\Omega_\Lambda \equiv \Lambda c^2/3H_0^2$. Hence, in the case were the cosmological constant is considered the acceleration cause (rather than a dark energy model), one can write Eq. (2.9) as

$$E^2(a) = \frac{H^2(a)}{H_0^2} = \Omega_r a^{-4} + \Omega_m a^{-3} + \Omega_\Lambda + \Omega_k a^{-2} \quad , \tag{2.17}$$

where Ω_k has been defined as $-kc^2/H_0^2$ via

$$\Omega_r + \Omega_m + \Omega_\Lambda + \Omega_k = 1 \quad . \tag{2.18}$$

Having discussed the different contributions to the energy content of the universe and their evolution, one may move on to consider distance measures as a function of the universe's expansion history.

The wavelength of an emitted photon is redshifted as it traverses the universe due to the expansion of the latter. The redshift of the source from which the photon was emitted is therefore defined as the ratio of the change in wavelength to the emitted wavelength. It can be shown to satisfy $1 + z = 1/a(t_{\text{emitted}})$.

The first characteristic scale one might consider is the maximum scale, which a comoving observer can be in contact with - the horizon:

$$r_{\text{horizon}}(z) = \int_0^{\frac{1}{1+z}} \frac{c}{H(a)a^2} da \quad . \tag{2.19}$$

The angular diameter distance, Fig. (2.2), relates the physical transverse size of an object to the subtended angle and is given by

$$D_A(z) = a(z) f_k(\chi) \quad . \tag{2.20}$$

The luminosity distance,

$$D_L(z) = \frac{f_k(\chi)}{a(z)} \quad , \tag{2.21}$$

relates the flux to the luminosity.

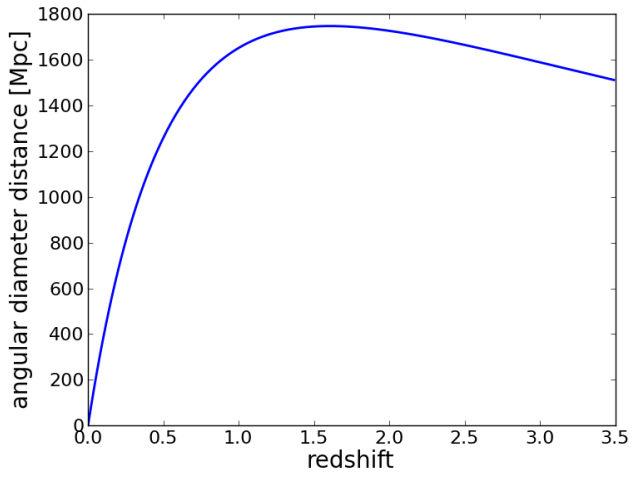

Figure 2.2: Angular diameter distance as a function of redshift for a fiducial ($\Omega_X = 0.7$, $\Omega_m = 0.3$, $H_0 = 70$, w = -1) cosmological model.

2.2 Results from recent experiments

The Planck and WMAP satellites have both mapped the angular power spectrum of the Cosmic Microwave Background (CMB) radiation up to multipoles of 2500 (Planck Collaboration XV) and 1200 (Larson et al. 2011) respectively. Recent results from the South Pole Telescope (SPT) (Keisler et al. 2011), the Atacama Cosmology Telescope (ACT) (Das et al. 2013) and APEX-SZ (Reichardt et al. 2009) have complemented these results at multipoles higher than 2500 (Fig. 2.3).

These results support the cosmological ΛCDM model which describes a spatially flat universe consisting of baryonic matter, dark matter, radiation and a cosmological constant. Dark matter (DM) is believed to be in the form of non-baryonic cold dark matter (CDM), which is characterised by its electromagnetic neutrality and sub-relativistic velocities. This dark matter is needed in order to explain the size of the CMB fluctuations, which, in its absence, would be predicted to be of the order of 10^{-3}. Its cold nature can be inferred from the observed structure distribution in the universe. In the hot or warm dark matter paradigm, structures would be smoothed out since dark matter would have sufficient energy to escape out of the potential wells. In addition, the presence of dark matter is needed in order to explain rotation curves in galaxies and the velocity dispersions in galaxy clusters (see Chapter 3).

Recent sole Planck temperature power spectrum fit results have shown that the baryonic and cold dark matter densities are $\Omega_b h^2 = 0.02207 \pm 0.00033$ (68% confidence level (CL)) and $\Omega_c h^2 = 0.1196 \pm 0.0031$ (68% CL), where $H_0 = 100h$ km s^{-1} Mpc^{-1}. The current critical density normalized dark energy density is $\Omega_\Lambda = 0.686 \pm 0.02$ (68% CL). The curvature parameter joint Planck+WMAP+ lensing +high multipole fit is consistent with

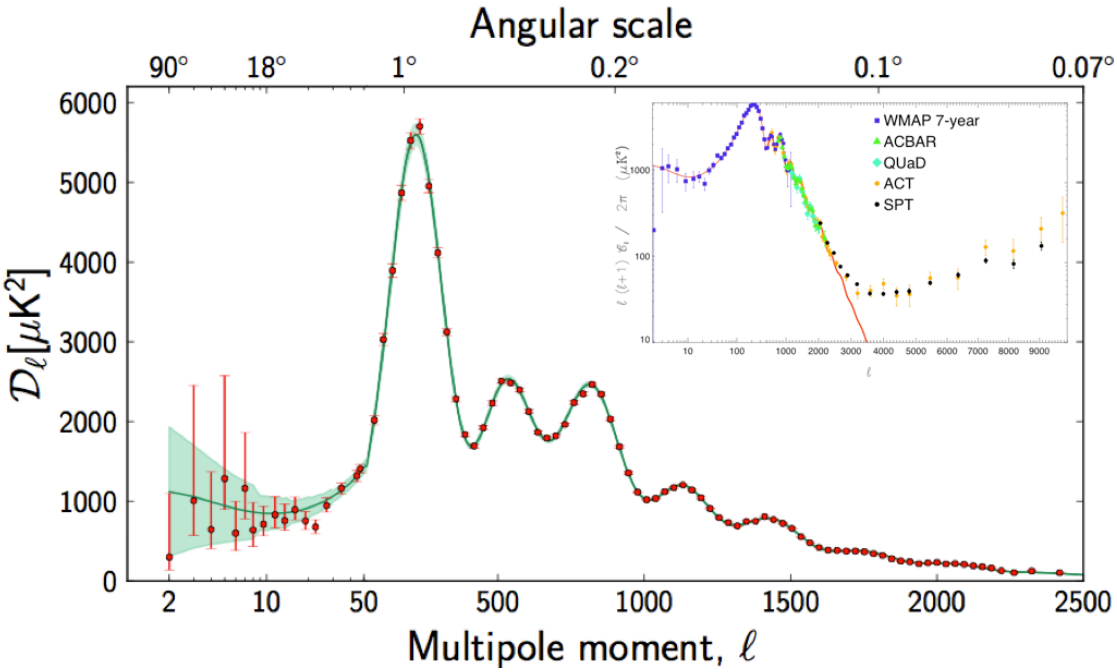

Figure 2.3: CMB power spectrum: The CMB power spectrum as mapped by Planck (Planck Collaboration XV 2013). The inset illustrates the complementary information at higher multipoles from ACT and SPT (Shirokoff et al. 2011, Luecker et al. 2010).(image credit: Planck Collaboration XV 2013, inset: Shirokoff et al. 2011)

a spatially flat universe, $100\Omega_k = -1.0^{+1.8}_{-1.9}$ (95% CL) (Planck Collaboration XVI 2013). The necessity for an Ω_X component (be it in the form of Ω_{DE} and/or Ω_Λ) can be seen from the energy budget of Eq. (2.18). Perlmutter et al. (1999) and Riess et al. (1998) have both shown that the expansion of the universe is currently undergoing acceleration from the distance-redshift relation of Supernova type 1a, which can be treated as standard candles. More recently, these results have been further confirmed by Suzuki et al. (2012) who studied SNe Ia over the redshift range $0.623<z<1.415$.

Constraints on the dark energy equation of state parameter from joint Planck,WMAP and Baryon Accoustic Oscillation (BAO), (Anderson et al. 2013, Planck Collaboration XVI 2013) information give $w = -1.13^{+0.24}_{-0.25}$, consistent with a cosmological constant parameter model.

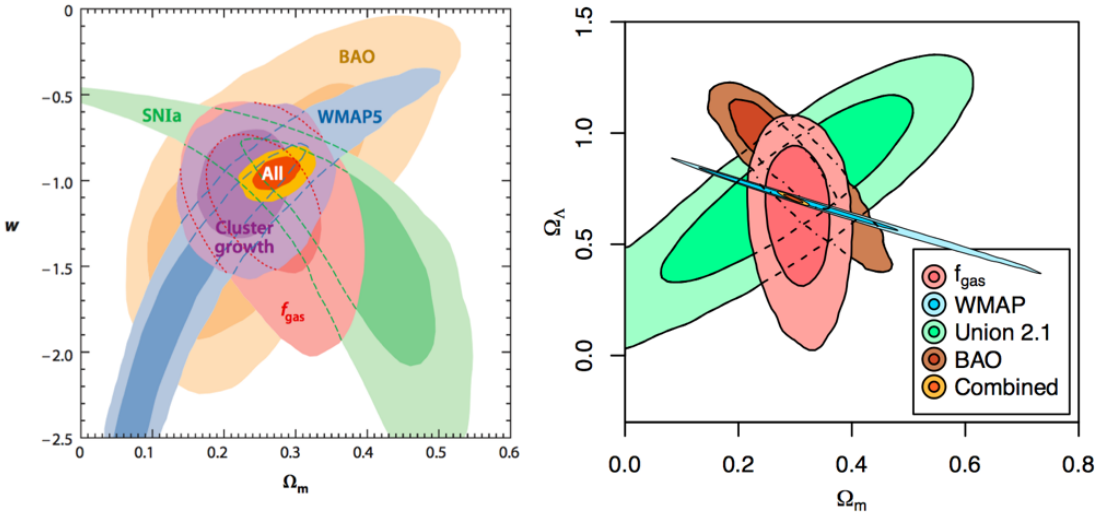

Figure 2.4: Cosmological estimates from joint data sets. *Left:* The 68.3% and 95.4% confidence levels in the dark energy equation of state parameter - matter density plane using information from galaxy cluster investigations through gas fraction, f_{gas}, measurements (Allen et al. 2008) and cluster number counts as a function of redshift (Mantz et al. 2010). The figure is taken from Allen et al. (2013) and also includes Supernova type 1a (Kowalski et al. 2008), WMAP (Dunkley et al. 2009) and BAO information (Percival et al. 2010). *Right:* The 68.3% and 95.4% confidence levels in the dark energy density - matter density parameter plane assuming a non-flat ΛCDM model are taken from Allen et al. (2013). The supernova information (Suzuki et al. 2012) is denoted by Union 2.1 and WMAP, BAO and $f_{\rm gas}$ levels were derived from Hinshaw et al. (2013), Anderson et al. (2013) and Suzuki et al. (2012) respectively.

In combining the results from cosmological investigations on galaxy clusters and supernova Type 1a investigations in conjunction with CMB and baryon accoustic oscillation (BAO) data, one can derive further estimates on w and Ω_Λ as is illustrated in Fig. 2.4. Galaxy cluster data therefore provides vital information in the $w - \Omega_m$ plane (Fig. 2.4), that complements the other techniques in use.

It can also be seen that the cluster growth information provides, at the present state, tighter constraints on the w parameter than gas mass fraction, $f_{\rm gas}$, measurements. Future high-redshift large sample galaxy cluster observations will decrease the acceptable parameter space in both galaxy cluster cosmological estimation techniques, allowing the nature of dark energy to be examined at greater precision.

2.3 Inflation and the seeds for structure formation

Having outlined the present findings on the cosmological parameters, it remains to be discussed how the CMB radiation can appear so uniform across the whole sky if only scales of 1° should have been in causual contact on the surface of last scattering - this denotes the horizon problem. In addition, for Eq. (2.18) to hold at the present epoch, it requires a considerable amount of fine-tuning in the past - the flatness problem. The lack of monopoles, predicted by a grand unified theory (GUT) phase transition, that describes the symmetry breaking resulting in the separation of the electroweak and strong forces, is another puzzle that cannot be solved directly.

These issues can be addressed via inflation theory - a theory that predicts a rapid expansion of the universe of the order of 60-70 e-foldings. I will give a qualitative explanation of inflationary theory below since the length of a mathematical description is beyond the scope of this introduction. For further details, readers are advised to consult review articles (Baumann et al. 2012) and Planck Collaboration XXII (2013). The mathematical approach relies on pertubing the Einstein field equations and choosing an appropriate gauge to describe the comoving curvature perturbations.

Inflation theory is based on the idea that there exists a scalar field ϕ which has an equation of state with negative pressure, giving rise to a period of rapid expansion. Different inflationary theories predict different starting conditions of the scalar field and different forms of the potential V(ϕ) (Fig. 2.5).

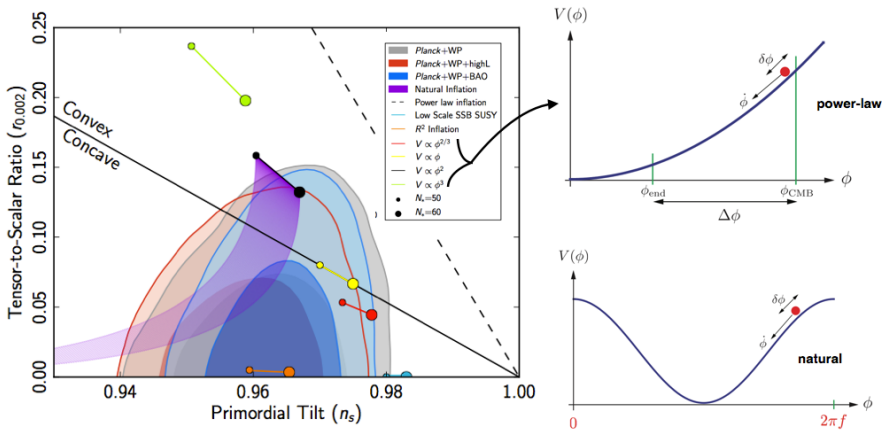

Figure 2.5: Planck predictions on inflationary models. *Left*: The tensor to scalar ratio plotted against the primordial tilt, defined in section 2.4, comparing the predictions of different inflationary models and forms of the inflaton potential with results from Planck and joint Planck+WMAP+BAO data with confidence levels (CL) of 68 % and 95 % (image credit: Planck collaboration XXII 2013). *Top right*: Potential form for chaotic inflation models (image credit: Baumann et al. 2012). *Botom right*: Potential form for natural inflation models. The periodicity is given by $2\pi f$ (image credit: Baumann et al. 2012).

In order for the rapid expansion period to be sustained under the assumption of a homogeneous scalar field, the theories predict that inflation be driven by the vacuum energy of the inflaton field. For inflation, the condition $\dot{\phi}^2 < V(\phi)$ must be met, which, in turn, implies that the potential must be sufficiently flat - the 'slow-roll' approximation.

For periods where the potential can be approximated to be flat, the scale factor grows exponentially, hence providing a solution for the flatness and horizon problems since small primordial perturbations are 'flattened out' and regions in space which are beyond today's horizon could have been in causual contact with each other at earlier times. Inflation ceases when the slow-roll condition is no longer satisfied and the field oscillates about its minimum. During the phase-transition of the scalar field, re-heating takes place which explains the thermal background after inflation. The reason for why a discussion on inflation is relevant for structure formation lies in the fact that it provides the seeds for the latter. This can be explained by the fact that the scalar field undergoes thermal quantum fluctuations. Due to the fact that field fluctuations link to perturbations in the stress-energy-momentum tensor, they also link to perturbations in the metric and thus to perturbations in space-time curvature.

These perturbations have scalar and tensor modes, the latter predicting gravitational waves. For the scalar modes, one can thus predict comoving curvature perturbations, under an appropriate gauge choice (choice of coordinate system), the details of which are outlined in Dimopoulos (2011). During inflation, the quantum fluctuations are inflated, the wavelength growing exponentially, while the amplitudes of the fluctuations are frozen in as they cross the horizon.

Inflation thus predicts super-horizon curvature perturbations, which can re-enter the horizon scale after the inflationary phase and are coherent, thus providing the seeds for the accoustic peaks in the power spectrum of the Cosmic Microwave Background (CMB) and subsequently also the seeds for the formation of structure. Recent BICEP2 experiment results (BICEP2 Collaboration, Ade et al. 2014) have, for the first time, shown a $>5\sigma$ detection of the CMB B-mode polarization, which puts further constraints on the r parameter in Fig. 2.5.

2.4 Linear and non-linear structure growth

As the curvature perturbations re-enter the horizon, they can be regarded as giving rise to fluctuations in the gravitational potential. A full treatment involves linking the perturbations of the energy-momentum tensor for a multi-component perfect fluid to the perturbations of the space-time metric. For small perturbations in the relative density contrast

$$\delta(\mathbf{x}, t) = \frac{\hat{\rho}(\mathbf{x}, t) - \bar{\rho}(t)}{\bar{\rho}(t)} \quad , \tag{2.22}$$

where $\hat{\rho}(\mathbf{x}, t)$ is the random density field depending on the comoving coordinate $\mathbf{x}$ and obeys gaussian statistics. The term $\bar{\rho}(t)$ denotes the average density at a given cosmic time t. For small perturbations, for which $\delta \ll 1$, one may use linear perturbation theory

on the continuity, Euler and Poisson equations for a perfect fluid. [3] Following the notation of Schneider (2010), one can therefore define a transfer function, T_k, that describes the evolution of the density contrast on different scales at an early epoch i to the current density fluctuation,

$$\frac{\delta_0(k)}{\delta_0(k_{ls})} = T_k \frac{\delta_i(k)}{\delta_i(k_{ls})} \qquad , \tag{2.23}$$

where k_{ls} denotes the wavenumber of a perturbation that entered the horizon in the matter-dominated phase and the subscript 0 denotes the current density contrast at the given scale. The initial properties of the density perturbations rely on isotropic homogeneous gaussian field statistics.

Knowing the evolution from linear perturbation theory, and the initial properties of the density field, one can therefore derive the power spectrum in the matter-dominated era to be related to the growth factor $D_+(a)$ via

$$P(k,a) = A k^{n_s} T_k^2 D_+^2(a) \qquad , \tag{2.24}$$

where $n_s \lesssim 1$ implies that, in the cold dark matter scenario, hierarchical structure formation is expected to proceed in a bottom-up approach with smallest scales collapsing first and then merging into larger scale structures. A is a normalization factor. The best fit value of n_s by Planck is 0.9603 ± 0.0073 (95% CL) (Planck Collaboration XXII 2013).

The normalization parameter is related to the dispersion of the density field when smoothed over a characteristic scale of $8h^{-1}$Mpc such that the dispersion parameter at this scale is defined as

$$\sigma_8^2 \equiv \sigma^2(8h^{-1}\mathrm{Mpc}) \qquad . \tag{2.25}$$

The rms variance of a linear density field smoothed on scale R is given by,

$$\sigma^2(R,t_i) = \frac{1}{(2\pi)^3} \int d^3k \;\; P(k,t_i) \mid W_R(k) \mid^2 \qquad , \tag{2.26}$$

where one can see that this is linked to the size-dependent, and thus R dependent, window filter function W and the linear matter power spectrum $P(k,t_i)$ at some early time t_i.

The linear regime is valid for very high redshifts but as shell-crossing, and therefore mode-mixing, takes place in the structure collapse, the linear approximation breaks down. One needs to resort to numerical simulations to follow the evolution of the dark matter and baryon density contrasts. There is one case though, in which one can make predictions into the non-linear regime: top-hat spherical collapse. The main assumptions rely on a homogenous Einstein de Sitter (EdS) universe in the matter-dominated phase filled with a collisionless fluid, which is affected by a single top-hat spherical perturbation. One can

[3] A full treatement of linearizing these equations follows from usual perturbation theory and the solving of second-order differential equations for sub-horizon perturbations.

follow the evolution of mass shells as a function of redshift during the expansion, eventual halt and collapse stages. The characteristic scales can be compared to the results of linear theory. The average overdensity of a virialized halo in this thought experiment can be shown to be ≈ 178, which is close to the $200 \times \rho_{cr}(z)$ often adopted in galaxy cluster studies.[4] Zel'dovich proposed a Lagrangian formalism which breaks down at a later stage than the linear model. It is based on the idea that a triaxial overdensity will collapse along the direction given by the largest eigenvalue of the deformation tensor describing how the particles, which the cosmological fluid is described by, move within a small time interval. This leads to the formation of sheets which then collapse into filaments and subsequently form halos.

2.5 Cosmological simulations

The Millenium Simulation explores the non-linear regime of structure formation by following the evolution of dark matter across a redshift range of $z = 127$ to $z = 0$ in a cube of side-length 500 h^{-1} Mpc containing 2160^3 particles (Springel et al. 2005).

A WMAP1 ΛCDM model is adopted and the initial conditions are based on gaussian perturbations. As one can see from Fig. (2.6), the dark matter distribution follows hierarchical structure formation with the smallest scales assembling first and then merging into larger halos along filamentary structures (Wechsler 2001).

There exist several methods of defining a DM halo in cosmological simulations, such as the Friends of Friends approach (FOF) (Davis et al. 1985). Navarro Frenk and White (1996) have shown that the NFW-profile, that describes the dark matter mass profile, takes the form

$$\rho(r) = \frac{\rho_s}{(r/r_s)(1 + r/r_s)^2} \tag{2.27}$$

where r_s is a scale parameter. In order to describe the inner cuspiness of simulated dark matter halos, Navarro (2010) tested the application of the Einasto profile (Einasto 1965). Navarro et al. (2010) were able to show that more peaked inner profiles better describe the shape of galaxy-sized halos. Recently, Okabe et al. (2013) have shown the NFW profile to be a good fit to a sample of stacked weak lensing measurements of 50 galaxy clusters across the redshift range $0.15<z<0.3$.

Since we cannot observe dark matter directly, re-simulations of dark matter halos including baryons and non-gravitational effects are vital (Planelles et al. 2013). Dolag et al. (2009) re-simulated a number of dark matter halos with different gas physics such as star formation and feedback, allowing the gas structure within galaxy clusters to be examined. This re-simulation is feasible as dark matter halos assemble first, with the baryon fluid falling into the dark matter potential wells at later stages since it experiences pressure forces that counteract collapse before the decoupling period of the baryon-photon fluid.

[4] The radius r_δ corresponds to the density contrast, δ, when compared to the critical density $\rho(z)$. The corresponding mass is denoted by M_δ.

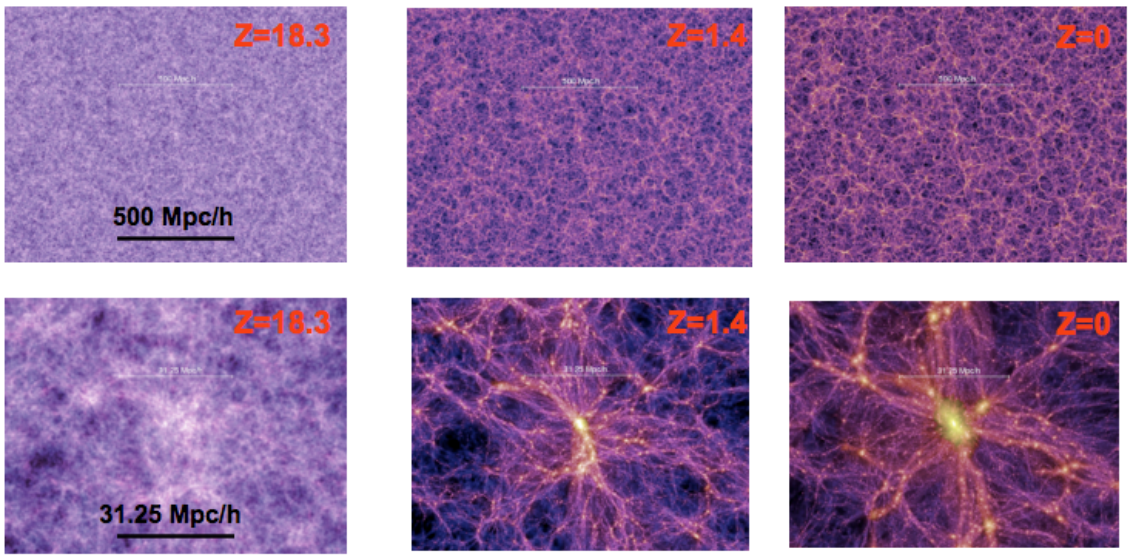

Figure 2.6: The Millenium simulation dark matter density cut-outs as a function of different redshifts (columns) and zoomed in regions (rows). One can clearly see small-scale structures forming first, which then agglomerate into larger scale structures along filaments. (Image credit: The Millennium Simulation Project webpage, VIRGO, Springel et al. 2005)

Due to the X-ray shape Theorem (Buote & Canizares 1994), the isodensity surfaces coincide with the dark matter iso-potential surfaces under the consideration of hydrostatic equilibrium

$$\nabla P \times \nabla \phi = \nabla \rho_{\rm gas} \times \nabla \phi = 0 \qquad . \tag{2.28}$$

Hence, one would expect the projected gas density and pressure distribution to be more spherical than the projected dark matter density. This can be seen in Fig. (2.7), which also illustrates that galaxy clusters become more spherical as a function of redshift[5]. Observations in the past years have suggested that non-gravitational processes can influence the gas properties such as the metallicity and entropy distributions in galaxy clusters. Subsequently, current hydrodynamical simulations are continuing to improve the modeling of processes such as winds, AGN feedback or pre-heating scenarios in order to reproduce the observed star formation rates and central cluster density profiles. The simulations in Fig. 2.7 follow the csf prescription that includes the effect of weak winds (Dolag et al. 2009).

[5] The JobRunner web application was constructed by Laurent Bourges and Gerard Lemson as part of the activities of the German Astrophysical Virtual Observatory.

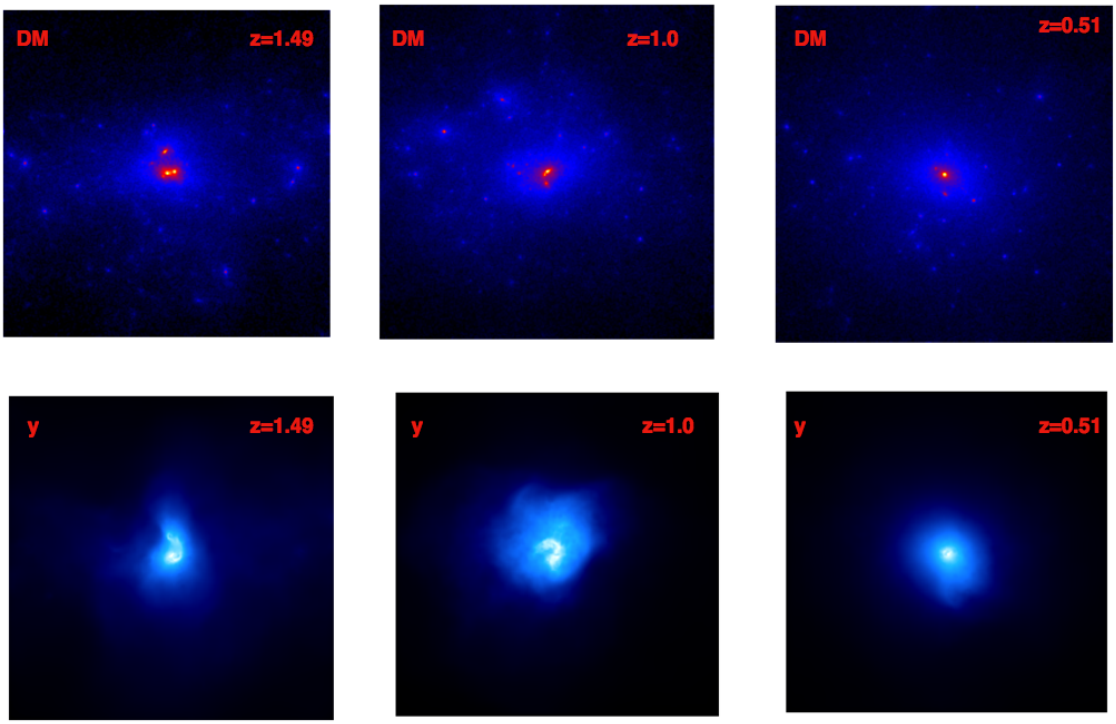

Figure 2.7: These simulations were made using Klaus Dolag's JobRunner tool (Dolag et al. 2009). The g51 cluster was chosen with the csf simulation model. The physical size of each image is 2 Mpc on each side. The units of the dark matter distribution (top row) are g/cm^2 and the gas simulations (bottom row) show the dimensionless Compton-y map, which is proportional to the integrated pressure along the line of sight. The ellipticity of the dark matter distribution decreases as a function of redshift. Merger events cause pressure variations, and therefore shock features, in the intra-cluster gas. The gas distribution is overall more spherical than the dark matter density distribution at a given redshift.

Chapter 3

Galaxy clusters: a cosmology perspective

Galaxy clusters are found in the intersections of filaments that form the cosmic web. Alluding to Feynman's quote, they are thus the knots in the fabric which reveal 'the organization of the entire tapestry'.
The abundance of galaxy clusters as a function of mass and redshift, their redshift-dependent angular size as well as their baryon budget probe the cosmological parameters which describe our universe.
This chapter gives an extensive overview on the present status of galaxy cluster research, drawing on the latest findings in multi-wavelength studies.
First, clusters are introduced from an observational viewpoint. This is then followed by a review on current galaxy cluster sample studies and their link to cosmological predictions. This subsequently promotes the necessity for studying the structure in galaxy clusters - the prime emphasis in this thesis being placed on high-resolution interferometric observations addressed from data and simulation perspectives.
I identified three major research foci - a pathfinder project on a single galaxy cluster using interferometric/bolometer single-dish Sunyaev-Zel'dovich data, simulations that assess the suitability of current and future interferometers in identifying relaxed and morphologically disturbed clusters, as well as mock observations of a merger-induced shock front using ALMA/ACA.

3.1 The anatomy of galaxy clusters

As their name suggests, galaxy clusters are assemblies of > 50 to 1000s of galaxies that, together with the intra-cluster gas and intra-cluster light, reside in dark matter potential wells. The size of galaxy clusters is of the order of a few Mpc and their masses range from $10^{14} - 10^{15} M_{\odot}$, with galaxy groups being in the lower mass range and usually containing < 50 galaxies.

Figure 3.1: A Hubble view of the galaxy cluster Abell 2218, exhibiting strong lensing arcs. (Image credit: NASA)

In 1933 Zwicky investigated the velocity dispersions of galaxies in the Coma cluster and, taking into account the mass to light ratio, postulated that 'dark matter is present with a much greater density than luminous matter' (Zwicky 1933). More recently, Becker et al. (2007) have shown the mean velocity dispersion of their massive cluster sample to be 854 ± 102 km s^{-1}. It is the dark matter which only interacts gravitationally that starts the formation of small-scale structure in the very early universe with the baryonic components falling into the dark matter potential wells later on since, before the era of decoupling, these are subject to radiation pressure forces. The brightest cluster galaxies, BCGs, are located at the bottom of a cluster's potential well and are preferentially aligned with its major axis (Niederste-Ostholt et al. 2010). The alignment of galaxies in galaxy clusters can thus be used as an indication for halo shapes (Hashimoto et al. 2008).

In this thesis, I mostly focus on the intra-cluster medium (ICM), which makes up $\sim 12\%$ of the mass of a galaxy cluster. In comparison, dark matter accounts for $\sim 85\%$ and stellar and galactic material for $\sim 3\%$. The intra-cluster light is a stellar component not confined to galaxies (Castro-Rodriguez et al. 2009). The intra-cluster medium is made up of a hot plasma with temperatures of the order of $10^7 - 10^8$ K and electron number densities of $10^{-4} - 10^{-2}$ cm^{-3} tracing the dark matter distribution in relaxed systems (as

opposed to dissociative merger events discussed in chapter 8).

As gas accretes onto the galaxy cluster from the filamentary structures, it undergoes adiabatic compression and shocks, thus giving rise to the high gas temperatures. For gas settled into the dark matter potential wells, under the assumption of hydrostatic equilibrium and spherical symmetry, hydrostatic equilibrium implies

$$\frac{1}{\rho_g}\frac{dP_g}{dr} = -\frac{d\phi}{dr} \qquad , \tag{3.1}$$

where ϕ is the cluster potential. For the ideal gas equation $P_g = \rho_g k_B T_g/(\mu m_u) = n_g k_B T_g$ this gives

$$M_{\rm total}(< r) = -\frac{k_B T_g(r) r}{G\mu m_p}\left(\frac{\partial {\rm ln}\rho_g(r)}{\partial {\rm ln}r} + \frac{\partial {\rm ln}T_g}{\partial {\rm ln}r}\right) \qquad , \tag{3.2}$$

where G is the gravitational constant, m_u is the atomic mass unit, μ is the mean molecular weight. $P_g(r)$, $n_g(r)$ and $T_g(r)$ denote the radially dependent gas pressure, density and temperature respectively. As the gas cools, star formation and black-hole accretion remove gas from the intracluster medium. Feedback processes are however thought to supply the ICM with sufficient energy to halter 'run-away' cooling, which provides an explanation for why the star formation rates (SFRs) are lower than expected from sole gravitational processes (McDonald et al. 2011, Hicks & Mushotzky 2005, Rawle et al. 2012). This balance between heating and cooling mechanisms is an active field of research with hydrodynamical simulations trying to match the observed temperature and entropy distributions of the intracluster gas to their feedback recipes. In current studies, particular focus is given to the amount of feedback, its onset and the relative contribution from supernovae, winds or AGNs (Battaglia et al. 2012).

3.2 Galaxy cluster research: current perspectives

Galaxy clusters provide an exciting interface between cosmology and astrophysics. As a result of hierarchical structure formation, their morphological states range from relaxed systems, hosting cooling cores, to systems whose states have become disturbed due to recent merger actitviy. If mere gravitational effects played a role in cluster formation, one would expect galaxy clusters to be scaled versions of each other. Departures from self-similarity arise due to the action of non-gravitational effects such as feedback processes or preheating scenarios. In addition, geometric assumptions such as spherical symmetry are thought to bias single-cluster mass estimates.

It is therefore vital for cosmological studies to ensure that mass estimation on individual clusters is as accurate and as precise as possible. With future and current instruments, such as e-ROSITA and Planck, being expected to produce large cluster catalogues, we are going to be limited mostly by our understanding of systematics rather than number counts. There is growing evidence that the study of a relaxed galaxy cluster subset should be preferred for obtaining cosmological estimates, since they exhibit less scatter than

disturbed systems in the observable-mass scaling relations. This factor will be ever more important in the current era in which surveys are detecting an increasing number galaxy clusters at redhifts above 1, the merger rate being higher at these redshifts than at the current epoch, stressing that the associated uncertainties in the effect of systematics need to be studied in detail. In addition, studying the merger history via simulations and the nature of shock fronts through observational studies of galaxy clusters gives insight into the nature of dark matter and the temperatures attainable in such merger scenarios.

3.2.1 An X-ray view of galaxy clusters

The hot diffuse intra-cluster medium cools through a combination of thermal bremsstrahlung, recombination and de-excitation radiation giving rise to extended X-ray emission (Sarazin 1988, Böhringer et al. 2010). The X-ray luminosity of galaxy clusters, L_X, ranges from 10^{43} to 10^{45} erg s^{-1}. X-ray observations with high-resolution spatial and spectral instruments such as those on the *Chandra* and *XMM-Newton* satellites, have enabled the study of density, metallicity and temperature profiles in galaxy clusters (Leccardi et al. 2008, Arnaud et al. 2010). The X-ray surface brightness of a cluster at redshift z , is given by

$$S_X = \frac{1}{4\pi(1+z)^4} \int n_e^2 \Lambda_{eH} dl \qquad , \tag{3.3}$$

where Λ_{eH} is the X-ray cooling function and the integral is performed along the line of sight. The electron density squared dependence implies that X-ray observations are particularly sensitive to regions in which the density is highest, as well as to clumping effects in cluster outskirts and shock structures in the central regions of clusters (Fig. 3.2).

The Perseus cluster, $z = 0.0179$, being the brightest X-ray observed cluster in the sky, is a prime example for illustrating the potential of X-ray observations. Recent observations with the Suzaku satellite have allowed cluster outskirts to be mapped out to beyond R_{200} (Simionescu et al. 2011, Urban et al. 2014). Urban et al. (2014) explain the mismatch between measured and expected density and pressure profiles due to the effect of gas clumping (Fig. 3.2).

Fabian et al. (2003, 2011) and Sanders & Fabian (2007) have studied the centre of the Perseus cluster with deep exposure Chandra measurements (Fig. 3.2). The resulting high-resolution X-ray image shows a highly disturbed intra-cluster medium, classified by a combination of a cold front, a shock structure (Churazov et al. 2003), sound wave ripples as well as two X-ray cavities. The latter are caused by relativistic plasma that is blown into the ICM through AGN radio jets, observed with the VLA (Fabian et al. 2003). It is the low redshift of the Perseus cluster, which enables such detailed analyses to be feasible in terms of a cost benefit analysis considering scientific outcome versus the required observation time. Due to the $1/(1+z)^4$ dependence of the X-ray surface brightness, it is not viable to invest an equivalent or even higher observation time on clusters at higher redshifts due to the decreased photon count statistics (Fig. 3.3).

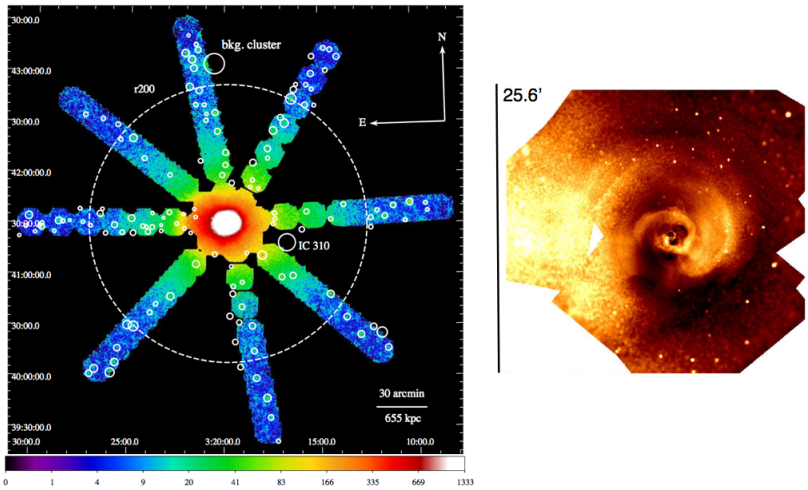

Figure 3.2: X-ray observations of the Perseus clusters. *Left*: An image by Urban et al. (2014) showing *Suzaku* observations of the Perseus cluster beyond the virial radius (dashed circle), the small circles indicating the presence of point sources. *Right*: An image by Fabian et al. (2011) showing the adaptively smoothed fractional variation image of an 1.4 Ms *Chandra* exposure. One can clearly see the X-ray cavities and associated sound waves, illustrating the sensitivity of X-ray observations to density contrasts.

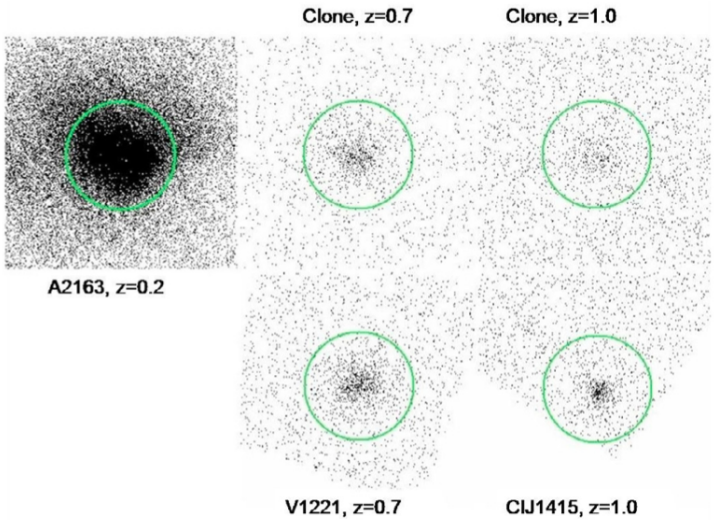

Figure 3.3: A mock simulations study taken from Santos et al. (2008), outlining the decreased photon count statistics at higher redshifts for clone clusters with the same properties as their lower-redshift counterpart A2163. A qualitative comparisons with real data at these redshifts is given below.

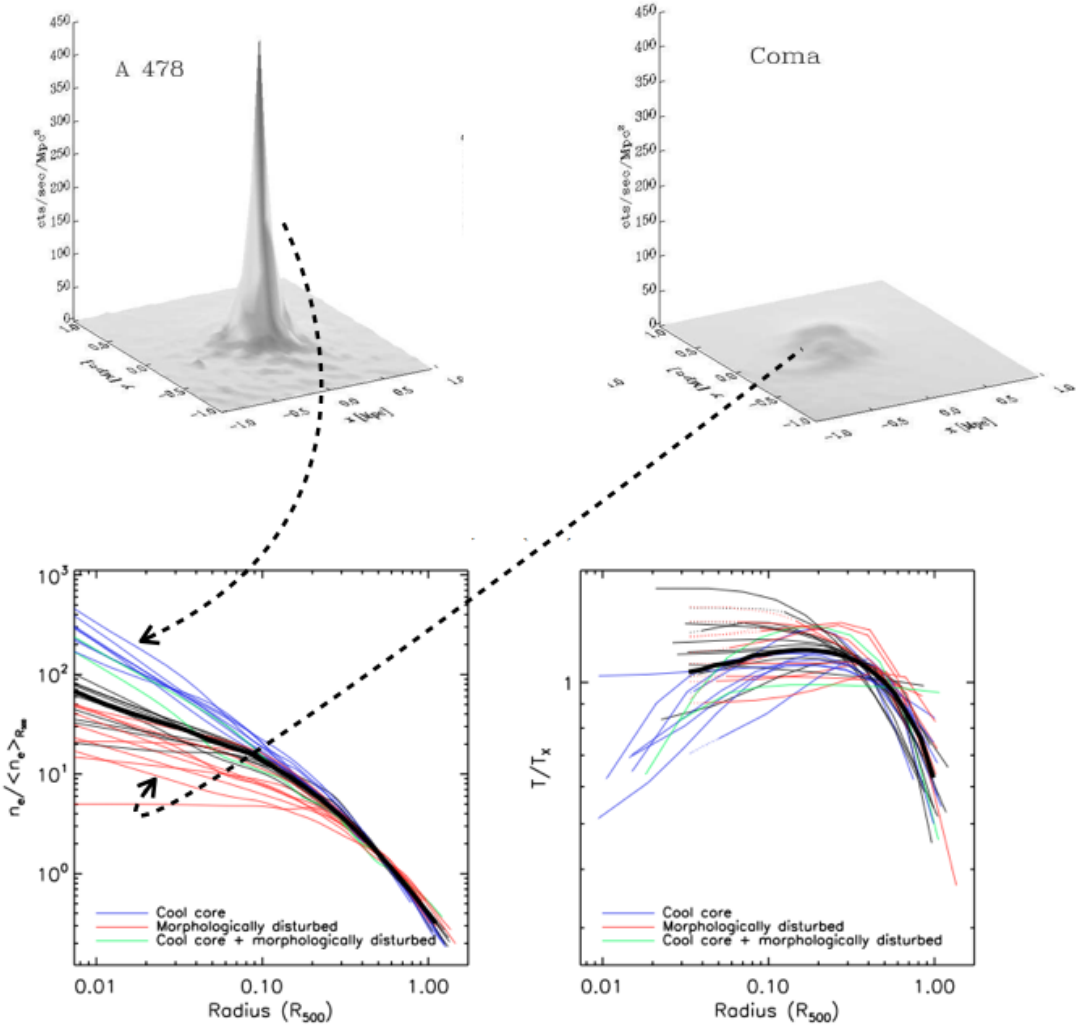

Figure 3.4: The Arnaud galaxy cluster sample illustrating relaxed and morphologically disturbed clusters. *Top*: Fabian & Sanders (2009) illustrate the difference in the nature of relaxed and morphologically disturbed galaxy clusters via the excess central surface brightness signature in the former, which also manifests itself in a higher central density profile *(bottom left)* and lower central temperature value *(bottom right)* as is illustrated by the the z<0.2 Arnaud cluster sample (Arnaud et al. 2010). The profiles are scaled to R_{500} and normalized by the respective mean density within R_{500} and the average spectroscopic temperature within [0.15 - 0.75] R_{500} (R_{500} denotes the radius at which the density is 500 times the critical density at the cluster's redshift).

Radial temperature information is usually obtained from spectral fitting in annular regions whose total areas are dependent on the photon count statistics.

In the early era of X-ray observations, Cavaliere & Fusco-Femiano (1976) put forward the isothermal beta profile. In galaxy cluster studies, this has been used extensively as a parametric description of galaxy clusters' surface brightness radial variations, such that

$$S_X = S_{X0}\left(1 + \frac{\theta^2}{\theta_c^2}\right)^{\frac{1}{2}-3\beta} \quad , \tag{3.4}$$

where S_{X0} is the central surface brightness, β is the slope parameter and θ_c corresponds to the angular core radius. The corresponding expression for the gas density under the assumptions of spherical symmetry, isothermal cluster properties and hydrostatic equilibrium gives

$$n_g(r) = n_{g,0}\left[1 + \frac{r^2}{r_c^2}\right]^{\frac{-3\beta}{2}} \quad , \tag{3.5}$$

where $n_{g,0}$ is the central gas density and r_c is the core radius. With high resolution Chandra and XMM-Newton X-ray satellite missions opening up the opportunity of $1''$-$6''$ angular resolution observations, annular spectroscopic temperature fitting has become possible in the past decade. It was shown that the isothermal assumption was not valid for clusters since radial temperature dependences were indeed observed (Arnaud et al. 2010, Fig. 3.4). In addition, a sub-sample of clusters were shown to exhibit excess surface brightness signatures in the centre of clusters (Fig. 3.4 (top)).

These clusters were thus termed cool-core clusters and the concept of a double-beta model fit with inner and outer normalization, core and slope parameters was suggested and applied to data. This discovery also led to the 'cooling-flow' problem on account of the low detected quantity of cold gas in the clusters' central regions and the lower than expected star formation rate from sole mass deposition rate estimates (Peterson & Fabian 2006). At redshifts below 0.2, Arnaud et al. (2010) illustrate that, on average, cool-core clusters exhibit a decline in temperature towards their central regions and can thus be distinguished from less relaxed systems.

A detailed discussion on the derived characteristic pressure and entropy profiles, as well as the possible solutions to the 'cooling flow' problem, will follow in section 3.4 and chapter 7.

3.2.2 The Sunyaev-Zel'dovich effect

The Sunyaev-Zel'dovich effect is caused by inverse Compton scattering of Cosmic Microwave Background photons off hot electrons in the intra-cluster gas (Fig. 3.5 a & b). This causes the CMB spectrum to be shifted to higher frequencies (Fig. 3.5c), resulting in a CMB decrement/increment below/above 217GHz in the cluster direction (Fig. 3.5e, Fig. 3.6), when only considering the pure thermal SZ effect.

The preferential up-scattering of CMB photons can be derived by calculating the probability of a single photon scattering event for a given frequency shift and electron velocity and by combining this with the properties of the electron velocity distribution (Birkinshaw et al. 1999). There is only a $\approx 1\%$ chance of a CMB photon scattering off an electron (Carlstrom et al. 2002).

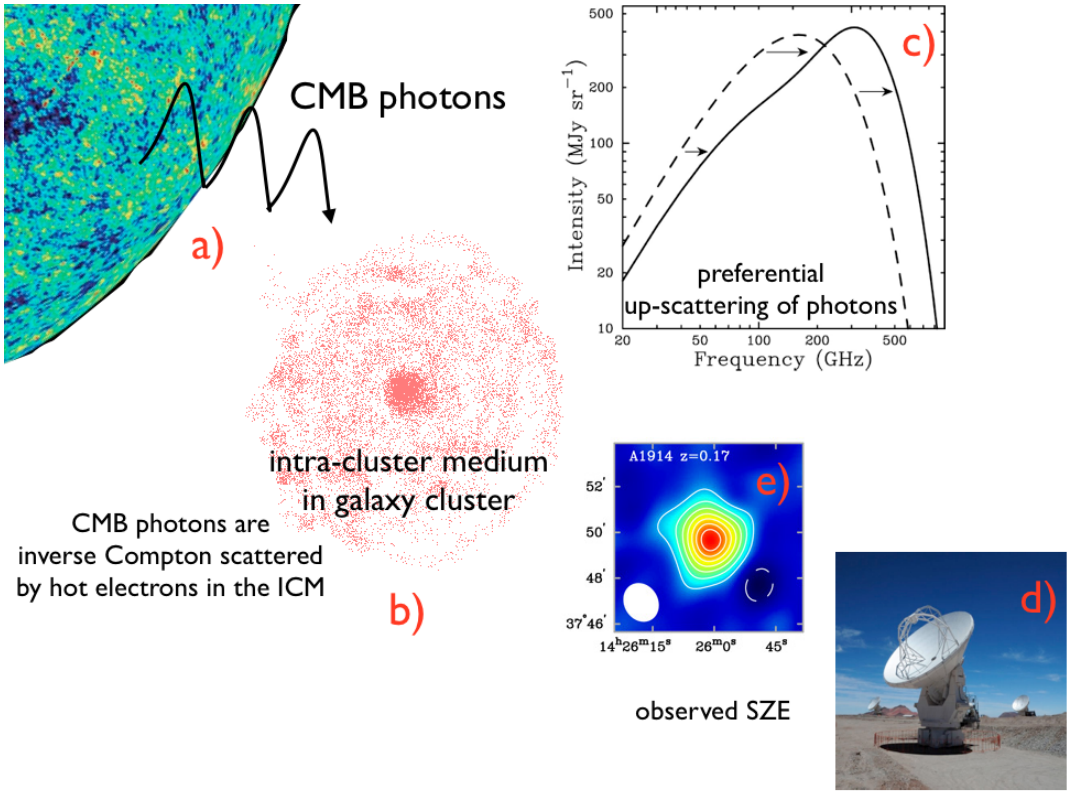

Figure 3.5: An illustration of the Sunyaev-Zel'dovich effect: CMB photons stream freely since the surface of last scattering (a) (image credit: NASA / WMAP Science Team). When they traverse a galaxy cluster and thus also its gas plasma (b), $\approx 1\%$ of these CMB photons are preferentially up-scattered towards higher frequencies (c) (image credit: Carlstrom et al. 2002) through inverse-Compton scattering. This effect can be observed with radio telescopes (d) (image credit: ALMA (ESO/NAOJ/NRAO), W. Garnier (JAO)) which detect a decrement signature in the sky at frequencies below 217 GHz (assuming a pure thermal SZE) (e) (image credit: Carlstrom et al. 2002).

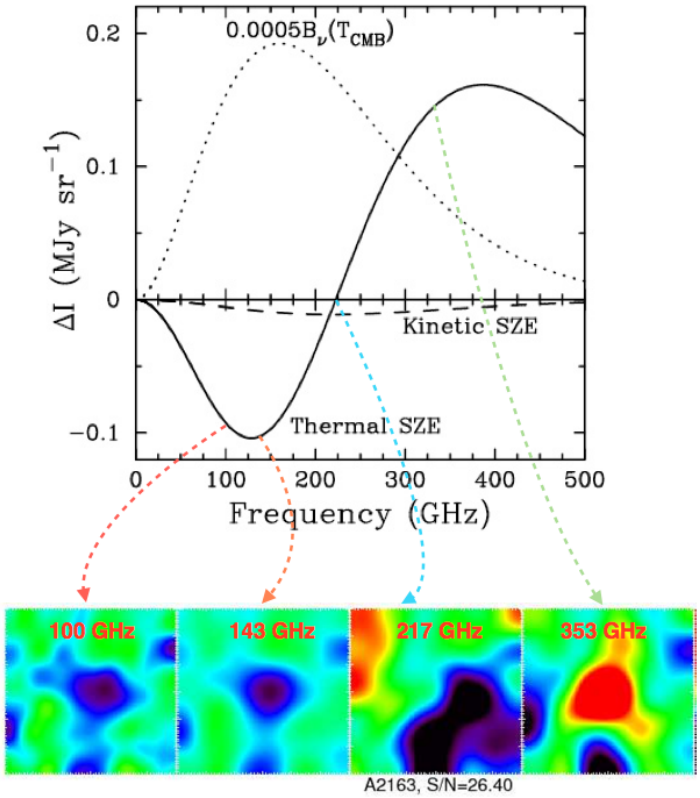

Figure 3.6: The spectral signature of the Sunyaev-Zel'dovich effect. *Top:* The thermal and kinetic SZ ($v_{peculiar}$ = 500 km s^{-1}) spectral CMB distorsions as a function of frequency taken from Carlstrom et al. (2002). *Bottom:* The frequency dependence is further illustrated through Planck multi-frequency cutouts of the galaxy cluster A2136 (Planck Collaboration Early results VIII 2011)

In the non-relativistic limit, the scattering process can be described by a so-called Kompaneet's scattering kernal, Fig. 3.7 (Birkinshaw et al. 1999), giving rise to the thermal Sunyaev-Zel'dovich effect, which fails to describe relativistic electron populations.

The spectral distorsion in terms of the dimensionless frequency $x \equiv h\nu/k_B T_{CMB}$ can be expressed as

$$\frac{\Delta T}{T_{CMB}} = f(x)y \qquad , \tag{3.6}$$

where y is a dimensionless parameter, the Compton y-parameter, which denotes the electron pressure integrated along the line of sight

$$y = \int \sigma_T \frac{k_B T_e}{m_e c^2} n_e dl \qquad . \tag{3.7}$$

The spectral distorsion is therefore redshift independent, the redshift merely affecting the angular size of clusters in the sky. The parameter f(x) describes the spectral signature via

$$f(x) = \left(x\frac{e^x+1}{e^x-1} - 4 \right) (1 + \delta_{\rm rel}(x, T_e)) \qquad , \tag{3.8}$$

where the $\delta_{\rm rel}(x, T_e)$ includes relativistic corrections. In terms of units of specific intensity, one can write

$$\Delta I = \frac{2(k_B T_{\rm CMB})^3}{(hc)^2} y \frac{x^4 e^x}{(e^x-1)^2} \left(x\frac{e^x+1}{e^x-1} - 4 \right) (1 + \delta_{\rm rel}(x, T_e)) \qquad . \tag{3.9}$$

Recently, the Planck satellite has mapped galaxy clusters from 44GHz to frequencies that probe the increment region of the Sunyaev-Zel'dovich effect, illustrated in Fig. 3.6.

The relativistic SZ effect can either be obtained via a higher order expansion of the scattering equations in the electron temperature (Challinor et al. 1998, Itoh et al. 1998), or indeed via the Boltzmann equation numerical integration approach (Itoh et al. 2004), this method being more accurate up to higher temperatures and frequencies. A comparison of the scattering kernal for non-relativistic and relativistic electrons is given in Birkinshaw et al. (1999) and shown in Fig. 3.7 (top). Fig. 3.7 (middle) shows the spectral distorsion using the Itoh et al. (2004) numerical fits and Fig. 3.7 (bottom) compares this to the electron temperature expansion of Itoh et al. (1998) in order to illustrate the validity of the latter as a function of the dimensionless frequency range.

The kinetic SZ effect (kSZ) is caused by the effect of the bulk motion of the ICM and therefore lends itself well to non-thermal pressure ICM studies. Recently, the detection of the kSZ in MACS J0717.5+3745 has been reported (Sayers et al. 2013). Future instruments such as CCAT will make kSZ measurements a promising tool for improving SZ power spectrum modeling (CCAT Scientific Memo in prep).

In the case of the isothermal beta model described in section 3.2.1, one can express the brightness temperature profile parametricallly as

$$\Delta T(\theta) = \Delta T_0 \left(1 + \frac{\theta^2}{\theta_c^2} \right)^{(1-3\beta)/2} \tag{3.10}$$

with ΔT_0 being the central brightness temperature change and $\theta = r_c/D_A$. Equivalently, one can define the central Compton-y parameter, y_0. A variable that is proportional to a galaxy cluster's total thermal energy content, is the spherically integrated Compton Y parameter

$$Y_{\rm sph}(r) = \frac{4\pi\sigma_T}{m_e c^2} \int_0^r P_e(r') r'^2 dr \qquad . \tag{3.11}$$

The cylindrically integrated Y parameter in terms of the radial 3D pressure profile $P_e(r)$ integrated over a projected radius R, can be expressed as

$$Y_{\rm cyl}(R) = \frac{2\pi\sigma_T}{m_e c^2} \int_{-\infty}^{\infty} dl \int_0^R P_e(r) r dr \qquad . \tag{3.12}$$

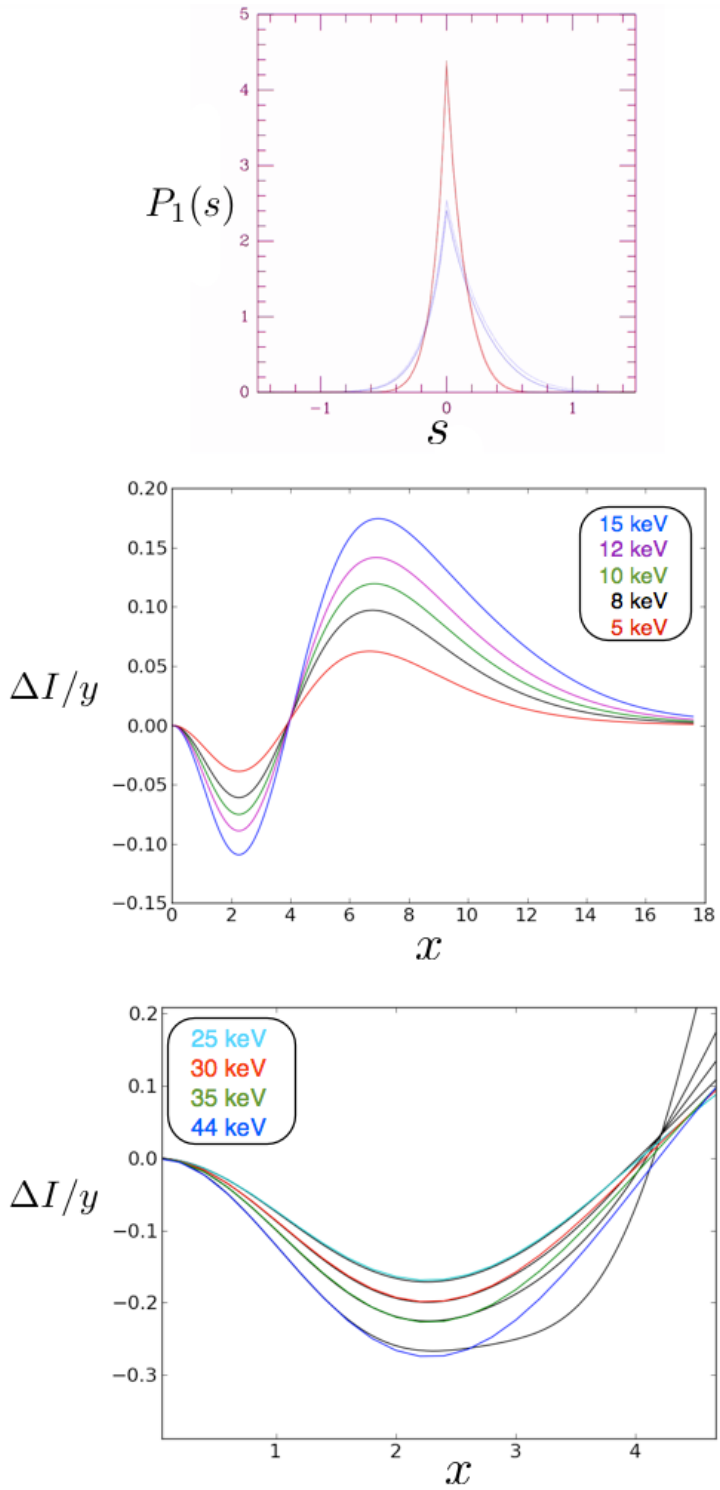

Figure 3.7: The relativistic SZ effect. *Top*: The scattering kernel as a function of the logarithmic frequency shift, s, for 5.1 keV (red) and 15.3 keV (blue) electron temperatures taken from Birkinshaw et al. (1999). This illustrates the necessity for using the relativistic formulation in the 15.3 keV case. *Middle*: The relativistic spectral distorsion for different electron temperatures as reported in the Itoh et al. (2004) numerical fits. *Bottom*: A comparison of the results by Itoh et al. (2004) (coloured lines) with the numerical higher order temperature expansion results of Itoh et al. (1998) (black lines) for different electron temperatures. As one can see, the disagreement is strongest for the highest electron temperatures.

3.2.3 Weak and strong lensing

Both, the Sunyaev-Zel'dovich effect and the X-ray emission are dependent on ICM gas properties and therefore rely on assumptions of hydrostatic equilibrium and non-thermal pressure support alongside with assumed symmetry properties in order to derive a galaxy cluster's total mass, unless the latter is derived from empirical scaling relations (section 3.5).

Weak and strong lensing probe the gravitational cluster potentials directly without having to rely on the assumed state of the ICM (Becker & Kravtsov 2011). Projection effects through the projected surface mass density dependence of weak lensing measurements are nevertheless present. Lensed arc statistics help in pinning down a galaxy cluster's dark matter triaxiality (Oguri et al. 2003). The concept of galaxy cluster gravitational lensing exploits the fact that light travels along geodesics following the curvature of space-time caused by the presence of the massive galaxy cluster.

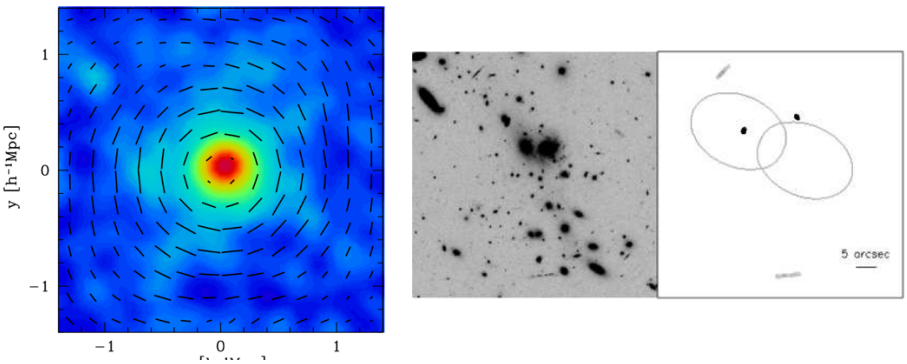

Figure 3.8: *Left*: The stacked lensing signal from 25 galaxy clusters. The figure is taken from Oguri et al. (2012). The lines indicate the smoothed orientation of the shear and the smoothed surface density map. *Right*: The strong lensing arcs in the galaxy cluster MS0451 with a sketch of the best model fit (Comerford et al. 2006). A more prominent example of lensing arcs can also be seen in Fig. 3.1.

Hence, light from background galaxies can be lensed into strong lensing arcs and multiple images if the lens is massive and the background source is close enough to the lens. In the weak lensing regime, one can statistically measure small distorsions of background sources (Fig. 3.8). Weak lensing analyses suffer from uncertainties in shape measurements (Young in prep) and source redshifts (Applegate et al. 2012, Gruen et al. 2013), a factor which needs particular attention at very high redshifts.

Mathematically, gravitational lensing can be characterized by three distances under the thin lens approximation, which treats the source and lens as planes in redshift space: the angular diameter distance from the source to the lens (D_{ds}), the angular diameter distance from the lens to the observer (D_d) and the angular diameter distance from the observer to the source (D_s), (Fig. 3.9). From these, one can derive the deflection angle,

α and the angle at which the source would be observed in the absence of the lens. In addition, one can define an angle, θ, with respect to the optical axis. For a detailed lensing review, the reader is advised to consult Schneider (2005), Bartelmann & Schneider (2001) and Umetsu et al. (2013), whose approaches are followed in this section.

The convergence, κ, is defined as the projected mass density, Σ, normalized by the critical density Σ_{cr}

$$\kappa(\vec{\theta}) = \frac{\Sigma(\vec{\theta}D_d)}{\Sigma_{cr}} \quad , \tag{3.13}$$

where

$$\Sigma_{cr} = \frac{c^2}{4\pi G D_d}\frac{D_s}{D_{ds}} \quad . \tag{3.14}$$

In the case where $\kappa \ll 1$, the weak field condition is satisfied such that weak lensing analyses apply.

One can write the deflection angle, $\vec{\alpha}(\vec{\theta})$ as

$$\vec{\alpha}(\vec{\theta}) = \frac{1}{\pi}\int d^2\theta' \kappa(\vec{\theta'})\frac{\vec{\theta}-\vec{\theta'}}{|\vec{\theta}-\vec{\theta'}|^2} \quad , \tag{3.15}$$

which can itself be related to the deflection potential ψ via the relation

$$\vec{\alpha} = \nabla\psi \quad . \tag{3.16}$$

In practice, the measured statistical shear distorsions (Kaiser et al. 1995), under the assumption of a randomly oriented background galaxy sample, can be related to the convergence through inversion, although the effects of mass-sheet degeneracy need to be considered.

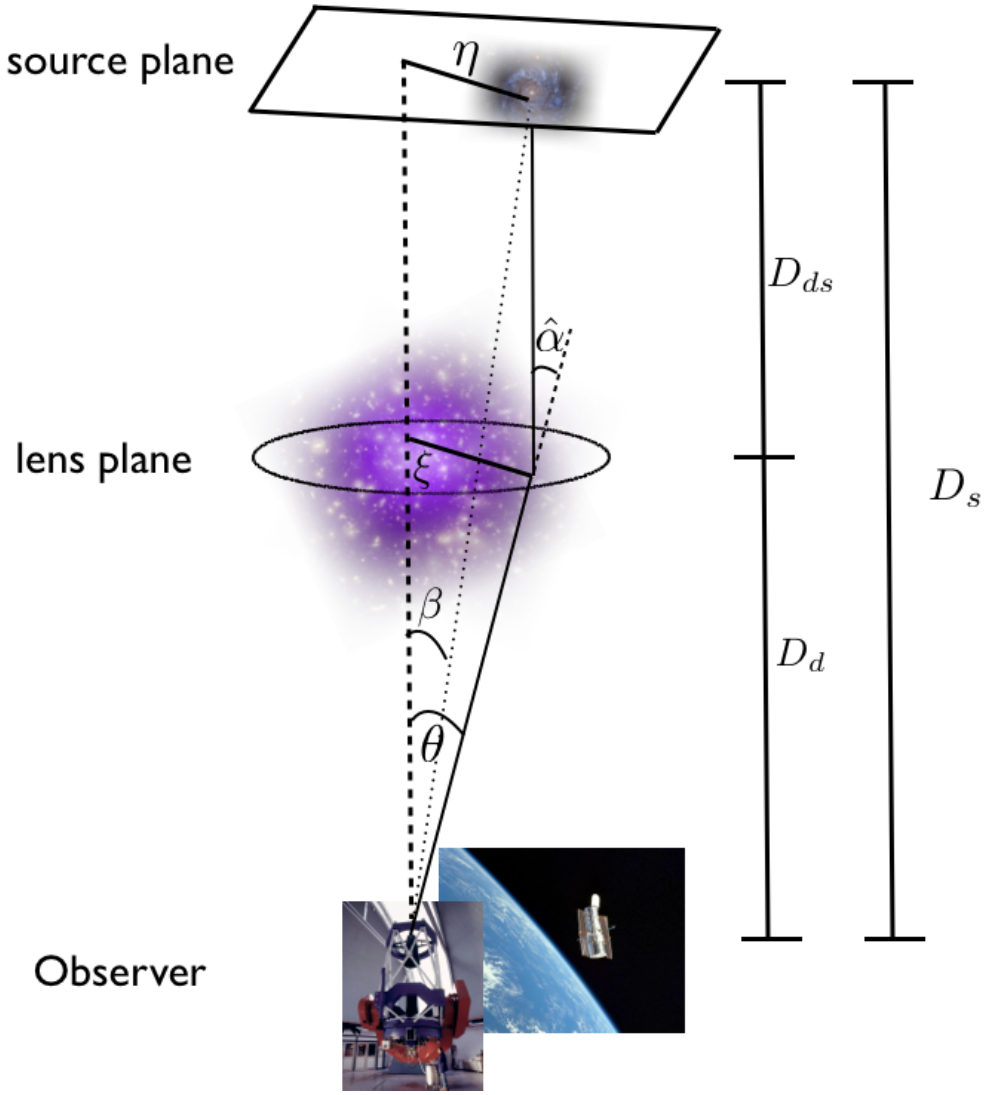

Figure 3.9: The concepts of gravitational lensing. The sketch is based on a figure in Bartelmann & Schneider (2001). It illustrates the source and lens planes as well as the observer in the form of space-based telescopes (Hubble, image credit: NASA) or ground-based mirrors (MPG/ESO 2.2-metre telescope, image credit: ESO/H.H.Heyer). The angular diameter distance from the source to the lens (D_{ds}), the angular diameter distance from the lens to the observer (D_d) and the angular diameter distance from the observer to the source (D_s) are also indicated. Only a single source in the source plane is sketched for clarity purposes.

3.2.4 IR and other cluster detection methods

Galaxy clusters can be identified via their red-sequence in colour-magnitude space (Gladders & Yee 2005). This has been exploited in the Red-Sequence-Cluster Survey (RSC), (Barrientos et al. 2003) and the second RCS2 survey, which aim to detect clusters up to redshift 1. In addition, the IRAC camera on Spitzer has allowed galaxy cluster searches to be conducted above redshift 1 using colour selection techniques (Papovich et al. 2010) (Fig 3.10).

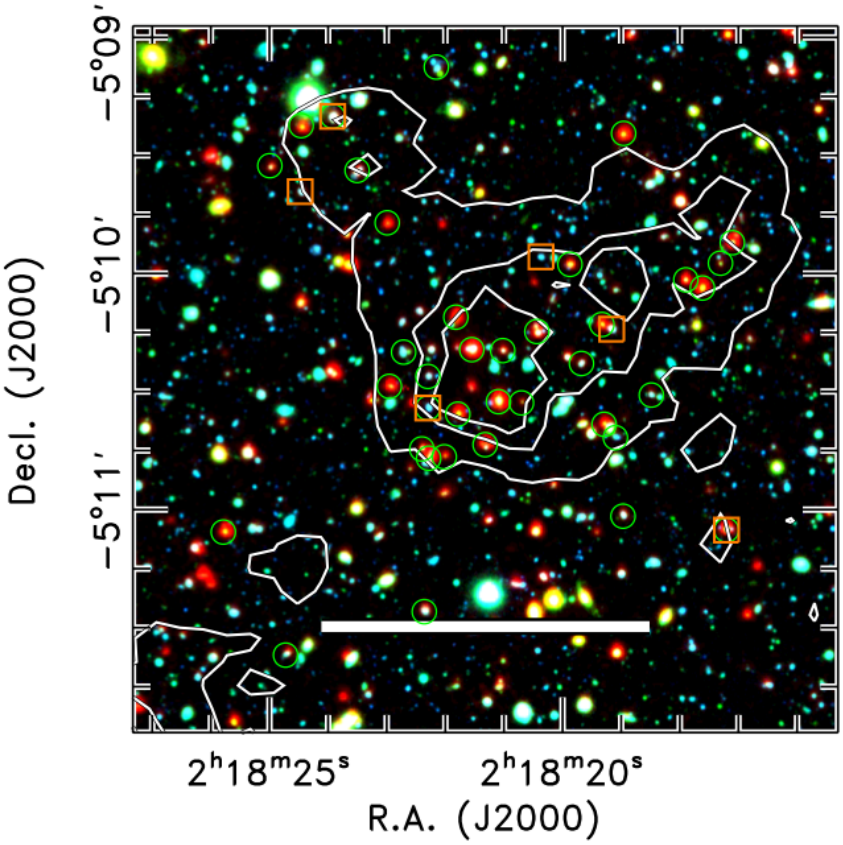

Figure 3.10: A Spitzer-detected galaxy cluster at redshift 1.62. The image is taken from Papovich et al. (2010) and constitutes a combined image of Spitzer 4.5 μm band and Suprime-Cam B and i-band data with green circles indicating potential cluster members.

Smolčić et al. (2007) present a study of a wide angle tailed radio galaxy whose tails are thought to be bent due to ram pressure. The presence of such bent jets has been suggested to be a good tracer of young galaxy clusters. This has been investigated as part of the FIRST survey by Blanton et al. (2003).

Non-thermal radiation from galaxy clusters has been observed in the form of synchroton radiation from radio relics, radio halos and radio mini halos due to the presence of the

order of μG magnetic fields (Bonafede et al. 2010).

Radio relics are highly polarized radio emission regions found in the cluster periphery (van Weeren et al. 2011, Venturi et al. 2013). Their bent shape suggests that they trace shock waves from merger events (Enßlin & Brüggen 2002). Radio halos represent diffuse emission with large-scale sizes of 1-2 Mpc. Radio mini-halos are located in the very central regions, a few hundred kpc in size (Donnert et al. 2013).

The mechanism that produces the large-scale unpolarized radio emission from galaxy clusters is a current active field of research with two scenarios being at the forefront of studies: the hadronic model versus the re-acceleration model. Both of these models have been motivated by the fact that the lifetime of cosmic ray electrons is far shorter than the characteristic time needed to cross the size of radio halos (Donnert et al. 2013). The re-acceleration model proposes that electons are accelerated by merger-driven turbulence plasma waves (Brunetti et al. 2012, Enßlin et al. 2011). The methods by which the flat extended cosmic ray profiles can be re-produced have been studied by Ensslin et al. (2011), who found streaming to be an important component in the generation of radio halos. The hadronic model is based on the fact that the lifetime of cosmic ray protons should be higher than cosmic ray electrons, overcoming the aforementioned need for cosmic ray electron re-acceleration to account for extended radio halos. The model predicts the generation of gamma rays (Brunetti et al. 2012) and secondary particles on account of a hadronic cascade (Donnert et al. 2013, Dermer 1986).

Future radio halo observations from LOFAR (Ferrari et al. 2012) and the SKA will provide a plethora of data in the next decades that will help to pinpoint the exact non-thermal processes in galaxy clusters.

The detection of gamma ray emission from galaxy clusters would shed light not only on the acceleration process that creates its emission but also on the possibility of dark matter annihilation. Supposing dark matter to be composed of weakly interacting massive particles (WIMPS), one of their annihilation products is predicted to be in the form gamma ray emission. The chosen dark matter candidates of WIMPs is motivated by their predicted abundance which matches the cosmological predictions well. Galaxy clusters are particularly well-suited for such annihilation fingerprint searches due to their high DM mass and recent formation histories (Pinzke et al. 2009).

The Large Array Telesope (LAT) instrument on the Fermi satellite makes gamma ray observations across the energy range 20 MeV to above 300 GeV (Atwood et al. 2009). Ackerman et al. (2013) have reported a tentative spectral line at 133 GeV with a significance of 3.3σ. They do not yet claim this to be a direct proof of a WIMP signal, but stress the need for further systematic bias studies before a firm conclusion can be reached.

The previous sections have thus given an overview of the multi-wavelength observational techniques used in galaxy cluster research, which will help in assessing the suitability of current and future instruments for detecting structures in clusters at different scales.

3.3 Significance of galaxy cluster studies for cosmology

Having established that galaxy clusters form from the seeds of rare primordial density fluctuations, it is therefore expected that their abundance and mass/redshift distribution should give insight into the matter power spectrum, the amount of dark and baryonic matter in the universe as well as the dark energy equation of state. There are several different ways in which galaxy clusters can be used for cosmological studies. Below, I illustrate how different cosmological parameters affect our current picture of structure distribution across a wide redshift range in our universe.

First, it is necessary to find an expression that describes how the cluster number density within a given physical scale changes as a function of redshift and cosmological parameters. In a 'perfect survey', survey-specific factors such as observable/mass survey limits, the survey spectral and spatial response and coverage do not need to be taken into account. Since, however, I will be discussing the neccessity of low-scatter scaling relations in section 3.4, this discussion will follow the approach and notation by Planck Collaboration XX (2013), which includes a discussion on survey limitations.

The galaxy cluster property which best describes its evolutionary state in the process of hierarchical structure formation is the mass M_Δ within a given radius r_Δ, characterized by the radius that encompasses a mean density, which is Δ times bigger than the critical density, $\rho_c(z)$, at the cluster redshift. Suppose that a survey with a survey completeness f_s detects galaxy clusters via the observable O_Δ through its signal amplitude $O_{f,\Delta}$ and characteristic angular extent $O_{\theta,\Delta}$. The number of clusters observed within a redshift element dz and solid angle $d\Omega$ is then given by

$$\frac{dN}{dzd\Omega} = \int f_s(M_\Delta, z, \epsilon, \eta)\frac{dN}{dzdM_\Delta d\Omega}dM_\Delta, \tag{3.17}$$

the survey completeness,

$$f_s = \int dO_{(f,\Delta)} \int dO_{(\theta,\Delta)} P(M_\Delta, z \mid O_{(f,\Delta)}, O_{(\theta,\Delta)}) f_{\rm instr}(O_{(f,\Delta)}, O_{(\theta,\Delta)}, \epsilon, \eta), \tag{3.18}$$

being dependent on the intrinsic properties of the measurement characteristics $f_{\rm instr}$ as a function of sky position (ϵ, η) and also on the probability that the measured quantity reflects the true mass, a topic to which I will return in the discussion on scaling relations. The instrument characteristics may include factors such as scanning strategies, beam characteristics as a function of position on the sky and sensitivity limitations of the survey.

As was discussed in the last chapter, in order to predict the evolution of linear density perturbations into the non-linear regime, N-body simulations are needed. Tinker et al. (2008) propose a mass function, that describes the number density of halos of mass M, based on the assumption that a halo can be described by a spherical overdensity, whose radial extent is defined by a given overdensity within this sphere measured with respect to the mean density at the redshift of the halo[1]

[1] I assume that, following Planck collaboration XX (2013) a conversion from the mean to the critical overdensity convention has been included, allowing the aperture radius to be labelled with Δ

$$\frac{dN}{dM_\Delta}(M_\Delta, z) = f_{mf}(\sigma)\frac{\rho_{m,0}}{M_\Delta}\frac{d\ln\sigma^{-1}}{dM_\Delta}, \tag{3.19}$$

where

$$f_{mf}(\sigma) = A\left[1 + \left(\frac{\sigma}{b}\right)^{-a}\right]\exp\left(-\frac{c}{\sigma^2}\right), \tag{3.20}$$

describes the evolution of the mass function with redshift since the parameters A, b,a,c depend on redshift. This non-universality is most likely caused by the evolution of the halo concentrations, which themselves are dependent on Ω_m. This mass function should therefore only be used up to a redshift of $z = 2.5$ and for cosmologies for which Ω_m is close to the flat ΛCDM cosmology (Tinker et al. 2008).

There are also analytical ways to approach the halo mass function, most notably the Press-Schechter mass function and the Press-Sheth-Torman mass function. The former relies on the spherical collapse model where the condition of collapse is given by the critical overdensity δ_c, whereas the latter apply an excursion set formalism to ellipsoidal collapse. Since M_Δ defines not only a certain mass but also a volume within which the mass is contained, $\frac{dN}{dzdM_\Delta d\Omega}$ is obtained from the multiplication of the cosmic volume element $\frac{dV}{dzd\Omega}$ with the cluster mass function above.
From these considerations, and a given cosmological model, one can subsequently compute:

- The expected number of galaxy clusters above a certain mass threshold at the current epoch as a function of the matter density and σ_8 (Rosati et al. 2002, Fig. 3.11a).
- The expected number of galaxy clusters for different matter densities and cosmological constant values as a function of redshift above a given mass threshold, given a uniform normalization at the current epoch (Rosati et al. 2002, Fig. 3.11b).
- The expected number of galaxy clusters as a function of redshift for a given dark energy content and σ_8 but for different dark energy equation of state evolution parameters (Mohr et al. 2003, Fig. 3.11c).

As one can see from Fig. (3.11 a), the cumulative mass function at $z = 0$ is most sensitive to Ω_m in comparison to Ω_X since, for a small redshift range, the sensitivity for any evolutionary charateristics is not given. Given a measured value for the cumulative mass function, a higher Ω_m predicts a lower σ_8. This is to be expected because a higher matter density requires lower initial amplitude fluctuations than a lower matter density for a given cumulative mass function value above a certain mass threshold at a given epoch.

A pedagogically intuitive illustration of the mass function dependence on the dark energy equation of state parameter is given in Mohr et al. (2003).
As one see in Fig. 3.11c , for a more positive w parameter than -1, i.e. a dark energy model instead of a cosmological constant model, structure forms more slowly at high redshift and the volume element is smaller than in the $w = -1$ case.

By investigating the cumulative mass function above a given mass threshold over a

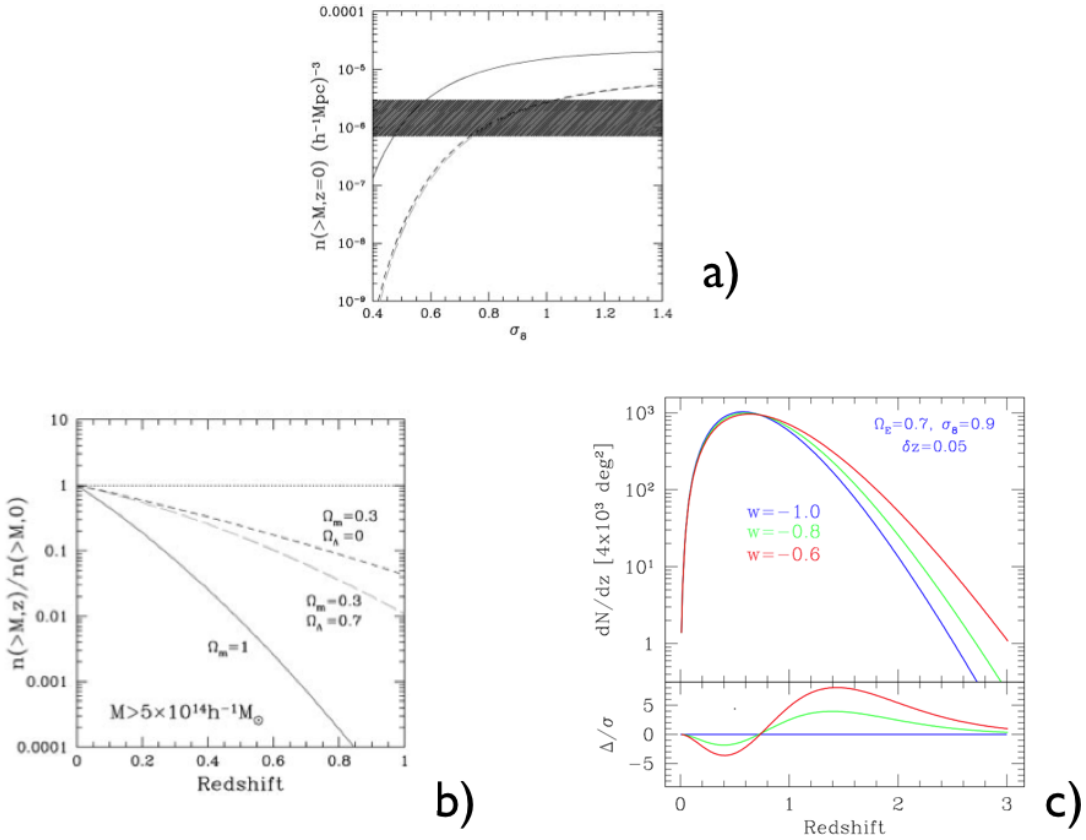

Figure 3.11: Cosmological predictions with galaxy clusters. a) The expected number of galaxy clusters above a certain mass threshold, $M > 5 \times 10^{14}$ h^{-1} M$\odot$, at the current epoch as a function of the matter density and σ_8 by Rosati et al. (2002). The coloured lines correspond to the same cosmological model colouring adopted in b. b) The expected number of galaxy clusters for different matter densities and cosmological constants as a function of redshift above a given mass threshold, given a uniform normalization at the current epoch by Rosati et al. (2002). c) The effect of different dark energy models on the cluster number counts (figure by Mohr et al. 2003).

wide redshift range in conjunction with knowledge of the current normalization, further studies on Ω_m and Ω_X can be made as is illustrated by Rosati et al. (2002), Fig. 3.11b. In addition, more recently, Vikhlinin et al. (2009) studied 86 galaxy clusters separated into a low-redshift sample of 49 cluster in z<0.25 and a high-redshift sample of 37 clusters for which 0.35<z<0.9. They examined the mass function as a function of mass and redshift. From their low-redshift sample, they derive constraints on σ_8 and Ω_m. Using this information, by comparing their high and low-redhsift samples, Vikhlinin et al. (2009) were able to constrain Ω_Λ and w_0 (see table 2 of Vikhlinin et al. (2009) for the results, including the information from other experiments).

The above discussion, focussed on examining the masses of galaxy clusters over a wide mass and redshift range. Single cluster studies that have higher masses than expected from the currently accepted cosmological model, can however also contribute to the testing of

these models. The high-mass/redshift test is particularly sensitive at high redshift. Recent high-redshift, high-mass clusters have all passed the ΛCDM model test, the most famous being 'El Gordo' from the ACT sample (Menanteau et al. 2012).

Under the assumption of spherical symmetry and exploiting the different distance dependences of X-ray and Sunyaev-Zel'dovich measurements, one can use galaxy clusters to measure the angular diameter distance as a function of redshift (Fig. 2.2).

Cosmological simulations show that the baryonic gas fraction in galaxy clusters should stay constant as a function of redshift. Hence, any evolution of the gas fraction must be attributed to an evolution due to the acceleration of the universe. This has been studied for a SZA/CARMA observed sample of clusters by LaRoque et al. (2006).

The lately reported tension in Planck number count derived and CMB-derived $\sigma_8 - \Omega_m$ parameter space (Planck Collaboration XX 2013) has led to numerous discussions as to its origins. It is currently believed to be caused by a combination of mass function estimates, total mass/mass-proxy scaling relations and neutrino mass considerations - the respective contribution of these possible explanations is still an active area of research. This, once again, stresses the need for accurate and precise mass estimations for galaxy cluster studies.

3.4 Redshift range of detected galaxy clusters

The Sunyaev-Zel'dovich effect is of particular importance in the study of high-redshift galaxy clusters due to its redshift independence, not taking into account the galaxy cluster angular diameter distance cosmic evolution. The examination of structure in galaxy clusters across a wide redshift range can also give important insight into the degree of disturbance in the ICM at different cosmic epochs.

In addition, having established that a wide redshift- and mass-range study is vital for galaxy cluster studies if one is to constrain the cosmological parameters to high accuracy, particularly with regard to the dark energy equation of state parameter and its evolution, it now remains to discuss the redshift range that current and future instruments can probe.

The Planck survey has detected galaxy clusters out to redshift $z = 0.99$ (Planck Collaboration XX 2013). In addition, the highest redshift clusters yet detected by the SPT and ACT surveys are at $z = 1.32$ (Stalder et al. 2013) and $z = 1.36 \pm 0.06$ (Hasselfield et al. 2013) respectively.

Mass-limited surveys, however, do not have the required sensitivity to detect clusters at very high redshift with low mass over a large survey volume. The IRAC Distant Cluster Survey (IDCS) identifies clusters via photometric studies, the redshifts being spectroscopically confirmed via follow-up studies. One such example is the cluster IDCS J1444.2+3306 at $\langle z_{\rm spec} = 1.89 \rangle$ (Zeimann et al. 2012).

In addition, Brodwin et al. (2012) followed up an IDCS detected cluster at $z = 1.75$ with 31 GHz SZA. This is one of the most distant cluster with a mass of $M_{200} = (4.3 \pm 1.1) \times 10^{14} M_{\odot}$ observed via SZ up till now. The XMM-Newton Distant Cluster project (XDCP) (de Hoon et al. 2013) discovered a $z = 1.45$ cluster whose surface brightness profile was fit with a beta model. Spectroscopic fitting in annular bins was however not feasible due to the low photon count statistics. Gobat et al. (2011) have reported the

existence of a mature cluster at redshift $z = 2.07$, first discovered via a galaxy overdensity in Sptizer data and then confimed by 3.5σ XMM-Newton observations of the galaxy cluster's extended ICM emission within $20'' - 30''$.

Selected future instruments

CCAT will be a 25 m telescope, to be completed by 2016, operating over a frequency range of $200 - 2200\mu$m. It will probe the ICM via Sunyaev-Zel'dovich observations out to high $z \sim 1 - 2$ redshifts (CCAT Cosmology Report 2013). It is the combination of wide frequency coverage and high sensitivity alongside with simultaneous multi-colour observations which will make it one of the most promising instruments in the next few years. In addition, its complementarity with high-resolution ALMA observations highlights the need for the development of tools for interferometer/sd combination techniques.

eRosita will start observing at the beginning of 2016 and will perform an all-sky survey detecting galaxy clusters with a median redshift of $z = 0.35$ (Pillepich et al. 2012). The planned X-ray Athena+ mission will enable a selection of the eRosita/Euclid/LSST clusters to be followed up at high spatial and spectral resolution out to redshifts around $z = 2$ (Pointecouteau et al. 2013).

The LSST will be a ground-based telescope that will cover six bands, allowing weak lensing studies to be made with a median redshift of 1.2 for observing set-ups that will give 56 galaxies per arcminute squared (Ivezic et al. 2008).

The Euclid satellite, to be launched in 2019, contains a 1.2m dish with which one will be able to study the clustering of galaxies and make weak lensing estimates over a wide redshift range (Euclid report 2011). It will cover 15 000 deg^2 in the wide survey, which will then be followed up with two deep field surveys a 20 deg^2.

The recently lauched NuSTAR satellite will enable the temperature in galaxy cluster shock fronts to be measured more accurately than Chandra. The latter suffers from its lack of ability in measuring high temperatures in soft bandpasses such that NuSTAR greatly enhances our current understanding of the very hot gas in galaxy clusters.

Future SZ targeted observations from Mustang 1.5 and MUSIC in conjunction with currently operating bolometer ACT, SPT and Bolocam instruments will further enhance our knowledge of the ICM in galaxy custers. Interferometric data from AMI, CARMA/SZA and ALMA/ACA will significantly complement this picture (Chapter 7).

Figure 3.12: Current and future instruments that have or are expected to have a significant impact on galaxy cluster studies. [Image credits: (SPT (KICP Chicago), Planck (ESA), ACT telescope (ACT), CCAT (Caltech: CCAT website), e-ROSITA (Merloni et al. 2012), LSST (LSST Collaboration), Spitzer (NASA/JPL), Euclid (ESA - C. Carreau), ALMA/ACA artist's impression (ESO/NAOJ/NRAO), CARMA/SZA (CARMA website), AMI (Astrophysics Group Cambridge website), Athena+ (Ettori et al. Athena+ supporting paper (The Astrophysics of galaxy groups and clusters)), Bolocam (Caltech: BOLOCAM website), APEX-SZ (APEX-SZ collaboration), MUSTANG 1.5 (NRAO website), GISMO (IRAM 30m, credit IRAM), Chandra (NASA/CXC/NGST/M.Weiss), XMM-Newton (ESA, D.Ducros), NuSTAR (NuSTAR), Hubble (NASA)]

3.5 Galaxy clusters: an in-depth view

In order to motivate the study of structure in the ICM of galaxy clusters, I outline the current status of galaxy cluster research with respect to their morphology-dependent characteristics at different spatial scales.

The fraction of galaxy clusters undergoing major merger events increases with redshift (Santos et al. 2008, Mann & Ebeling 2012). This is a direct consequence of hierarchical structure formation, which describes the formation of massive halos from the merging of smaller halo systems. A major merger, categorized by the collision of galaxy clusters or groups and the subsequent equilibrium disruption (Cohn & White 2005), is to be distinguished from the continuous accretion of gas from the filamentary structures (Simoniescu et al. 2011), which is present in all clusters. In addition, from an observational perspective, one should distinguish head-on merger events that are taking place very close to the plane of the sky and are thus better suited for modeling (Markevitch et al. 2002), to multiple merger systems in which consecutive merger events disturb the cluster system before the relaxation time of the first major merger event (Hsu et al. 2013).

Galaxy clusters can therefore be described by their morphological state. Classifying galaxy clusters as relaxed or disturbed systems and finding appropriate identifiers across a wide redshift range is one of the main challenges for current and future X-ray/Sunyaev-Zel'dovich surveys. The necessity for such morphological galaxy cluster classifications is motivated by the need for low-scatter scaling relations that link the observables to the total galaxy cluster mass. It is therefore necessary to identify methods, with which the degree of disturbance in clusters can be determined quantitatively.

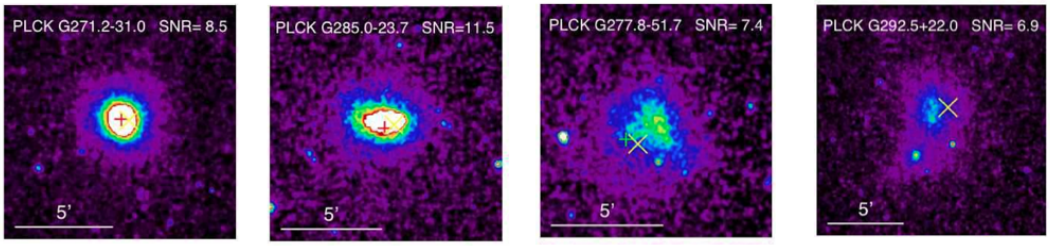

Figure 3.13: An X-ray view of selected Planck clusters (Planck Collaboration Early Results IX 2011) illustrating the vast range in the degree of ICM disturbance.

Morphologically disturbed clusters have often been classified via the brightest cluster galaxy (BCG) offset, defined as the offset, as seen in projection, between the X-ray gas emission peak or SZ peak and the position of the BCG (Lin & Mohr (2004), Mann & Ebeling (2012), Sanderson et al. (2009), Song et al. (2012)), a larger offset indicating more disturbed systems.

In the case of X-ray observations, the centroid shift parameter, w_{cs}, has been used in numerous publications (O'Hara et al. (2006), Poole et al (2006)). It is based on computing the variance of the computed emission centroid as a function of the projected radius within

which the peak is determined. In addition, disturbed clusters are thought to exhibit more ellipsoidal dark matter distributions than relaxed clusters, with higher redshift systems at a given mass being more ellipsoidal than their low-redshift counterparts (Limousin et al. 2013), (Fig. 2.7). This led to the the use of power ratio and eccentricity measure methods (Buote et al. 1995, Weißmann et al. 2013). The degree of mean eccentricity evolution with redshift is currently under debate with deduced halo ellipticities from numerical simulations (Floor et al. 2004) being in slight disagreement with X-ray observations (Jeltema et al. 2005).

Maughan et al. (2008) studied a sample of 115 Chandra-observed galaxy clusters in a redshift range of $0.1<z<1.3$. They see a decreasing fraction of cool-core clusters at high redshift in conjunction with a decreasing metallicity. They classify clusters according to their ellipticity and centroid shifts, finding the centroid shift parameter to be a better indicator of the morphological state of clusters since little ellipticity evolution is observed. Weißmann et al. (2013) challenge previous results on the disturbed cluster fraction with increasing redshift determined via the power-ratio method (Buote & Tsai 1995) of Jeltema et al. (2005) and Andersson et al. (2009). They argue that decreasing X-ray data quality at high redshift may bias the power ratio redshift-evolution derived in previous studies towards a positive trend. They report the centre shift parameter to be less sensitive to Poisson noise effects but also find a mere mild evolution of w_{cs} across their samples with redshifts spanning $0.05<z<1.08$.

On the radio side, simulations have shown (Ricker & Sarazin 2001) that double radio relics can indicate binary merger events, creating shock waves at the outskirts that are symmetric in shape. Weak lensing analyses can exhibit multiple peaks in the convergence maps, which therefore directly indicates a merger event (Ragozzine et al. 2012). However, currently, it may not be feasible to do detailed weak lensing analyses for a large sample of galaxy clusters over a wide redshift range since, especially at high redshift, this requires a lot of observation time with Hubble. In addition minor mergers might not show up due to high noise in the shear estimates.

Relaxed clusters at low redshift are easily characterized by their peaked X-ray surface brightness profiles in the centre. In the 90s, this lead to the 'cooling flow problem', first put forward by Fabian (1994). These clusters were found to have cooling times, defined as $t_{\rm cool} = 69(n_e/10^{-3}{\rm cm}^{-3})^{-1}(T/10^8 K)^{1/2}$ Gyr, which were shorter than a cluster's age (Sanderson et al. 2006). Such a cooling rate would predict gas flow to occur at a rate of several hundreds of solar masses per year (Fabian 1994). However, only a small fraction of the cold gas expected at the centre was indeed detected (Peterson & Fabian 2006). In a study by Morris & Fabian (2005) of A2597, the cooling rate was shown to be $\approx 100 M_\odot {\rm year}^{-1}$. O'Dea et al. (2008) computed the 62 BCG sample star formation to be $\approx 1-10\ M_\odot {\rm year}^{-1}$ and thus a factor 10 to 100 lower than the expected mass deposition rate (McDonald et al. 2011), suggesting that the ICM is re-heated to higher temperatures, which prevents it from cooling and forming stars.

Feedback

X-ray cavities, such as those observed in the Perseus cluster (Fabian et al. (2011), Fig. 3.2) suggest that periodic AGN feedback outflows over a galaxy cluster's lifetime may heat up the cooling gas (Heinz et al. 2006). The entropy injection may therefore be just sufficient to prevent the gas from cooling below a given entropy level.

The entropy of the intra-cluster gas is defined as $K = k_B T / n_e^{2/3}$ and tends to $K \propto r^{1.1}$ (Voit et al. 2005) in the absence of feedback. Departure from this relation can thus give indications to the nature of the feedback present (Chaudhuri et al. 2012). A galaxy cluster's entropy profile therefore contains information on the ICM's entire thermal history. Alternative, or indeed supplementary, mechanisms to AGN feedback such as supernova winds and pre-heating have also been suggested. Pre-heating describes a scenario in which gas is heated at very high redshhifts $3<z<10$ (Vazza et al. 2011) by processes that are speculated to involve star formation, supernova and a hard X-ray background as outlined by Tozzi & Norman (2001) and Younger & Bryan (2007).

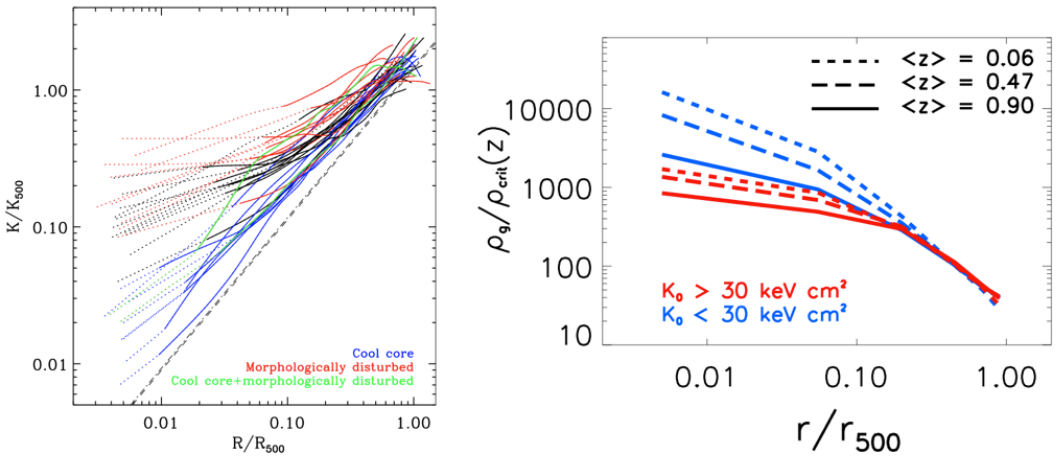

Figure 3.14: Entropy distribution and central density evolution. *Left*: The dimensionless entropy distribution as a function of radius from the Arnaud cluster sample showing high scatter in the central regions with morphologically disturbed systems exhibiting, on average, higher central entropy levels. The self-similar expectation is indicated via the dashed line. (image credit: Pratt et al. 2010) *Right*: The evolution of the density profile of clusters with central entropy levels $K_0<30$ KeV cm^2 is shown, indicating that cool-core systems have evolved from cooling-flow clusters (image credit: McDonald et al. (2013)).

The gas in cool core clusters does not seem to cool below entropy levels of $K_0<10$ KeV cm^2 and their central density is higher than in more disturbed clusters. McDonald et al. (2013) found that there is a dichotomy in the central entropy of cool-core clusters compared to non-cool disturbed clusters. This dichotomy was also seen in BCG offset/cooling times.

Recent simulations have tried to incorporate feedback, preheating, cooling and star formation (Kay et al. 2007, Borgani et al. 2002, Kravtsov et al. 2006). In particular, Fabjan et al. (2010) investigate the effect of AGN activity via simulations of galaxy clusters, finding that it does indeed quench the star formation rate. Such simulation studies are far from being complete. The role of turbulence in transferring the energy from the plasma bubbles, formed by AGN jets, to the ICM is an active area of research (Nath et al. 2011, Scannapieco et al. 2009). Recently, Short et al. (2010) have managed to reproduce cool-core clusters via hydrodynamical simulations that do not suffer from the over-cooling problem often observed in such simulations. In their study of simulated galaxy groups, McCarthy et al. (2011) suggest quasar mode feedback at high redshift to be the dominant source for the high-entropy gas.

Cluster pressure profiles

Arnaud et al. (2010) examined a sample of 33 galaxy clusters from the REFLEX catalogue at redshifts below $z<0.2$ with *XMM-Newton* observations. In classifying the morphological states of galaxy clusters via the central gas density measurements and centre shift parameters, they divide their sample up into morphologically disturbed (non-cool core), relaxed (cool core) and cool core (CC) + morphologically disturbed (NCC) systems. Using annularly binned temperature measurements, pressure profiles were calculated and rescaled according to the clusters' redshifts and masses in terms of R_{500} and M_{500} respectively. As one can see in Fig. (3.15), relaxed clusters manifest themselves through both, peaked density and pressure profiles. Parametric models in the form of a generalized NFW (GNFW) profile were fitted to the ensemble average as well as to the relaxed and disturbed sub-sets. The GNFW pressure profile incorporates one normalization parameter, one scale parameter as well as three slope parameters (see chapter 7 for a detailed discussion). Recent Arnaud-profile fitting procedures for multiple observing telescopes and samples are further outlined in chapter 7.

Evolution of cluster properties

The profiles from the Arnaud sample were fit in a low-redshift range and it remains to be tested up to which redshift they remain valid approximations to the actual galaxy cluster pressure profiles. The evolution of the fraction of cool-core galaxy clusters as a function of redshift has been studied, amongst others, by Vikhlinin et al. (2007), Andersson et al. (2009), Santos et al. (2008) and Maughan et al. (2008), with the general consensus being that the fraction of strong cool-core clusters diminishes at higher redshift. With the merger fraction increasing at higher redshift (Mann & Ebeling 2012), it was discussed for a long time whether mergers could destroy cool-cores. Poole et al. (2008) find that cool-cores are only destroyed in head-on or multiple collisions.

McDonald et al. (2013) observed 83 SPT-detected clusters with Chandra spanning a redshift range $0.3<z<1.2$. They found that the gas in these clusters never reaches entropy levels below 10 keV cm^2 and that the cooling properties, described by the central mass deposition rate, cooling time and central entropy value exhibit very little evolution.

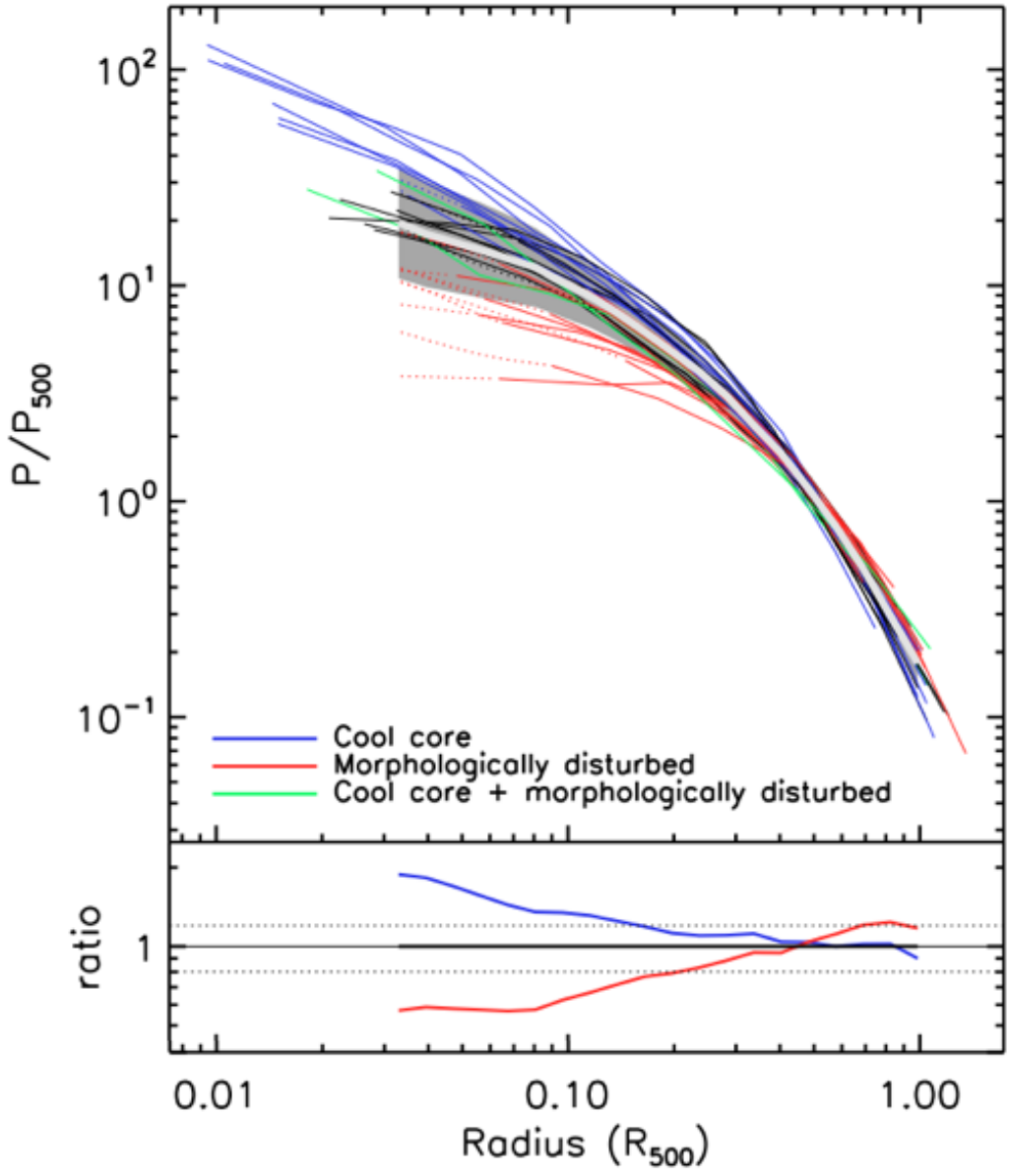

Figure 3.15: Pressure profile from the Arnaud sample. This figure is taken from Arnaud et al. (2010) and shows the re-scaled pressure profiles with cool-core systems (blue) and morphologically disturbed clusters (red) agreeing beyond r_{500}, but showing morphologically characteristic dispersions in the central regions.

This suggests that clusters develop from cooling cluster to cool-core clusters, implying that the feedback mechanisms have been active for a very long time.

McDonald et al. (2013) find a threshold of $z = 0.75$ beyond which they find no cuspy surface brightness profiles in their clusters that mark them as cool cores. A redshift margin should be allowed around this redshift threshold to take into account the limited sample size of 83 clusters, though selection effects for or against cool core clusters can be neglected for the SPT survey (Sun et al. in prep). McDonald et al. (2013) therefore deduce that cool-core clusters, as we know them at low redshifts with their cuspy surface brightness profiles, have built up from higher redshifts where the central density of relaxed clusters was lower but the type of feedback was similar to what is observed at the current epoch. Their lower limit for the onset of feedback matches the assumptions of AGN themal feedback onset in simulations (Vazza et al. 2011). The low X-ray number counts at high redshift do not allow for detailed radially-fit spectra, so that the error bars in the central cluster region cannot distinguish a self-similar temperature evolution from additional feedback heating. As a consequence, radial pressure profiles could not be derived for the sample, leaving the issue on the validity of the Arnaud pressure profile at high redshifts open (for further discussions see Chapter 7).

Cluster outskirts

Having focussed on the difference between cool-core and non-cool core clusters within or close to R_{500}, it remains to be discussed how galaxy cluster outskirts can be characterized. A recent combination of the Planck pressure profile with ROSAT density profiles, Eckert et al. (2013), allowed temperature and entropy profiles to be analysed out to radii beyond R_{500} without the need for spectroscopic follow-up under the assumptions of hydrostatic equilibrium and spherical symmetry. Eckert et al. (2013) not only analyse sample-averaged profiles but also single cluster systems of which 6 are cool-core (CC) and 12 non-cool core (NCC) clusters, as determined from their central entropy value. Both types of clusters show declining temperatures in the outskirts. CC systems were found to agree with expectations in the entropy profile from gravitational collapse at outer radii, $1 - 2\ R_{500}$,whereas NCC clusters lie, on average, below these expectations. They argue that this could be explained by a higher clumping factor of 1.23 ± 0.06 at R_{200} in NCC systems. These results are in tension with recent Suzaku observations of the Perseus cluster by Urban et al. (2014), who report a flattening of the entropy profile at large radii. Eckert et al. (2013) II also find substantial differences in the cluster gas mass fractions of CC and NCC systems at R_{200}, with CC system gas mass fractions converging to the expected cosmic baryon fraction.

Cluster scaling relations

Understanding the balance between cooling and feedback in galaxy clusters is enriching our knowledge of clusters per se, but in light of cosmological predictions, it remains to discuss its effect on scaling relations. One of the most important steps in making cosmological predictions from galaxy cluster studies is relating the observables to the mass of a galaxy cluster, encompassed in the formula $P(M_\Delta, z \mid O_{(f,\Delta)}, O_{(\theta,\Delta)})$ in Eq. (3.18).

Kaiser et al. (1986) proposed simple scaling relations between cluster properties under the assumptions of purely self-similar evolution.

Any deviation from self-similarity as a function of redshift or indeed in a small redshift range, should therefore indicate the degree to which non-gravitational processes play a role. In addition, any assumptions involved in obtaining the derived observables such as hydrostatic equilibrium, spherical symmetry or the extent of non-thermal pressure support can lead to a higher systematic scatter in these relations. For a recent review on scaling relations, see Giodini et al. (2013). It has been shown in numerous scaling relation studies (Pratt et al. 2010, Maughan et al. 2008, Mantz et al. 2010) that X-ray luminosity is very sensitive to baryonic processes in the core regions, biasing the scaling relations, if the central regions of cool-core clusters are not removed. In contrast, weak-lensing-based total mass estimates do not make assumptions on the ICM gas state since they indirectly measure the shear of background galaxies caused by the joint dark matter and baryonic matter mass over a statistically large sample of background galaxies. The lensing mass/gas-derived mass observable relations are therefore of particular significance since they can give vital insight into scatter originating from systematics due to departures from hydrodynamical state assumptions.

In the case where spherical dark matter NFW profiles are assumed for both, weak-lensing and ICM-derived properties, the systematics due to shape assumptions cannot be pinned down. For a large cluster sample, the effect of sphericity assumptions should cancel out, given that the sample is a fair representation of the galaxy cluster distribution and does not favour any particular orientation of galaxy clusters. An example case for such a scenario - a sample consisting primarily of strong lensing clusters - has a higher probability of being orientation biased, since it has been shown that strong lensing clusters have their major axis preferentially oriented close to the line of sight (Limousin et al. 2013). The need for full triaxial galaxy cluster analyses will be further discussed in the next discussion item.

The scatter in total mass/mass proxy relations can be studied via simulation studies, for which the total mass in galaxy clusters is known, such that any systematic biases can be quantified. Krause et al. (2012) tested 30 galaxy groups and clusters from Dolag et al. (2006, 2009) and constructed Compton y maps. They find the extent to which the $M_{200-}(Y_{200})$ relation deduced mass to be biased low can reach more than 10% within a Gyr after a cluster merger event. Krause et al. also note that, since mergers are more frequent at higher redshift, the scatter in $M_{200} - (Y_{200})$ should be expected to be redshift dependent. It has also be shown by Maughan et al. (2012) in a study of 114 Chandra observed clusters over a redshift range $0.1<z<1.3$ that the core-excised X-ray luminosity/temperature relation, $L_X - T_X$, is in agreement with the self-similar model for relaxed clusters, as classified by X-ray surface brightness cuspiness, centroid shift parameter and the core-flux ratio. This was in tension with the results by Pratt et al. (2009) who found a steeper slope. Maughan et al. (2012) account the difference due to both, morphological state classification and sample selection - their sample favouring higher mass systems. This stresses, once more, the need to find robust estimators for a galaxy cluster's degree of disturbance away from a relaxed state in conjunction with scaling relation studies over wide mass ranges.

In addition, it is vital to specify over which radial range the scaling relations are de-

termined and over which radius the cool-core cut-out is made. Maughan et al. (2012) find that unrelaxed cluster deviate from the self-similar $L_X - T_X$ out to $0.7R_{500}$. One might, of course, argue that the $L_X - T_X$ relation is not the most favourable scaling relation for galaxy cluster, exactly due to the parameters' sensitivities to a cluster's dynamical state. Extensive studies have therefore been tailored towards finding proxies, based on ICM observations, that prove to have better mass-related properties than a cluster's average temperature. One such suggested parameter for X-ray observations is $Y_X = M_g T_X$, where M_g denotes the gas mass. This was first proposed by Kravtsov et al. (2006) on account of its direct dependence on the thermal ICM energy content. Simulations have shown Y_X and its SZ equivalent, $Y_{\rm SZ}$, to have low scatter and to be less affected by the cluster' s dynamical state.

The degree to which the assumption of HSE biases the derived Y values has been studied by Mahdavi et al. (2013) and Maughan et al. (2007). Wik et al. (2008) use a set of hydrodynamical simulations of binary galaxy cluster merger events in order to study the effect on the maximum y_{max} and the spherically integrated Comptonization paramter Y. Both parameters are boosted during a merger, the boost lasting around four times longer for Y which is lower at the boost than in the final 'completeley-merged-Y' stage. They find an overall scatter of 2 % and 24 % for the $Y - M$ and $y_{max} - M$ relations respectively, in line with the results by Motl et al. (2005). As has been suggested by Y_X, global values are therefore to be preferred to central values for cosmological estimations.

Weak-lensing/SZ scaling studies have only recently been performed. Most notably, the APEX-SZ collaboration has collected lensing data of up to 40 galaxy clusters, which are compared to integrated $Y_{\rm SZ}$ measurements from the APEX-SZ experiment that covers a redshift range of 0.152 - 1.450 with 19 morphologically disturbed and 20 relaxed clusters, the 3 remaining cluster not being included in the scaling relations (APEX-SZ collaboration, Bender et al. submitted, M. Klein PhD Thesis). Six non-detections are also included in the sample. Smaller sample, weak-lensing/SZ scaling relations have been performed using CARMA/SZA data by Marrone et al. (2012) and Hoekstra et al. (2012), their covered redshift range and sample size being smaller than the APEX-SZ collaboration's follow-up program. More recently, Gruen et al. (2013) have reported a weak-lensing follow up of a small subset from their SPT sample.

Cluster triaxiality

All previous discussions have assumed spherical symmetry of the dark matter potential and subsequently also of the three-dimensional intra-cluster gas shape. It was Corless et al. (2009), Sereno et al. (2006, 2007, 2012) and Morandi et al. (2010, 2011, 2012) who pioneered the study of combined triaxial multi-wavelength analyses. These studies were motivated by the fact that, for some clusters the weak-lensing and X-ray derived total galaxy cluster masses were discrepant by up to 50%, as was the case for Abell 1689. In addition, the over-concentration problem was shown to partially originate from the triaxial nature of lensing-selected, and also X-ray selected, samples (Sereno et al. 2010, Meneghetti et al. 2011). Since triaxiality could not explain the derived high concentration parameters for all outliers, further studies needed to be made. The mass-concentration relation and its evolution as a function of redshift was studied by Oguri et al. (2012) and

Sereno & Zitrin (2012). More recently Sereno et al. (2013) suggest that, following Ludlow et al. (2012), more concentrated halos may represent less relaxed systems.

Multi-wavelength studies in conjunction with a triaxial analysis have only been computed for a few galaxy clusters, MACS 1423 (Morandi et al. 2012), A383 (Morandi & Limousin 2012), A1835 (Coreless et al. 2009) and A1689 (Morandi et al. 2011a, 2011b) and their analyses rely heavily on the adopted priors, which help to narrow down the most likely parameter space. Triaxial analyses will become ever more important once large galaxy cluster multi-wavelength follow-up catalogues are constructed and cross-calibrated. Discrepant results for which high levels of disturbance can be ruled out as a cause for inaccurate and inconsistent mass determinations across a wide redshift range, will be the prime targets for triaxial analyses. Besides contributing to more accurate mass measurements of galaxy clusters, the ellipticity of clusters in the plane of the sky has also been suggested by Ho et al. (2006) to be a function of the cosmological parameters themselves. This effect still needs to be tested more extensively for different cosmological models via simulations and for a large sample of observational data. Limousin et al. (2013) have also reported cluster ellipticity to be a tool for studying the degree of self-interaction of dark matter, relying on results by Yoshida et al. (2000).

Galaxy cluster shocks

Shocks in galaxy clusters can also contribute in deriving an upper limit for the dark matter cross-section. Markevitch et al. (2004) outline three different methods for the case of the dissociative 'Bullet Cluster' merging system - a system nearly aligned in the plane of the sky showing a post-near-core-passage sub-cluster, the bullet, travelling through a more massive cluster. The resultant shock front is clearly visible in X-rays and there is a distinct offset between the gas and the dark matter distribution as derived from weak lensing measurements (Clowe et al. 2004), see Fig. 3.16b.

Under the assumption that the sub-cluster's scattering depth is less than 1 (Markevitch et al. 2004), and further modeling a spherical sub-cluster, one can derive an expression for the dark matter (DM) collision cross section, σ, for a particle mass m via

$$\tau_s = \frac{\sigma}{m}\Sigma_s \qquad , \tag{3.21}$$

where τ_s is the scattering depth and Σ_s is defined by Markevitch et al. (2004) as the 'subcluster's DM mass surface density'. The so far lowest upper bound on the dark matter cross-section from the Bullet Cluster system stems from the mass to light ratio of the sub-cluster and its dark matter mass loss during its trajectory (σ/m<1 cm^2 g^{-1}). In addition, Markevitch outlines how the sub-cluster's velocity can be used to derive a second estimate for the dark matter cross-section. This relies on the fact that a non-negligible cross-section implies additional drag forces alongside those from the gas stripping during the sub-cluster's passage. By calculating the average momentum loss during each dark matter particle collision, p, Markevitch derived a formula for the velocity decrease, assuming the main contributor to drag forces being dark-matter particle collisions,

$$v - v_{ff} = \frac{p\sigma}{m^2}\Sigma_m \qquad , \tag{3.22}$$

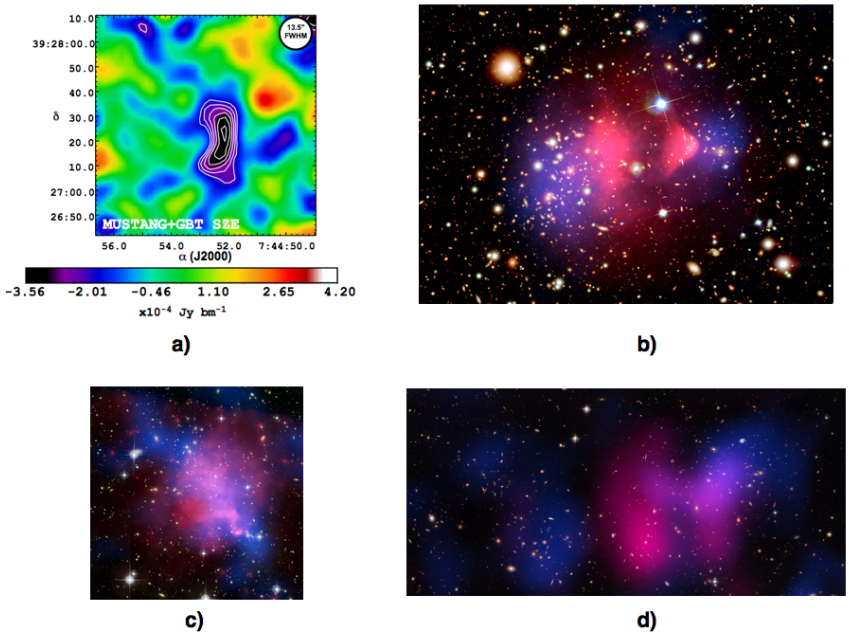

Figure 3.16: Shock fronts in galaxy cluster and gas/dark matter offsets. a) Sunyaev-Zel'dovich MACS0744 observations with MUSTANG showing a pressure discontinuity. b) The Bullet Cluster of galaxies (X-ray: pink, optical: white/orange, lensing map: blue) c) The trainwreck cluster Abell 520 (X-ray: pink, lensing: blue, optical: yellow, orange). d) The Musket Ball Cluster (X-ray: red-purple, projected mas map: blue, optical background: red, green, blue). [Image credits: (a) Korngut et al. (2011), (b) X-ray: NASA/CXC/CfA/M.Markevitch, Optical and lensing map: NASA/STScI, Magellan/U.Arizona/D.Clowe, Lensing map: ESO WFI, (c) X-ray: NASA/CXC/UVic./A.Mahdavi et al. 2007, Optical/Lensing: CFHT/UVic./Mahdavi, A. et al, 2007, (d) NASA/CXC/STScI/UC Davis/W.Dawson et al. 2012, X-ray: NASA/CXC/UCDavis/W.Dawson et al. 2012; Optical: NASA/STScI/UCDavis/W.Dawson)]

where Σ_m is defined by Markevitch as the 'mass column density of the main cluster along the sub-cluster's trajectory' and v_{ff} is the free-fall velocity. As one can see, the sub-cluster velocity is an important factor in this equation. In the case of the Bullet Cluster, this has been derived from the Mach number of the shock front. Besides being good laboratories for studying the nature of dark matter, shock features near the plane of the sky also offer a window into the ICM attainable temperatures during such collisions. A further discussion will be given in Chapter 8, describing the famous case of the Bullet Cluster in more detail.

3.6 Milestones for interferometric SZ studies

Thesis outline: The main motivation for this thesis was not only to identify those areas of galaxy cluster research which can benefit from high-resolution interferometric Sunyaev-Zel'dovich follow-up, but also to quantitatively demonstrate how these concepts can be put into practice via data/simulation analyses.

Below, I will incentivize the identified topics formed on the basis of the previous introduction and pose the questions that initiated work on this thesis.

Bolometer single-dish and interferometric SZ observations

Single-dish SZ measurements from ACT, SPT, BOLOCAM and APEX-SZ cannot map the SZ signal at angular resolutions lower than $1'$ and may suffer from systematics inherent to bolometer single-dish data reduction. Hence, cross-calibration between interferometric and bolometer single-dish measurements are vital to assess any biases in their respective data analyses.

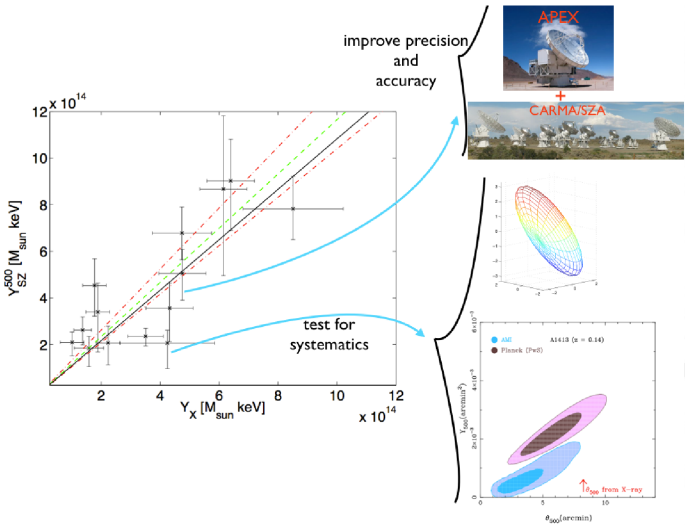

Figure 3.17: The combination and comparison of interferometric and single-dish data is motivated by the need to improve the accuracy and precision of mass-proxies as well as to assess systematics through morphology-induced or instrumental effects. This is exemplified via the latest SPT scaling relations (Saliwanchik et al. 2013, *left*) as well as the AMI/Planck comparison, illustrating a mismatch between Planck and AMI data (Planck intermediate Results II, 2013, *bottom right*). The proposed approach in this thesis is to assess these effects in a single-cluster APEX-SZ follow-up study with interferometric observations (instrument image credit: CARMA, APEX-SZ collaboration). Note that the 'test for systematics error' merely serves as an indicative illustration for a possible galaxy cluster parameter mismatch and does not address the specific cluster.

Recently, AMI and Planck observations of 11 clusters in the redshift range $0.11<z<0.55$ were compared in the $Y_{500} - \theta_{500}$ plane (Planck intermediate Results II, 2013). In the majority of cases, the interferometric visibility fitting results in best-fit models, that are fainter and smaller than those inferred from the Planck data, with 3 clusters showing disagreement between the derived acceptable parameter spaces. They speculate the cause of these differences to being either of a systematic nature or due to a limited and inappropriate parameter space choice. Such cross-calibrations, not only between different observing strategies but also between similar wavelength studies, will become ever more important as we are reaching observable/mass-proxy relations that are limited by systematics.

Questions:

- How good is the cross-calibration between clusters from our APEX-SZ sample and interferometric observations ?
- How can interferometric and single-dish observations be combined in the image plane ?
- How well do parametric fits of the single-dish and interferometric SZ data agree and in what ways can they complement each other in galaxy cluster pressure profile studies ?

Applied approach

Being part of the APEX-SZ collaboration, which made targeted APEX-SZ cluster observations, several clusters from this bolometer single-dish SZ data set lend themselves to interferometric follow-up. Further details on the APEX-SZ sample selection criteria and observations are given in chapter 4. The radio interferometer choice for the follow-up program was based on uv-coverage, uv-range, and required on-source integration time given the typical array flux sensitivity and resulted in choosing a combination of the SZA/CARMA arrays.

Two proposals for CARMA/SZA observations (PI: Sandra Burkutean) of the galaxy cluster MS0451 were accepted and observed. The galaxy cluster and interferometer choice for this pilot study are outlined in chapter 5. In addition, interferometric data analysis and its combination with APEX-SZ data is described in this chapter.

I developed a Bayesian Markov Chain Monte Carlo model fitting approach to test the suitability of interferometric and single-dish data in probing the chosen galaxy cluster's pressure profile. This is outlined in chapter 6. In view of an elliptical elongation of MS0451 in the plane of the sky, as seen from SZ and X-ray observations, the theoretical and computational frameworks for a triaxial cluster analysis are given in chapter 9. More recently, a third SZA proposal in the form of a collaboration proposal on three additional galaxy clusters was accepted for which I undertook the proposal planning and writing on behalf of the APEX-SZ collaboration.

During the course of this thesis, data, which were not yet publicly availble at the onset of this project, have now become publicly available. These new data offer the opportunity to extend the single cluster MS0451 study to a wider investigation, using the techniques developed in this thesis. The 'Future Investigations and outlook' chapter further sketches out the possible analyses on a cluster-by-cluster basis.

Distinguishing cool-core from non-cool core galaxy clusters

It is particularly in the core regions that CC and NCC clusters have been shown to differ. Hence, in light of the need to classify clusters as cool-core/cooling-core or morphologically disturbed systems, surveys could indeed benefit from high-resolution SZ follow-up. Under the assumption of hydrostatic equilibrium and spherical symmetry a pressure profile could be obtained from such investigations for clusters whose X-ray photon count statistics might not be sufficient for an annularly binned temperature profile fit. This is particularly motivated by the need for high-redshift galaxy cluster studies for which the cosmological dimming is a particular issue with regard to the required X-ray on-source observation time.

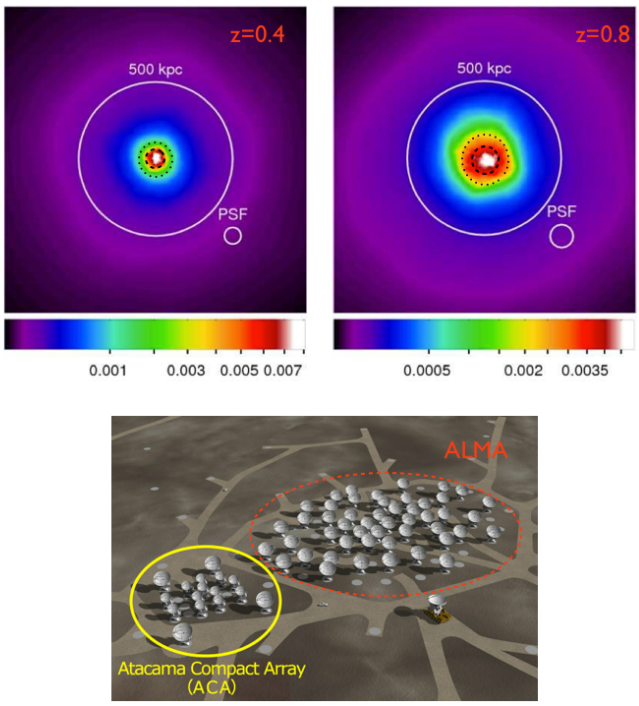

Figure 3.18: The motivation for pressure profile studies. *Top:* Simulated luminosity maps of cool-core clusters by Andersson et al. (2009) with annotated maximum recoverable angular scales for ALMA (dashed circle) and ACA (dotted circle). The colour scale is in units of 10^{44} erg s^{-1} (")$^{-2}$. An artist's impression of the full ALMA/ACA array is given below (image credit: top) Andersson et al. (2009), bottom) ALMA (ESO/NAOJ/NRAO))

A morphological galaxy cluster classification that complements already exisiting methods such as surface brightness excess and BCG offset, would allow the evolution of scaling relations to be monitored more effectively out to very high redshifts. In addition, the nature and evolution of cool-core or, in fact, cooling core, systems in terms of any evolutions in the characteristic cluster pressure profiles could also be mapped if such a follow-up study was made for a well-defined cluster sample. With the new ALMA interferometer being close to completion, the potential for a new era of combined high-resolution and high-sensitivity interferometric SZ observations has opened up.

Questions:

- Which interferometer combination is best suited for galaxy cluster profile studies?
- Over which mass and redshift range can morphologically relaxed and disturbed clusters be imaged for realistic on-source integration times and weather conditions ?
- To what extent can different pressure profiles be distinguished quantitatively with interferometric SZ observations ?

Applied approach

As in the case of the follow-up MS0451 project, the choice of the interferometer combination focusses mainly on uv-coverage and required observation times. Since no joint SZ ALMA/ACA observations are available up to this date, this investigation is based on interferometric mock simulations in conjunction with the developed Bayesian MCMC interferometric visibility fitting code. The pressure model choice is described in chapter 6 and image galleries provide an overview of the results (Appendix B).

Shocks in galaxy clusters

In order to distinguish shock fronts from cold fronts in galaxy clusters via X-ray observations, both density and temperature profiles are needed. The profile deprojection greatly depends on the assumed shock symmetry and modeling.

Sunyaev-Zel'dovich observations, being directly dependent on the integrated pressure along the line of sight, can greatly contribute to galaxy cluster shock studies (Korngut et al. 2011, Mason et al. 2010). For cases with optimal geometric projection, the pressure jump can be used to derive the Mach number of the shock, which in itself can contribute in giving upper limits on the dark matter cross-section. The temperatures attainable in such shock structures can also help our understanding of the nature of electron-proton equilibration. Using the gas equation of state and assuming a particular 3D shock structure, information on the integrated pressure can therefore greatly help in pinning down this issue.

Figure 3.19: A sketch of a galaxy cluster collision scenario taking place in the plane of the sky, involving a small-mass sub-cluster that passes through the centre of the main cluster causing gas to be stripped from the sub-cluster. A shock front is produced in front of the sub-cluster. The ALMA/ACA artist's impression is taken from ALMA (ESO/NAOJ/NRAO).

High-resolution SZ observations of the Bullet Cluster will thus allow us to address the following questions:

I What electron temperatures are present in the most prominent galaxy cluster merger shock front known?

II What are the processes that heat the plasma electrons in the shock front ?

III What is the upper limit of the dark matter collisional cross-section computed from the sub-cluster Bullet velocity via joint SZ and X-ray information ?

Since interferometric observations of the most famous case for such a shock feature - the Bullet cluster - are not yet available, one has to resort to simulations to identify the feasibility of such high-resolution observations. I therefore address the following topics:

- Given that hydrodynamical simulations of the Bullet cluster shock structures were not publicly available, how can one model the Bullet cluster shock structure ?
- Which combination of ALMA/ACA observations of the Bullet cluster is both, feasible and realistic ?
- Can different post-shock temperature scenarios be distinguished from the strength of the SZ shock feature in the mock simulated images ?

Applied approach

Since high-resolution hydrodynamical simulations were not availabe to our group, I used a simplified model based on the results of Markevitch et al. (2002). The suitability and potential shortcomings of this model are discussed in chapter 8 alongside with a comparison to previous Bullet Cluster simulation studies. In addition, mock simulations using ALMA /ACA Cycle 2 configurations are presented for different mean post-shock temperature models.

Chapter 4

Technical Background

In sight of the fact that the following chapters will assess and compare interferometric and bolometer single-dish measurements of the Sunyaev-Zel'dovich effect in galaxy clusters, the different technologies and data processing techniques are outlined in this chapter.
The concept of radio interferometers, described in its most basic sense as an array of multiple telescopes, is exemplified via the consideration of a simple two-element system, whose extension to a full array is further outlined via my interferometric simulator and its subsequent comparison with the simulator built into the CASA data reduction software.
In the bolometer array data reduction overview, the focus is layed on APEX-SZ, particularly with regard to the pipeline processing developed by the APEX-SZ collaboration. My project within this collaboration, being the interferometric follow-up and comparison of single clusters from the APEX-SZ galaxy cluster sample, relies on the concepts of the pipeline transfer function and bolometer map cleaning methods, developed by the APEX-SZ collaboration and introduced in this chapter.

4.1 A brief introduction to Radio Interferometry

Radio interferometers consist of several antennas whose output signals are brought together in a correlator. In the case of very long baseline interferometry (VLBI), these antennas can be placed thousands of kilometres apart, spanning whole continents. In this thesis, I will focus on connected-element arrays such as CARMA/SZA, JVLA and ALMA/ACA whose maximum baselines, the physical distance between two antennas, range from less than ten metres to several kilometres and whose operation is based on mechanical dishes rather than omni-directional antennas, as is the case for LOFAR.

The largest mechanically movable single-dish telescope is the Green Bank telescope with 100 m ×110 m, followed by the Effelsberg telescope, which measures 100 m in diameter. Building larger single dish telescopes is unfeasible from engineering considerations, so that one must turn to interferometers if one requires higher angular resolution measurements than those currently offered by single-dish telescopes at a given frequency.

Before delving into the full principle of aperture synthesis, one may start by examining a simple two-element system Fig. (4.1). The subsequent discussion follows the approach of Taylor et al. (1999) and Thompson, Moran & Swenson (2001). Suppose that the astronomical source under investigation is a long way away such that the incoming signal can be described by the plane wave approximation. In order to simplify the following discussion, I will neglect polarization which would require a matrix notation. In addition, a homogeneous array will be considered. One may also imagine a situation in which the signal is not attenuated along its path or, in other words, that the space between the emission region and the observer is empty. Please note that this assumption will break down in reality due to absorption, emission and re-emission processes. These can have their origin in astrophysical sources, or indeed, through the effect of the Earth's atmosphere through which the radiation must pass before reaching our telescopes.

In the two-element interferometer set-up, one can see from Fig. (4.1) that there will be a geometric path delay of $\tau_g = (\mathbf{B} \cdot \mathbf{s}_0)/c$ between the antenna ant1 and antenna ant2 separated by a baseline $\mathbf{B}$, since the plane wave reaches ant1 before ant2. This delay is compensated for by an instrumental path delay τ_i in one of the antenna's signal paths, Fig. 4.1 (4), such that the source can be tracked. In order to introduce the concept of time-domain fringes, first consider the case where $\tau_i = 0$ and $V_1(t)$ and $V_2(t)$ denote the time-varying voltage outputs of ant1 and ant2 respectively. These voltages are then multiplied in a correlator, giving the cross-correlation in the form of a cosine fringe pattern

$$R_{12}(\tau_g) = \frac{1}{2}\langle V_1(t)V_2(t)\rangle = \frac{V_1V_2}{2}cos(2\pi\nu\tau_g). \tag{4.1}$$

The astronomical fringe rate depends on the Earth rotation and is thus known. This fringe rate is different from contributions from the atmosphere, ground-spill or other terrestrial interference. The angular pattern of the normalized reception pattern, the primary beam $\mathcal{A}$, of a single dish consists of a main lobe and lower amplitude side-lobes away from the pointing centre, $\mathbf{s}_0$. For a monochromatic point source passing above the 2-element interferometer as the Earth rotates, under the assumption that the effect of bandwidth

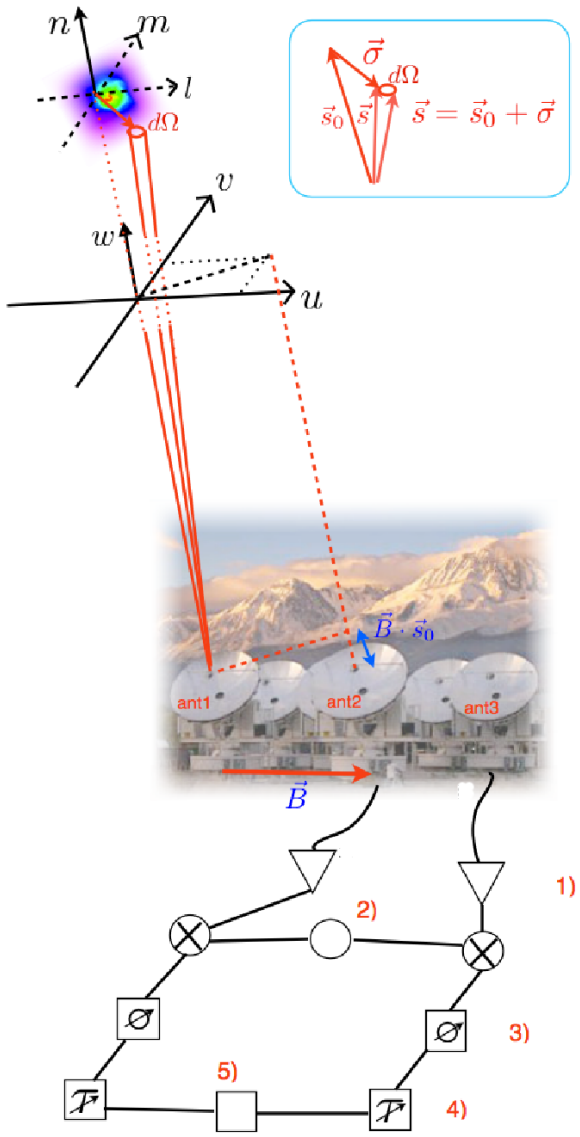

Figure 4.1: The workings of a radio interferometer: Radiation from the tracking centre in direction $\vec{s}_0$ is received at ant1 and ant2 with a time delay that is accounted for by an instrumental time delay added to the signal of one of the antennas (4) after initial amplification (1), frequency down-conversion through mixing with a local oscillator signal (2) and additional phase corrections (3) as well as potential other phase corrections (4) to both antennas. The signals are then cross-correlated in a complex correlator (5). The projected baseline is shown in the uv-coordinate system defined by $(\mathbf{u}, \mathbf{v}, \mathbf{w})$ whose normal is in the tracking centre direction and thus parallel to the sky coordinate axis $(\mathbf{n})$. The latter is orthogonal to the tangent plane in wich (l, m) lie. (SZA image credit: CARMA, sketch made after example in Thompson, Moran & Swenson (2001))

can be neglected, one can write an expression for the corresponding visibilities $V_{i,j}(u,v)$, exploiting the geometry in Fig. 4.1 and applying the small-angle approximation

$$V_{i,j}(u,v) = \int\int \mathcal{A}(l,m) B_\nu(l,m) e^{-2\pi i(ul+vm)} dl dm, \tag{4.2}$$

where $A(l,m)$ is the antenna response and $B_\nu(l,m)$ is the source brightness distribution. We can therefore recover both, the amplitude and the phase, since $V_{i,j}$ is complex. This means that, if we had complete uv-coverage, one would recover the source brightness distribution through a 2D Fourier Transform for a source small in extent such that the small angle approximation holds. Complete uv-coverage would, however, imply an infinite number of baselines which is clearly not possible for interferometric arrays. Interferometric arrays are designed in such a way as to optimize the uv-coverage for a given number of telescopes, producing a characteristic sampling function whose inverse Fourier Transform gives the synthesized beam. The sampling function, $S(u,v)$, is zero at all points in the uv-plane except for at the interferometrically sampled uv points, giving

$$I_{\text{dirty}} = \int\int V(u,v) S(u,v) e^{2\pi i(ul+vm)} du dv \qquad . \tag{4.3}$$

The noise in the image plane for a homogeneous array made up of N antennas is

$$\sigma_s = \frac{2kT_{\text{sys}}}{\epsilon_q \epsilon_c A_{\text{eff}} \sqrt{N(N-1) n_p \Delta\nu t_{\text{int}}}} \qquad , \tag{4.4}$$

with a correlator efficiency ϵ_c, a quantization efficiency, ϵ_q, number of polarizations, n_p, bandwidth per polarization, $\Delta\nu$, on-source integration time, t_{int}, system temperature, T_{sys} as well as an effective area A_{eff}, which itself is related to the rms surface accuracy through the Ruze formula and the geometrical dish area.

'Aperture Synthesis Imaging Simulator'

In order to verify the proper workings of the earlier versions of CASA's interferometric simulator (simdata in CASA V. 3.2 and below), I wrote an interferometric simulator code, that can simulate the uv-coverage and synthesized beam, given a set of antenna positions. In addition, the workings of CASA's natural and uniform weighting were examined with my simulator. The results from the two simulation packages were found to aggree when set to the same observing conditions. This cross-check was, at the time, important since several mock interferometric simulations were used to make predictions for ALMA, JVLA and CARMA/SZA proposals for which accurate predictions on the trade-off between uv-coverage, observation time and required sensitivity were crucial.

My simulator had the advantage to earlier CASA simulators in that flagging due to elevation limits could more easily be identified and manual noise addition was more intuitive. The simulator code was extensively used in the initial testing phase of my visibility fitting

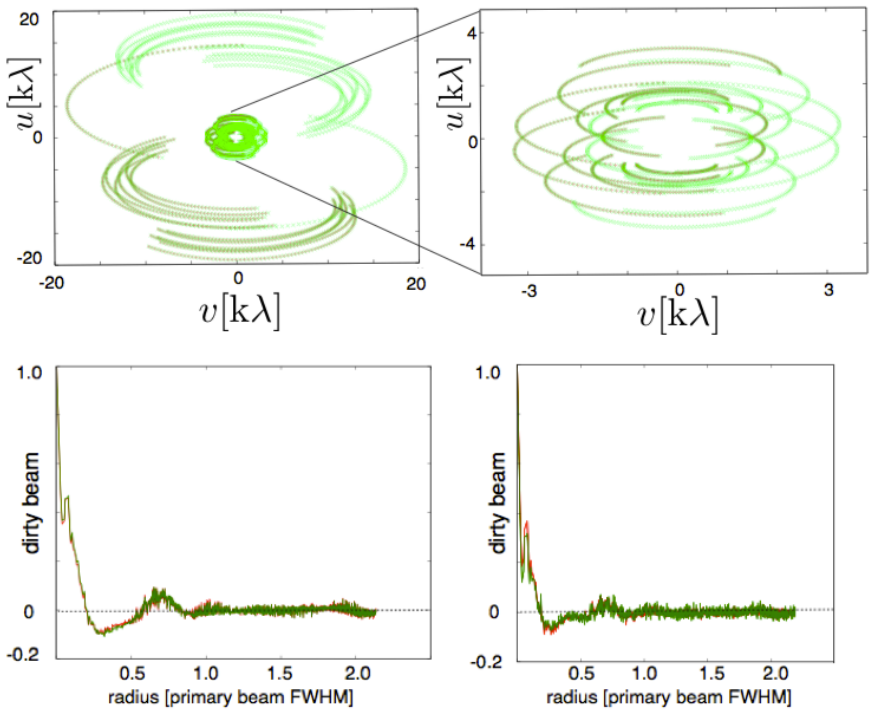

Figure 4.2: Simulator comparisons. *Top:* A uv-coverage comparison of simulated SZA array observations via my simulator (green) and CASA (red) with the central uv-coverage being shown as a zoomed in image (top right). CASA exploits the symmetry in the uv-plane such that only half the visibilities are diplayed. *Bottom:* Weighting comparison between my simulator (green) and CASA (red) for natural (left) and uniform (right) weighting.

code (Chapter 6). In the latest CASA versions, the aforementioned difficulties have now been rectified through the option to display flagged visibilities on top of the non-flagged data as well as through the availability of separate 'simobserve' and 'simanalyze' tasks that separate the aperture synthesis and imaging steps. The first step in my simulator/CASA comparison lies in the examination of the uv-coverage for a given set of antenna positions and subsequent Earth sysnthesis.

The SZA is taken as an example array and the corresponding CASA and my simulated uv points agree very well (Fig. 4.2). In order for the visibilities to be transformed back to the image plane, they need to be gridded onto a regular grid before being subjected to the Fast Fourier Transform (FFT) algorithm that is computationally much faster than conventional fourier transforming.

Before inversion, the visibilities can be weighted taking into account factors such as tapering, system temperature and single visibility accumulation time or, indeed, the density of weights in the uv-plane. Uniform weighting applies the same weight to all visibilities by applying a weighting factor proportional to the inverse of the number of visibilities

within a specified small sub-set of the uv-plane such as a box or circular region. It thus maximizes the attainable angular resolution at the cost of decreasing sensitivity. Natural weighting does not apply such a weighting factor and therefore retains information of the intrinsic density variations in the uv-plane. As such, it results in maximum sensitivity but does not give as high an angular resolution as the uniform weighting case (Fig. 4.2).

Due to the fact that incomplete sampling introduces sidelobes in the final dirty image, de-convolution algorithms such as CLEAN or MEM need to be applied to generate cleaned images. The clean algorithm is introduced via its application to bolometer single-dish data in section 4.3.5, whose basic principles follow the interferometric clean method, the most important difference lying in the interferometric clean beam peak normalization to 1.

4.2 A selection of current interferometers

The specifications of interferometers with relevance to galaxy cluster observations as well as open proposal calls are given in Fig. 4.3. Only those arrays with current calls for open observing time are included. As one can see from the offered frequency bands and baseline ranges, all three istruments are suitable for SZ observations. The sensitivities as well as the uv-coverage are the limiting factors in determining the array choice. This stresses the need for interferometric simulations that quantitatively illustrate these effects.

Interferometers	Number of antennas	Frequency (GHz)	minimum baseline	maximum baseline
JVLA	27 x 25m	1-2 (L-Band) 2-4 (S-Band) 4-8 (C-Band) 8-12 (X-Band) 12-18 (Ku-Band) 18-27 (K-Band) 27-40 (Ka-Band) 40-50 (Q-Band)	35 m	36 km
ALMA/ACA	50 x 12m 12 x 7m 4 x 12m (TP)	31- 45 (Band1) 67- 90 (Band2) 84-116 (Band3) 125-163 (Band4) 163-211 (Band5) 211-275 (Band6) 275-373 (Band7) 385-500 (Band8) 602-720 (Band9) 787-950 (Band10)	9m (ACA) 15m (ALMA)	16 km
CARMA/SZA	9 x 6.1m (BIMA) 6 x 10.4m (OVRO) 8 x 3.5m (SZA)	27-36 85-116 215-265	4.5m (SZA) 7m (15-array)	2 km

Figure 4.3: Interferometers suitable for SZ cluster observations and the available frequency bands and baselines. Numbers in blue indicate planned future frequency bands.

4.3 APEX-SZ

The APEX telescope is located on Llano de Chajnantor at 5107 m altitude in the Atacama desert, Chile. Its design is an on-axis Cassegrain with 12-m diameter. The APEX-SZ experiment is a collaboration between Berkeley, University of Bonn, MPIfR, University of Chicago, Onsala, Cardiff, MPE and ESO operating a 280 element bolometer camera during 2007−2010 at the APEX telescope. Targeted observations of over 40 X-ray selected galaxy clusters were made.

4.3.1 APEX-SZ - technology

For the APEX-SZ observations, the signal was collected by the APEX-SZ primary mirror and then reflected by re-imaging optics in the Cassegrain cabin into the cryostat (Fig. 4.4). The latter encompassed filters, lenses as well as the bomometric array and superconducting quantum interference devices (SQUIDs) readout electronics (Schwan et al. 2011). A Pulse-tube cooler and a 3-stage helium sorption refrigerator ensured that the bolometers are cooled down to 280 mK.

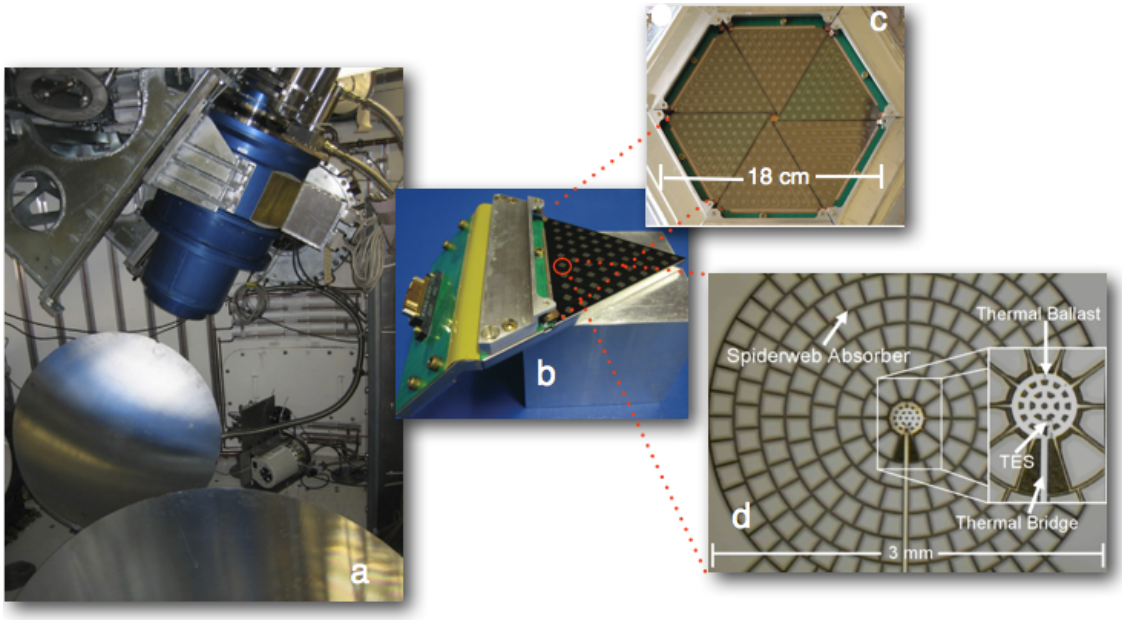

Figure 4.4: APEX-SZ: the technology. *a)* The cryostat and two mirrors at the bottom (Dobbs et al. 2006) *b)* a bolometer wafer (Schwan et al. 2011) *c)* 330 element bolometer array composed of 6 bolometric wafers (Schwan et al. 2011) *d)* A single pixel showing the location of the TES (Westbrook et al. 2009).

The bolometer array consisted of 6 bolometric wafers each having 55 elements (Fig. 4.4). It was found that one of the sub-arrays was not functional and that a further 14 elements had faulty SQUIDs and a few did not have the desired optical efficiency (Schwan et al. 2012). This meant that, during the observations, typically 170-180 of the remaining 280 channels could be used (Fig. 4.6b).

4.3.2 Operation of a bolometer

The response of incoherent detection is proportional to the power of the incoming radiation. Bolometers operate on the principle of direct thermal detection and offer both, high sensitivity and wide bandwidth in the sub-mm range. The detectors of the APEX-SZ receiver are sub-arrays of transition-edge sensor (TES) bolometers whose operation is described below. A summary of the work done by the APEX-SZ collaboration on data aquisition and processing is also presented.

Bolometer elements consists of an absorber with heat capacity C and a thermistor, which are thermally connected to a heat sink of temperature T_s through a thermal conductance, G, as depicted in Fig. 4.5.

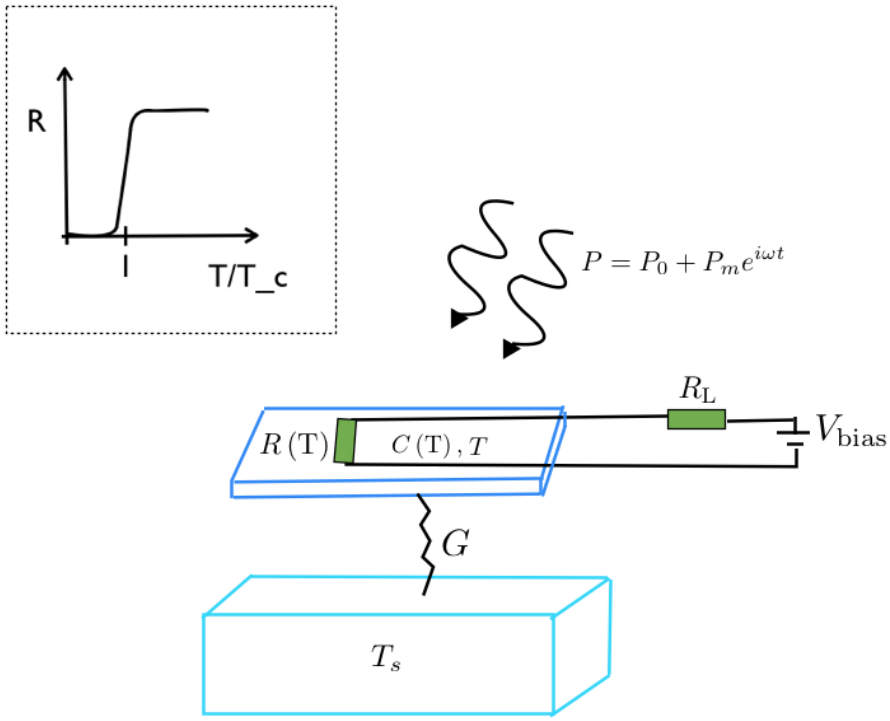

Figure 4.5: A sketch of the main components of a bolometer element and a typical resistance-temperature sketch for a Transition Edge Sensor (TES) bolometer.

A thermistor is a device whose resistance changes as a response to a temperature change. In this case, a temperature change of the absorber is brought about by the incident power of the photons that have been reflected into the detector. A typical time constant indicating the time between independent measurements is the intrinsic thermal time constant τ_0, given by the ratio of the heat capacity of the absorber to the conductance of the thermal link

$$\tau_0 = \frac{C}{G} \qquad , \tag{4.5}$$

since it is the thermal link through which the cooling process takes place. This change in temperature thus results in a change in resistance. Ideally, one would like to use a thermistor whose resistance changes as much as possible for a given temperature change. One type of thermistor is the semiconducting bolometer whose resistance is dependent on temperature via the relation

$$R(T) = R_0 e^{\left(\frac{\delta}{T}\right)^{\frac{1}{2}}} \tag{4.6}$$

and is thus exponentially dependent on the root of the ratio between the band gap and the bolometer temperature. In recent years, it has become possible to manufacture bolometer arrays of superconducting bolometers via micro-lithographic processes. These bolometers operate in the superconducting transition, i.e. the transition between the normal and the superconducting state, and are named Transistion Edge Sensor (TES) bolometers. The APEX-SZ detector is composed of such arrays of TES bolometers (Fig. 4.4). They have a very sharp resistance-temperature relation near the critical temperature, 465 mK and 570 mK for the type-1 and type-2 APEX-SZ TES bolometers (Schwan et al. 2011), as shown by the sketch in Fig. 4.5.

In order for a TES bolometer to be stable, it needs to be voltage biased so that the total power remains constant through negative electrothermal feedback (ETF), thus ensuring that the TES stays in the transition state. This can be exemplified by the following consideration of energy conservation which follows Lee et al. (1998)

$$P_0 + \delta P e^{iwt} + \frac{V_b^2}{R} - \frac{V_b^2}{R^2}\frac{dR}{dT}\delta T e^{iwt} = \overline{G}(T - T_s) + G\delta T e^{iwt} + iwC\delta T e^{iwt} \quad , \tag{4.7}$$

where V_b is the bias voltage and the first term on the rhs gives the power flowing through the thermal link. The conductance is

$$G = \frac{A}{l}\left(\frac{1}{Ts - T}\int_T^{T_s} \kappa(T) dT\right) \tag{4.8}$$

where $\kappa(T)$ is the thermal link conductivity, A is the cross-sectional area and l is the length of the thermal link. The last term in Eq. 4.7 on the rhs originates from the power stored in the heat capacity of the detector C. As one can see by inspecting the time-invariant and time-variant parts of Eq. 4.7 separately, for a detector with $\frac{dR}{dT} > 0$, an increase in the

power incident on the detector leads to an increase in the detector's resistance, and thus to a decrease in the bias power through the term $-\frac{V_b^2}{R^2}\frac{dR}{dT}\delta T e^{iwt}$. This can be quantified by a single parameter, the loop gain,

$$\mathcal{L}(\omega) = \frac{P_b \alpha}{GT(1 + i\omega\tau_0)} \quad . \tag{4.9}$$

Since it is the change in current as a function of a change in received power that one is interested in, one defines the responsitivity to be

$$\frac{\delta I}{\delta P} \approx -\frac{1}{V_b} \tag{4.10}$$

in the limit where $\omega << \frac{1}{\tau}$ and $\tau = \frac{\tau_0}{\mathcal{L}+1}$. It is this change in current which is then measured with the superconducting quantum interference devices (SQUIDs) (Schwan et al. 2011).

4.3.3 APEX-SZ data analysis

Two scanning strategies were used with APEX-SZ for science and flux calibrator observations - a raster scan pattern at constant elevation and, primarily, a drift circle scan pattern fixed in azimuth/elevation for each pass, different passes being separated by elevation increments (Fig. 4.6a).

The latter was the preferred scanning strategy for science targets. One set of circular scans fixed in azimuth/elevation typically consists of 20 circular subscans each of 5 second duration with a circular scan radius chosen as a function of redshift (M. Sommer PhD Thesis). Not only does the full cluster radial extent need to be covered but the circles must also cover a sufficiently extended region in order to be able to baseline relative to the primary CMB (M. Sommer PhD Thesis). The resultant timestreams of the observations are the data products. Below, a brief outline of the APEX-SZ data processing developped by the APEX-SZ collaboration is given (for a detailed discussion see Martin Sommer's and Amy Bender's PhD theses).

In order to determine the overall instrument beam size, a point source such as Mars (seen in relation to the final beam) was observed in a raster mode. Co-adding the data from all working bolometers, Fig. 4.6b, yielded a beam shape whose best gaussian fit has a FWHM of $58''$ (Fig. 4.6c). The central frequency was found to be 151 GHz via

$$\nu_c = \frac{\int F(\nu)\nu d\nu}{\int F(\nu) d\nu} \tag{4.11}$$

where $F(\nu)$ is the bandpass shape. Absolute flux calibration was also done with Mars observations.

The data processing included the removal of bad channels as well as of spikes and glitches in the data timestreams. In addition, timestream atmosphere removal was ensured through a joint polynomial + elevation-dependent term fitting and subtraction. Signals

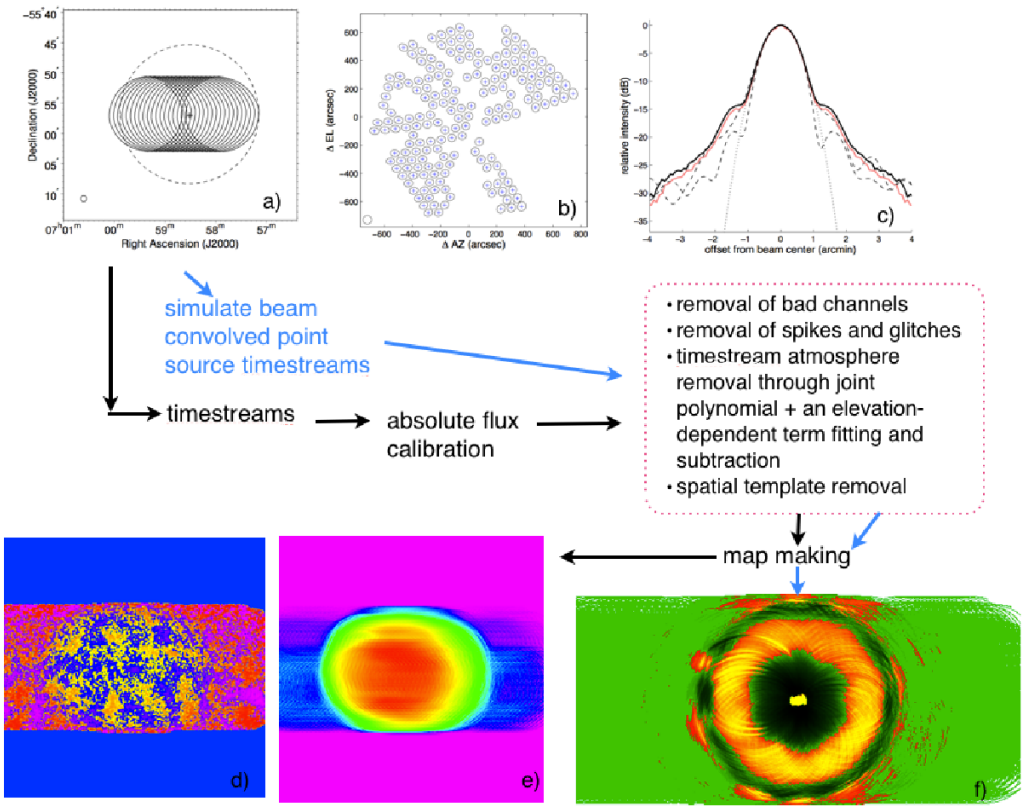

Figure 4.6: A summary of the main reduction steps of APEX-SZ. *a*) A circular sub-scan scan pattern in constant EL/AZ (image credit: Amy Bender Thesis). *b*) Individual bolometer beams for the TES bolometers in the wafers that are operational (Schwan et al. 2011). *c*) The beam pattern obtained from the co-added beam map (Schwan et al. 2011). *d*) A raw map of APEX-SZ MS0451 data.*e*) The weight map of the galaxy cluster MS0451. *f*) The MS0451 point source transfer map zoomed into the scanning pattern. All APEX-SZ maps were produced by Martin Sommer.

correlated across the array were also removed (Nord et al. 2009). The map-making included weighting by the inverse rms squared of individual channels (individual bolometer signals). With the reduction pipeline being in operation, it was then possible for the APEX-collaboration to quantify the sum of all steps via a point source transfer function (PST). This PST was obtained by passing a beam-convolved point source through the same pipeline steps, that were previously used for the particular galaxy cluster observation. The derived transfer function can therefore be used to predict the effect of the pipeline on a given input cluster model,

$$\mathcal{M}_{\rm pipe} = \mathcal{M}_{\rm model} \otimes \mathcal{T} + \mathcal{N} \tag{4.12}$$

where $\mathcal{M}_{\rm model}$ is the input model, $\mathcal{T}$ is the point source transfer function and $\mathcal{N}$ is an APEX-SZ noise map. The jack-knived noise maps are formed by multiplying half of the timestreams by -1 before the mapping steps (Nord et al. 2009). It has recently been found that the circular scan pattern and its subsequent intrinsic non-uniform map coverage affect the viability of the transfer function. In this thesis, the point source transfer method is nevertheless adopted.

4.3.4 APEX-SZ sample

The APEX-SZ sample consists of 43 galaxy clusters, a sub-set of which constitutes 11 out of 13 clusters from the statistically complete X-ray selected REFLEX-DXL sample by Zhang et al. (2006). The redshift distribution of the extended DXL and low-redshift samples is illustrated in Fig. 4.7. Note that a few selected clusters supplement the sample at higher redshifts and are not included in the graph. The morphological classification of all 43 clusters was obtained from literature (see chapter 7).

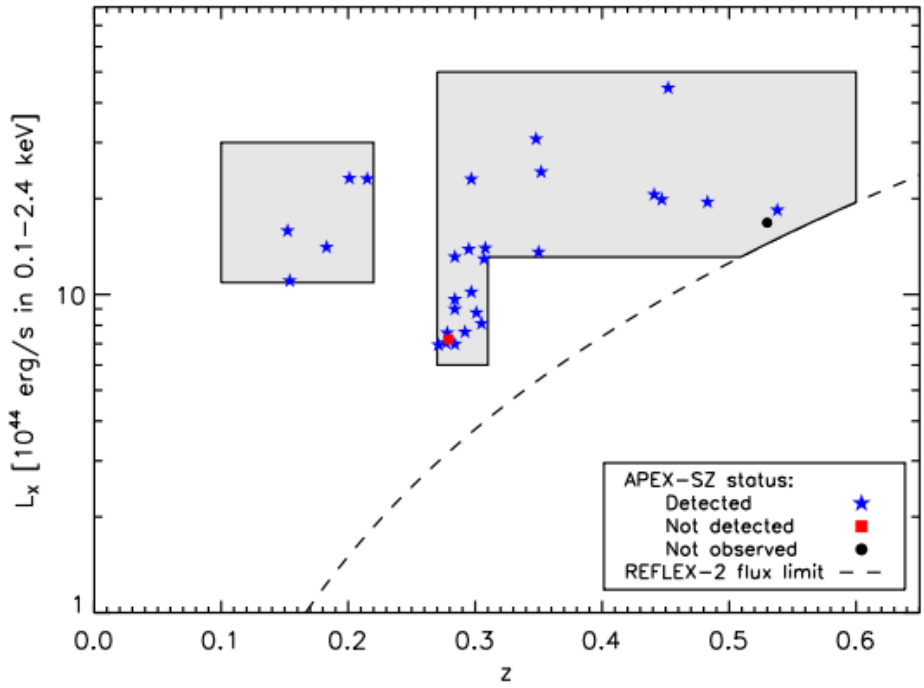

Figure 4.7: The X-ray selected sample (image credit: F. Pacaud). These targets are complemented with supplementary cluster observations, some of which are at higher redshift and don't belong to the X-ray selected sub-set.

4.3.5 The APEX-SZ CLEAN method

Within the framework of his PhD thesis, Martin Sommer developed a way to de-convolve bolometer single-dish maps given a point source transfer function. The clean method relies heavily on the validity of the PST, since it assumes that the final map can be thought of as the sum of PST convolved point sources,

$$\mathcal{M}_{\rm pipe} = \sum_{i=1}^{i=N_1} \sum_{j=1}^{j=N_2} \alpha_{cl}(i,j)\delta(i,j) \otimes \mathcal{T} + \mathcal{N}(i,j) \tag{4.13}$$

for a map, $\mathcal{M}_{\rm pipe}$, of size $N_1 \times N_2$ and clean components with amplitudes $\alpha_{cl}(i,j)$. As with for every type of clean algorithm, the maximum peak is located in the map, which is, in this case, a beam-smoothed signal-to-noise map. This extra smoothing helps to avoid primarily picking up pixel noise.

A conversion factor quantifies the effect of the joint convolution with the PST and the smoothing kernel on a unit point source at the position of the peak. The peak signal is then corrected by this conversion factor and the result is added as a clean component to the clean map.

The PST convolved point source is then subtracted from the raw map and the process of peak searching is repeated on the new kernal smoothed SNR residual map. After cleaning, the clean components are convolved with the APEX-SZ beam and added to the final residual map.

4.4 Conclusion

This chapter thus presents my interferometric simulation code, placing it in comparison with the available CASA software simulator. This investigation is vital as it lays the foundation for the testing of my interferometric visibility fitting code, having examined, and subsequently reassured, the proper workings of the CASA visibility generation. The outlined pipeline transfer function as well as the jack-knive noise generation, both developed by the APEX-SZ collaboration, provide the vital inputs for my APEX-SZ galaxy cluster pressure profile fitting code, which is further described in Chapter 6.

Chapter 5

CARMA/SZA observations of MS0451

During the course of this thesis, I devised a single cluster pilot study via two accepted proposals (PI: Burkutean) for the CARMA/SZA interferometric arrays, giving a total interferometric observation time of 75 hours.
The cluster choice was tailored not only towards cross-calibration of the interferometric and the available APEX-SZ data sets but also towards a more involved multi-wavelength triaxial galaxy cluster study, the theoretical simulation framework of which is described in chapter 9.
The interferometric data from the SZA/OVRO/BIMA arrays was analysed with separate and joint-heterogenous imaging. The visibility data itself covered a far wider uv-range than the previously reported 30 GHz OVRO observations. I also present an image plane combination of the cleaned APEX-SZ and interferometric maps. This, in turn, motivates the parametric fitting approach in chapter 6.

5.1 Scientific and technical objectives

Having established in the previous chapters that cluster scaling relations rely heavily on accurate and precise mass proxy deductions, which themselves may be subject to instrument-induced systematics or, in fact, due to an intrinsic morphological bias, these factors can be studied with the available APEX-SZ cluster sample, which lends itself well to follow-up high resolution studies with interferometers. In order to design such an interferometric APEX-SZ follow-up project, I chose a galaxy cluster out of the APEX-SZ sample in order to explore two projects; one that has a scientific focus and another that is of a more technical nature.

Scientific project

The scientific goal of this particular investigation is based on examining the pressure profile of the intra-cluster gas. This is motivated by the need to find accurate and precise measurements of the integrated SZ signal over a given radius, in the case of $Y_{\rm sph}$, or aperture for $Y_{\rm cyl}$, in order to serve as a mass proxy for cosmological investigations. Its immediate use for a single-cluster study is to provide a means to diplay the acceptable parameter space for the interferometric and single-dish data and thus to examine the advantages and disadvantages of both observing methods. This, in turn, will motivate a joint interferometric/single-dish follow-up program of additional clusters, that is outlined in Chapter 9.

Technical project

The technical project is concerned with the nature of single-dish and interferometric data combination, which, in the particular case of Sunyaev-Zel'dovich observations, has not been done to this date. This involves both, combinations in the image plane as well as comparisons in the visibility plane. The latter opens up the possibility to compare interferometric and single-dish parametric Markov Chain Monte Carlo Bayesian model fittings (Chapter 6). In the era of ALMA and future CCAT observations, such techniques will become ever more important since the unprecedented sensitivity of current interferometric arrays as well as future single-dish experiments will enable detailed Sunyaev-Zel'dovich studies of individual clusters to be made, covering scales from a few arcseconds to several arcminutes (Chapter 7). Combining single-dish and interferometric Sunyaev-Zel'dovich data is thus an approach, which will have numerous applications in the near future.

Future scientific outlook

In order to infer the 3D pressure profile of the ICM gas in galaxy clusters, most investigations assume spherical symmetry alongside with hydrostatic equilibrium. It has only been recently, (Sereno et al. 2011, Morandi et al. 2011), that a multi-wavelength triaxial structure analysis including dark matter and ICM parameters, has been put forward. The aim of such modeling is to infer the 2D likelihood regions of the triaxial cluster shape parameters in conjunction with non-thermal pressure support factors. Such triaxial shape determinations are crucial when examining outliers in weak-lensing mass/gas-derived mass

comparisons, that may bias scaling relations. These outliers may originate from very disrupting merger events or from spherical shape assumptions being imposed on more triaxially-shaped clusters. For large samples, shape variations will average out (Battaglia et al. 2012) and spherical symmetry assumtions are believed to be sufficient. The study of cluster ellipticity as a function of redshift will profit from triaxial analyses, if one is to infer knowledge of the acceptable shape parameter space, or indeed lack thereof. Within this thesis, the computational framework for such triaxial fitting has been initiated (Chapter 9), which will later be applied to a full multi-wavelength analysis on the chosen cluster. Preliminary X-ray analyses of archival Chandra data are also discussed in Chapter 9.

5.2 The CARMA interferometer: a first overview

The Combined Array for Research in Millimeter-wave Astronomy (CARMA) is an interferometric array located in the desert Owen's Valley at Cedar Flat, California, at 2200m altitude. It is jointly operated by the California Institute of Technology, the University of California Berkeley as well as the Universities of Illinois, Maryland and Chicago. The heterogeneous interferometric CARMA array is made up of the Owens Valley Radio Observatory array (OVRO), the Berkeley Illinois Maryland Array (BIMA) and the Sunyaev-Zel'dovich Array (SZA). For each observing cycle, 30 % of the total allocated time is given to institutions outside of the CARMA collaboration.

Figure 5.1: The CARMA interferometer is composed of the 3.5m diameter SZA antennas as well as the 10.4 and 6.1m diameter OVRO and BIMA arrays. These can operate as 8-element, 15-element or 23 element arrays. (image credit: CARMA)

The array comprises 23 antennas that can operate as a joint array or as two OVRO/BIMA and SZA sub-arrays. The 15-element sub-array consists of 6 OVRO antennas with a dish diameter of 10.4 m and 9 BIMA antennas with a dish diameter of 6.1 m.

The 8 SZA antennas, with a dish diameter of 3.5m, have 26-36 GHz and 85-115 GHz single-sideband receivers. Up until the 2012b semester, the 15-element array had 215-265 GHz and 85-116 GHz double-sideband receivers. It was equipped with single-sideband 26-36 GHz receivers in the 2013a semester. The 10.4 and 6.1 m antennae correlator provides a maximum bandwidth of 4 GHz per sideband. During the time of observations reported in the next sections, the SZA had a fixed correlator setting of 15 bands, each consisting of 15×31.25 MHz channels, giving a total 7.5 GHz bandwidth.

The 15-element array has 5 different configurations with maximum angular resolutions ranging from 0.3" to 10" at 100 GHz. The SZA has two different configurations, named SH and SL, for high and low declination targets respectively.

The SZA antenna positions were devised such that the array consists of 6 closely-spaced antennas which are supplemented by two outer antennas that provide the long baselines necessary for high-resolution point source detection.

Instrument selection

The APEX-SZ observations span a galaxy cluster declination range of ≈ -56deg to $\approx +17$deg. In terms of interferometer-based pressure profile follow-up studies, this narrows down the interferometer selection to the JVLA, CARMA-SZA, AMI and ALMA/ACA arrays. The JVLA does not provide the desired uv-coverage and sensitivity within reasonable observation times. In addition, it lacks the short baselines necessary for APEX-SZ/interferometric cross-calibration studies.

ALMA/ACA does provide shorter baselines than the JVLA due to its 7 m dishes that can be closely packed at 9 m distance from each other. However, the lack of Band 1 receivers makes the annular overlap region with APEX-SZ insufficient for cross-calibration of the wide angular scale signal. The AMI instrument would provide the required scales but has no public opening for proposal submission. Its location demands long observing times to reach sensitivity levels required for cluster Sunyaev-Zel'dovich observations.

The CARMA/SZA array overcomes these shortcomings, with the 3.5m dishes having Band 1 and Band 3 receivers and the location being at high altitude in a dry climate. Its choice as the prime instrument for APEX-SZ cluster follow-up projects is further outlined in section 5.4.

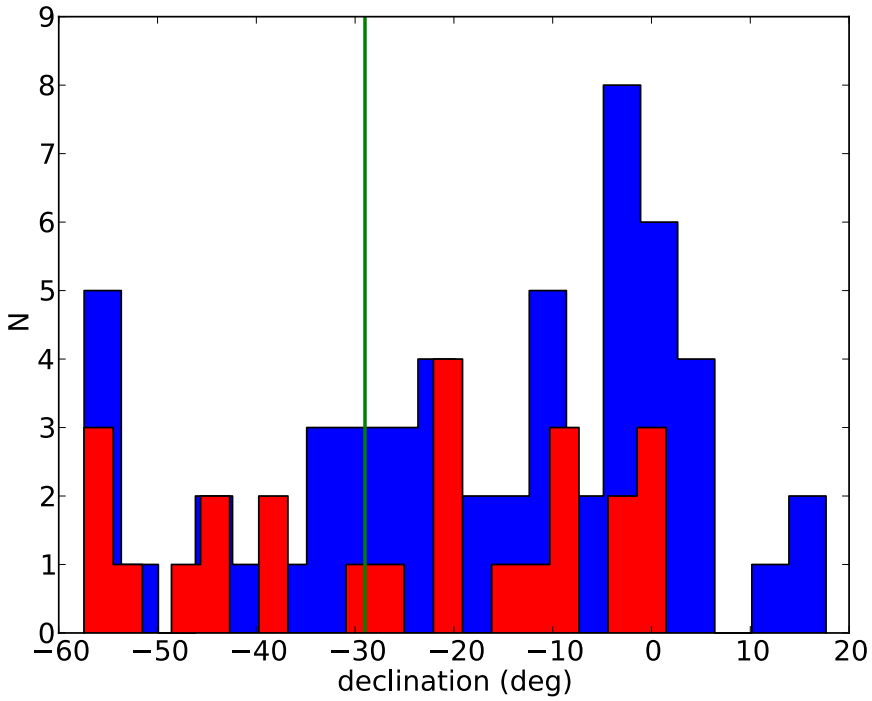

Figure 5.2: APEX-SZ sample declination range for the whole sample (blue, using the APEX-SZ pointings) and the combined low redshift eDXL and high redshift Lx sample (red, using the X-ray centres) (X-ray information by F. Pacaud). The limit below which CARMA/SZA observations are not feasible is denoted by a green line. Observations with a declination margin above -25 deg are to be preferred for a decent tracking of the source.

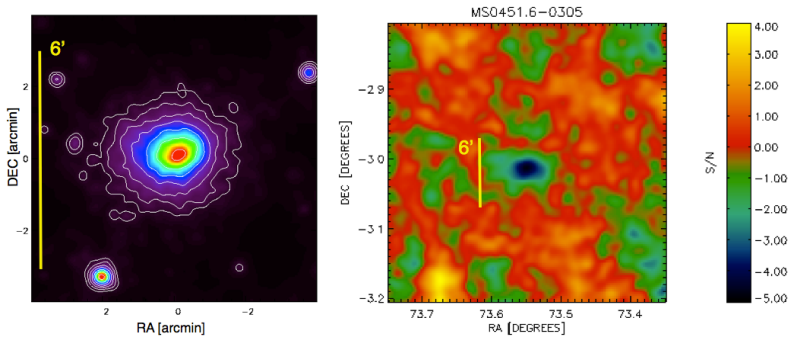

Figure 5.3: The galaxy cluster MS0451. *Left*: An adaptively smoothed XMM-Newton X-ray image by F. Pacaud. *Right*: The APEX-SZ signal to noise image by M. Sommer. Both images indicate an elliptical projected shape.

5.3 Galaxy cluster choice

Taking CARMA/SZA as the desired follow-up instrument, limits the galaxy cluster selection to higher declination targets, since observations beyond and excluding -30deg (CARMA sensitivity calculator) are not feasible from antenna shadowing considerations for the low declination SZA antenna configuration SL (Fig.5.2). With this selection criteria, there are 38 clusters (including APEX-SZ non-detections) suitable for the desired pilot study. Out of this sub-sample, the galaxy cluster choice was driven by the availability of high quality complementary X-ray data, weak lensing archival data, strong lensing information as well as evidence for an elliptical shape in the APEX-SZ image in order to offer the broadest scientific single-cluster study possible. MS0451.6-0305 is one of the most X-ray luminous clusters, $L_X = 3.8 \times 10^{11} L_\odot$ (Donahue et al. 2003), and has a mass of $M_{500} = (8.6\text{-}8.9) \times 10^{14} h^{-1} M_\odot$.

In addition it exhibits a projected elliptical gas distribution as can be seen in our signal to noise APEX-SZ map (Fig. 5.3). Recent results, Sereno et al. (2010), suggest this cluster is strongly elongated along the line of sight. Archival Suprime-Cam Subaru data, sufficient for at least a 3 filter weak lensing analysis, are available to allow for a high resolution multi-wavelength study of MS0451. All these factors make MS0451 the ideal target for a combined interferometric/single-dish study in terms of pressure profile parameter space comparisons, which have the potential for future multi-wavelength analyses. In addition, its declination of -03d01m01.3s is well below the critical declination range near -25 deg in which shadowing becomes a serious issue. It should however be noted that the uv-coverage is not optimal for declinations near 0 deg.

5.4 Detailed justification for the interferometer choice

There are two complementary methods to assess an interferometer's suitability for the planned observations. One is the generation of mock simulations, as was done for the CARMA proposals described below, the other is direct inspection of the uv-coverage. The uv-coverage and radially binned visibility histograms are illustrated in Figs. 5.4 and 5.5. In this case, the actual observed data, as opposed to the mock simulated visibilities, have been used. As one can see in Fig. 5.4, the uv-tracks are quite flat owing to the low declination of -3.01 deg of the target cluster. One can clearly see the two outrigger antennas of the SZA (red) in Fig. 5.4, whose baselines will be used in the later sections to construct a high-resolution map of the target cluster in order to detect and remove points sources present in the field. The uv-density relates to the sensitivity at the probed scales. However, binned visibility histograms (Fig. 5.5) do not account for primary beam attenuation at the larger scales. Hence, the characteristic scale beyond which the signal cannot be recovered, typically 1/3 to 1/2 of the primary beam FWHM, has been labeled in each plot for the SZA and CARMA antennas respectively. The baseline-type colour coding will be consistent throughout this chapter. One should also note the characteristic 'hole' in the uv-range for the SL-SZA configuration near 2 kλ. This gap will now be filled with the recently installed Band 1 receiver on the OVRO and BIMA antennas, that was not yet present at the time of proposal submission.

5.5 Accepted Proposals

In order to assess the frequency and CARMA configuration choice for the proposed MS0451 observations for the CARMA December 2011 call for proposals, I made an extensive study via simulated mock observations with the CASA simulator tool.

The results showed that a total of 24 hours total observation time (with overheads) in the CARMA E configuration and 9 hours observation time in the SZA configuration at 90 GHz under typical weather conditions would ensure CARMA/APEX-SZ uv-overlap with sufficient sensitivity, while offering synthesized beams of $13.7'' \times 8.9''$ and $53'' \times 36''$.

The proposal was accepted as program c0879 (P.I. Burkutean) for the 2012a semester, which gave A priority to the SZA and B priority to the E-configuration MS0451 observations (Table 5.1). The priority level indicates the likelihood of a programme being observed and gives an indication into the effort being made to schedule the observations under good weather conditions.

In the c0879 program, no 30 GHz SZA array observations were asked for, in order to focus on spatial scales smaller than or comparable to the APEX-SZ beam of $58''$.

In my next proposal, the technical goal focussed on an extension of the cross-calibration analysis between interferometric and single-dish data as well as on an investigation into joint interferometric/single-dish data, in order to reveal systematic errors from the necessarily simplifying assumptions underlying each analysis and thus required 30 GHz data.

In this proposal run, a total of 52 proposals were accepted for the 30 and 90 GHz SZA array of which 48 projects were B-priority and only 4 programmes were given A-priority.

My proposal was accepted as A-priority programme c1015 (P.I. Burkutean) and permission was granted for additional observing time at 30 GHz beyond the time that was requested (Table 5.1).

Table 5.1: CARMA programmes c0879 and c1015 (PI: Burkutean)

Array	Central Frequency GHz	Priority	Total observation time with overheads (hrs)
SZA	31.2	A	17.6
SZA	90.3	A	20.7
CARMA-E	93.1	B	36.8

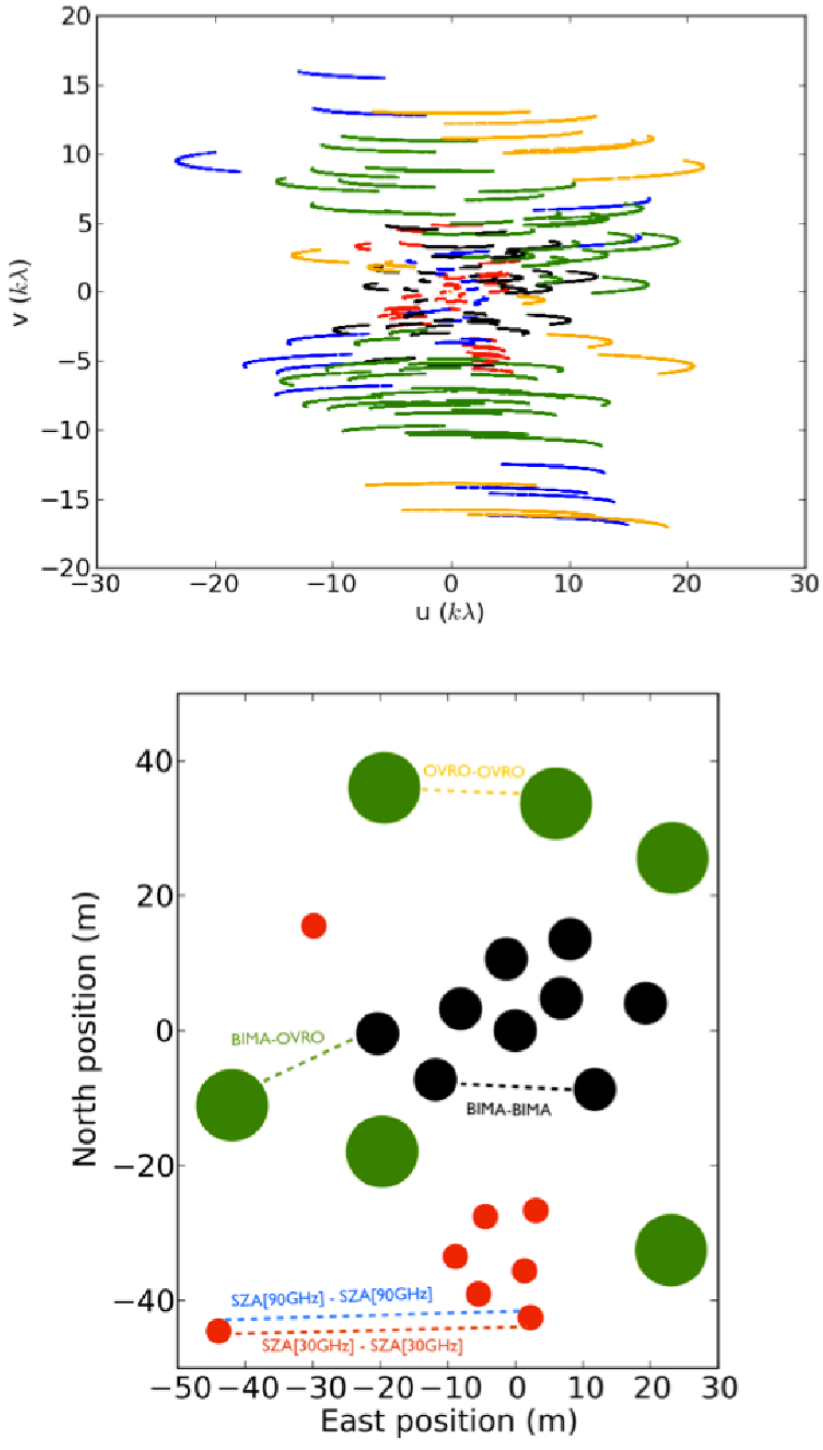

Figure 5.4: Visibility coverage of CARMA and the SZA. *Top*: UV-tracks of my MS0451 observations (section 5.5). Due to symmetry in the uv-plane only half of the baselines are plotted. *Bottom*: The physical positions of the antennas. The dotted lines show representative baselines. The baseline colour coding in both graphs is 30 GHz SZA (red), 90 GHz SZA (blue), 93 GHz BIMA-BIMA (black), 93 GHz BIMA-OVRO (green), 90 GHz OVRO-OVRO (orange).

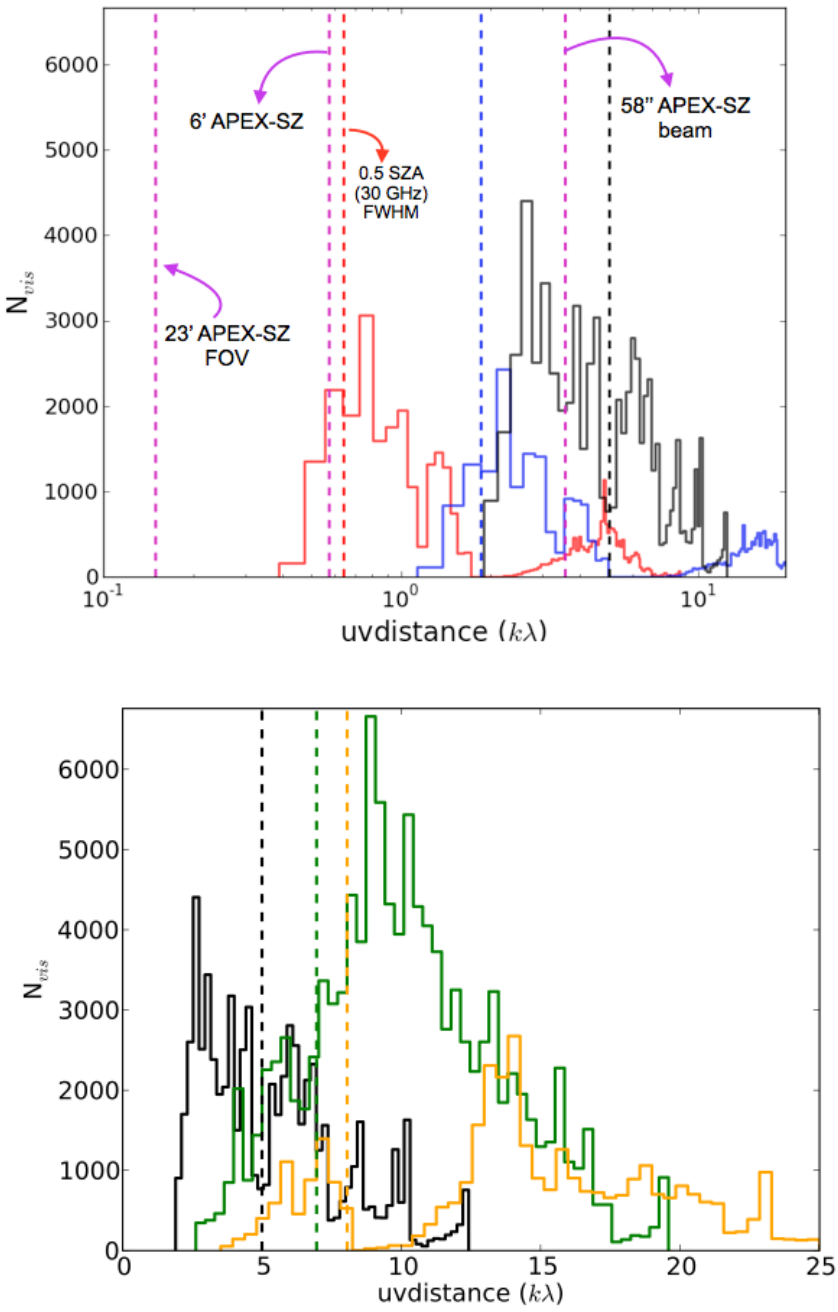

Figure 5.5: Visibility histograms of CARMA and the SZA. *Top:* Radially binned visibility histogram for the 30 GHz SZA (red), 90 GHZ SZA (blue) and 93 GHz BIMA-BIMA (black) baselines. The vertical dashed lines denote the scales beyond which no signal can be recovered. The vertical dashed magenta lines denote the minimum and maximum scale to which a signal can be recovered in the single-dish APEX-SZ observations. *Bottom:* Radially binned visibility histogram for the 93 GHz BIMA-BIMA (black), 93 GHz BIMA-OVRO (green), 90 GHz OVRO-OVRO (orange) baselines. The vertical dashed lines note the scale beyond which no signal can be recovered and correspond to 1/3 primary beam FWHM .

5.5.1 Interferometric data reduction and imaging

The observed visibilities, $V_{i,j}^{obs}$, contain spectral and temporal variations from instrumental and atmospheric effects

$$V_{i,j}^{obs}(u,v,\nu) = g_{ij}g_i(t)g_j(t)\left[B_i(\nu,t)\,B_j^{\star}(\nu,t)\right]V_{i,j}e^{i(\theta_i(t)-\theta_j(t))}\,, \tag{5.1}$$

where B_i denotes the complex bandpass for antenna i and g_{ij} is the baseline term, i.e. the gain between antennas i and j. The antenna dependent complex gain is described by the gain amplitude $g_i(t)$ and the gain phase $\theta_i(t)$. Interferometric data reduction aims to correct for these spectral and temporal changes unrelated to the source emission in order to deduce $V_{i,j}$, from which the source information can be obtained.

Data reduction procedure

The data were reduced with the data reduction package MIRIAD (Sault et al. 1995).

First, times when one antenna is shadowed by another are flagged. This is then followed by baseline correction in which updated antenna positions are written into the data set. Next, linelength corrections are applied. These take into account fiber length changes due to temperature variations.

The system temperatures for each antenna are inspected as a function of observation time and very high temperatures are flagged. Malfunctioning antennas can also be identified this way. The optical depth values at 230 GHz as a function of observing time were used to identify bad weather periods which were then flagged accordingly.

Whenever a source observation was not bracketed by a phase calibrator observation on either side due to flagging, this on-target period was also flagged since no proper phase calibration would be possible in this time window.

After edge channel flagging, the data are bandpass calibrated using a flat-spectrum bandpass calibrator source to take out instrumental frequency-dependent effects. This is then folowed by phase calibration of the phase calibrator which was chosen such that it was close to the target since, in applying the derived phase solutions to the target data, one assumes that both are subject to the same atmospheric fluctuations.

Absolute flux calibration with a planet or quasar of known flux from the CARMA calibrator archive was done to derive the flux scaling of the gain calibrator. The flux calibration using URANUS is described in more detail in the next section. Gain calibration is then done using the derived bootstrapped gain calibrator flux and the solutions are copied to the rest of the data. The amplitude and phases of the resultant calibrated calibrators are inspected as a function of time and baseline for each antenna.

The data imaging was also done in MIRIAD using natural weighting in which the gains were included along with the system temperatures in the variance-based weight calculation.

5.6 CARMA/SZA data reduction

The data from the c0879 and c1015 projects were first analyzed via frequency and antenna-type baseline separation so as to properly take into account point source removal. This is vital for obtaining accurate SZ flux estimates as point sources can contribute considerable positive flux to the negative SZ signal, thus partially, or even completely, canceling the SZ decrement. This, in the case of no removal, leads to an underestimate of the SZ flux.

30 GHz all baselines

The SZA observations, with a central frequency of 31.1 GHz, were made between October 2012 and January 2013. The total on-source integration time was 11.35 hours and the data spans the uv-range $0.39 - 8.67$ kλ. The primary beam at 31.1 GHz has a FWHM of 10.7 arcmin (Hasler et al. 2012).

Three out of my four 30 GHz SZA tracks used Uranus as an absolute flux calibrator. Uranus was chosen since Mars and Neptune were not visible at the time of observation. The default brightness temperature used in the MIRIAD bootflux task corresponds to 220 K, which is too high compared to the measured values by WMAP (Weiland et al. 2011), Fig. 5.6, and the VLA measurements by de Pater et al. (1991).

Thus, within the bootflux routine, Uranus' brightness temperature was manually set to the WMAP value, which also lies within the error bars of the 30 GHz data point in the de Pater plot.

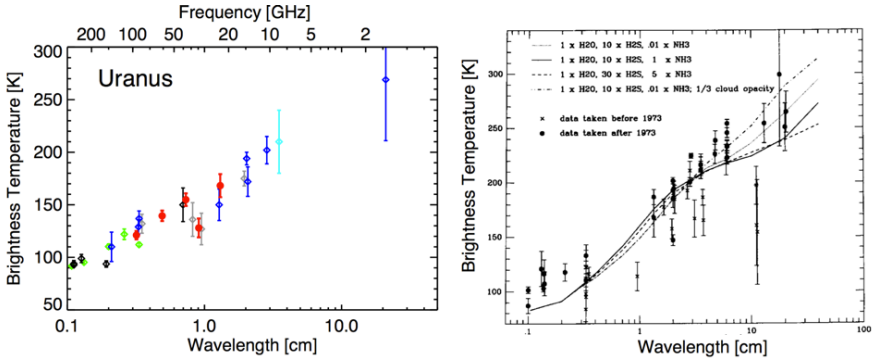

Figure 5.6: Uranus' brightness temperature as measured by WMAP (*left*) Weiland et al. (2011) and by the de Pater et al. (1991) investigation (*right*). The dip in the brightness temperature near 30 GHz is clearly visible in both plots.

Point source removal

Point source confusion, or in other words the effect that point sources within the FOV can cancel the SZ decrement, lead to an underestimation of the overall SZ signal. Single band single-dish observations, such as APEX-SZ, which cannot use spectral fitting to isolate the point source population component, suffer particularly from this effect.

An example of possibly such a scenario may be present in the APEX-SZ RXCJ2014 observation. The cluster contains a bright NVSS point source in its centre, Fig. 5.7 (I will return to this issue in chapter 9). The 1.4 GHz continuum NRAO VLA Sky Survey (NVSS) mapped the sky north of -40 deg with a map sensitivity of 0.49 mJy/beam at 45 arcsec resolution (Condon et al. 1998). It can be used to indicate potential flat-spectrum radio sources in the SZA 30 GHz map.

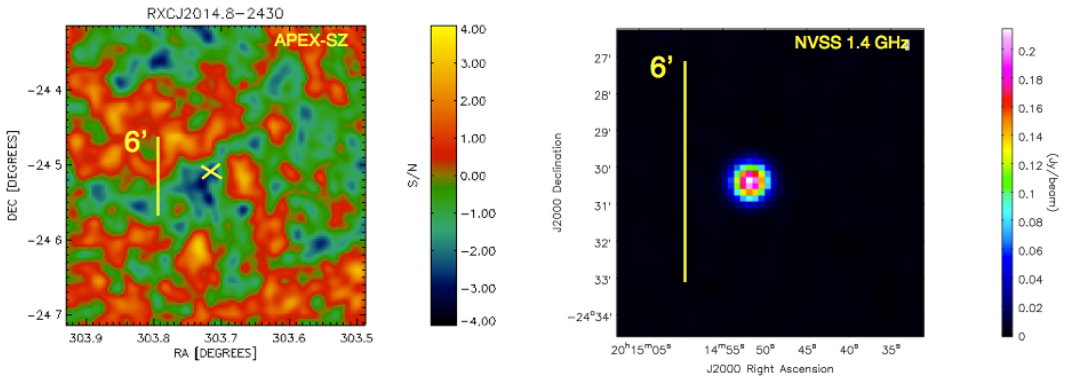

Figure 5.7: A potential example case of a point source canceling the SZ decrement. *Left:* APEX-SZ 150 GHz SNR map of the cluster RXCJ2014 by M. Sommer. *Right:* A 0.24 mJy/beam point source in the NVSS catalogue at 1.4 GHz. This source could potentially be the cause of the noisy RXCJ2014 map.

Interferometers with extended baselines can be used to constrain the position and flux of point sources. The two outer antennas of the SZA allow for such point source imaging. In the case of MS0451, the 30 GHz data was first imaged using the whole uv range with natural weighting (Fig. 5.8). This weighs down low-density regions in the uv-plane. The noise level in this image is 0.19 mJy/beam, which is lower than the 0.27 mJy/beam obtained from the CARMA sensitivity calculator for good weather conditions. This can be explained by the fact that the average antenna system temperature is slightly below the 40 K assumed in the calculator. My weighting scheme includes the gains in the system temperature weightings and on two days the opacity was 30% below that expected. The overall observing conditions were thus better than expected in 50% of the tracks.

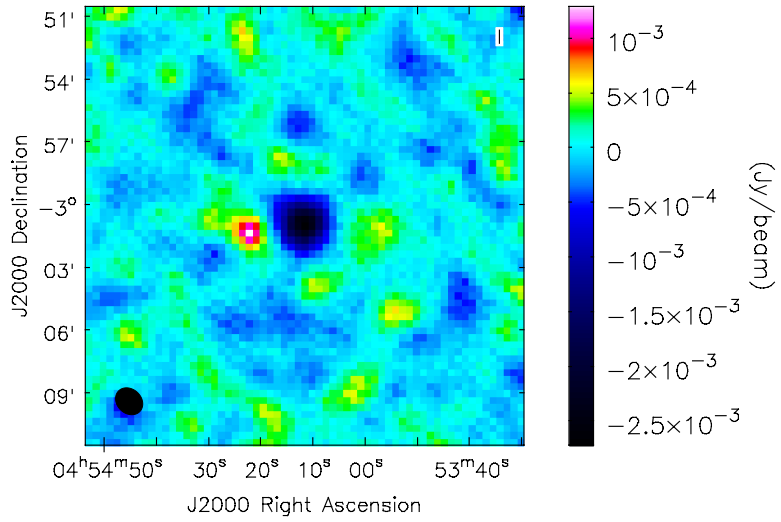

Figure 5.8: A cleaned map of the 30 GHz SZA observations including all baselines. The point source next to the SZ decrement is clearly visible.

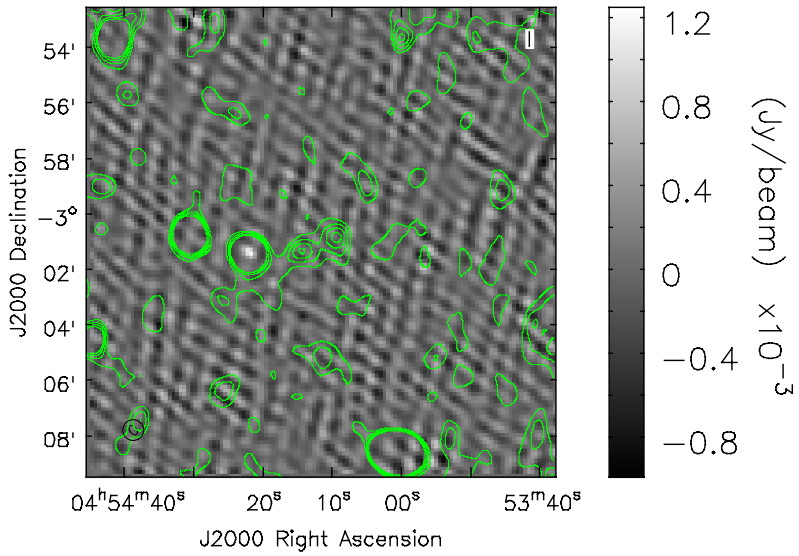

Figure 5.9: A cleaned map of the 30 GHz SZA observations including only the baselines >2 kλ. The NVSS contours in 1σ steps of the NVSS map are overlayed.

Another high-resolution MS0451 30 GHz image using only the $2-8\mathrm{k}\lambda$ baselines was imaged and cleaned (Fig. 5.9). The NVSS contours were then overlayed and a single NVSS point source was confirmed.
These images are not primary beam corrected. The primary beam corrected point source value at a central frequency of 31 GHz is $1.48^{+0.28}_{-0.28}$ mJy/beam which confirms the OVRO/BIMA result of $1.41^{+0.26}_{-0.26}$ mJy/beam at 30 GHz by Reese et al. (2002).

Point-source removed 30 GHz - short baselines

Having determined the position and flux of the point source, one can model the interferometric response and directly subtract the point source with the corresponding phase in the visibility plane.

After successful point-source removal, the 30 GHz data were imaged in the uv-range $0-2\mathrm{k}\lambda$ and the resultant cleaned image was primary beam corrected, Fig. 5.10.

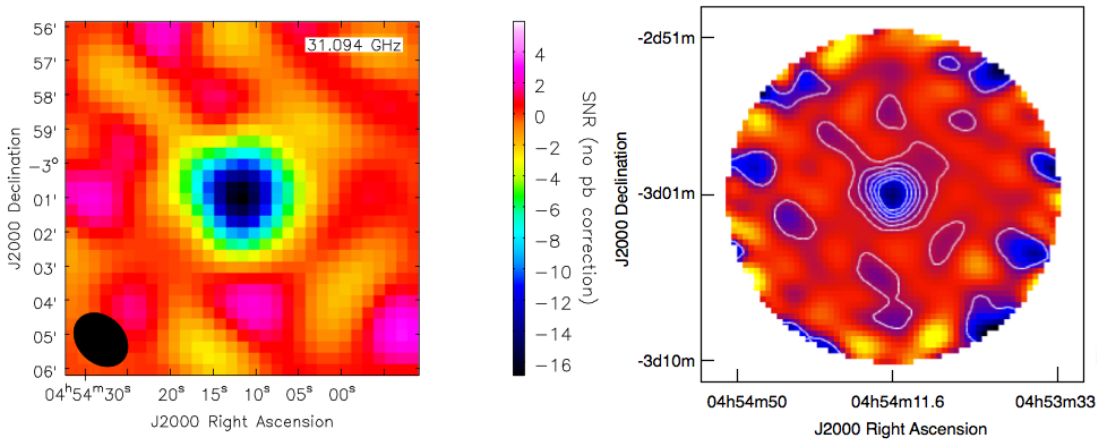

Figure 5.10: 30 GHz SZA cleaned tapered images after point source removal. *Left:* UV-tapered, $0-2\mathrm{k}\lambda$, 30 GHz SZA cleaned image with an rms noise of 0.2 mJy/beam and a beam size of 105.8×81.9 arcsec^2. *Right:* The corresponding primary beam corrected image with contours in steps of 2σ.

SZA - 90 GHz Data

The 90 GHz data were tapered to a uv-range of $0 - 5\text{k}\lambda$, giving a synthesized beam of $37.5'' \times 32.8''$ and a noise level of 0.92 mJy/beam for a total on-source integration time of 8.28 hours. The noise level is above the predicted sensitivity from the CARMA sensitivity calculator of 0.79 mJy/beam for typical weather conditions and 0.58 mJy/beam for good weather conditions since the overall observing conditions were worse than what is assumed in the calculator.

The image in Fig. 5.11 shows the cleaned non-primary beam corrected map and the corresponding synthesized beam with the $0 - 5\text{k}\lambda$ taper applied.

The long baselines were also imaged in order to look for point sources in the field but none were detected. Using the NVSS and 30 GHz point source data, and assuming a uniform spectral index across the frequency range, the point source detected in the 30 GHz map would be expected to have a flux of 0.6 ± 0.1 mJy/beam in the 90 GHz map, which, given the map noise of 0.92 mJy/beam, is below the detection threshold in the 90 GHz data. The primary beams and corresponding clean beam sizes using natural weighting for all observations and CARMA baseline combinations are given in table 5.2.

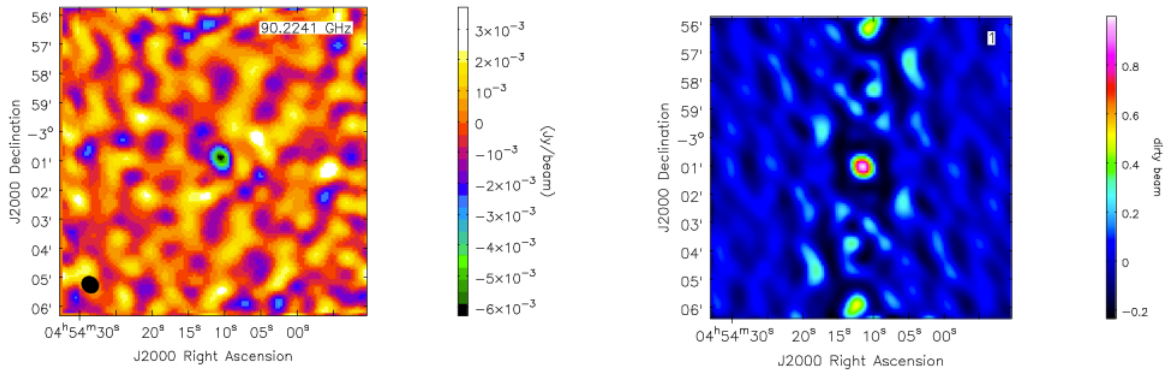

Figure 5.11: MS0451: 90 GHz SZA cleaned tapered, $0-5\text{k}\lambda$, image and the corresponding synthesized beam.

Table 5.2: SZA/CARMA characteristic beams, natural weighting

Array	Central Frequency GHz	primary beam FWHM (arcmin)	selected uv range (kλ)	clean beam ($'' \times ''$)
SZA	31.2	10.7	0-2	105.8×81.9
SZA	90.3	3.7	0-5	37.5×32.8
BIMA-BIMA	93.1	1.94	all	31.9×12.0
BIMA-OVRO	93.1	1.48	all	10.0×7.6
SZA	31.2	10.7	all	83.3×66.4

CARMA E-array data

The CARMA array is a heterogeneous array. The data were first imaged jointly, taking into account the different primary beam weightings from each antenna. The resultant image was mostly affected by the high noise in the OVRO-OVRO and OVRO-BIMA baselines. Hence, I decided to image the OVRO-OVRO, OVRO-BIMA and BIMA-BIMA baselines separately, effectively splitting the heterogenous array into two homogeneous and one heteorgeneous combination. The OVRO-OVRO and OVRO-BIMA baselines were both found to merely include noise with no significant detection, thus decreasing the overall image quality of the joint image.

Sole imaging of the BIMA-BIMA baselines improved the cleaned image (Fig. 5.12). Hence, even though the number of possible correlations per integration time was reduced from 105 to 36, I decided to merely use the BIMA-BIMA baselines for the purpose of imaging and later model fitting.

The resultant noise in the image of 0.15 mJy/beam is higher than that deduced from the CARMA sensitivity calculator of 0.08 mJy/beam. Note that the conversion from the calculator value which includes all baselines to the corresponding BIMA-BIMA noise level involves taking into account the root of the ratio of correlations and the different beam sizes. The weather was thus worse than typical weather conditions, which was expected from examining the data and also explains the noisy BIMA-OVRO and OVRO-OVRO baselines.

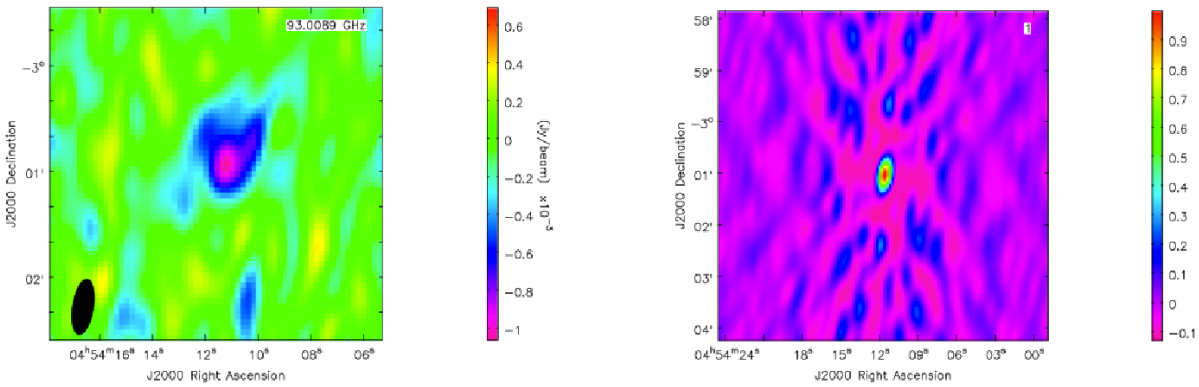

Figure 5.12: Splitting the CARMA data. *Left:* Cleaned CARMA BIMA-BIMA baseline map. No primary beam correction is applied. *Right:* The equivalent synthesized beam of size $31.9'' \times 12.0''$.

5.7 Heterogeneous imaging

The data reduction package MIRIAD has the option to do Steer, Dewdney Ito (SDI) cleaning for heterogeneous imaging, the operational principle being described in Sault (2004) and, in a more detailed mathematical outline, in Koda et al. (2011). Below, I will follow the notation adopted in these two publications.

For a heterogeneous data set, or indeed a heterogeneous combination of homogeneous sub-arrays, as is the case for the MS0451 SZA/BIMA-BIMA data set, the heterogeneous techniques rely on the creation of a primary beam corrected dirty image via

$$I^{dm}_{\rm joint}(l,m) = W_{\rm SZA30}\frac{I^{dm}_{\rm SZA30}}{P_{\rm SZA30}} + W_{\rm SZA90}\frac{I^{dm}_{\rm SZA90}}{P_{\rm SZA90}} + W_{\rm BIM\text{-}BIM}\frac{I^{dm}_{\rm BIM\text{-}BIM}}{P_{\rm BIM\text{-}BIM}} \tag{5.2}$$

with

$$W_{\rm SZA30} + W_{\rm SZA90} + W_{\rm BIM\text{-}BIM} = 1 \tag{5.3}$$

and

$$W_A(l,m) = \frac{P_b^2(l,m)\Delta\nu N_{vis} t_{vis}}{C^2_{i,j} T_{sys,i} T_{sys,j}} \quad , \tag{5.4}$$

where P denotes the primary beam, I^{dm} is the dirty image, W_A are the weighting factors of sub-array A, which themselves are array noise and primary beam dependent. N_{vis}, t_{vis} and $\Delta\nu$ are the total number of visibilities, the visibility accumulation time and total bandwidth of the individual sub-array, whose baseline factors, numbered via ij, are given by $C_{i,j}$ in combination with the associated antenna system temperatures $T_{sys,i}$ and $T_{sys,j}$. The factor $C_{i,j}$ is given by

$$C_{i,j} = \frac{2k_B}{\sqrt{2}\eta_q\sqrt{(\eta_{a,i}A_i)(\eta_{a,j}A_j)}} \quad , \tag{5.5}$$

where η_q and η_a are the quantum and aperture efficiencies for antenna areas A.

The MIRIAD task *mossdi* handles multi-frequency synthesis primary beam corrected imaging. The task *restor* was run using a gaussian fit of the jointly modeled point spread functions.[1] The respective joint SZA(90 GHz)/BIMA data sets as well as the full SZA30/SZA90/BIMA combination are shown in Figures 5.14 and 5.13 respectively. It should be noted that 90 GHz SZA and BIMA-BIMA data sets are re-scaled to a central frequency of 31.1 GHz to take into account the spectral SZA signature including the relativistic correction for MS0451. The latter assumes the temperature of 9.11 ± 0.45 keV reported in Ettori et al. (2009).

[1] This is not explicitely outlined in Sault et al. (2004) but described in detail for the individual MIRIAD tasks by Koda et al. (2011).

The task *linmos* uses a 'joint approach' for indvidually de-convolved and restored images I_i via

$$I(l,m) = \frac{\sum_i P(l-l_i, m-m_i) I_i(l_i,m)/\sigma_i^2}{\sum_i P^2(l-l_i, m-m_i)/\sigma_i^2} \quad , \tag{5.6}$$

as described by Sault (2004) and thus incorporates primary beam correction after the de-convolution process as well as weighting according to the field noise variance (Fig. 5.15). The primary beam models are updated to the values in table 5.2, so as to include the updated beam FWHM for the OVRO, BIMA and SZA antennas.

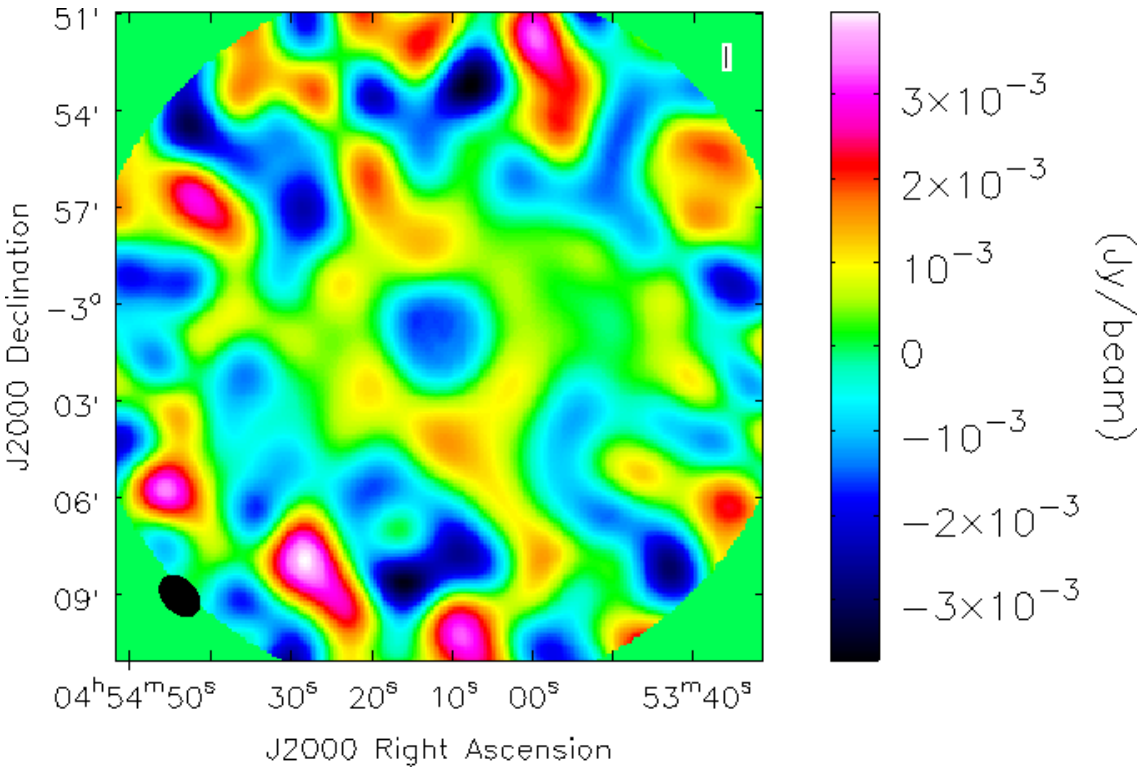

Figure 5.13: The heterogeneously cleaned joint (30+90) GHz SZA + BIMA-BIMA image.

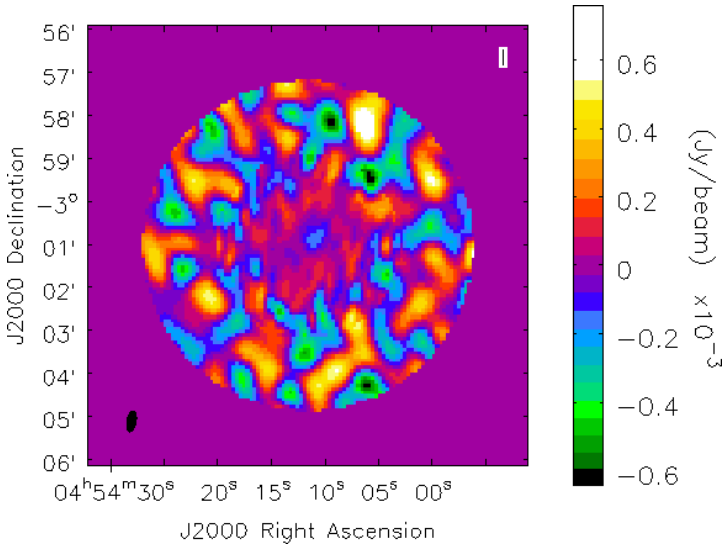

Figure 5.14: The heterogeneously cleaned joint 90 GHz SZA + BIMA-BIMA image.

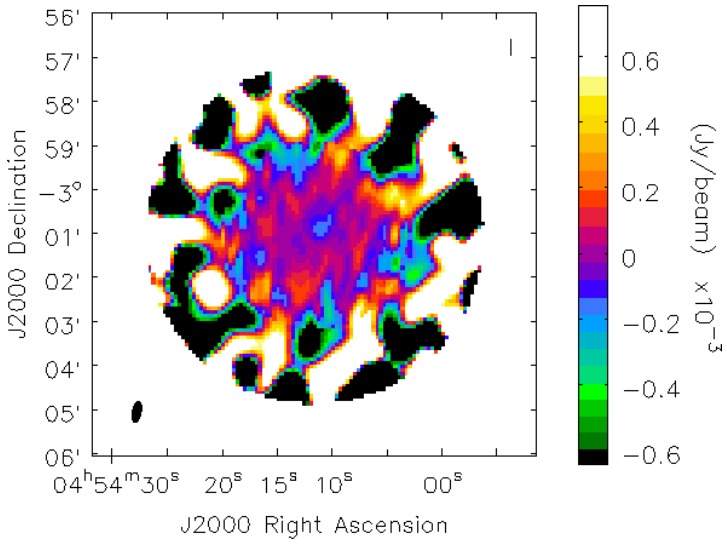

Figure 5.15: The combined 90 GHz SZA + BIMA-BIMA image using the *linmos* task.

5.8 Single-dish/interferometric data combination

The combination of interferometric and bolometer single-dish data is motivated due to recent and future advances in single-dish SZ imaging, most notably APEX-SZ, BOLOCAM, SPT, ACT, MUSTANG and future CCAT. The spatial scales probed with these instruments are complementary to current CARMA and ALMA/ACA arrays, providing information on the larger scales that cannot be imaged via high-resolution interferometry. It is therefore evident that interferometric/single-dish combination techniques will find an increasing scope of application in galaxy cluster pressure profile studies across wide redshift ranges.

The combination of single dish and interferometric data has been discussed in previous works, most notably Stanimirovich et al. (2002) and Koda et al. (2011). Interferometer/single dish combination can be performed before, during and after de-convolution.

Combination in the uv-plane, and thus data joining before de-convolution, requires single dish data that can easily be de-convolved. The APEX-SZ noise properties do not facilitate a direct de-convolution approach due to the subsequent significant noise amplification in the map. The APEX-SZ clean method, developed by M. Sommer and outlined in Chapter 4, aims to remove the effects of the pipeline on the signal, but does not deconvolve the APEX-SZ beam, as the clean components are convolved with the latter before residual noise addition is performed in the cleaned map.

Hence, for the MS0451 data, the combination method after de-convolution is applied. The heterogeneously imaged CARMA/SZA data is feathered with the cleaned MS0451 data yielding the image in Fig. 5.16.

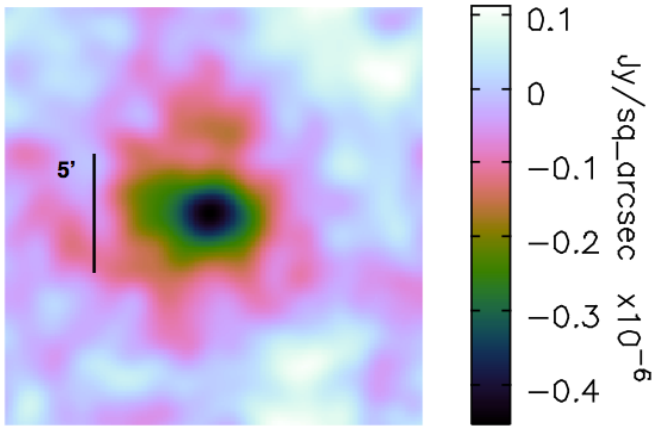

Figure 5.16: The feathered APEX-SZ/ SZA cleaned map.

Due to the fact that the probed scales by the SZA and APEX-SZ data on MS0451 do indeed overlap owing to the interferometric beam of $121'' \times 97''$ and maximum recovered scale of $\approx$ 5', the main effect of the applied combination is an effective smoothing, while the elliptical shape information offered by the APEX-SZ data is retained. The full potential of the feathering routine is outlined in chapter 8 as the latter explores simulated high-resolution ALMA/ACA interferometric data.

On a more technical note, I developed a graphical user interface for the CASA software reduction package (see Appendix A). This GUI allows the user to interactively select the relevant weighting scales for hybrid imaging as well as feathering. Hybrid imaging involves a circular top hat weighting function in the uv-plane, while the feathering method employs a gaussian weighting. The CASA task 'feather' has an implemented gaussian weighting scheme but does not offer the flexibility in weight exploration of the resultant combined images, that are therefore implemented in the presented GUI.

Image combination during de-convolution is already implemented in CASA. It relys on the fact that the single dish image helps to guide the CLEAN or maximum entropy method (MEM) algorithm towards low spatial frequencies.

Image combination before de-convolution relies on the production of so-called single dish pseudo-visibilities. These represent de-convolved single dish data that have been multiplied by the interferometric primary beam before Fourier Transforming to the visibility plane in which they fill the low-frequency region up to a diamter of D-d, where D is the diameter of the single dish, while d is the diameter of the interferometric dish, assuming a homogeneous array.

Due to the fact that the transfer function cannot be de-convolved directly, the only way to address this method is via the APEX-SZ clean algorithm. It was however observed, that the residual map can contain noise flux gradients across the map, owing to the extent of arbitrariness in the cleaning depth.

Since such an uncertainty is hard to quantify, the subsequent combined map would yield a qualitative, rather than a quantitatively applicable image. As such, the noise gradients represent a non-linearity, whose effect might itself deteriorate if this map was introduced in the intrinsically non-linear de-convolution process.

A second GUI was written for the CASA software, that implements a single dish/ interferometer algorithm via pseudo-visibility production and is currently in the development stage. It will be applicable to single dish data that can directy be de-convolved.

It can therefore be concluded that, though a feathered MS0451 interferometric/single-dish image was constructed, the current uncertainties in the MS0451 cleaned map's residual noise properties imply that this method, at this stage, lends itself primarily to a qualitative approach. A quantitative parametric analysis is presented in the next chapter in terms of a Bayesian MCMC fitting to the APEX-SZ map.

5.9 Visibility inspection

Within the framework of a preliminary interferometric SZA/CARMA data examination, the weighted average of the visibilities in radial uv-distance bins were examined as follows,

$$V\left(r_j\right) = \left(\frac{g(\nu_{31.1GHz})}{g(\nu_{freq})}\right) * \left(\frac{\sum_{i=1}^{n} \frac{V_i}{\sigma_i^2}}{\sum_{i=1}^{n} \frac{1}{\sigma_i^2}}\right) \tag{5.7}$$

where $V\left(r_j\right)$ denotes the average weighted visibility in the jth radial uv-distance bin and n is the number of visibilities within that bin.

Band 3 data are down-converted to 31.1 GHz using the known spectral shape of the thermal Sunyaev-Zel'dovich effect along with its relativistic correction via a scaling factor $g(\nu_{convert})$. This approach was chosen as opposed to taking out the spectral dependence through

$$V\left(r_j\right) = \left(\frac{1}{g(x)I_0}\right) * \left(\frac{\sum_{i=1}^{n} \frac{V_i}{\sigma_i^2}}{\sum_{i=1}^{n} \frac{1}{\sigma_i^2}}\right) \tag{5.8}$$

since one can directly compare the new CARMA/SZA data to the old non-public OVRO 30 GHz observations by Reese et al. (2002), Figs. 5.17 - 5.20.

Such a comparison of multi-frequency data is of a qualitative nature as a result of the different array primary beams, whose effects are not removed in the visibility plane. A proper Bayesian MCMC analysis is outlined in chapter 6.

5.10 Conclusion

This chapter thus presents an overview of the data obtained from my two accepted CARMA/SZA proposals. The combined APEX-SZ/CARMA map lays the groundwork for future higher-resolution interferometric/single-dish combinations, further illustrated in chapter 8. The technical framework is described in Appendix A, which outlines the developed GUI interface for the CASA software. The APEX-SZ cleaned residual map's uncertainties currently hamper its suitability for cleaned map model fittings, which motivates a parameteric fitting approach. A preliminary visibility inspection in comparison with literature data on the cluster MS0451, clearly illustrates the superior data quality and uv-coverage (particularly with regard to the 30 GHz SZA data in comparison to the OVRO 30 GHz data) of the new CARMA/SZA observations - a fact that will be quantitatively demonstrated in the following chapter.

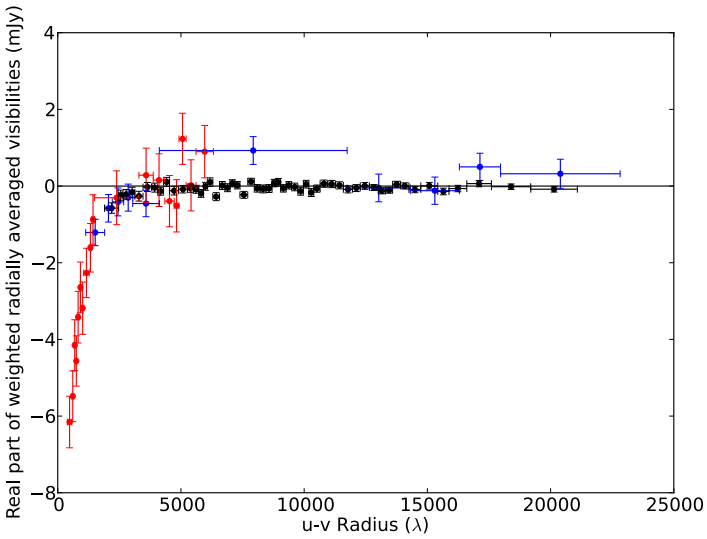

Figure 5.17: Radially averaged visibilities of the 30 GHz SZA data (red), 90 GHz SZA data (blue) and CARMA data (black), showing the real part of the visibilities.

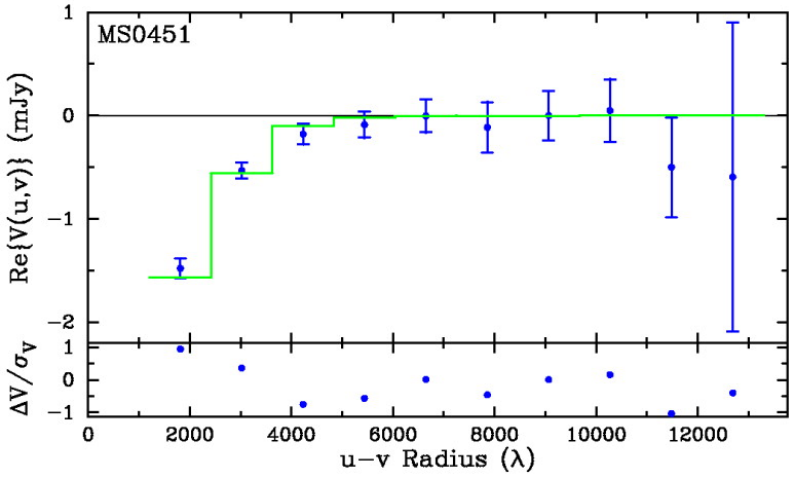

Figure 5.18: Radially averaged visibilities of the old 30 GHz OVRO data showing the real part of the visibilities. The gray line is the best-model joint SZ/X-ray fit. (image credit: Reese et al. 2002)

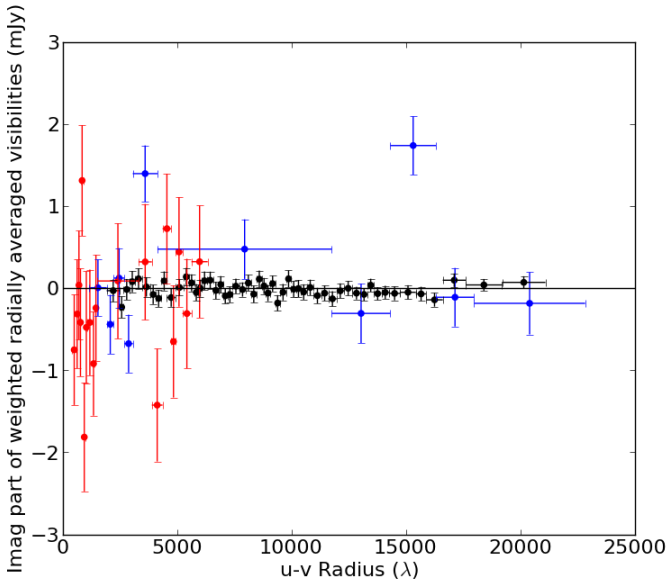

Figure 5.19: Radially averaged visibilities of the 30 GHz SZA data (red), 90 GHz SZA data (blue) and CARMA data (black), showing the imaginary part of the visibilities.

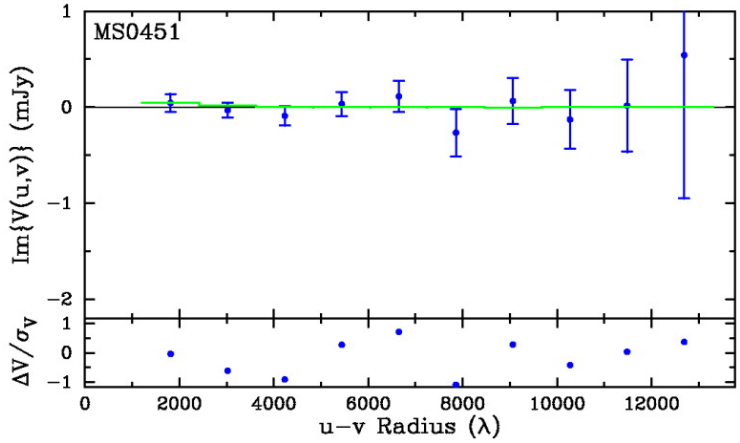

Figure 5.20: Radially averaged visibilities of the old 30 GHz OVRO data showing the imaginary part of the visibilities. The gray line is the best-model joint SZ/X-ray fit. (image credit: Reese et al. 2002)

Chapter 6

Parametric APEX-SZ and SZA/CARMA MS0451 comparison

The preceding data reduction of the CARMA/SZA-observed galaxy cluster MS0451 as well as the available APEX-SZ data present a viable opportunity for a comparison study of interferometric and bolometer single-dish observations. This is further supported by the significant APEX-SZ uv-ovelap with the interferometric array, which facilitates the advantages and disadvantages of both observational methods to be investigated.
Bayesian Markov-Chain Monte Carlo (MCMC) methods allow for data to be compared to models given any available prior information. They facilitate the model parameter space to be explored and are thus ideal for comparing the suitability of different observational methods in parametric studies.
In order to realize such a fitting algorithm, I developed, tested and applied a heterogeneous interferometric Bayesian MCMC visibility fitting code for the CARMA/SZA data as well as an additional APEX-SZ data Bayesian MCMC code, so as to map the acceptable normalization and scale radius parameter space in the pressure-based ICM gas parameterization.
In this chapter, I outline the analysis approaches as well as the subsequent insights gained from the examination of the single-dish APEX-SZ and interferometric SZA/CARMA 2D-Likelihood parameter spaces.

6.1 Motivation for data analysis approach

Future joint CCAT/ALMA/ACA observations will have the potential to probe the Sunyaev-Zel'dovich effect in galaxy clusters at complementary, and indeed matching, spatial scales. It is therefore of utmost importance to develop methods that probe to what extent both, interferometric and single-dish, observations can constrain galaxy cluster pressure profile parameters.

This approach is employed for the interferometric and APEX-SZ data sets for parametric β-model as well as generalized NFW pressure profile fits. The former assumes the gas to be of an isothermal nature whereas the latter is motivated by the fact that the gas follows the shape of the dark matter potential, though it is more spherical than the dark matter distribution itself.

6.2 A Bayesian MCMC method

The Bayesian approach differs from the frequentist's through the consideration of all information that is available besides the data being considered. It can therefore be summarized as a relation between the data $\mathbf{D}$, the model or hypothesis $\mathcal{M}$ and the parameter vector $\boldsymbol{\theta}$, which describes the model. It relies on the product rule of conditional probability theory

$$P(\boldsymbol{\theta} \mid \mathbf{D}, \mathcal{M}) = \frac{P(\mathbf{D} \mid \boldsymbol{\theta}, \mathcal{M}) P(\boldsymbol{\theta} \mid \mathcal{M})}{P(\mathbf{D} \mid \mathcal{M})}, \tag{6.1}$$

where $P(\boldsymbol{\theta} \mid \mathbf{D}, \mathcal{M})$ denotes the posterior distribution, $P(\boldsymbol{\theta} \mid \mathcal{M})$ is the prior distribution encompassing any prior information in the form of a normalized probability distribution in the parameter space of the model $\mathcal{M}$ and $P(\mathbf{D} \mid \boldsymbol{\theta}, \mathcal{M})$ is termed the likelihood distribution $\mathcal{L}(\boldsymbol{\theta})$. The evidence, $P(\mathbf{D} \mid \mathcal{M})$, is not dependent on the model parameters $\boldsymbol{\theta}$ and is of importance when different models are compared.

Using the product rule of probability theory for N independent data sets that are described by the same model encompassing the parameters in the parameter vector $\boldsymbol{\theta}$, the joint likelihood is the product of the individual likelihoods

$$\mathcal{L}_{comb}(\boldsymbol{\theta}) = \prod_{i=0}^{i=N} \mathcal{L}_i \qquad . \tag{6.2}$$

The form of the likelihood depends on the particular data set. In the case of statistically Poisson-distributed data, it can be written as

$$\ln\mathcal{L} = \sum_{i=0}^{n} D_i \ln(D_i^{\mathcal{M}}) - D_i^{\mathcal{M}} - \ln(D_i!) \qquad , \tag{6.3}$$

where $D_i^{\mathcal{M}}$ is the model prediction, which is compared to the number counts of the actual data in the ith binned entity, D_i. If one assumes the data itself to be distributed in a gaussian manner around the expected values, then the likelihood can be written as

$$\mathcal{L} = \frac{1}{(2\pi)^{n/2} \mid \mathbf{C} \mid^{1/2}} \exp\left(-\frac{(\mathbf{D}-\mathbf{D}^p)^T \mathbf{C}^{-1} (\mathbf{D}-\mathbf{D}^p)}{2}\right) \quad , \tag{6.4}$$

where $\mathbf{C}$ is the noise covariance matrix, $\mathbf{D}$ is the data vector of size n and $\mathbf{D}^p$ is the data vector predicted by the model $\mathcal{M}$ using the parameters $\boldsymbol{\theta}$. Rather than doing a grid-based parameter space exploration in the following analyses, a Markov Chain Monte Carlo technique is used to map out the posterior distribution.

6.2.1 MCMC Statistics - The Metropolis-Hastings algorithm

Markov Chain Monte Carlo Statistics are a way of sampling a given distribution, the target distribution, from a proposal distribution. It generates a sequence of states where the next state is only dependent on the previous one and the transition from one to the other is given by a transition probability function. In addition, after a burn-in period, defined as the first few iterations which will centre around the starting position of the chain, the chain represents a series of samples drawn from the stationary distribution, which, ideally, will consist of samples of the target distribution.

The general principle is that the density of explored points in the parameter plane is a fair representation of the posterior distribution. The properties of the proposal distribution define the type of MCMC algorithm - here I will focus on the Metropolis and the Metropolis-Hastings algorithms. An ergodic sequence can be built up from the condition

$$\pi(x_1)t(x_2 \mid x_1) = \pi(x_2)t(x_1 \mid x_2), \tag{6.5}$$

where π is the target distribution and $t(x_2 \mid x_1)$ denotes the distribution that determines the probability of x_2 being sampled after x_1. One may therefore choose any distribution $q(x_2 \mid x_1)$ such that the acceptance probability of the newly sampled value is given by

$$\alpha(x_1, x_2) = min\left(1, \frac{\pi(x_2)q(x_1 \mid x_2)}{\pi(x_1)q(x_2 \mid x_1)}\right) \tag{6.6}$$

since

$$\pi(x_1)q(x_2 \mid x_1)\alpha(x_1, x_2) = \pi(x_2)q(x_1 \mid x_2)\alpha(x_2, x_1), \tag{6.7}$$

such that the sampled distribution reflects the probability of the target distribution. The Metropolis-Hastings algorithm differs from the Metropolis algorithm in the sense that the former has an asymmetric proposal distribution. The convergence statistics and the speed of convergence depends on the choice of proposal distributions. For highly degenerate parameter spaces, convergence with independent gaussian proposal distributions for all parameters may lead to a high fraction of rejected samples as the multi-parameter acceptable parameter space might be very narrow compared to the explored parameter space.

In general, a proposal distribution is best chosen such that it is similar to the target

distribution but also effective enough to rule out the parameter space at a wide enough margin around the target distribution. In recent years, sophisticated algorithms such as nested sampling have been developed for such situations since one might not always be able to 'guess' the form of the target distribution. In addition, target distributions may be multi-modal and so care needs to be taken that the chain does not get stuck in a uni-modal region.

6.2.2 Interferometric visibility fitting

Fitting to the interferometric data is not done in the image plane but in the visibility plane as noise in the image plane is correlated, whereas noise in the real and imaginary components of the visibilities is not. Additionally, in the image plane, there is always a degree of arbitrariness left in the deepness of the cleaning process. Even though care was taken to include only as many clean iterations as were necessary, the condition for which was determined by the leveling off of the total cleaned flux, the extent to which one under- or over-cleans the image is still a source of uncertainity as not only one unique solution exists in the de-convolution process, owing to the missing information in the uv-plane. Visibility fitting has become common practice for instruments such as the SZA or the Arcminute Microkelvin Imager (AMI) (Reese et al. 2002, Hasler et al. 2012, Bonamente et al. 2012). MIRIAD only contains a fitting algorithm for the simplest of models such as gaussians, disks and point sources.

I therefore wrote a visibility fitting code that can be applied to the MS0451 CARMA/SZA data, given the uv-points and the corresponding predicted noise properties as listed in the CARMA/SZA visibility files. The testing of this code relied heavily on my interferometric simulator introduced in Chapter 4. The real and imaginary components are fitted simultaneously and independently, such that the likelihood can be written as

$$\ln(\mathcal{L}_{\rm intf}) \propto \sum_i -\frac{1}{2}(\Delta\mathcal{R}_i^2 + \Delta\mathcal{I}_i^2)\mathcal{W}_i \qquad , \tag{6.8}$$

where $\Delta\mathcal{R}_i$ and $\Delta\mathcal{I}_i$ denote the difference between the visibility data and the corresponding model predicted visibility at u-v point i for the real and imaginary components respectively and $\mathcal{W}_i = 1/\sigma_i^2$ denotes the corresponding noise component weighting.

In the fitting algorithm, all uv-points are used for the interferometric fitting (no tapering is applied in the uv-plane). In the case of CARMA observations, only the BIMA-BIMA baselines were used in the fit since the OVRO-OVRO and OVRO-BIMA images were dominated by noise, which also suggests noise-dominated complex visibilities. Information on the position and flux of possible point sources in the data can be left as free parameters in the MCMC fit. Having examined the long-baseline 30 and 90 GHz SZA maps beforehand, only one point source was detected, any other peaks being consistent with noise. The point source was removed through modeling in the visibility plane before the interferometric fitting, thus bypassing the inclusion of its properties in the chain.

Galaxy cluster pressure models

In the following analyses, two different ICM pressure models are fitted to the data: a β-profile and a generalized NFW profile.

In the case of the β-model fit, this involves constraining the normalization parameters, y_0 and ΔT_0, as well as the angular core radius parameter θ_c in the plane of the sky following,

$$\Delta T(\theta) = \Delta T_0 \left(1 + \frac{\theta^2}{\theta_c^2}\right)^{(1-3\beta)/2} \tag{6.9}$$

and

$$y = y_0 \left(1 + \frac{\theta^2}{\theta_c^2}\right)^{(1-3\beta)/2} \quad . \tag{6.10}$$

The slope parameter, β, was kept fixed owing to the high degree of degeneracy between the respective parameters. In order to assess any ellipticity in the interferometric image, an elliptical beta model fit with the following parameterization was made

$$y = y_0 \left(1 + \frac{((x-x_c)\cos\phi + (y-y_c)\sin\phi)^2}{\theta_c^2} + \frac{((y-y_c)\cos\phi - (x-x_c)\sin\phi)^2}{\epsilon\theta_c^2}\right)^{(1-3\beta)/2} , \tag{6.11}$$

where, $[x_c, y_c]$, ϕ and ϵ are the centre coordinates, angular position and major to minor axis ratio respectively. For the GNFW model

$$P_e(r) = \frac{P_0}{(r/r_p)^c \left[1 + (r/r_p)^a\right]^{(b-c)/a}} \quad , \tag{6.12}$$

the slope parameters were fixed to the best-fit values of (a=0.9, b=5.0, c=0.4) found by Plagge et al. (2010). The corresponding SZ signal is computed from the integration of Eq. 6.12 along the line of sight and the fitting is done for the corresponding normalization, ΔT_0, and scale radius, r_p, parameters. The associated y_0 is also derived from Eq. 6.12 via application of Eq. 3.7. In addition, the β-profile and GNFW model derived y_0 and ΔT_0 values are not equivalent in their mathematical meaning since the GNFW model is not defined at zero scale radius unless $c == 0$.

In all model fits, delta priors were adopted for the central position and slope parameters. The centre was fixed at 04h54m11.6 -03d01m01.3s following LaRoque et al. (2006) . In order to compute the relativistic corrections, the best-fit temperature value of 9.11 ± 0.45 KeV was adopted following Ettori et al. (2009), whose r_{500} value [1] from the constant temperature model was also taken as 1446 ± 124 kpc.

In the elliptical β-model fits, $|\phi| < \pi/2$ and $0 < \epsilon <= 1$ box priors were set. In addition the normalization and scale radius parameters were constrained to be greater than 0.

[1] The radius r_δ corresponds to the density contrast, δ, when compared to the critical density $\rho(z)$. The corresponding mass is denoted by M_δ. This definition is adopted throughout the rest of this thesis when referring to r_{500} and M_{500}.

MCMC chain examination

The parameter space was explored using a Markov Chain Monte Carlo approach via the Metropolis algorithm.

In order to assess the MCMC chain convergence, the trace, a plot of the accepted parameter values as a function of the number of iterations, was examined to indicate the quality of the chain (Fig. 6.1).

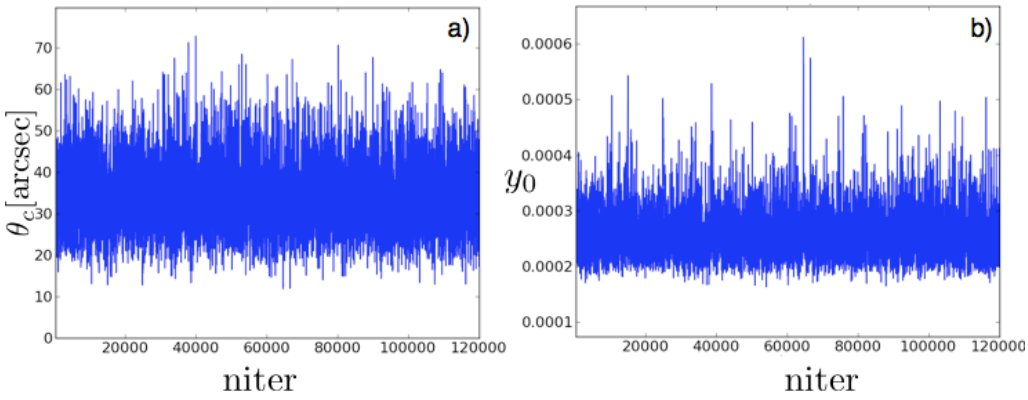

Figure 6.1: Trace diagnostics for the scale radius (a) and normalization (b) parameters for the $\beta = 0.806$ β-model fits on my 30 GHz SZA data.

In addition, a moving average plot was used to indicate the burn-in period - the first part of the chain which is dependent on the initial starting conditions (Fig. 6.2). As the chain moves towards the maximum likelihood region, any memory of these initial conditions is lost, therefore representing the final chain used for the analyses.

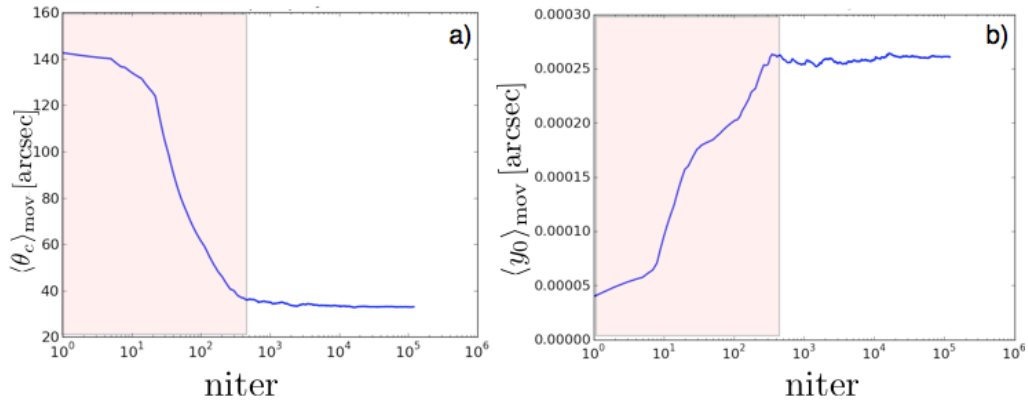

Figure 6.2: Moving average plots of the the scale radius (a) and normalization (b) parameters, illustrating the need for a burn-in phase that is not included in the final chain for the $\beta = 0.806$ beta-model fits on my 30 GHz SZA data.

Rubin-Gelman statistics which compare the in-between variance to the intrinsic variance of the chain were also used to indicate convergence. In addition, a plot of the explored parameter space versus the accepted parameter space was made for all 2D parameter spaces to rule out any insufficient exploration of the local parameter region probed (Fig. 6.3).

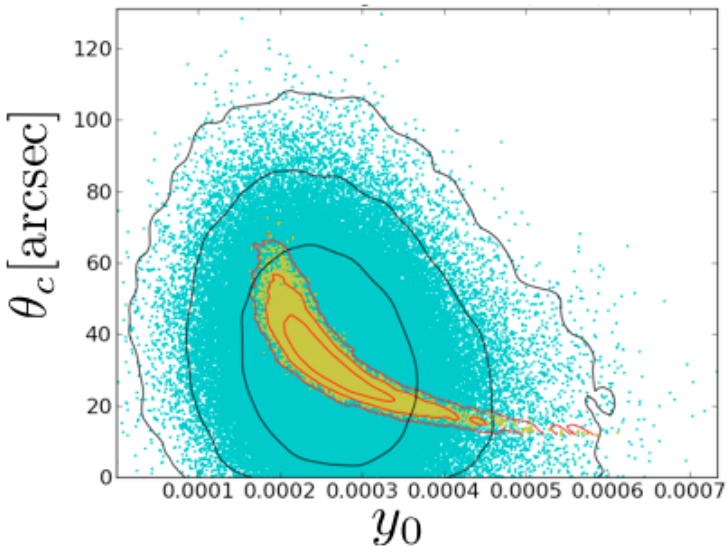

Figure 6.3: The explored (blue) vs the accepted (yellow) parameter space with associated 68.3%, 95.5% and 99.7% contours for the $\beta = 0.806$ beta-model fits on my 30 GHz SZA data. This is used to inspect whether the chosen number of iterations and the sampling function explore the parameter space sufficiently for an expected uni-modal distribution.

The proposal distribution was chosen in such a way as to never yield an acceptance rate greater than 25% in order to satisfy the former criteria as well as to satisfy the condition that the explored parameter space forms a wide-enough margin around the accepted parameter space in order to ensure sufficient parameter space exploration under the assumption of a uni-modal solution. Thinning of the chain, ie the use of every ith point in the chain, can also be used to reduce the in-chain correlation.

The best-fit parameters are given in terms of the median and the 68% confidence interval of the respective marginalized likelihood distributions in the analysis below.

Beta-profile fit with $\beta = 0.806$ and $\beta = 0.86$

In order to compare the new SZA data's best-fit values for the scale radius and normalization parameters with the published 30 GHz OVRO array values, a β-profile fit was made with the β slope parameter set to 0.806 (Reese et al. 2002).

The resultant accepted parameter space with indicated 68.3%, 95.5% and 99.7% confidence levels is shown in Fig. 6.4. The corresponding histograms illustrate the likelihood of the marginalized probabilities with the median and 68% confidence levels being shown as magenta and green lines respectively. The accepted vs explored parameter space is demonstrated in Fig. 6.3 and depicts a sufficient parameter exploration.

My sole 30 GHz SZA Sunyaev-Zel'dovich profile best-fit values were then compare to the normalization and core radius parameters from the joint OVRO+ROSAT fit by (Reese et al. 2002). The centre parameter for the OVRO+ROSAT fit was fixed but the corresponding position in RA and DEC was not listed in Reese et al. (2002). Examination of their SZ and X-ray smoothed images suggest however a pointing centre close to my chosen value at 04h54m11.6 -03d01m01.3. This will add some uncertainty to the comparison. In addition, they use a best-fit temperature of $10.4^{1.0}_{-0.8}$ keV from Donahue et al. (1996) whereas the 30 GHz SZA fit adopts a value of 9.11 ± 0.45 keV (Ettori et al. 2009) in line with the 100kpc cut best-fit Chandra value of $9.95^{+0.76}_{-0.69}$ keV (LaRoque et al. 2006). This will have a maximum 1% difference in the relativistic corrections for each analysis at 30 GHz. The 9.11 ± 0.45 keV (Ettori et al. 2009) temperature is assumed in all SZ relativistic correction frequency down-conversions to 30 GHz. For the comparison with APEX-SZ data, $\beta = 0.86$ was chosen, Fig. 6.5, following Plagge et al. (2010).

The role of systematics should of course not be neglected. These enter from primary CMB contribution, unremoved point sources, the effects of radio halos and calibration systematic uncertainties. The contribution from primary CMB isotropy was reported to be 355^{+137}_{-122} μK^2 for $2000<l<3500$, 80-90 μK^2 of which Sharp et al. (2010) account for the primary CMB component and is thus primarily entering the CARMA/SZA data as visibility noise.

The ability to detect and remove point sources is greatly enhanced by the available two-band information. Given the 30 and 90 GHz data reduction and following Hasler et al. (2012), the associated systematic uncertainty is of the order of 1%. The contribution of a kinetic SZ effect due the the cluster's bulk motion is of the order of 4%, assuming the reported X-ray temperature of 8 keV and a line of sight velocity of 300 km/s, as was adopted in Bonamente et al. (2006).

The gain calibration uncertainty for the CARMA array has been shown to be $\pm 3\%$ (Hasler et al. 2012) and the absolute flux calibration uncertainty due to the URANUS dip is estimated with a conservative $\pm 3\%$. It should therefore be noted that, besides the reported statistical uncertainties in the following discussion and tables, the above-mentioned systematics additionally contribute to the total error.

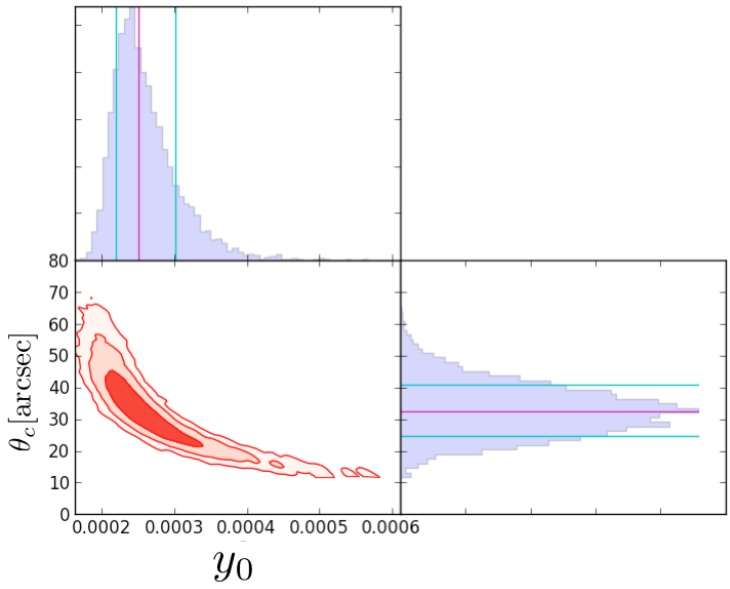

Figure 6.4: 30 GHz SZA beta-model fit for fixed $\beta = 0.806$ with associated 68.3%, 95.5% and 99.7% 2D likelihood contours. Marginalized likelihoods are plotted in histogram format indicating the median (magenta) and the 68% confindence (blue) interval as lines.

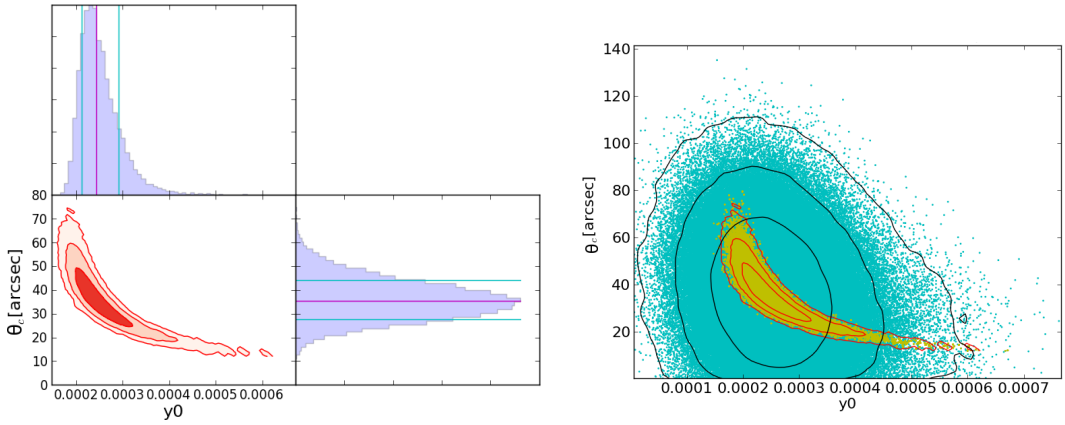

Figure 6.5: 30 GHz SZA beta-model fit for fixed $\beta = 0.86$ (note that this paramter is different than in Figs. 6.3 and 6.4). *Left:* The 2D θ_c-y0 likelihood space with associated 68.3%, 95.5% and 99.7% 2D-likelihood contours and marginalized probability distributions, the magenta and blue lines denoting the median and 68% cofidence interval. *Right:* The explored (blue) vs the accepted (yellow) parameter space with associated 68.3%, 95.5% and 99.7% contours.

As can be seen from Table 6.1, my SZA 30 GHz fit agrees with the published OVRO 30 GHz data by Reese et al. (2002). The error bars in the Reese et al. (2002) fit are smaller, since they are derived from a joint OVRO/ROSAT fitting routine. In addition, the centre parameters were left as free parameters (the final derived centre coordinates are not reported in Reese et al. 2002) but the OVRO/SZA pointings agree.

Table 6.1: β-model comparison with Reese et al. (2002)

DATA	y_0 10^{-4}	θ_c arcsec
30 GHz SZA	$2.50^{+0.51}_{-0.31}$	$32.6^{+8.2}_{-7.9}$
30 GHz OVRO	$2.69^{+0.18}_{-0.19}$	$34.7^{+3.9}_{-3.5}$

It remains to discuss how 30 GHz SZA can recover the normalization and scale parameters so well for a given β-slope value. Due to the fact that the 30 GHz primary beam is 10.7', scales up to $\approx$ 5' can be recovered.

In addition, under the assumptions of spherical symmetry and a pressure profile that can be described by a continuously parameterisable function, the shape of the profile can also be deduced from incomplete knowledge at scales larger than 5', provided that there is sufficient uv-coverage beyond the scale radius of the profile. Hence, it is not surprising that the 30 GHz contours do indeed follow a region of approximately constant cylindrically integrated Y (Fig. 6.6), where the aperture radius is chosen to be the r_{500} value of Ettori et al. (2009).

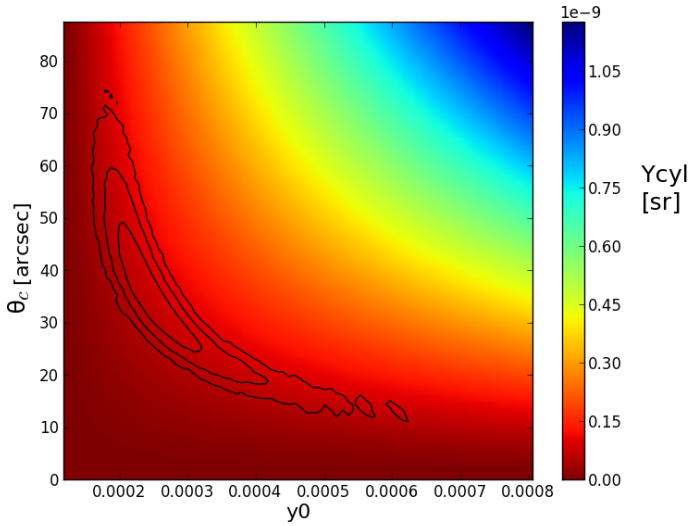

Figure 6.6: 30 GHz SZA beta-model fit for fixed $\beta = 0.86$ with associated 68.3%, 95.5% and 99.7% 2D-Likelihood contours overplotted on the $Y_{\rm cyl}$ space. The likelihood contours follow a region of $\approx$ constant $Y_{\rm cyl}$ integrated over an aperture of size r_{500}.

Joint 30 GHz SZA + 90 GHz SZA + CARMA fits

Since 90 GHz SZA data are also available, the 90 GHz visibilities are re-scaled to the central frequency of the 30 GHz data set according to the formalism in Eq. 3.9, the resultant fit being shown in Fig. 6.7. Due to the fact that the OVRO-OVRO and BIMA-OVRO baselines were very noisy, they were excluded from the joint CARMA+(30+90 GHz) SZA fits (Fig. 6.8). The 93 GHz BIMA-BIMA baselines were down-converted to 31.1 GHz.

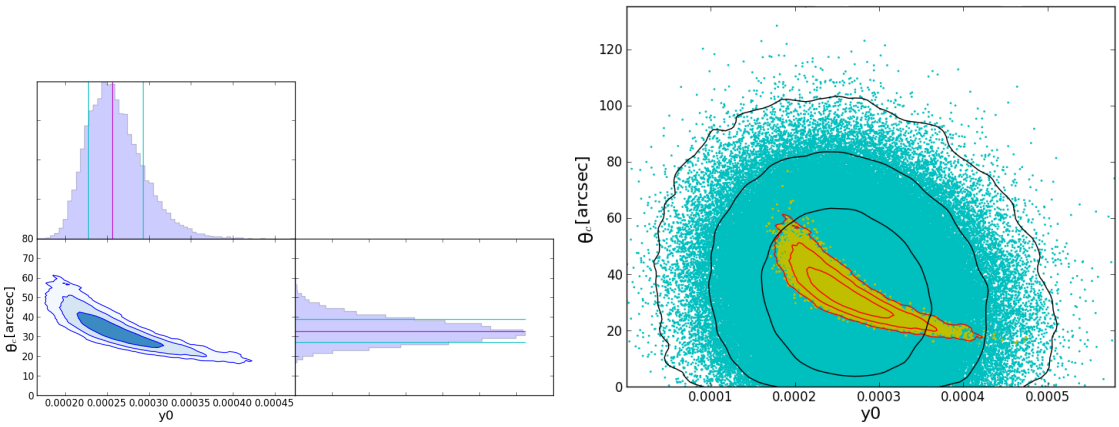

Figure 6.7: Joint 30 GHz + 90 GHz SZA fit with $\beta = 0.86$. Description as in Fig 6.5

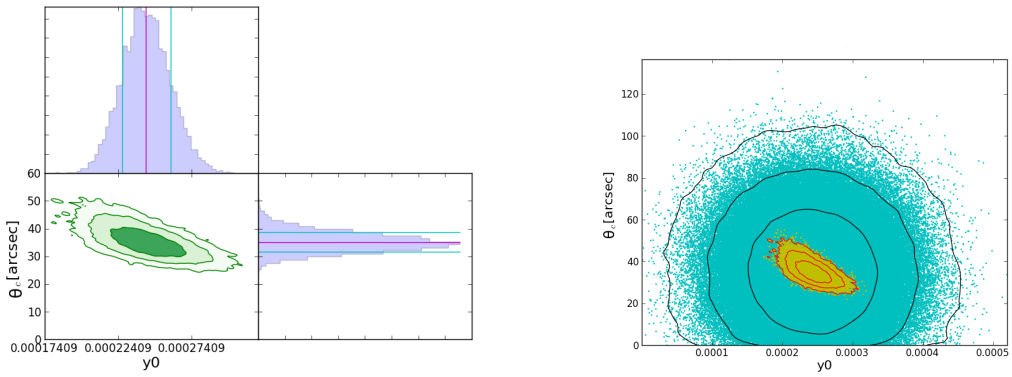

Figure 6.8: Joint 30 GHz + 90 GHz SZA + 93 GHz BIMA-BIMA baseline fit with $\beta = 0.86$. Description as in Fig 6.5

Comparison between fits

The resultant confidence levels for the beta model fits are overplotted in order to illustrate the compatibility of the sole 30 GHz, 30+90 GHz SZA and 93 GHz BIMA-BIMA+(30 GHz+90 GHz SZA) visibility fits as well as the increasingly constrained accepted parameter space (Fig. 6.9), which is also illustrated in Table 6.2.

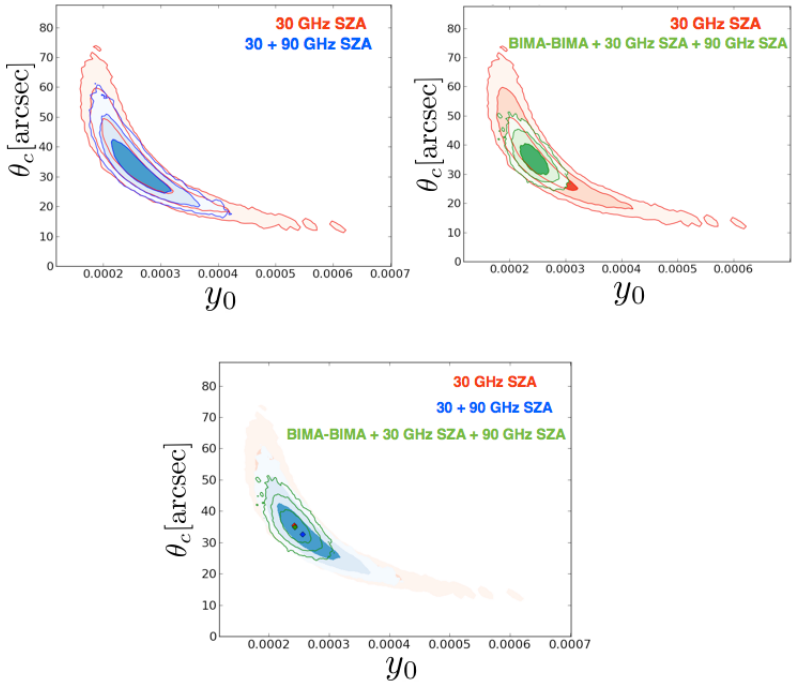

Figure 6.9: Beta-model fit comparison study for joint CARMA/SZA, (30+ 90) GHz SZA and sole 30 GHz SZA fits. The BIMA-BIMA baselines along with the 90 GHz data are shown to improve the fit considerably. All fits are consistent with each other within 1σ in the 2D-Likelihod space. 68.3%, 95.5% and 99.7% 2D-Likelihood contours are shown.

Table 6.2: β-model comparison with $\beta = 0.86$

DATA	y_0 10^{-4}	θ_c arcsec
30 GHz SZA	$2.42^{+0.49}_{-0.30}$	$35.5^{+8.7}_{-7.9}$
(30 + 90 GHz) SZA	$2.56^{+0.37}_{-0.29}$	$32.6^{+6.4}_{-5.4}$
(30 + 90 GHz) SZA + BIMA-BIMA	$2.42^{+0.17}_{-0.16}$	$35.0^{+3.7}_{-3.3}$

Elliptical β-model fit

In the APEX-SZ map, the MS0451 cluster has a projected elliptical shape. X-ray analyses (Donahue et al. 2003) found best-fit values for ϕ and $(1-\epsilon)$ of 15 ± 2 deg and 0.271 ± 0.016. In addition, recent BOLOCAM fits (Sayers et al. 2011) support this result, reporting 10 ± 8 deg and 0.26 ± 0.06 for ϕ and $(1-\epsilon)$ respectively.

Hence, an MCMC chain using an elliptical β-model was run on the 30 GHz data. The resultant parameter values for the angular position, ϕ, and major to minor axis ratio, ϵ, give $-29.6^{+41.9}_{-24.5}$ and $0.87^{+0.08}_{-0.10}$, which is illustrated in Fig. 6.12. The angular position parameter does not match the previously found value by Donahue et al. (2003). Inclusion of 90 GHz SZA and BIMA-BIMA baselines merely confirmed the 30 GHz fit, which, taking into account the lower than expected baseline sensitivity, was to be expected.

In order to investigate the cause for the discrepant fits, 30 GHz data were simulated using the same uv-coverage and noise levels as the actual data. The results of the marginalized histograms for the ϕ and η parameters are illustrated in Fig. 6.10.

It could be shown that, out of 10 mock simulations and resultant MCMC elliptical β-model fittings, only one simulation yields the expected result for the angular position. This demonstrates that it is indeed the limited uv-coverage of the MS0451 tracks of the 30 GHz data that makes an elliptical profile fitting aimed at constraining ϕ to high accuracy and precision unfeasible. The lower than expected sensitivity on the 90 GHz SZA and CARMA baselines, which were originally planned to help to constrain the projected ellipticity, did not allow for more precise and accurate projected ellipticity fitting.

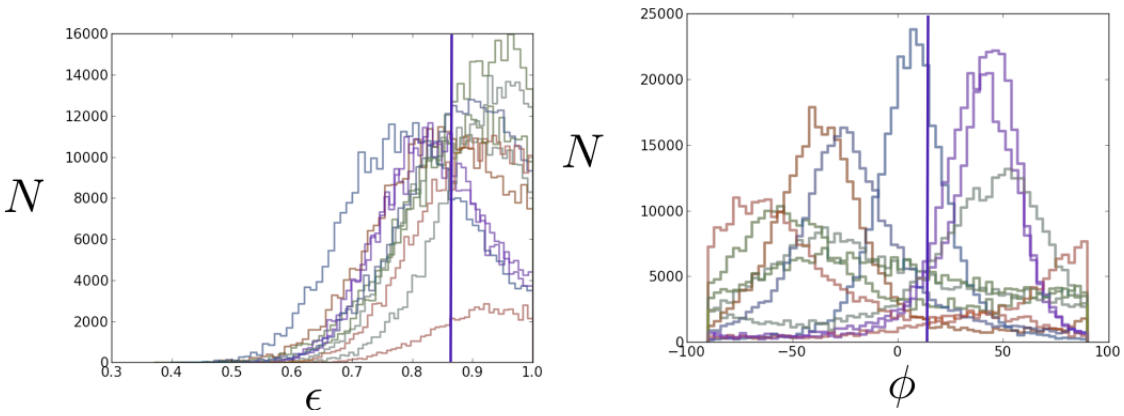

Figure 6.10: The marginalized probability distributions for ten SZA 30 GHz mock simulations and subsequent visibility fitting for ϵ and ϕ, the vertical line indicating the input value. Only one simulation recovers the correct value of ϕ.

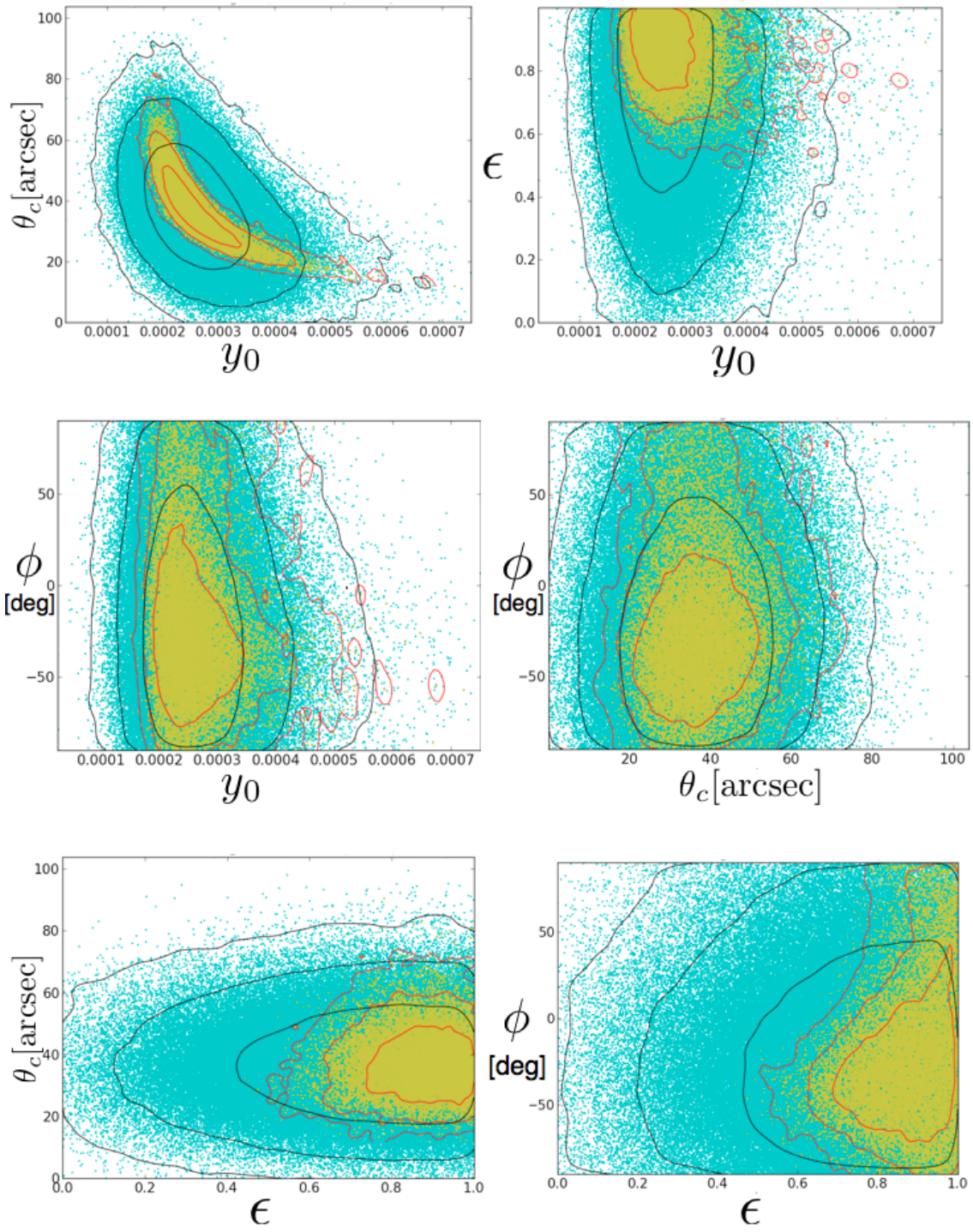

Figure 6.11: The explored (blue) vs the accepted (yellow) parameter space with associated 68.3%, 95.5% and 99.7% contours for the 30 GHz elliptical beta-model fit with $\beta = 0.86$.

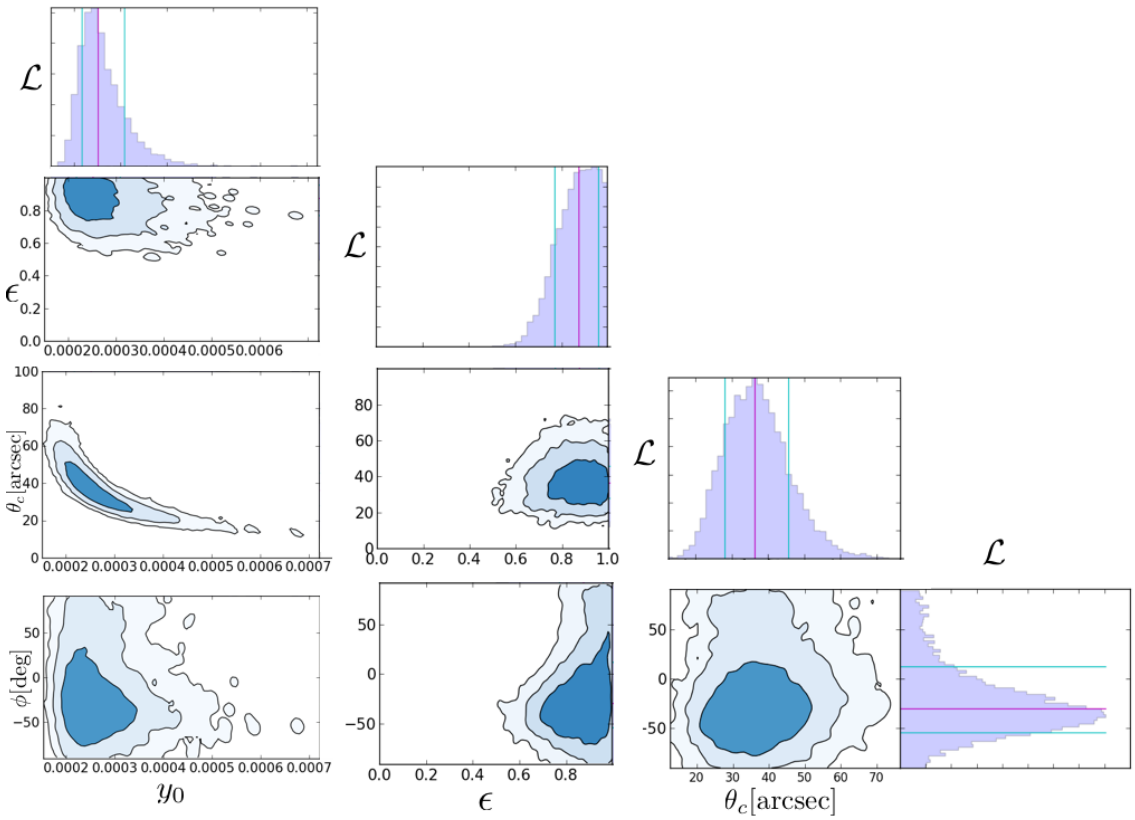

Figure 6.12: 30 GHz SZA elliptical β-model fit for fixed β= 0.86 with associated 68.3%, 95.5 % and 99.7% 2D-Likelihood contours. Marginalized probability distributions are also shown, the magenta and blue lines denoting the median and 68% confidence interval.

GNFW profile visibility fitting:

The GNFW fits for 30 GHz, (30+ 90) GHz SZA and the joint CARMA/SZA data (Fig. 6.13) were made with delta priors on the slope parameters ($a = 0.9, b = 5.0, c = 0.4$), following the best-fit values by Nagai et al. (2007). This fit could easily be done for the universal Arnaud profile. However, at the time of the simulations, APEX-SZ data were still being fitted with the reported Nagai values and, to ease the comparison, this approach was also followed for the interferometric data.

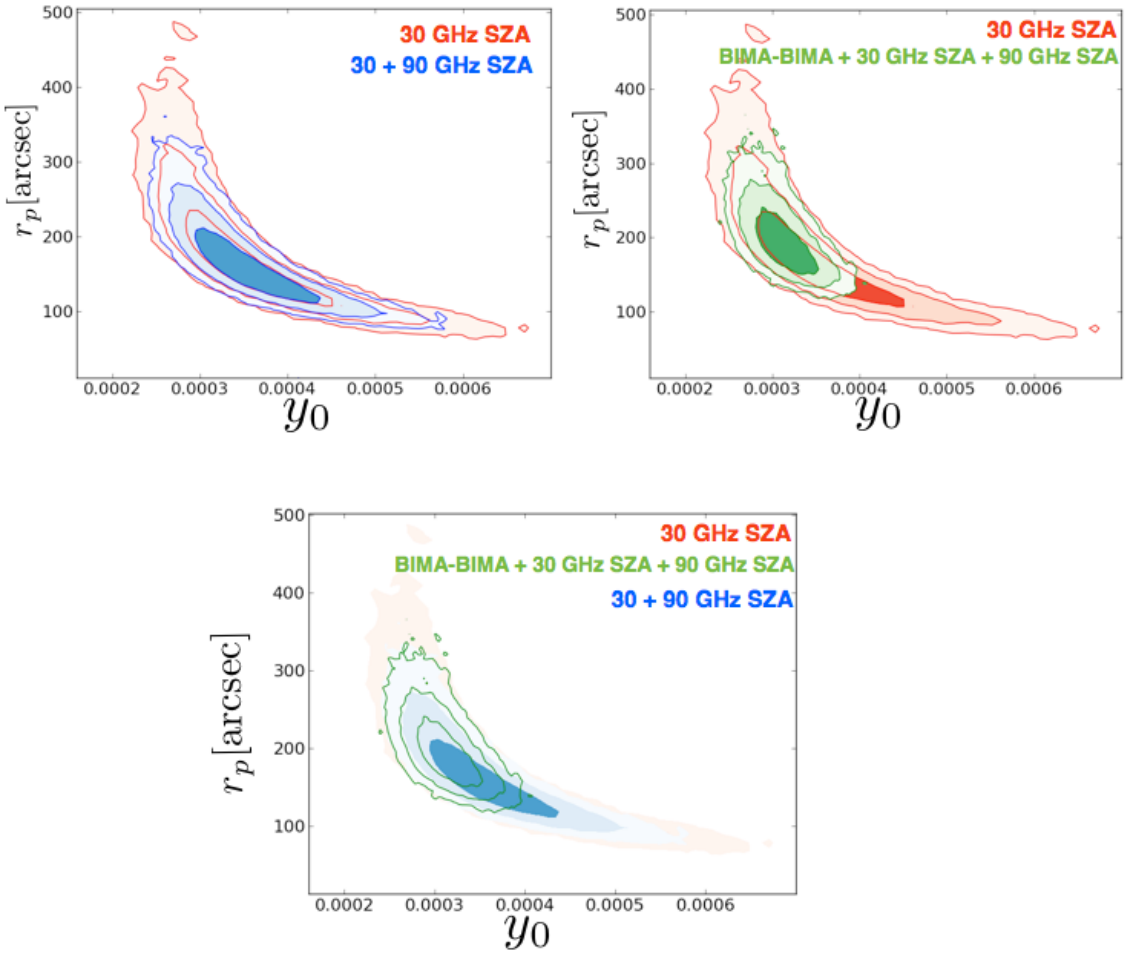

Figure 6.13: GNFW fit comparison study for joint CARMA/SZA, (30+90) GHz SZA and sole 30 GHz SZA fits. The BIMA-BIMA baselines along with the 90 GHz data are shown to improve the fit considerably. The OVRO-BIMA and OVRO-OVRO baselines were not included in the fit. All fits are consistent with each other within 1σ in the 2D-likelihod space. The associated 68.3%, 95.5% and 99.7% 2D-Likelihood contours are shown.

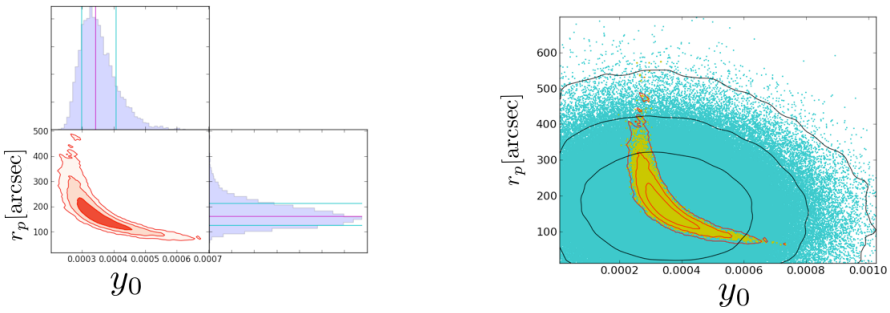

Figure 6.14: 30 GHz SZA GNFW fit. *Left:* The 2D rp-y0 likelihood space with associated 68.3%, 95.5% and 99.7% 2D-Likelihood contours and marginalized probability distributions, the magenta and blue lines denoting the median and 68% confidence interval. *Right:* The explored (blue) vs the accepted (yellow) parameter space with associated 68.3%, 95.5% and 99.7% levels.

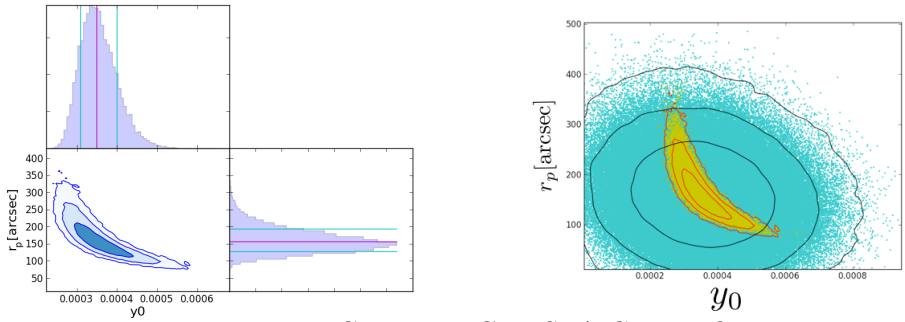

Figure 6.15: Joint 30 GHz + 90 GHz SZA GNFW fit. Description as in Fig 6.14

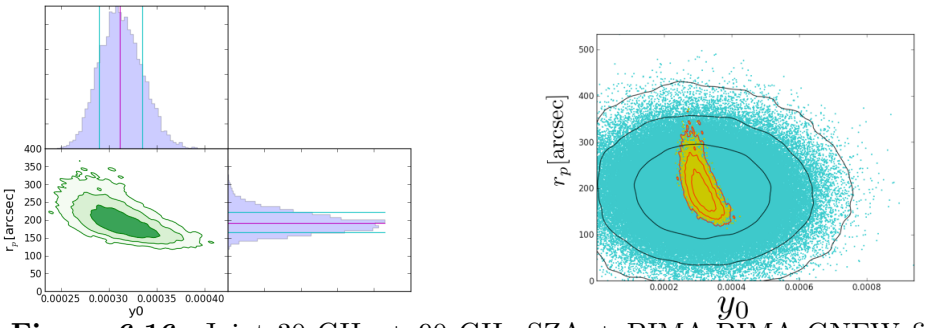

Figure 6.16: Joint 30 GHz + 90 GHz SZA + BIMA-BIMA GNFW fit. Description as in Fig 6.14

6.2.3 APEX-SZ data

The model fitting process of APEX-SZ data relies both, heavily on the assumptions of noise stationarity, which requires the noise properties to stay constant in the time domain, as well as on the validity of the point source transfer function.

Noise properties

Noise stationarity was studied by A. Bender (see A. Bender PhD thesis) through examination of simulations comprising a β-model cluster immersed in Gaussian noise under non-uniform coverage conditions. Work by the APEX-SZ collaboration has suggested that, restricting model fits to a $10'$ length region centred on the cluster, ensures that the non-diagonal components of the noise covariance matrix can be assumed to be zero.

Transfer function

The transfer function depicts the joint effect of the beam and the pipeline reduction steps on a two-dimensional unit delta function. Two different pipelines exist for the APEX-SZ data reduction; the BOA pipeline was developed by M. Sommer in Bonn and the MATLAB pipeline was constructed by A. Bender and collaborators. One can examine the differences in the data reduction pipelines via comparisons of the respective MS0451 galaxy cluster transfer functions.

The difference map (Fig. 6.18) highlights the azimuthal deviations and the heavier filtering processes in the MATLAB pipeline are illustrated by Fourier Transforming both transfer functions and comparing the power response as a function of spatial scale.

The validity of the point source transfer function as a function of cluster scale radius is still an active area of research within the collaboration. It will be adopted in the MS0451 analysis, which is, at first glance, reasonable given the redshift of 0.54 and the associated angular size of the cluster in comparison with the APEX-SZ beam and coverage.

Noise estimation

The assumption of noise stationarity implies that the diagonals of the Fourier Transformed noise covariance matrix correspond to the power spectral distribution (PSD). This is obtained through the averaging of 'jack-knifed' noise maps, that are constructed from the direct inversion of half of the scan maps and their subsequent co-addition.

Since APEX-SZ scans a sky region of size 21', the effect of CMB contamination needs to be addressed. 100 CMB realizations were made from a CMB map generation code provided by F. Pacaud, which was based on a code by C. Reichardt. The WMAP 5-only lensed power spectrum was used (Hinshaw et al. 2009) for the CMB map realisations. After filtering with the transfer function, these were then added linearly to the jacknife noise maps. The APEX-SZ data have an overall flux calibration uncertainty of $\pm 5.5\%$ (Halverson et al. 2009), which needs to be taken into account besides the intrinsic confidence intervals listed in Table 6.3.

The fitting procedure

In the fitting process, a two dimensional model is convolved with the point source transfer function and compared to a $10' \times 10'$ cut-out of the raw APEX-SZ map using the noise covariance matrix whose matrix element population is described in the sections above, giving

$$\chi^2 = (\mathcal{FT}[\mathcal{D}] - \mathcal{FT}[\mathcal{M}_{\rm model} \otimes \mathcal{T}])^T \widetilde{\mathbf{C}_n}^{-1} (\mathcal{FT}[\mathcal{D}] - \mathcal{FT}[\mathcal{M}_{\rm model} \otimes \mathcal{T}]) \quad , \quad (6.13)$$

where $\mathcal{D}$ is the $n_{\rm cut} \times n_{\rm cut}$ pixel map, $\mathcal{M}_{\rm model}$ is the input model map and $\widetilde{\mathbf{C}_n}^{-1}$ denotes the Fourier domain inverse noise covariance matrix.

In the following fitting analyses, a delta prior is employed for the cluster centre position and set to the interferometer pointing direction, which, in the case of MS0451, corresponds to 04h54m11.6s -03d01m01.3s . In addition, any speculative DC offset parameter is set to zero. The priors on the model parameters are the same as for the interferometric fitting process described in section 6.2.2.

In the following analysis the BOA transfer function is used in the fitting routine.

APEX-SZ β-profile with $\beta = 0.86$ using the BOA transfer function

Figure 6.17 displays the β-profile fit with central coordinates fixed to 04h54m11.6s -03d01m01.3s and $\beta = 0.86$. There is a positive slant in the accepted APEX-SZ parameter space at high θ_c, which, when examining the parameterization, should not occur. When running the MCMC fit with my fitting routine using the MATLAB point source transfer function, this slant is not observed.

After relaxing the flagging conditions in the MATLAB pipeline and thus mirroring the BOA pipeline, a new MATLAB point source transfer function was obtained by J. Kennedy. This new transfer function produces a similar slant in the accepted parameter space as the fit using the BOA PST. Further analyses into the exact origin of the reduction pipeline step that causes this effect was omitted at present, since non-linearities in the point source transfer function are still being investigated by the APEX-SZ collaboration.

It is evident from Fig. 6.17 that the constraints in the scale parameter/normalization likelihood space are not very tight. This is most likely caused by the high noise in the APEX-SZ map as well as on the validity of the point source transfer function itself, particularly in the large scale radius region.

Currently, the APEX-SZ collaboration is refraining from trying to fit for both of these parameters. Solely the normalization is fit while keeping the scale radius to the best-fit value obtained from the universal pressure profile model concentration parameter by Arnaud et al. (2010) and the value of r_{500} from the r_{500}-T scaling relation by Vikhlinin et al. (2006) under the assumption of spherical symmetry (Bender et al. submitted).

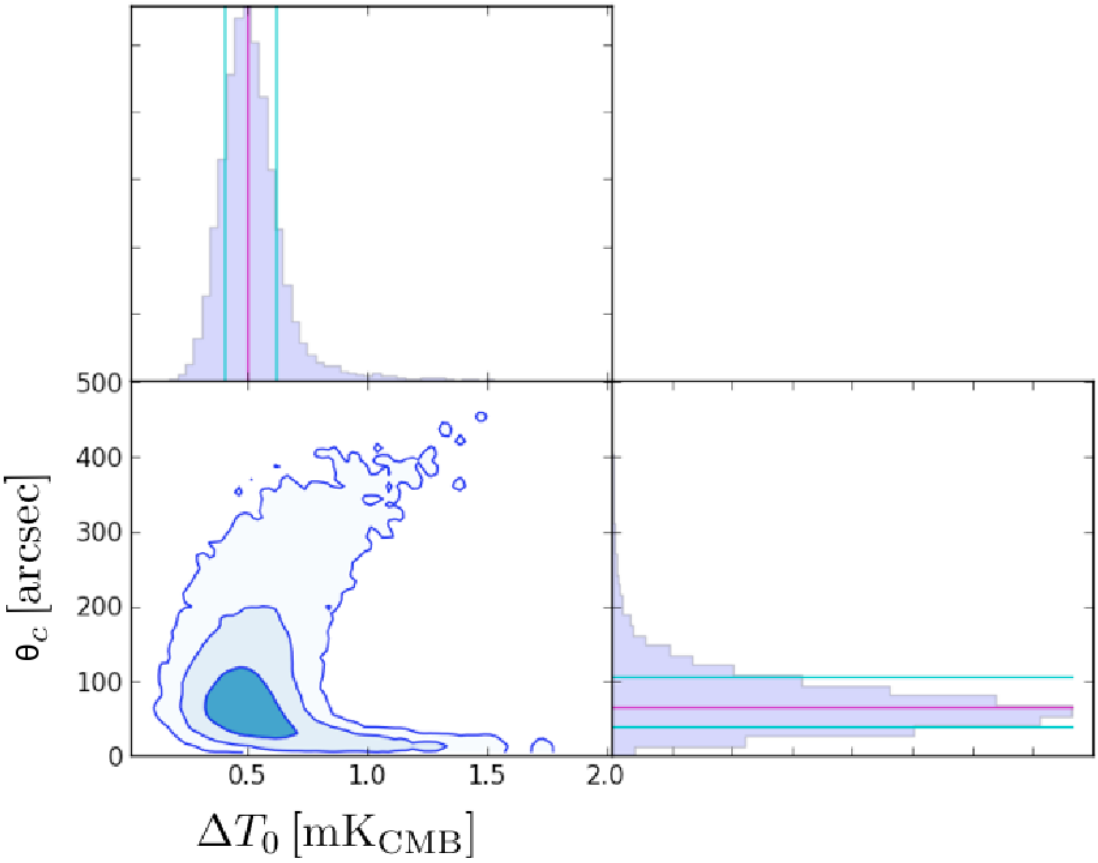

Figure 6.17: APEX-SZ β-model fit for fixed $\beta = 0.86$ with associated 68.3%, 95.5% and 99.7% 2D-Likelihood contours. Marginalized probability distributions are also shown, the magenta and blue lines denoting the median and 68% confidence interval.

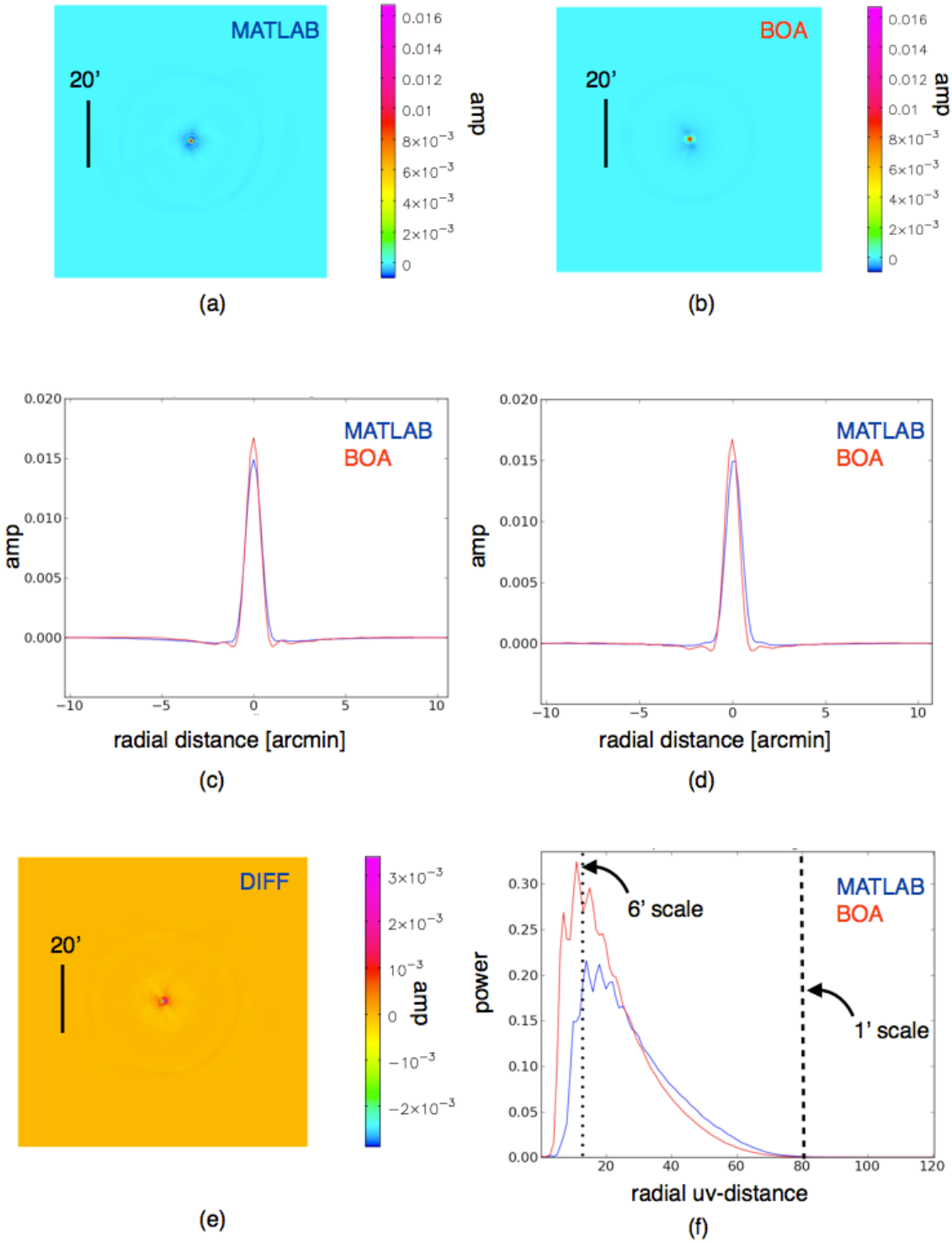

Figure 6.18: APEX-SZ Point Source Transfer Function (PST) Comparison of the MATLAB and BOA pipelines. *a)* MATLAB PST, *b)* BOA PST, *c)* horizontal cuts through the MATLAB and BOA PSTs, *d)* vertical cuts through the MATLAB and BOA PSTs, *e)* Difference image between the MATLAB and BOA PST, *f)* Power as a function of uv-distance, illustrating the heavier filtering of the MATLAB pipeline at large scales.

APEX-SZ elliptical β-model fit using the BOA transfer function

An elliptical β-profile model fit was made for the APEX-SZ data and yields values of $-5.2^{+19.1}_{-19.8}$ deg and $0.63^{+0.19}_{-0.17}$ for ϕ and ϵ respectively, in line with previously reported values in Donahue et al. (2003) and Sayers et al. (2011). This thus stresses the superiority of bolometer single-dish observations to my 30 GHz SZA interferometric data, which suffers from insufficient spatial sampling and thus cannot constrain the elliptical shape of the SZ signal, given the worse than expected data quality of the 90 GHz SZA and CARMA data. A complementary interferometric/single-dish approach thus ensures that constraints can be placed on a cluster's projected shape and orientation in the plane of the sky.

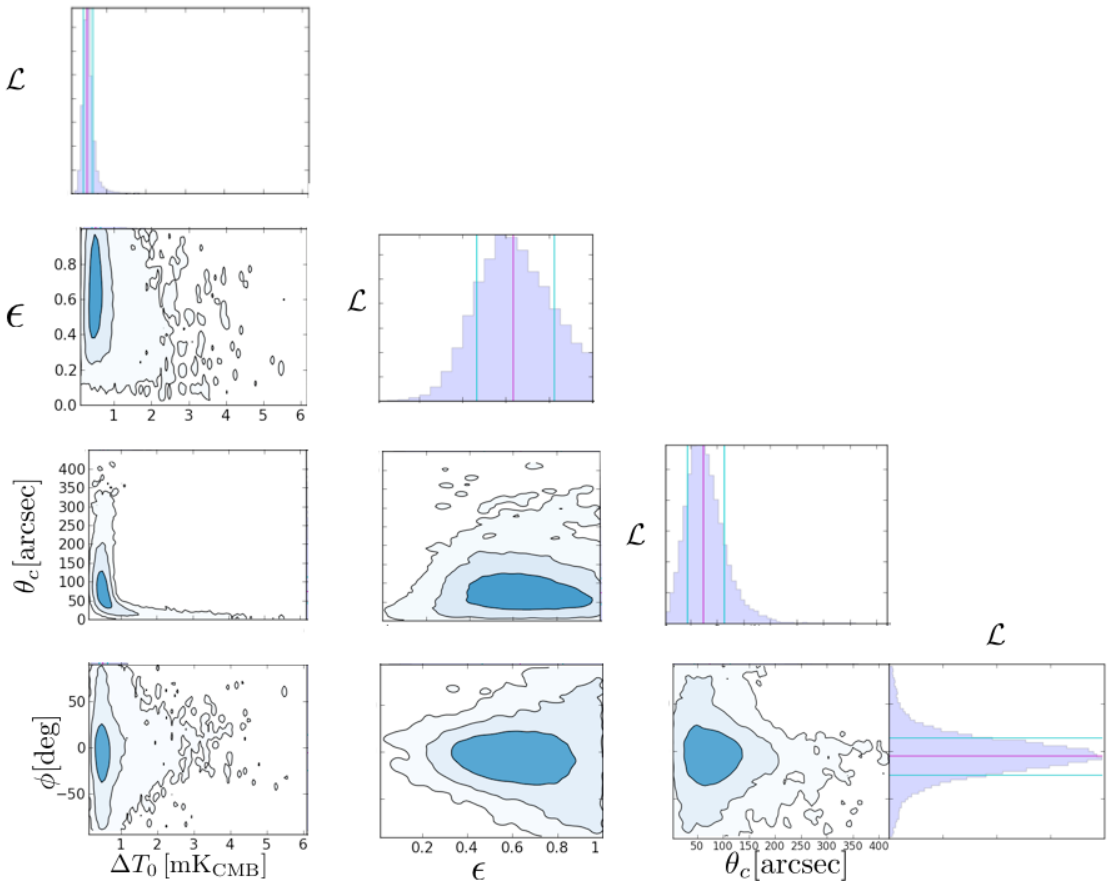

Figure 6.19: APEX-SZ elliptical β-model fit for fixed $\beta = 0.86$ with associated 68.3%, 95.5% and 99.7% 2D-Likelihood contours. Marginalized probability distributions are also shown, the magenta and blue lines denoting the median and 68% confidence interval.

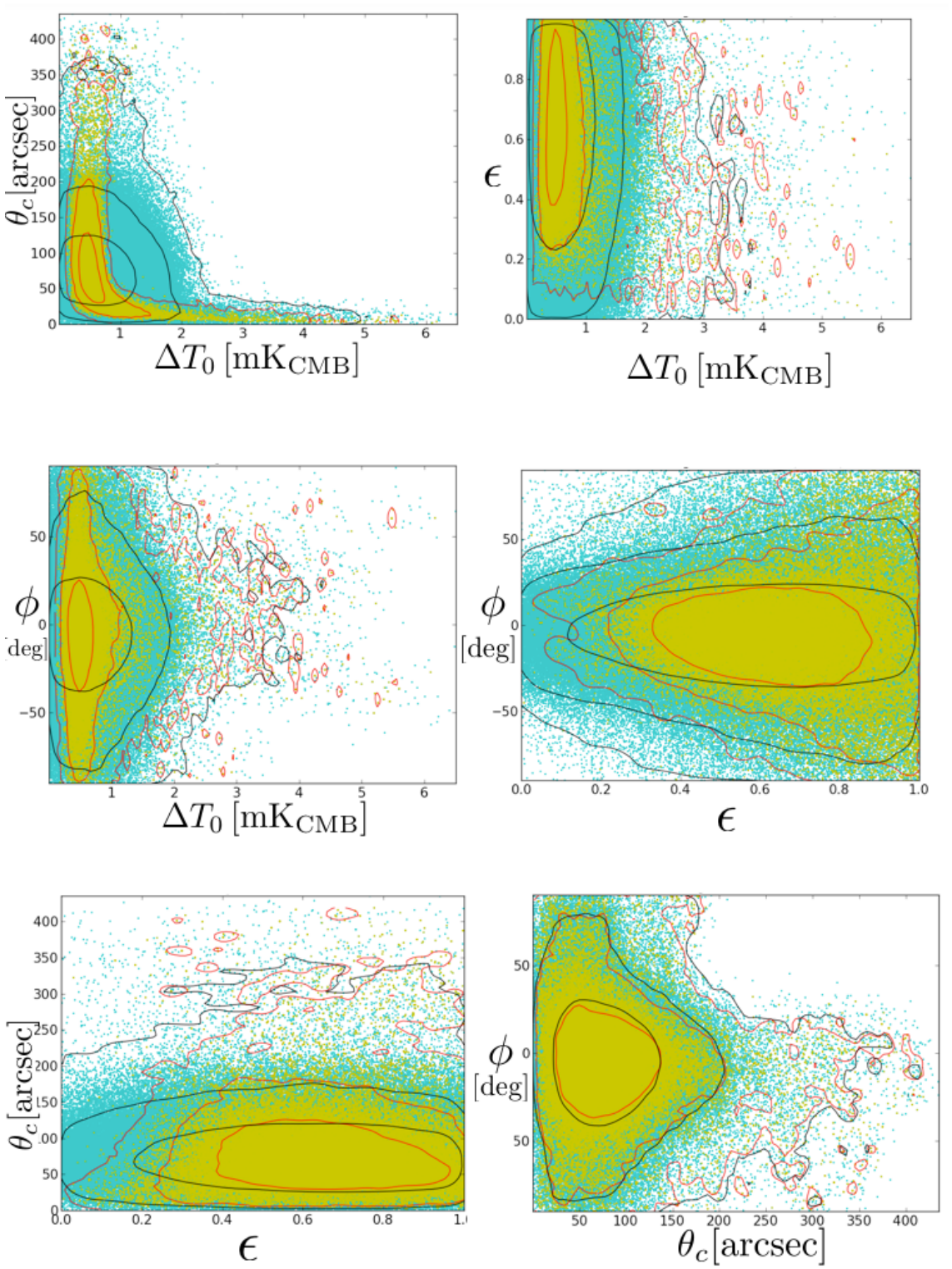

Figure 6.20: APEX-SZ - elliptical β-model fit explored parameter space. The explored (blue) vs the accepted (yellow) parameter space with associated 68.3%, 95.5% and 99.7% contours.

APEX-SZ GNFW fit without a scale radius priors

The GNFW APEX-SZ fits were performed with centre coordinates fixed to 04h54m11.6 -03d01m01.3s and $a = 0.9, b = 5.0, c = 0.4$, using the BOA transfer function. As one can see in Fig. 6.21, the accepted parameter space extends out to very large radii and the slant at high r_p, also observed in the θ_c parameter in the β-model fit, is visible in the GNFW fit, again suggesting possible transfer function dependent effects or non-diagonal noise covariance entries, that could lie at the origin of this unrealistic positive slant.

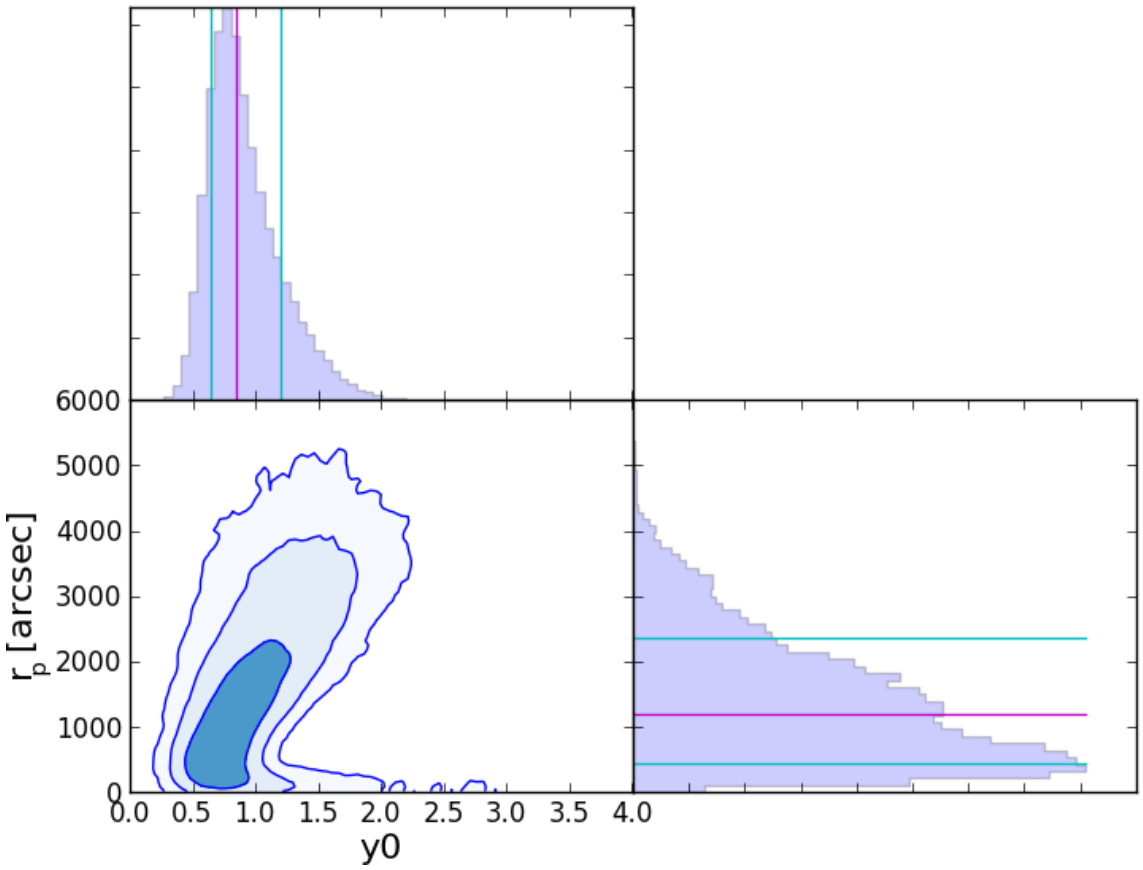

Figure 6.21: APEX-SZ GNFW-model fit for fixed (a,b,c) slope parameters with associated 68.3%, 95.5% and 99.7% contours. Marginalized probability distributions are also shown, the magenta and blue lines denoting the median and 68% confidence interval.

6.2.4 SZA/APEX-SZ comparison

Having shown that interferometric SZA/CARMA data can greatly benefit from APEX-SZ data in elliptical model fitting procedures, it remains to explore how well the two data sets aggree for the spherically symmetric fits. As can be seen in Fig. 6.22, the GNFW fits with an applied box prior on r_p at 230", which is close to the reported r_{500} value in Ettori et al. (2009), 30 GHz SZA and APEX-SZ data sets agree very well with each other within 1σ. For the fits with (Fig. 6.22) and without (Fig. 6.23) a scale radius prior in the GNFW parameterizations, the interferometric accepted parameter space is far tighter than the APEX-SZ fits.

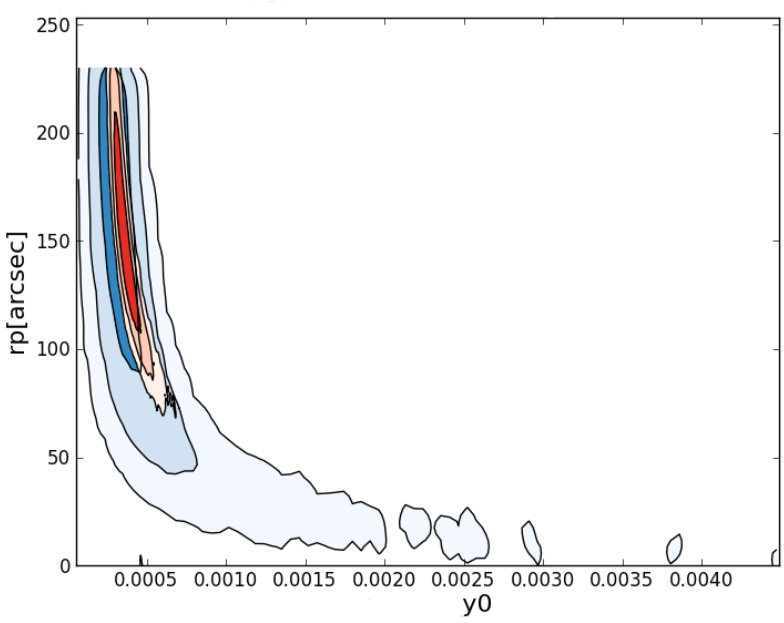

Figure 6.22: GNFW 30 GHz (red) and APEX-SZ (blue) comparison with an applied upper r_p prior at 230 " with associated 68.3%, 95.5% and 99.7% contours.

Table 6.3: GNFW SZA and APEX-SZ fits with an applied upper r_p prior.

DATA	y_0 10^{-4}	r_p arcsec
30 GHz SZA	$3.57^{+0.61}_{-0.43}$	$151.6^{+36.2}_{-30.5}$
APEX-SZ	$3.28^{+1.02}_{-0.70}$	$156.5^{+47.3}_{-58.2}$

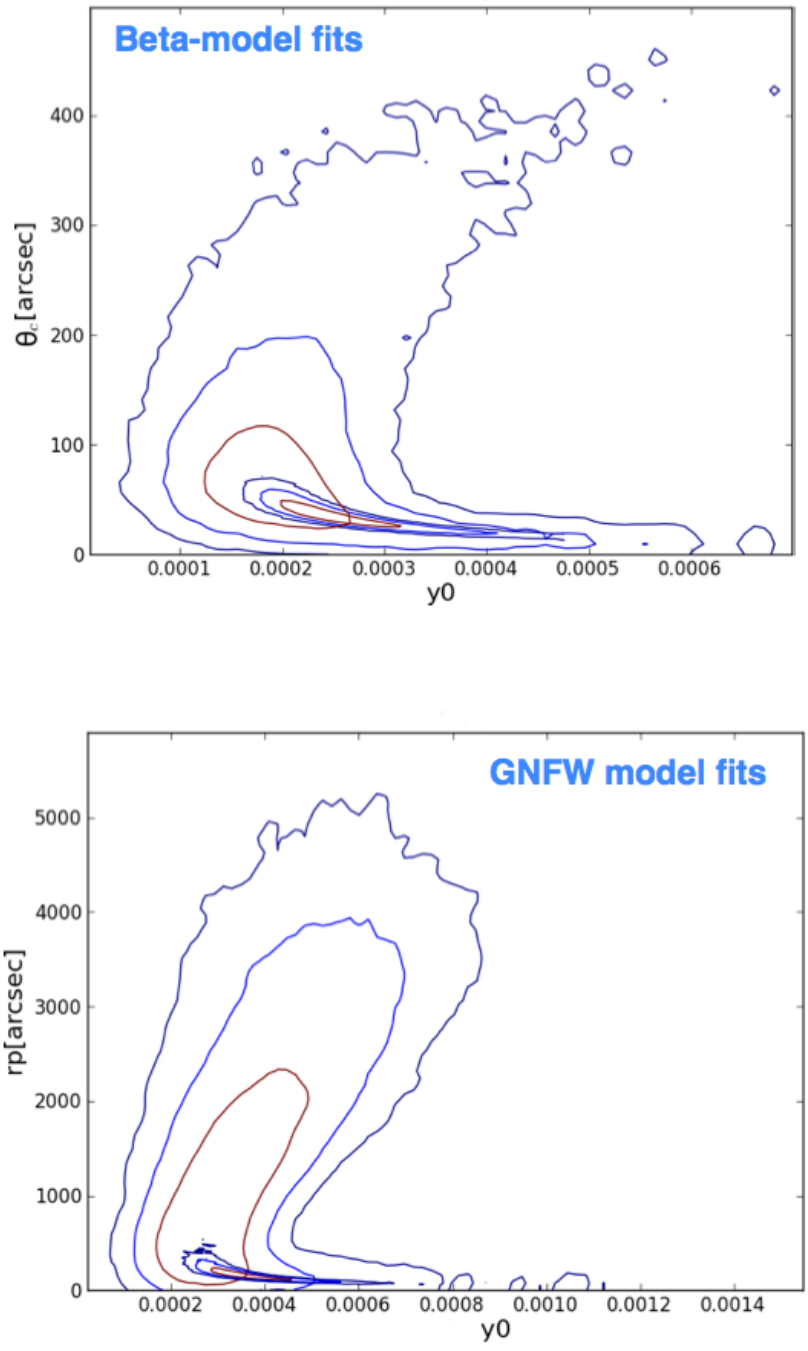

Figure 6.23: GNFW 30 GHz and APEX-SZ comparison without upper scale radius priors for the β-model (top) and GNFW model (bottom) fits. The contours indicate the 68.3%, 95.5% and 99.7% 2D-Likelihood contours.

6.3 Conclusion

It has therefore been demonstrated that my Bayesian MCMC visibility fitting code faithfully explores the accepted parameter space of the MS0451 joint SZA/CARMA fits, illustrating that the 30 GHz SZA 2D $y_0 - \theta_c$ likelihood contours follow regions of approximately constant $Y_{\rm cyl}$ integrated over an r_{500} aperture.

The 30 GHz SZA data did not allow for the angular orientation of the elliptical β-model to be constrained on account of the long- to intermediate-baseline sensitivity (baselines $>2\mathrm{k}\lambda$) - a fact that was confirmed via sole 30 GHz SZA visibility fitting of mock simulated visibilities. This factor was aimed to be compensated for by the 90 GHz SZA and CARMA E-array data. These, however, had lower than expected visibility sensitivities which, while improving the normalization-scale radius constraints in the joint spherically symmetric SZA(30+90GHz)/BIMA-BIMA fits, was not sufficient to allow for the projected elliptical shape to be determined.

Sole SZA interferometric observations, though they offer better precision in the spherical pressure profile normalization and scale radius parameter space, greatly benefit from supplementary APEX-SZ data, as the APEX-SZ map gives essential insight into a cluster's elongation and orientation in the plane of the sky. With an applied box prior on the scale radius at r_{500}, successful cross-calibration between 30 GHz SZA and APEX-SZ MS0451 data was confirmed to within 1σ in the spherically symmetric GNFW fit. The origin of the inferior precision of the APEX-SZ spherically symmetric fits compared to the interferometric data mainly lies in the high noise of the bolometer single-dish data as well as in possible uncertainties in the linearity of the transfer function.

Chapter 7

A galaxy cluster evolution study with the SZE

In this study, the feasibility of high-resolution interferometric Sunyaev-Zel'dovich observations of relaxed and morphologically disturbed galaxy clusters over a wide mass and redshift range is investigated, relying heavily on the assumption that the characteristic morphologically segregated Arnaud pressure profiles are valid for z>0.2, an issue which is currently being tested by several surveys and which will be further discussed in this chapter.
I present a suitability study in the form of mock simulations of current interferometers, which relies extensively on my extended interferometric visibility Bayesian MCMC fitting code within this simulation framework. The presented findings provide the basis for future potential multi-instrument SZ observations involving ALMA.

7.1 Motivation

Galaxy cluster cosmological studies are going to be mainly limited by systematics rather than number counts in the future. With galaxy cluster searches extending out to ever higher redshifts, which is necessary for studies probing dark energy, one needs to understand to what extent non-gravitational effects influence the observable-mass scaling relations and therefore the degree to which clusters deviated from self-similar systems. The framework for such investigations lies in the classification of galaxy clusters according to their morphological state and the associated dependence on accurate and precise mass determinations from galaxy cluster observables.

It is thus vital to study the ICM properties as a function of redshift in order to assess whether high-redshift samples show departures from self-similarity and whether sub-samples based on morphological selection criteria may help to reduce the scatter in mass proxy relations. Particularly cluster studies at high redshift will greatly benefit from Sunyaev-Zel'dovich observations as X-ray observations often suffer from lack of photon counts for annularly binned spectral temperature investigations at high redshift. The SZ-derived pressure profiles will greatly contribute in deriving galaxy clusters' pressure profiles, which have been shown to correlate with the morphological states of galaxy clusters at low redshift.

7.2 Validity of the Arnaud pressure profile

Arnaud et al. (2010) fit characteristic cool-core (CC), morphologically disturbed (NCC) as well as a uniform (UNIV) cluster pressure profiles, Table (7.1), to their 33 *XMM-Newton* observed galaxy cluster sample at z<0.2 via the parametric form

$$P(r) = P_{500}\frac{P_0}{(\frac{r}{r_s})^c\left(1+(\frac{r}{r_s})^a\right)^{\frac{(b-c)}{a}}}\left(\frac{M_{500}}{3\times 10^{14}h_{70}^{-1}M_{\odot}}\right)^{\alpha_p+\alpha_p^{'}} \quad . \tag{7.1}$$

The characterisitic pressure at r_{500}, denoted by P_{500}, is defined as

$$P_{500} = \frac{3\mu}{8\pi\mu_e}f_B M_{500}^{2/3}\left[\frac{500G^{-1/4}H(z)^2}{2}\right]^{4/3} \tag{7.2}$$

with α_p and $\alpha_p^{'}$ taking into account the mass biases of the profiles [1]. The scale radius, r_s is defined as $r_s = \frac{r_{500}}{c_{500}}$.

[1] This is caused by the hydrostatic equilibrium assumption in the M_{500}-Y_X relation and the corresponding normalization correction through α_p and its associated radial dependence through $\alpha_p^{'}$

It has only been recently, that such profiles have also been fitted to SZ observations from different instruments spanning a wider redshift range than the Arnaud sample. The redshift distribution for cool-core (CC) and non-cool core (NCC) clusters is shown in Fig. 7.2 for the reported Planck release 1, Bolocam, Arnaud, SPT and APEX-SZ samples.

All of these experiments use partially different classifications for cooling core galaxy clusters. Arnaud et al. (2010) define cooling cores by their central density and morphologically disturbed systems by their centre shift parameter. The condition for cooling core classification is $\mathrm{h(z)}^{-2}\mathrm{n}_{e,0} > 4\times10^{-2}$ cm^{-3}. The Planck sample uses the same classification criteria. The BOXSZ sample defines cooling core clusters via the X-ray luminosity ratio within $R < 0.05\ R_{500}$ and R_{500} (Sayers et al. 2013). Morphologically disturbed systems are defined by the centroid shift parameter under the condition that $w_{500} \geq 0.01$, following the classification by Arnaud et al. (2010) (see section 3.5). The APEX-SZ sample takes the morphological classifications from literature relying, amongst others, on cooling time estimates, central surface brightness peak strength and the degree of projected ellipticity (Bender et al. submitted).

The SPT sample of 83 high redshift, $0.3 > \mathrm{z} < 1.2$, clusters explores several classification parameters (McDonald et al. 2013). The galaxy cluster sample selection in Fig. 7.2 was made via the central entropy grading selection; $K_0 < 30$ keV cm^2 indicating cooling cores and $K_0 > 30$ keV cm^2 describing morphologically disturbed clusters.

Table 7.1: Arnaud model best-fit parameter values

Morphology	P_0	c_{500}	a	b	c
Cool Core	3.249	1.128	1.2223	5.49	0.7736
Universal	8.403 $h_{70}^{-3/2}$	1.177	1.051	5.4905	0.3081
Non-Cool core	3.202	1.083	1.4063	5.49	0.3798

The galaxy cluster number statistics at high redshift is still quite low and some of the samples are biased towards lower redshifts from the CC side. This is not surprising since the fraction of classical core galaxy clusters is thought to decrease with increasing redshift (Vikhlinin et al. 2007) - cool core clusters being thought to evolve from cooling core clusters that have less pronounced X-ray central peaks (McDonald et al. 2013).

The Planck, Arnaud and Bolocam experiments fit GNFW profiles to their samples, varying not only the normalization and scale parameters, as is currently done with APEX-SZ data, but also the slope parameters of the profiles. The fixed parameters are determined according to the characteristic scales probed by the different instruments.
Arnaud et al. (2010) leave all the parameters as free variables except for the outer slope parameter, b, which is fixed at 5.4905. BOXSZ fix the concentration parameter and vary the normalization and all three slope parameters. The Planck sample keeps the central slope parameter, c, fixed to 0.31 while varying all other parameters. In all samples, P_{500} was derived from the $M - Y_X$ relation.

The corresponding best-fit 3D de-projected pressure profiles are shown in Fig. 7.1 for the universal, cool-core and non-cool core cases. The BOXSZ best-fits are consistent with

the Arnaud profiles within the error bars (Sayers et al. 2013). The Planck profiles agree with the Arnaud profiles within the range $0.1 - 1.0R_{500}$ (Planck Intermediate Results V 2013).

Due to the lack of information of the Arnaud, Planck, APEX-SZ and Bolocam samples at high-redshift, the evolution of the inner pressure profile could not be probed. Recently, SPT has mapped 83 high redshift, $0.3 < z < 1.2$, galaxy clusters, McDonald et al. (2013), the sample being shown in the magenta histogram in Fig. 7.2. These SPT clusters were followed up with Chandra. The Chandra exposure time does not allow for a detailed spectroscopic analysis to be made but under the assumptions of hydrostatic equilibrium, spherical symmetry and using constraints from the Duffy mass-concentration relation, Duffy et al (2008), and the $M_{500} - P_{500}$ relation by Nagai et al. (2007), McDonald et al. (2013) derive a 3-bin temperature profile for each cluster.

Subject to these assumptions, a central temperature value was extrapolated towards small radii, $r < 0.012R_{500}$ (McDonald et al. 2013), and in combination with the central density parameter, which was obtained from X-ray surface brightness observations, the central cooling times and entropies were derived for their galaxy cluster sample. The main findings by McDonald et al. (2013) concentrate on the property of cool-core clusters at high redshift. Although the central brightness cuspiness decreases as a function of redshift, the cooling properties of the clusters do not, suggesting that galaxy clusters have been cooling over a long time with a feedback mechanism that prevents cooling below entropy levels of 10 keV cm^2. Whereas the central density profiles show a mild evolution as a function of redshift for morphologically disturbed clusters, the average central density profile of clusters with central entropy levels <30 keV cm^2 increases significantly as a function of decreasing redshift.

McDonald's temperature fitting technique does not allow for annular spectroscopic fitting in the central cluster regions due to low X-ray photon number counts but an iterative joint dark matter profile/temperature/surface brightness fit under the assumptions of hydrostatic equilibrium and sphericity suggests that cooling flow clusters were cooler at higher redshift, though the significance of this result is affected by the high uncertainties in the derived central temperature values.

If the feedback properties should indeed change as a function of redshift, this would have consequences for the mass/observable scaling relations since these non-gravitiational effects could introduce potential biases into mass-proxy analyses (McDonald et al. 2013). In addition, the lack of strong cool-core systems at high redshift (z<0.75) suggests that high redshift studies will need to resort to methods complementary to the surface brightness peak parameter characteristics in order to select morphologically relaxed systems for scaling relations that reduce the intrinsic scatter caused by morphological bias effects.

At low redshifts, the pressure profile from morphologically disturbed clusters and relaxed clusters can be discriminated in the central regions. So far, the highest redshift clusters for which Arnaud profiles have been fitted via SZ observations come from the APEX-SZ and Bolocam samples. The APEX-SZ sample adopts a GNFW fit with fixed slope parameters set to (a=0.9, b=5.0, c=0.4), whereas the BOXSZ sample leaves all slope parameters and the normalization parameter as free parametrs only fixing the concentration. One can therefore deduce from Fig. 7.2 that the highest redshift morphologically disturbed cluster which was included in an Arnaud/Gnfw model fit with free slope param-

eters is at $z = 0.833$.

The evolution of the cluster pressure profile as a function of redshift is therefore still an open issue, although the central gas density evolution shown by McDonald et al. (2013) in conjunction with their tentative decreasing mean central temperature discovery for cool-core clusters, suggests that the cool-core pressure profile could become more shallow in the central cluster regions as a function of redshift.

The study of galaxy cluster pressure profiles as a function of redshift would thus shed light on the following issues:

- The dependence of the evolution of pressure profiles on different morphological states.
- In combination with X-ray surface brightness information and global temperature measurements under the assumption of spherical symmetry, pressure profiles can be used to derive the temperature profiles for a sample of clusters, enabling the study of their morphology dependence.
- The items above will enhance our understanding of feedback processes in galaxy clusters, which, in turn, will help to quantify the influence of non-gravitational effects on cluster scaling relations.

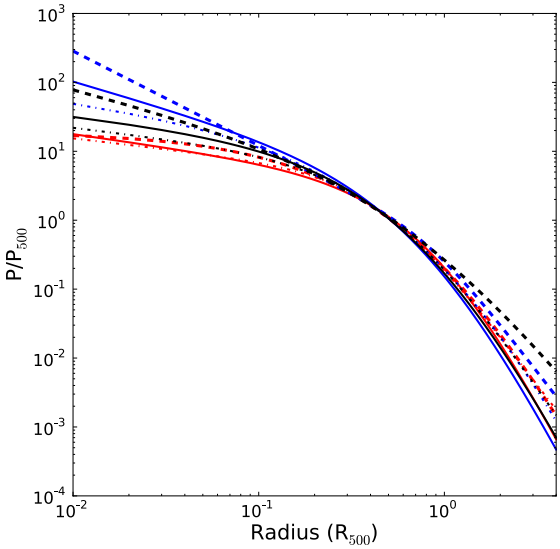

Figure 7.1: A Comparison of the best-fit 3D universal (black), cool-core (blue), non-cool core (red) profiles for the Arnaud (solid), Bolocam (dashed) and Planck (dot-dashed) sample. The confidence intervals are omitted for the purpose of clarity. The BOSX sample is reported to be consistent with the Arnaud profile (Sayers et al. 2013) and the Planck sample agrees with it within the range $0.1 - 1.0$ R_{500} (Planck Intermediate Results V 2013).

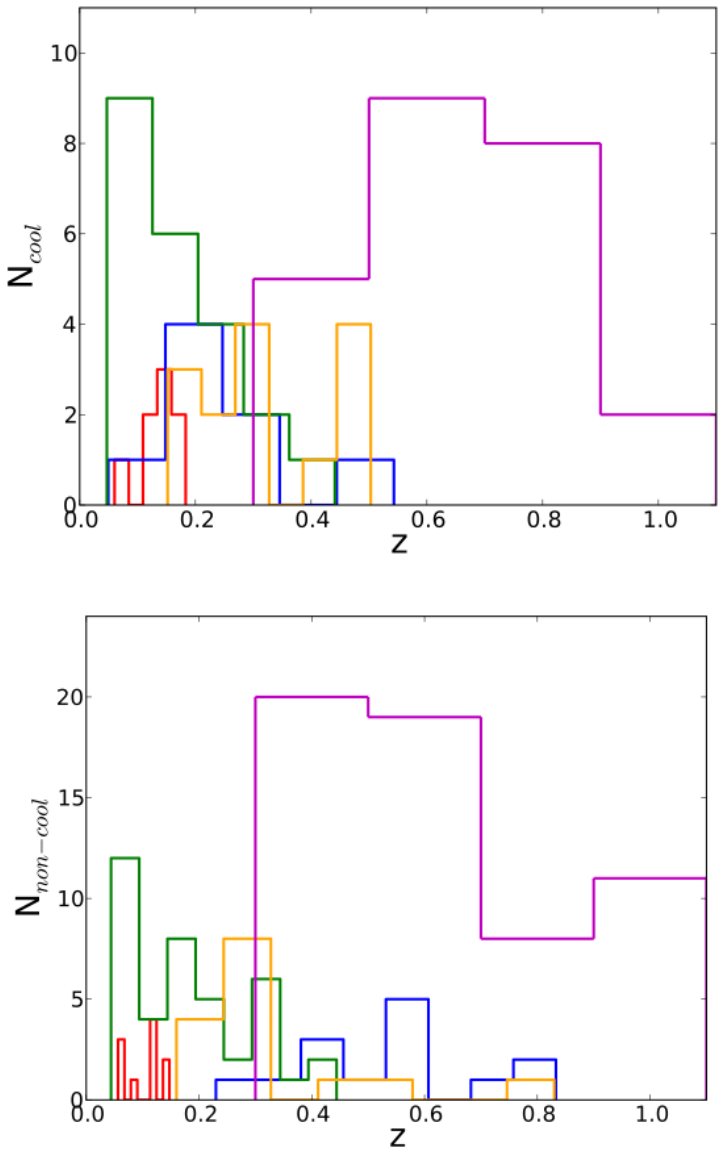

Figure 7.2: Sample redshift distribution for relaxed (top) and morphologically disturbed (bottom) clusters: Arnaud (red), Planck (green), SPT (magenta), Bolocam (blue), APEX-SZ (orange). The Chandra observed X-ray follow-up SPT sample by McDonald et al. (2013) has greatly extended the redshift range over which cool-core and non-cool core clusters are studied via X-ray observations. The analysis of the samples in terms of profile fittings differ in the number of fixed parameters.

7.3 Interferometric studies of cluster pressure profiles

The study of the evolution of cooling cores and morphologically disturbed clusters and their associated characteristic structure is thus vital for our understanding of the feedback processes within clusters as well as for the assessment of possible biases in the observable-mass relations.

Hence, I utilize a method that will complement high-redshift X-ray galaxy cluster studies - *high-resolution interferometric Sunyaev-Zel'dovich observations*.

Altough interferometers, such as the SZA and AMI, have already imaged high-redshift clusters (Muchovej et al. 2007), they lack the resolution and sensitivity to accurately probe cluster pressure profiles across a wide range of spatial scales. Hence, in the case of detailed pressure profile studies, the interferometer choice needs to be tailored towards scales characterized by regions smaller, comparable and larger than the scale radius, the latter being dependent on the redshift for a cluster of a given mass with a given Arnaud profile.

The full ALMA/ACA array will present us with an unrivalled combination of angular resolution and sensitivity. This will allow for solid and significant imaging of the central parts of the SZ profile. The planned addition of Band 1 receivers to both, ALMA and ACA antennas, will greatly enhance the uv-overlap with other interferometers, such as the SZA, or indeed single-dish instruments like CCAT, BOLOCAM as well as the observed APEX-SZ targets.

The range of scales spanning the angular resolution to the maximum angular scale of selected interferometric (Table 7.2) and single-dish instruments is illustrated in Fig. 7.3 in comparison with the characteristic Arnaud profile at two different redshifts. This presents a mere indication of the spatial scale coverage since the true coverage is affected by the individual instrumental response and sampling functions.

Table 7.2: Characteristic instrument scales

	central freq (GHz)	FWHM (')	MAS (")	beam (") × (")
ALMA BAND3	100	1.01	24.8	4.7 × 3.7
ALMA BAND2	79	1.27	31.3	5.9 × 4.7
ALMA BAND1	38	2.65	65.0	12.3 × 9.8
ACA BAND3	100	1.72	41.3	17.1 × 15.3
ACA BAND2	79	2.18	52.2	21.7 × 19.5
ACA BAND1	38	4.54	108.6	45.4 × 40.0
SZA	31	10.70	≈ 270	60.7 × 52.2

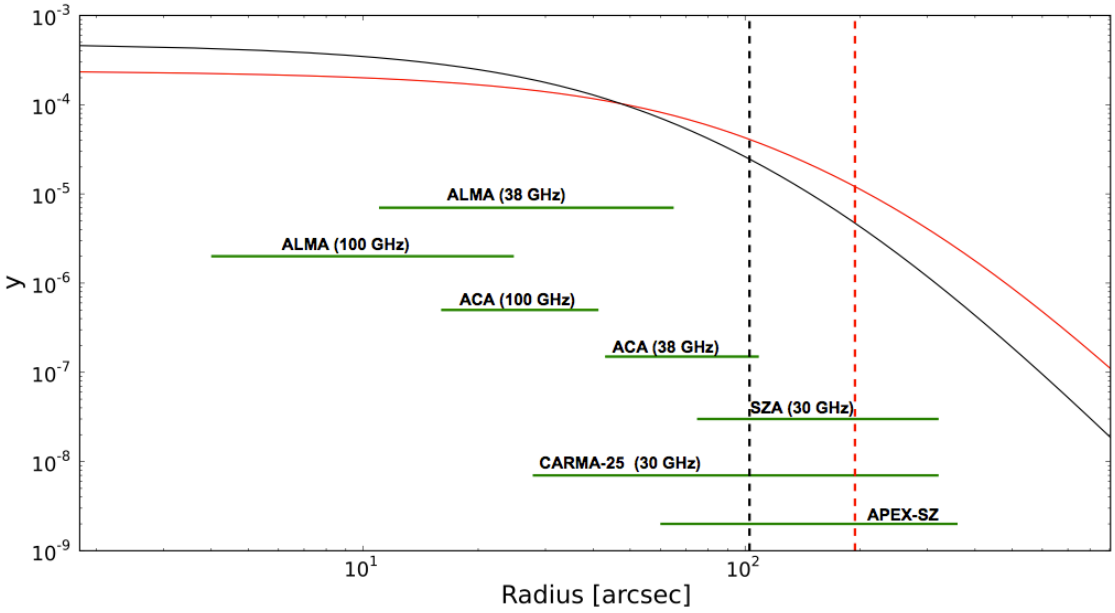

Figure 7.3: The integrated Comptonization parameter of a masive $M_{500} = 8 \times 10^{14}$ $M_{\odot}$ cluster at redshifts 0.4 (red) and 1.0 (black) derived from the universal Arnaud profile, the characteristic scale radius being shown for each redshift by the dashed vertical lines. The green horizontal lines with arbitrary vertical positions show the angular range of the instruments, the leftmost part being the angular resolution and the rightmost, the maximum angular scale that can be imaged.

As one can see from Fig. 7.3, current and future ALMA/ACA Band 3 observations have the potential to probe the centre of galaxy clusters over a wide redshift range.

In order to complement this with large-scale information, the SZA at 30 GHz or APEX-SZ data present viable instrument choices. The advantages and disadvantages of these two instruments as well as their mutual compatibility have been outlined in chapter 6.

Based on experience gained from the SZA/CARMA/APEX-SZ MS0451 data sets, 30 GHz SZA was chosen as the preferred 'large-scale probing' instrument for the following simulation study, although the same analysis can be implemented with joint interferometric and single-dish data sets including APEX-SZ, BOLOCAM or indeed Planck. ALMA/ACA Band 1 will provide significant uv-overlap with ALMA/ACA Band 3 and SZA/APEX-SZ data, allowing the cluster pressure profile to be probed at higher significance across a wider range of spatial scales in the clusters' central regions.

Throughout the simulation study, I assume the best-fit Arnaud profiles for morphologically disturbed, universal and cooling-core galaxy clusters to be valid across the redshift range $0.4 - 1.2$.

Given the evolution of cooling core clusters indicated by McDonald et al. (2013), it is unlikely that the cooling-core pressure profile will still be valid at redshifts above 0.75, though a margin would need to be considered around this redshift due to low sample

statistics in this redshift range.

In particular, the galaxy cluster XMMU J1230 at $z = 1.39$ has been fitted with a double β-model (Rosati et al. 2009) as the surface brightness profile has a cuspy inner shape, suggesting that one can find cool-core clusters even at this high redshift. This justifies the use of a cool-core Arnaud pressure profile for high redshift clusters in this simulation study, in order to illustrate an upper bound, the morphologically disturbed cluster profile forming the lower bound, for characteristic cluster profiles.

The aim of the following investigation can be summarized in a single question:

How well can galaxy clusters be imaged over a wide mass and redshift range with joint ALMA/ACA + 30 GHz SZA observations ?

This issue is approached from several different angles through:

- The generation of mock simulation image galleries spanning masses from $2.0 \times 10^{14} - 1.1 \times 10^{15} M_{\odot}$, redshifts from $z = 0.4$ to $z = 1.2$ and characteristic Arnaud profiles. This will illustrate the covered spatial scales and the core region detection significance for different pressure models.
- Bayesian Markov Chain Monte Carlo visibility fitting over the pressure profile parameter space for two mass and redshift test cases. This will allow for a quantitative view of :
  - the ablity to recover the pressure profile parameters as a function of mass at a given redshift
  - the ablity to recover the pressure profile parameters as a function of redshift for a given mass
  - the advantage of additional ALMA/ACA Band 1 observations to ALMA/ACA (Band3) + 30 GHz SZA data
  - the quantitative effect of the previous 3 items on the ability to recover different cluster morphologies characterized by the Arnaud pressure profiles

  Though only a few test cases will be considered here, the method can easily be generalized to other mass/redshift/instrument combinations.
- The generation of mock simulation studies using hydrodynamical simulations by Klaus Dolag at high redshift, z>1.2, with ALMA Band 3 observations.

7.4 Mock simulation set-up

In order to assess the suitability of joint ALMA/ACA/SZA observations, viable observation times and characteristic observing conditions need to be chosen. In addition, the clusters need to be studied over realistic regions in the mass-redshift space, so as to avoid focusing on unrealistically high-mass clusters for a given cosmological model or, in other words, 'pink elephants'.

The adopted cosmological model follows that in Arnaud et al. (2010) of $(\Omega_M, \Omega_\Lambda, H_0, f_B) = (0.3, 0.7, 70\text{km s}^{-1}\text{ Mpc}^{-1}, 0.175)$.

7.4.1 Instrumental considerations

In view that this project is a feasibility study, characteristic and realistic observing set-ups were chosen.

This includes selecting a target declination for the source, which minimizes shadowing of the ALMA/ACA and SZA antennas and offers sufficient uv-coverage. Shadowing of antennas becomes problematic for the SZA at elevations lower than -25 deg. Fig. 7.4 illustrates the shadowing fraction of ALMA/ACA cycle 1 configurations for a 2 hour integration time alongside with the SZA shadowing fraction for a 4 hour integration time.

Given that a track typically lasts for approximately 4 hours, one should note that the ALMA/ACA full array shadowing fraction is likely to be higher for a given declination compared to the shorter 2 hour cylce 1 on-source integration time. In addition, for a feasibility study, one should avoid synthesized beams that are too elliptical on account of a low declination source position.

Not only the spatial coverage, but also the sensitivity at a given spatial scale determines whether the central and near scale radius regions of the projected pressure profiles can be recovered by the interferometric combinations within reasonable array observation times. The chosen configurations for ALMA/ACA correspond to the full-array configurations alma.out01.cfg and aca.i.cfg (CASA software). Since a low-declination position is chosen for the source (see below), the SL configuration and associated antenna positions from the MS0451 data were used for the mock SZA simulations. The declination of the source plays an important role, particularly for the SZA, as this affects not only the shadowing fraction but also the resultant uv-coverage, which is illustrated for a 3.3 hour on-source integration time mock simulation study for varying declinations in Fig. 7.4

Hence, the target declination was chosen to be at -15 deg since this presents a good compromise between uv-coverage for all intrumental baselines, Figs. 7.5-7.6, and the shadow fraction for a track length longer than 2 hours, alongside with elevation-dependent flagging. In addition, the resultant ALMA/ACA beams are nearly circular (Table 7.2). Calibrator switching is not included in the simulations. The lack of source uv-coverage 'calibrator holes' is a secondary effect though, whose contribution is insignificant in comparison with the total on-source integration time for the presented simulations.

In addition, the best observing time combinations of ALMA/ACA and SZA needed to be chosen. Here, I diverted from the current relative observing time ratio for ALMA/ACA of 1 : 3 (ALMA Cylce0+1) and 1 : 2 (ALMA Cycle 2). For cluster profile studies, high-resolution observations in the central regions are essential and thus require a long integration time, whereas ACA observations, with a lower resolution, do not necessitate three times/twice this observation time to map the profile beyond the characteristic radius.

The observing time set-up shown in Table 7.3 was sufficient for the analysis and excludes flagged times due to source elevation shadowing. It also offers sufficient sensitivity at the required scales, which is discussed in the next section.

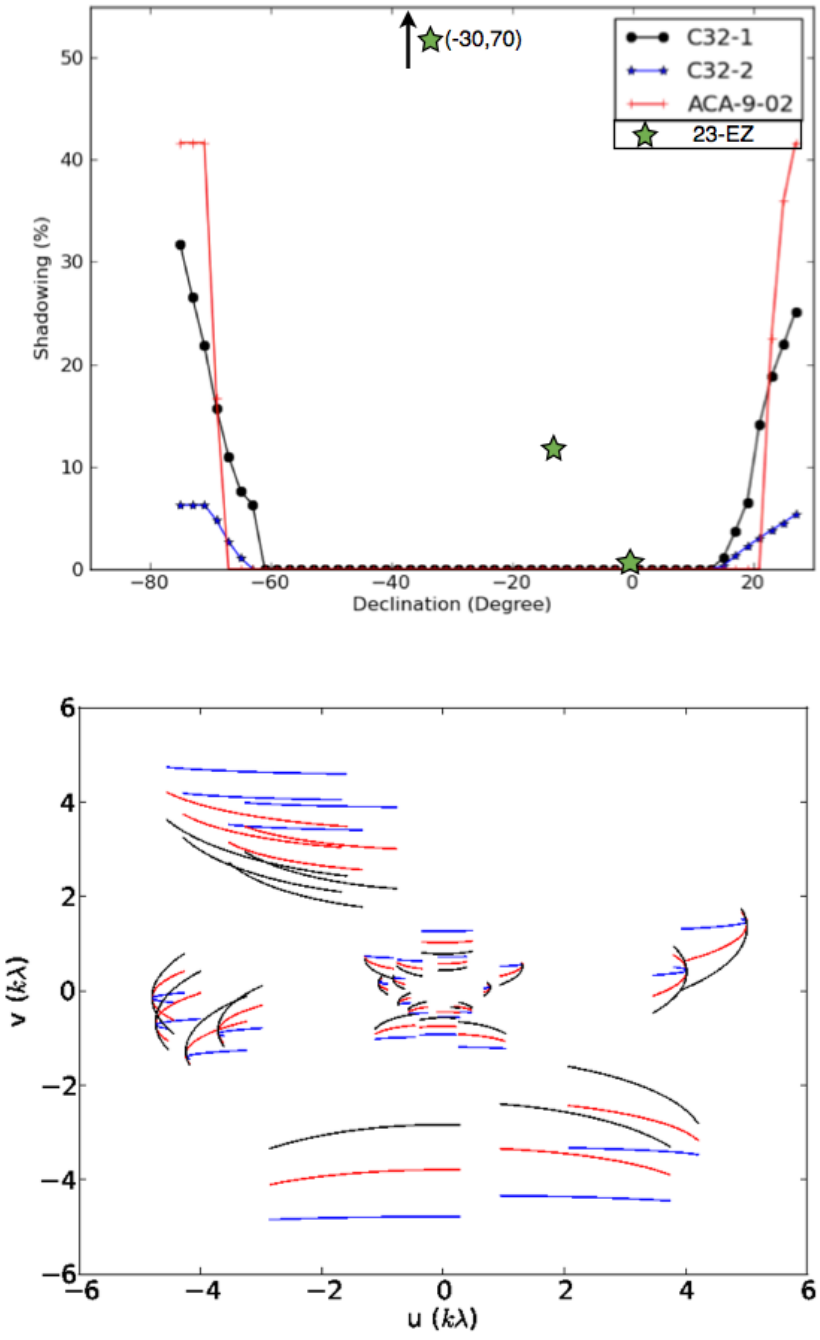

Figure 7.4: Source declination choice. *Top:* The ALMA, ACA and SZA shadowing fractions for a 2h ALMA/ACA and 4h SZA on-source integration time (Lundgren (2012) ALMA Technical Handbook Cycle 1, Wright (2004) CARMA-memo 25). *Bottom:* The uv-coverage for the SZA SL configuration at declinations -3 deg (blue), -15 deg (red) and -25 deg (black).

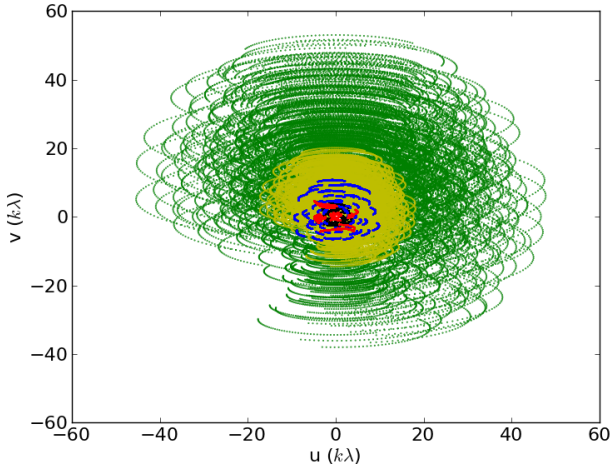

Figure 7.5: UV-coverage with the chosen observational set-ups and an ALMA visibility accumulation time of 600s as opposed to 10s for the ACA. The colour coding is ALMA Band 3 (green), ALMA Band 1 (yellow), ACA Band 3 (blue), ACA Band 1 (black) as well as the SZA (red). Note that, due to symmetry considerations, only half of the baselines are shown.

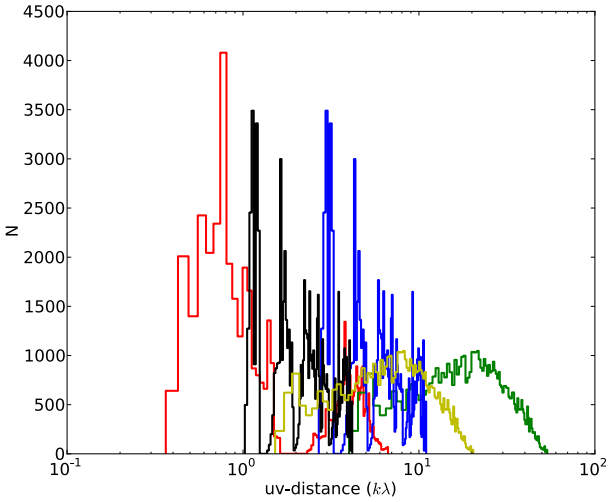

Figure 7.6: Visibility histogram, following the set-up and colour coding above. The ALMA visibility accumulation time of 600s, as opposed to 10s for the ACA, results in a lower visibility number. In the simulations, the increased accumulation time results in a decreased noise per visibility compared to a 10s accumulation time ALMA set-up.

7.4.2 Sensitivity set-up

The observing times were estimated in conjunction with the expected observing conditions and thus the expected sensitivities. The relevant parameters are listed in Tables 7.3 and 7.4.

The SZA sensitivity calculator was found to make rather pessimistic assumptions when comparing it to actual data (MS0451 project c1015). The mock simulations as well as the later Bayesian MCMC fits (section 7.6) and the aperture flux integration graphs were all run with MS0451-like 30 GHz SZA sensitivity levels.

All ALMA/ACA mock observations were run in dual polarization observation mode, giving 7.5 GHz bandwidth per polarization for ALMA/ACA as reported in the ALMA sensitivity calculator. A total bandwidth of 7.0 GHz was assumed for the SZA, in line with the MS0451 data (8 GHz are reported in the specification of the new 30 GHz receivers installed in 2013). This is thus a conservative estimate, taking into account potential missing or faulty spectral window ranges.

The necessity for ACA array information that supplement the ALMA data is best understood when examining the uv-coverage and the associated probed spatial scales, Figs. 7.5 and 7.6, as this supplementary array bridges the gap between ALMA and 30 GHz SZA uv data.

Table 7.3: Observational set-up: On-source integration time

	central freq (GHz)	on-source observation time (hrs)
ALMA BAND3	100	7.6
ALMA BAND1	38	7.6
ACA BAND3	100	3.3
ACA BAND1	38	3.3
SZA	31	15.9

Table 7.4: Observational set-up: Sensitivity[a]

	SZA30	ALMA100	ACA100	ALMA38	ACA38
central frequency[GHz]	31.2	100.0	100.0	38.0	38.0
system temperature[K]	44.6	80.0	80.0	41.1	41.1
surface accuracy[μm]	–	25.0	20.0	25.0	20.0
antenna efficiency	0.66	0.712	0.715	0.719	0.719
correlator efficiency	0.983	0.88	0.88	0.88	0.88
Jy/K factor	434.65	34.28	100.32	33.95	99.71

[a] The good SZA condition parameters comparable to the MS0451 data quality are given. The quantization efficiency of 0.96 was neglected in the ALMA/ACA noise calculation (the effect on the sensitivity is however only at the 4% level).

7.4.3 Model set-up

In order to make sure that the simulations were performed over a realistic mass-redshift cluster property space for a given cosmological model, the cumulative cluster number function was studied (Fig. 7.7).

My CC/UNIV/NCC simulations were run over the mass range M_{500} = 2.0 - 11.0 $\times$ $10^{14} M_{\odot}$ within a redshift range of 0.4-1.2, thus covering realistic galaxy cluster cases, though at the high-redshift end, the higher mass clusters become scarce (Fig. 7.7). Examples for such massive clusters include the 'El Gordo' cluster at $z = 0.87$ with $M_{500,c} = 1.67^{+0.2}_{-0.2} \times 10^{15} h_{70}^{-1} M_{\odot}$ (Menanteau et al. 2012) and the massive, $M_{T_X,500} = 0.92 \pm 0.37 \times 10^{15} h_{70}^{-1} M_{\odot}$ cluster at $z = 1.132$ (Foley et al. 2011).

Single-cluster in-depth follow-up studies via Bayesian MCMC heterogeneous fitting were performed for the mass test cases $M_{500} = 8.0 \times 10^{14} M_{\odot}$ and $M_{500} = 5.0 \times 10^{14} M_{\odot}$ at redshifts 0.4 and 0.8.

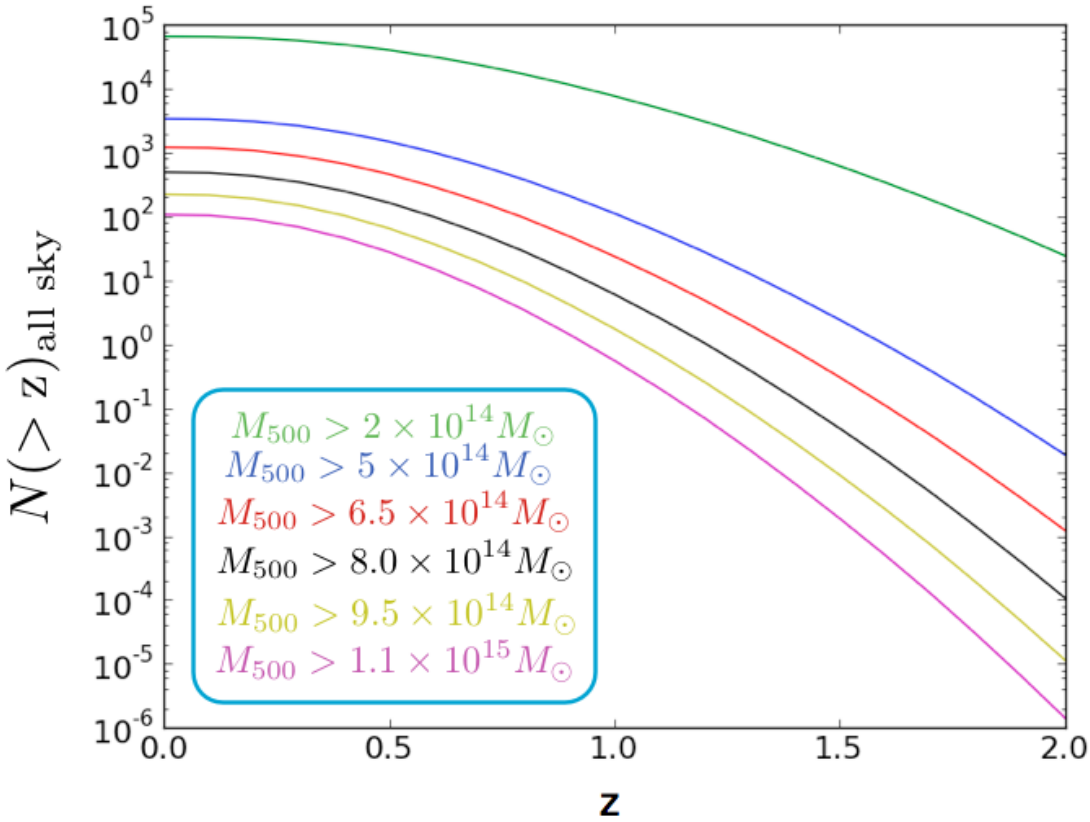

Figure 7.7: The cumulative mass distribution as a function of redshift. The input table was provided by F. Pacaud.

7.5 Image gallery

The CASA simulator was used to create a gallery of cleaned images to assess the ability of joint ALMA/ACA/SZA observations to image the SZ effect in galaxy clusters as a function of morphological state, mass and redshift.

The simulations were set up for the noise characteristics described in Table 7.4 and the resultant dirty images were cleaned within a clean box the size of the primary beam using a clean threshold equivalent to the expected image noise. Point sources were not included in the simulations as it was assumed that bright point sources in real observations can be removed via the long baselines of ALMA (Band 3 and Band 1) as well as via the two outrigger antennas of the SZA (30 GHz). The residual contamination due to unsuccessfully removed point sources in the image plane was therefore neglected, as the prime focus of this investigation was to test whether the ALMA/ACA/SZA uv-coverage itself is sufficient for distinguishing CC/UNIV and NCC clusters over a wide mass and redshift range. A proper treatment of point source contamination would have involved the modeling of the evolution of the point source population across a wide redshift range as well as their spatial distribution in clusters themselves. In order to mimic real data reduction, the 30 GHz SZA data was imaged with both, the full and 0-2 kλ tapered uv-range. Before combining the data sets using the *feather* task in CASA, ALMA/ACA Band 3 and Band 1 data are re-scaled to 30 GHz, knowing the spectral signature of the Sunyaev-Zel'dovich effect with the relativistic and kinetic components set to zero.

The full image gallery of all mock array simulations and resultant feathered combinations is presented in Appendix B. A single case study of a galaxy cluster of mass $M = 8.0 \times 10^{14} M_{\odot}$ at redshift $z = 0.8$ is illustrated in Fig. 7.8 for ALMA/ACA Band 3 and 30 GHz 0-2 kλ SZA observations with good realistic weather conditions as a function of the cluster's morphology classified by the Arnaud pressure profile. The peaked pressure profile of relaxed cool-core clusters is clearly reproduced in the ALMA 100 GHz cleaned image when compared to the universal and morphologically disturbed cases. The advantage of adding ACA 100 GHz and SZA 30 GHz data to the ALMA/ACA Band 1 mock observations is clearly illustrated in the increased SNR of the joint 30 GHz feathered images (Fig. 7.9). Since, for the upcoming surveys, one will specifically be interested in how well low-mass clusters can be imaged at high resolution via SZ, the integrated flux as a function of integration circular aperture radius was computed for ALMA 100 GHz as well as for feathered ALMA(Band 3)/ACA(Band 3)/SZA and ALMA(Band 1+3)/ACA(Band 1+3)/SZA mock observations using the mass test case $M = 2.0 \times 10^{14} M_{\odot}$ (Fig. 7.12). From the images in appendix B, one can already deduce that the respective per beam significance is relatively low. The integrated flux as a function of flux integration aperture radius does however give insight into the overall recoverable signal as a function of scale. The noise within a given aperture radius was computed from the corresponding 1σ region of 70 noise-only simulations, depicted in Fig. 7.10 and Fig. 7.11 for the ALMA 100 GHz and feathered SZA$(0 - 2\mathrm{k}\lambda)$/ALMA/ACA cases. Such noise realizations were necessary in order to account for the decrease in sensitivity as a function of the distance away from the pointing centre caused by the primary beam correction after the cleaning process for each instrument/frequency map.

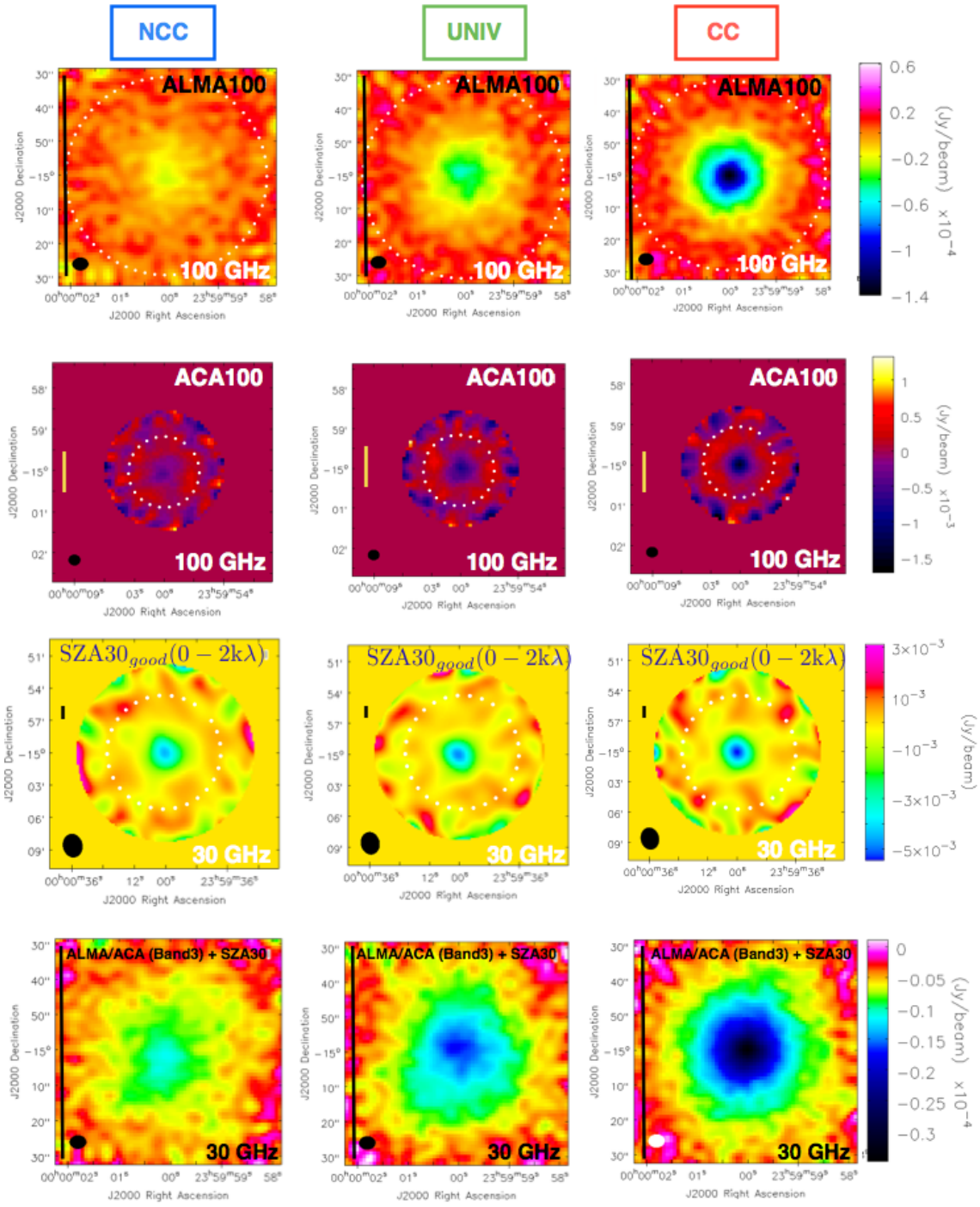

Figure 7.8: NCC/UNIV/CC cleaned images for different Arnaud pressure profile morphological states for a cluster of mass $M_{500} = 8.0 \times 10^{14} M_{\odot}$ at $z = 0.8$. The feathered ALMA/ACA(Band3)+SZA images are for the (0-2kλ) tapered SZA combination case. The vertical line denotes a 1' scale and the size of the FWHM is illustrated via the dashed white circle.

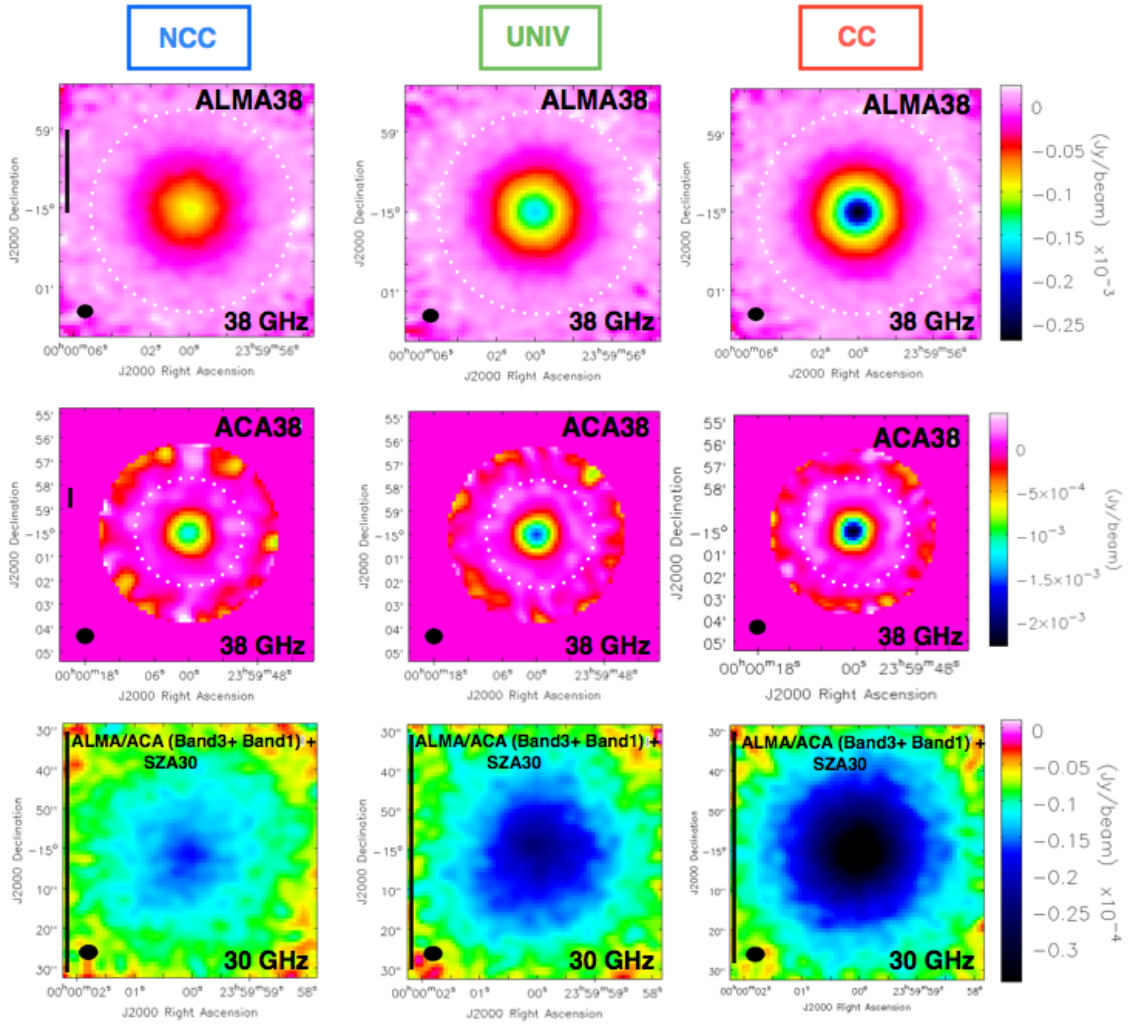

Figure 7.9: NCC/UNIV/CC cleaned images for different Arnaud pressure profile morphological states for a cluster of mass $M_{500} = 8.0 \times 10^{14} M_{\odot}$ at $z = 0.8$. The feathered ALMA/ACA(Band3)+ALMA/ACA(Band1)+SZA images are for the (0-2kλ) tapered SZA combination case. The colour scale in the feathered image is the same as that in Fig. 7.8. The vertical line denotes a 1' scale and the size of the FWHM is illustrated via the dashed white circle.

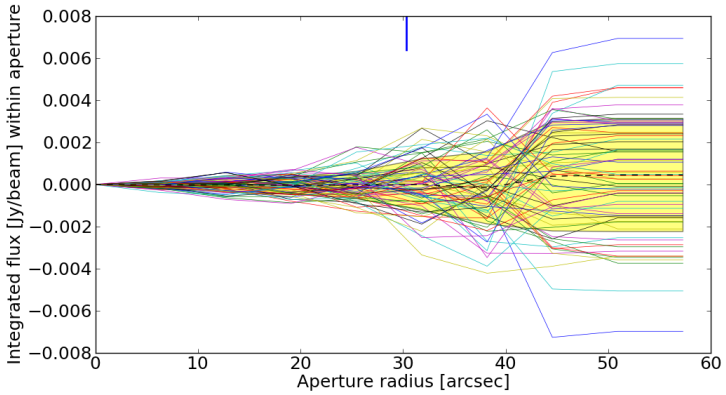

Figure 7.10: The noise on the aperture integrated flux as a function of aperture radius for 70 ALMA 100 GHz noise-only simulations. The vertical line denotes an aperture radius corresponding to half the FWHM and the yellow region corresponds to 1σ.

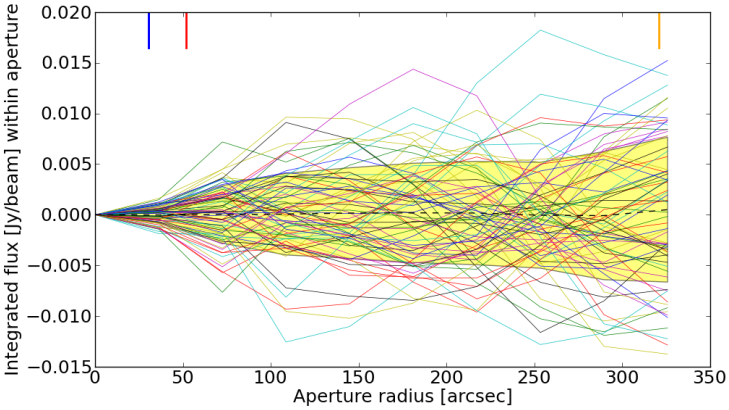

Figure 7.11: The noise on the aperture integrated flux as a function of aperture radius for feathered ALMA/ACA 100 GHz and SZA noise-only simulations. The vertical lines denote an aperture radius corresponding to half the FWHM of ALMA Band 3 (blue), ACA Band 3 (red) and SZA(30 GHz) (orange). The yellow region corresponds to 1σ.

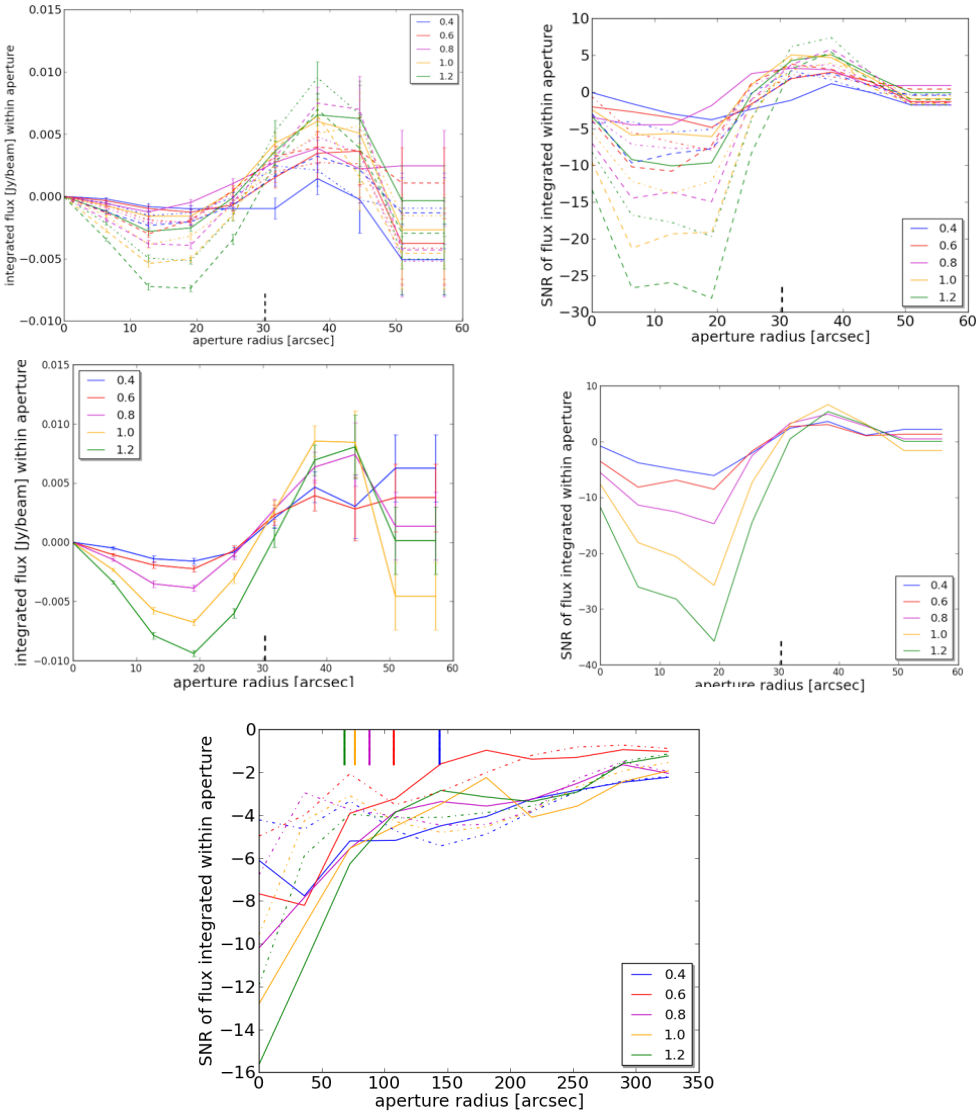

Figure 7.12: The aperture integrated flux/SNR as a function of aperture radius for different redshifts and morphological states. *Top left*: Integrated aperture flux at varying redshift for a CC (dashed), UNIV (dot-dashed) and NCC (solid) profile $M_{500} = 2.0 \times 10^{14} M_{\odot}$ cluster in an ALMA 100 GHz only mock observation. *Top right*: As in (top left) but plotted as the SNR. *Middle left*: Integrated aperture flux at varying redshift for a NCC (solid) profile $M_{500} = 5.0 \times 10^{14} M_{\odot}$ cluster in an ALMA 100 GHz only mock observation. *Middle right*: As in (middel left) but plotted as the SNR. *Bottom*: SNR of the integrated aperture flux for a feathered ALMA/ACA/SZA(tapered) mock observations with (solid) and without (dashed-dot) ALMA/ACA Band 1 for a CC $M_{500} = 2.0 \times 10^{14} M_{\odot}$ cluster. The black dashed line denotes the aperture radius corresponding to half FWHM and the coloured vertical lines represent the respective r_{500} values. The corresponding redshifts are denoted in the legend.

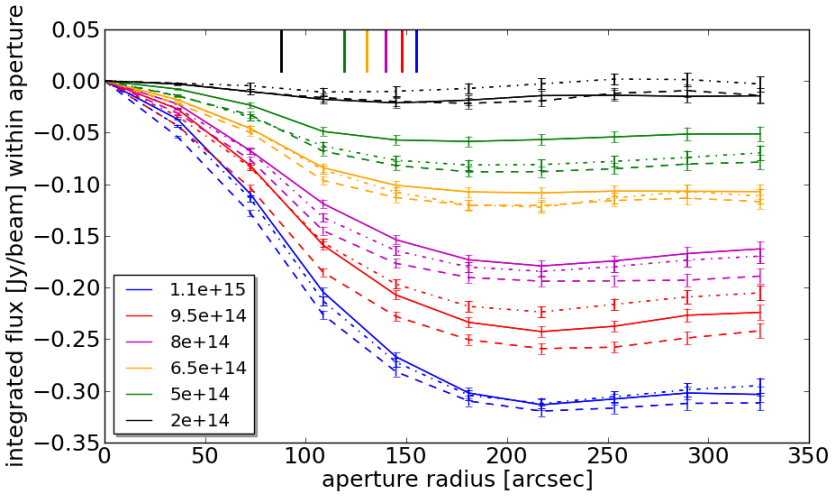

Figure 7.13: The aperture integrated flux as a function of aperture radius at redshift $z = 0.8$ for different masses as well as CC (dashed), NCC (solid) and UNIV (dot-dashed) profiles for feathered ALMA/ACA (Band3) + SZA mock observations. The coloured vertical lines represent the respective r_{500} values. The corresponding M_{500} masses are denoted in the legend in units of $M_{\odot}$.

The flux integrated within an aperture as a function of aperture radius gives an indication into how well low-mass clusters, of the order of $M_{500} = 2.0 - 5.0 \times M_{\odot}$ can be mapped. As can be deduced from Fig. 7.12, the detection of $M_{500} = 2.0 \times 10^{14} M_{\odot}$ clusters is not very significant for UNIV/NCC clusters at redshifts of 0.4 and 0.6. The detection significance can greately be improved by the addition of joint ACA 100 GHz and SZA observations (Fig. 7.12 (bottom)), the addition of ALMA/ACA Band 1 improving the central SNR by a factor of 1.5 for the CC $M_{500} = 2.0 \times 10^{14} M_{\odot}$ redshift 0.4 cluster case, though it should be noted that these values are for single simulations. A multi-simulation study would have been computationally time expensive and was thus not performed.

The integrated aperture flux as a function of aperture radius for varying masses and profiles at a given redshift is illustrated in Fig. 7.13 for feathered ALMA/ACA (Band3) + SZA observations. One can clearly observe the convergence of the integrated flux at large radii, stressing that the feathering reduces effects of left-over positive sidelobes after the cleaning process, that are visible in the ALMA 100 GHz aperture radius graphs in Fig. 7.12.

7.6 Mock Bayesian MCMC fitting analysis

Tough the previous analyses illustrate the detection significance as a function of the integrated flux within an aperture radius, they do not probe the pressure profile slope parameter degeneracies, whose inspection is vital if one is to claim that the combined ALMA/ACA/SZA arrays, under attainable and realistic observing conditions, have the potential for distinguishing relaxed from morphologically disturbed clusters through their characteristic radial pressure distributions.

Hence, I developed a multi-array Bayesian MCMC visibility code - a visibility fitting approach that has been used in literature (Bonamente et al. 2004, 2006) but is not included for models beyond simple gaussians or disks in the MIRIAD software, thus necessitating a new code development. The declination range, on-source integration times as well as the observing conditions were chosen to be the same as in section 7.4.2 under the assumption of MS0451-like weather conditions for the SZA.

In addition, in order to avoid parameter space exploration in regions giving rise to unrealistic ICM thermal energy contents, slope parameter box priors were set to be non-zero over the regions (P_0>0, c_{500}>0, a>0, 0<c<3.0).

The SZA cannot constrain the pressure profile shape parameter beyond the scale radius, b, due to the combined effect of primary beam tapering and the relatively scarce uv-coverage at small baselines, particularly with regard to the chosen low declination. Such large-scale information can only be obtained from Planck observations (Planck collaboration Intermediate results V).

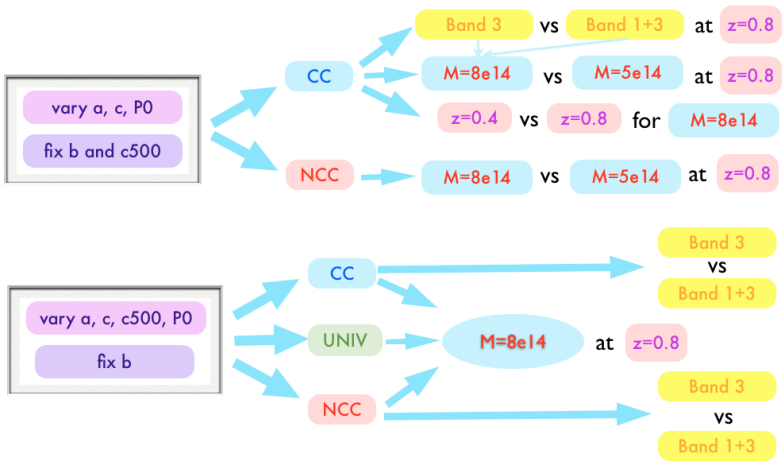

Figure 7.14: MCMC sketch outlining the explored mass/redshift/morphology/instrument combinations. The masses correspond to M_{500} and are given in units of $M_{\odot}$.

Effect of mass on a high-redshift, non-relaxed cluster mock observation

In order to assess the ability to recover the central and middle slopes as well as the normalization parameter as a function of mass for a given morphologically-disturbed cluster profile, two MCMC visibility fits for clusters of mass $M_{500} = 8.0 \times 10^{14} M_{\odot}$ and $M_{500} = 5.0 \times 10^{14} M_{\odot}$, both at redshift $z = 0.8$, were made.

The 2D-Likelihoods of the two mass cases are consistent with each other within 1σ, Fig. 7.15, and the 68% confidence interval in the marginalized posterior parameter distributions, Fig. 7.16, encompass the input parameter values. Multiple simulation runs would allow this result to be generalized. The elongated shapes of the accepted parameter spaces illustrates the considerable parameter degeneracy. Though it is expected that high-mass clusters allow for tighter parameter space constraints, this is the first time that this has been quantitatively shown via a Bayesian MCMC visibility fitting example case for joint high-resolution ALMA/ACA and SZA mock observations.

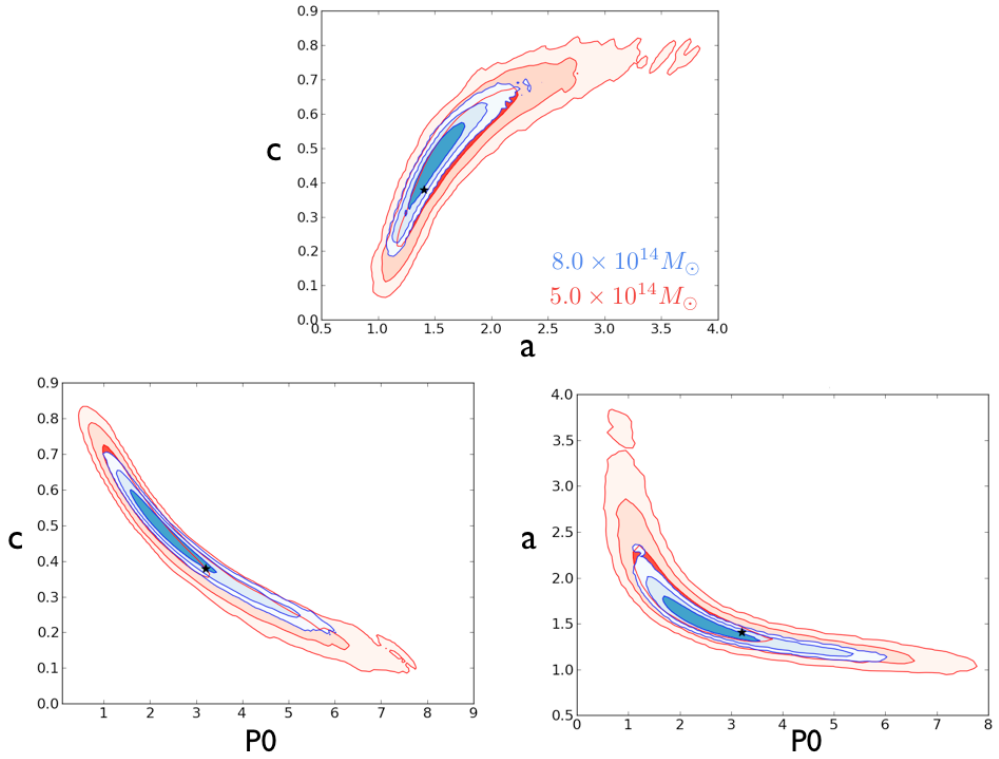

Figure 7.15: The effect of mass on a $z = 0.8$ NCC cluster for fixed c_{500} and b with $M_{500} = 8.0 \times 10^{14} M_{\odot}$ (blue) and $M_{500} = 5.0 \times 10^{14} M_{\odot}$ (red). The contours illustrate the 68.3 %, 95.5 % and 99.7% confidence levels. The stars indicate the expected values.

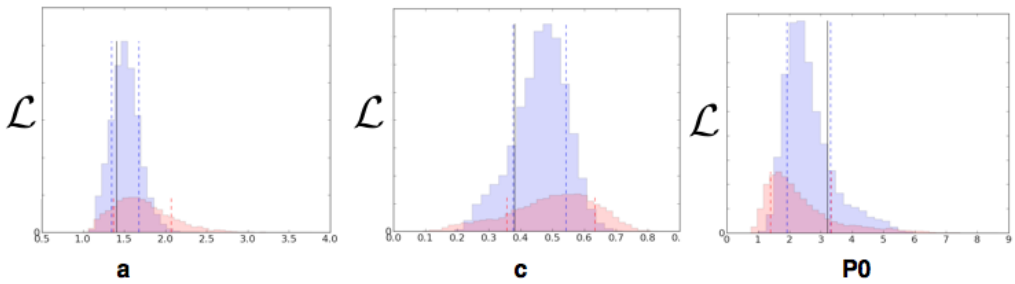

Figure 7.16: Marginal distributions of the sampling parameters for $M_{500} = 8.0 \times 10^{14} M_{\odot}$ (blue) and $M_{500} = 5.0 \times 10^{14} M_{\odot}$ (red). The dashed lines illustrate the 68% confidence levels. The black vertical line denotes the input values given by the best-fit NCC Arnaud model.

Effect of mass on a high-redshift relaxed cluster mock observation analysis

In order to assess how the aforementioned morphologically disturbed cluster 2D-parameter likelihood mass dependence compares to an equivalent investigation for the Arnaud cool-core cluster pressure profile, these fits were performed for relaxed clusters of mass $M_{500} = 8.0 \times 10^{14} M_{\odot}$ and $M_{500} = 5.0 \times 10^{14} M_{\odot}$, both at redshift $z = 0.8$.

The degree to which the 2D-Likelihood acceptable parameter space is constraint is higher for the CC than for the NCC case, Fig. 7.17. The scale radius is slightly different for the two cases due to the different c_{500} parameters (for $M_{500} = 8.0 \times 10^{14} M_{\odot}$: $r_p(CC) = 124''$ and $r_p(NCC) = 129''$ and for $M_{500} = 5.0 \times 10^{14} M_{\odot}$: $r_p(CC) = 106''$ and $r_p(NCC) = 110''$). In comparison with the SZA beam, this difference is however small, such that the above claim still holds. The high-mass case recovers the parameters within 1σ, whereas the $M_{500} = 5.0 \times 10^{14} M_{\odot}$ case 1σ contours do not coincide with the actual parameters, which is also illustrated in the marginalized parameter distribution plot in Fig. 7.18. This is mainly linked to the expected variance caused by the fact that only single simulations for each studied case are run.

Ideally, one would need to run several simulations, each with different noise realizations to ensure the statistical significance of this claim.

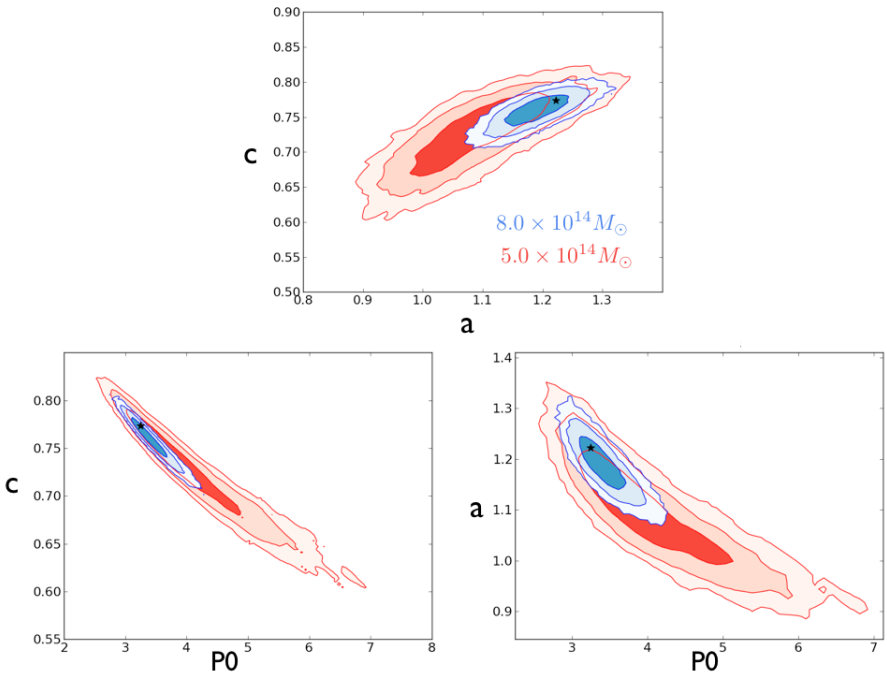

Figure 7.17: The effect of mass on a $z = 0.8$ CC cluster for fixed c_{500} and b with $M_{500} = 8.0 \times 10^{14} M_{\odot}$ (blue) and $M_{500} = 5.0 \times 10^{14} M_{\odot}$ (red). The contours illustrate the 68.3 %, 95.5 % and 99.7% confidence levels. The stars indicate the expected values.

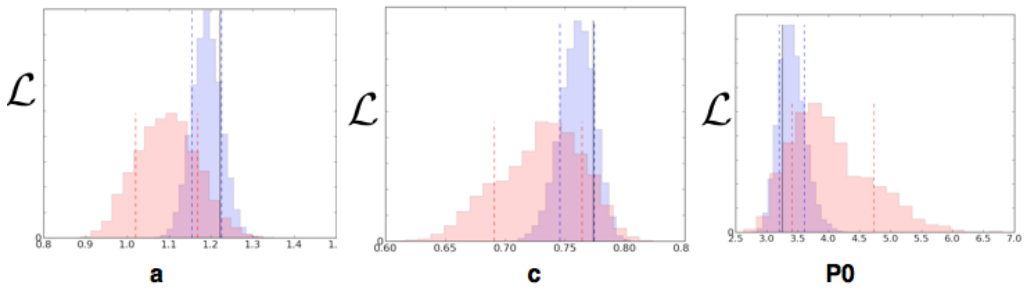

Figure 7.18: Marginal distributions of the sampling parameters for $M_{500} = 8.0 \times 10^{14} M_{\odot}$ (blue) and $M_{500} = 5.0 \times 10^{14} M_{\odot}$ (red). The dashed lines illustrate the 68% confidence levels. The black vertical line denotes the input values given by the best-fit CC Arnaud model.

Effect of redshift on a high-mass relaxed cluster mock observation

For a given mass and morphological state, the angular size of a cluster will evolve as a function of redshift according to the angular diameter distance relation. One needs to stress though, that this redshift comparison underlies the assumption of the universality of the Arnaud pressure profiles alongside with a self-similar evolution. Hence for a given instrumental sampling function, different physical scales will be probed if a given cluster shape is observed at different redshifts. The quantiative effect on the slope and normalization accepted parameter space for a cool-core $M_{500} = 8.0 \times 10^{14} M_{\odot}$ cluster is illustrated in Fig. 7.19 for redshifts $z = 0.4$ and $z = 0.8$.

Both the high and low redshift fits are consistent within 1σ, the higher redshift cluster offering tighter constraints on the accepted parameter space, as can be seen in the marginalized parameter distribution in Fig. 7.20.

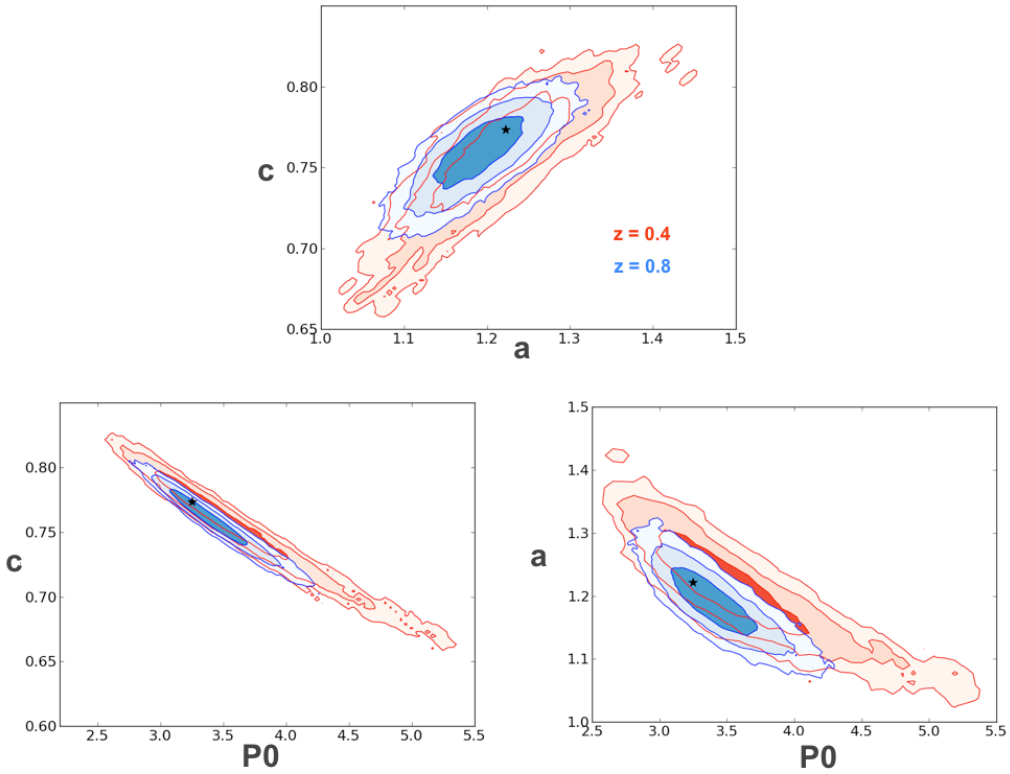

Figure 7.19: The effect of redshift on a $M_{500} = 8.0 \times 10^{14} M_{\odot}$ CC cluster for $z = 0.8$ (blue) and $z = 0.4$ (red). The contours illustrate the 68.3 %, 95.5 % and 99.7% confidence levels. The stars indicate the expected values.

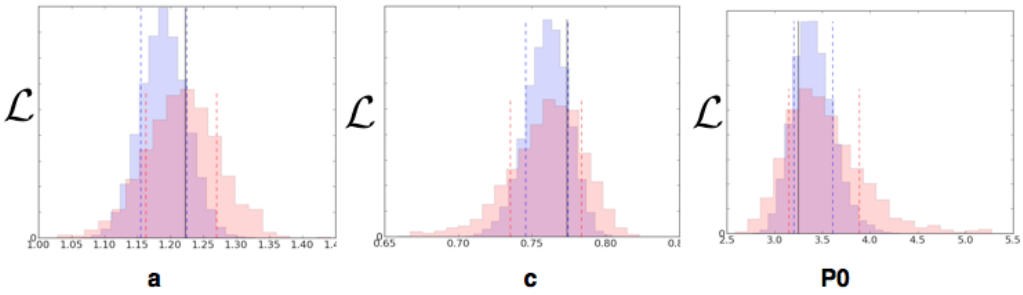

Figure 7.20: Marginal distributions of the sampling parameters for $z = 0.8$ (blue) and $z = 0.4$ (red). The dashed lines illustrate the 68% confidence levels. The black vertical line denotes the input values given by the best-fit Arnaud models.

ALMA/ACA Band 1: a high-redshift, high mass relaxed cluster mock study

The input model comprises a mass, $M_{500} = 8.0 \times 10^{14} M_{\odot}$, redshift $z = 0.8$ mock observation of a cool-core cluster and therefore represents a cluster in the redshift range beyond which classic cool-cores are thought to become rare events. It therefore represents an ideal case for joint ALMA/ACA Band 1+ Band 3 and 30 GHz SZA observations as the signal strength in the central cluster region designates the best single cluster study case.

In light of current ALMA/ACA proposal oversubscription rates, one might imagine choosing such a real cluster case for a pilot study in order to observationally confirm ALMA/ACA's suitability for high-resolution cluster studies and to promote future less favourable cases at lower redshift, lower mass and/or with a higher degree of ICM disturbance.

As one can see in Figs. 7.21 and 7.22, the degree to which ALMA/ACA Band 1 can add information to joint ALMA/ACA Band 3 and 30 GHz SZA mock observations is considerable, therefore facilitating a more precise inference on the cluster parameter slopes and normalization in this particular simulation on account of a combined effect of improved uv-coverage and sensitivity. If computation time allows, more simulations, each with different noise realizations, are planned in order to strengthen this case as well as to quantify the relative contribution of sensitivity and uv-coverage to the accepted parameter space constraints.

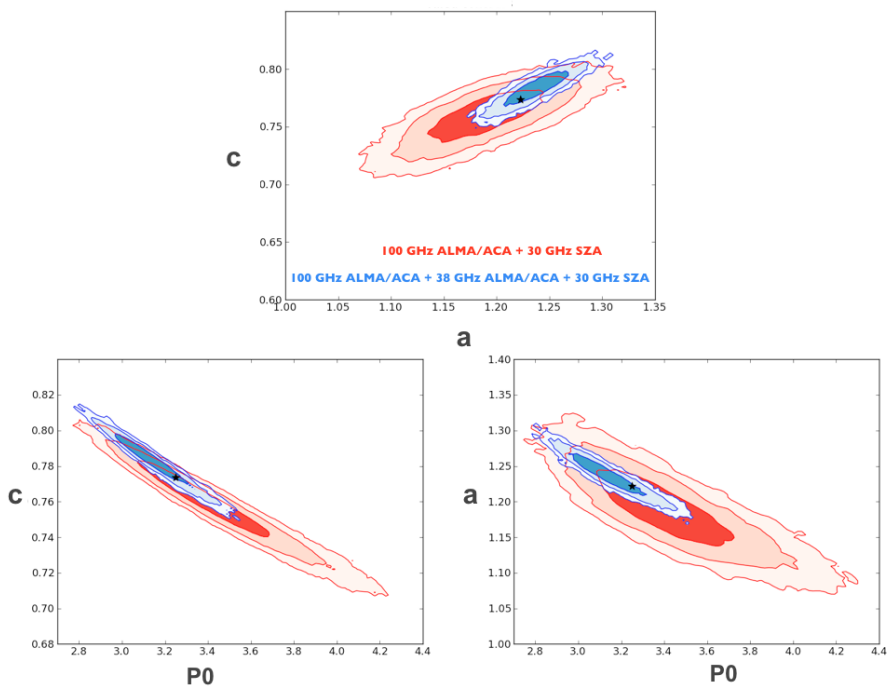

Figure 7.21: The effect of supplementary ALMA/ACA Band 1 mock observations (blue) on a CC $M_{500} = 8.0 \times 10^{14} M_{\odot}$ cluster at redshift $z = 0.8$ compared to mere ALMA/ACA Band3 + 30 GHz SZA (red). The contours illustrate the 68.3 %, 95.5 % and 99.7% confidence levels. The stars indicate the expected values.

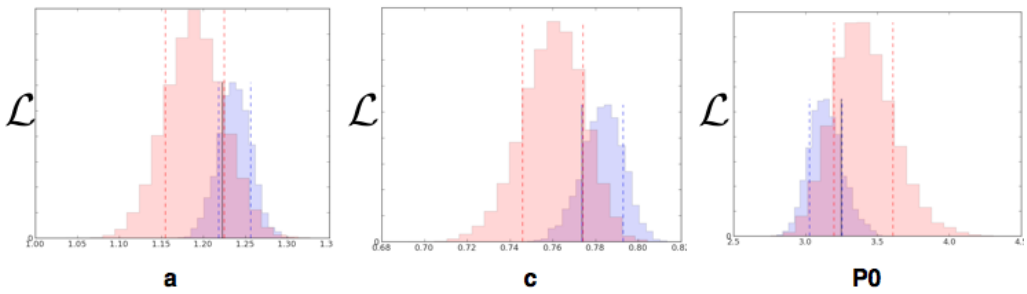

Figure 7.22: Marginal distributions of the sampling parameters for supplementary ALMA/ACA Band 1 mock observations (blue) and ALMA/ACA Band3 + 30 GHz SZA (red). The dashed lines illustrate the 68% confidence levels. The black vertical line denotes the input values given by the best-fit CC Arnaud model.

Can cool-core, universal and non-cool core pressure profiles be distinguished with interferometric observations ?

In order to assess whether ALMA/ACA Band 3 + 30 GHz SZA observations have the potential to distinguish cool-core from non-cool core galaxy clusters, the aforementioned analysis is not sufficient as c_{500} is kept fixed. The outer slope parameter, b, is almost exactly the same for all three Arnaud pressure profiles (CC: 5.49, UNIV: 5.4905, NCC: 5.49) and cannot be determined via SZA observations. For real observations, Planck will greatly contribute in fitting for this parameter.

I ran an example case with c_{500} as a free parameter in order to illustrate that CC,UNIV and NCC pressure profiles can indeed be distinguished via joint 30 GHz SZA + ALMA/ACA Band 3 mock observations. A high-mass, high-redshift cluster was chosen at $M_{500} = 8.0 \times 10^{14} M_{\odot}$ and $z = 0.8$ (Fig. 7.23). This simulation specifically addresses the need for a pressure-profile based Sunyaev-Zel'dovich morphological state indicator for high-redshift galaxy clusters. As one can see in Fig. 7.23 the CC profiles can best be distinguished from the NCC/UNIV cases in the 2D $[c, P_0]$, $[c, c_{500}]$ and $[c, a]$ likelihood spaces. Comparing the respective expected c values, one could have expected this result from mere considerations of the difference in the expected c parameters of CC,UNIV and NCC profiles. However, as can be seen in the $[a, c_{500}]$ accepted parameter space, uncertainties in the measurement can lead to significant overlap in the 2D likelihood regions, thus stressing the need for a quantitative illustration. NCC and UNIV profiles are best distinguished via examination of the $[c, P_0]$ and $[c_{500}, P_0]$ accepted likelihood spaces. The corresponding marginalized posterior parameter distributions are given in Fig. 7.24.

Removing the delta priors on all pressure profile parameters except for the outer slope parameter, b, for the single-cluster study of cool-core and non-cool core ($M = 8.0 \times 10^{14} M_{\odot}$, $z = 0.8$) clusters, one can extend the above analysis by investigating the effect of joint ALMA/ACA (Band 1 + Band3) and 30 GHz SZA observations.

In the NCC case, Fig. 7.25, the elongated shapes in the 2D-Likelihood parameter spaces clearly illustrate the degeneracy of the parameters, the free c_{500} leading to a broadening of the overall contours. It can also be seen that the mock simulated observations containing ALMA/ACA Band 3 and those with additional ALMA/ACA Band 1 information are consistent within 1σ and also recover the best-fit parameters within 1σ. The biggest improvement in the parameter region constraints for joint BAND 1 + BAND 3 observations is seen for the parameters a and c_{500}, which is expected as the ALMA/ACA Band 1 observations add uv-coverage at scales comparable to the scale radius. This effect is also observed in the CC case, Fig. 7.27, which, as in the case of Fig. 7.16, offers tighter constraints on the 2D accepted parameter spaces than the NCC case, though the marginalized posterior parameter distributions, Fig. 7.28, of the Band 1-included simulation do not recover the parameters to within 1σ. This is most likely due to a high-noise realization used in this mock-simulation, though multiple MCMC runs on simulations with different noise should be run in order to test this claim, which I did not pursue in this investigation for computing reasons, though it should be stressed that a future investigation on this issue is forseen.

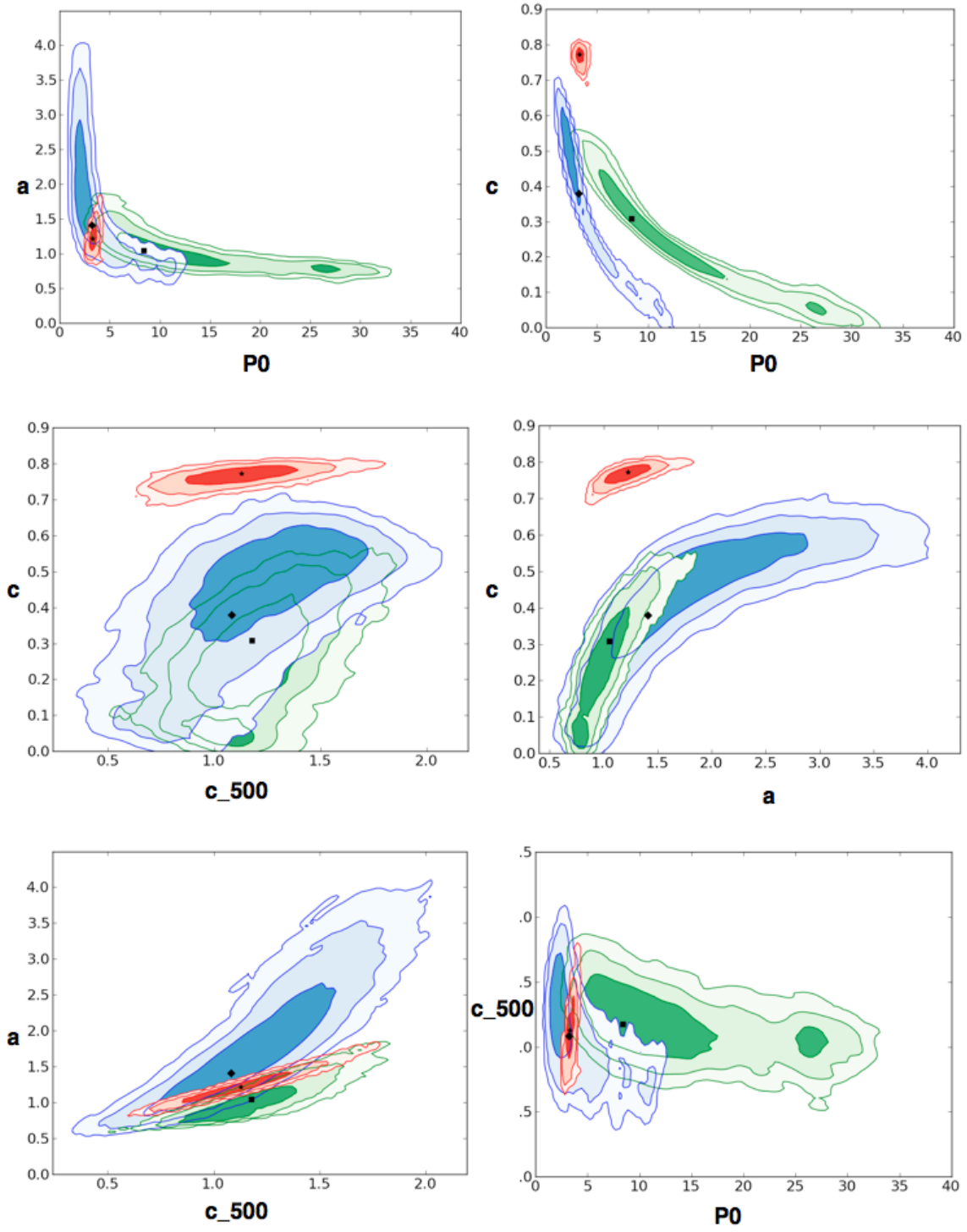

Figure 7.23: A graph to illustrate the ability of joint ALMA/ACA (Band3) + 30 GHz SZA observations to distinguish universal (green), CC (red), NCC (blue) cluster pressure profiles for $M_{500} = 8.0 \times 10^{14} M_{\odot}$ at $z = 0.8$. The contours illustrate the 68.3 %, 95.5 % and 99.7% confidence levels. The expected values are denoted by a star (CC), square (UNIV) and diamond (NCC).

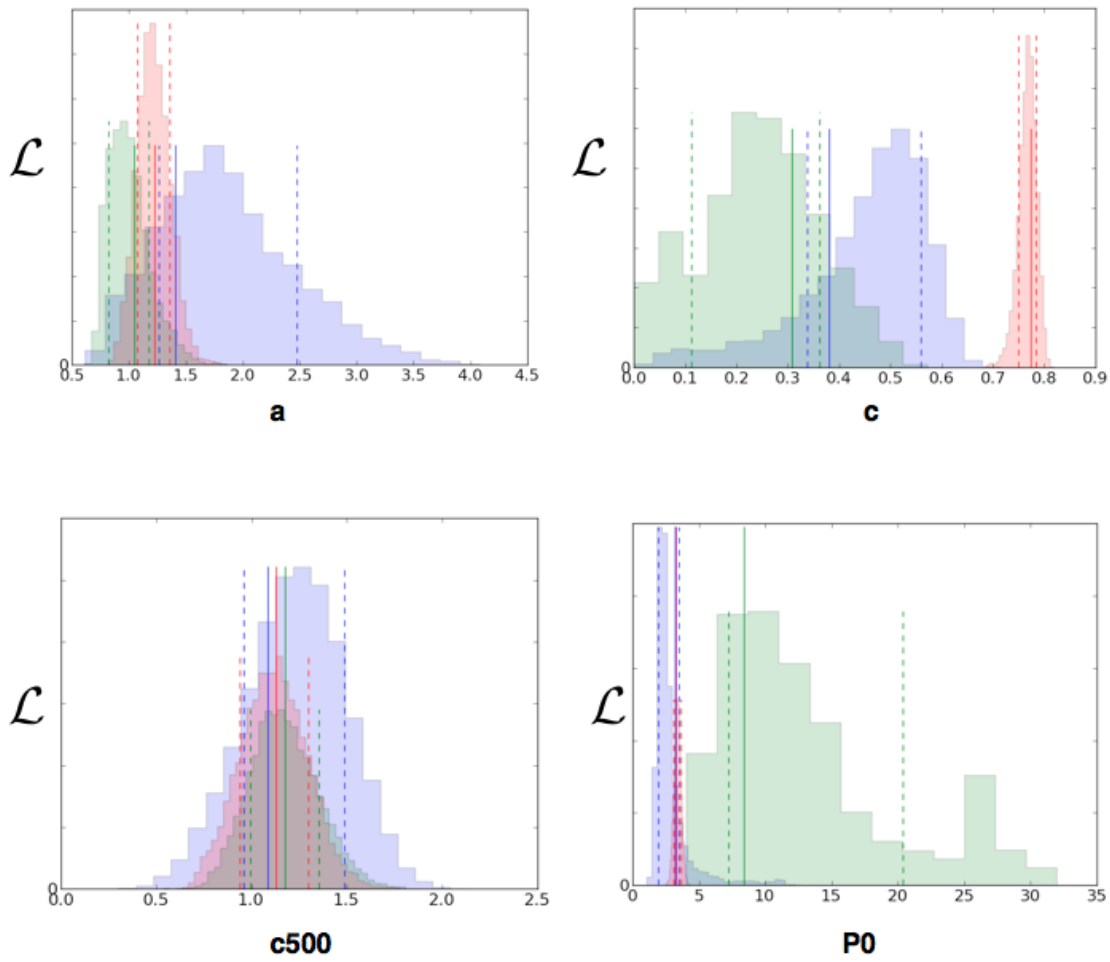

Figure 7.24: Marginal distributions of the sampling parameters for universal UNIV (green), CC (red), NCC (blue) cluster pressure profiles for $M_{500} = 8.0 \times 10^{14} M_{\odot}$ at $z = 0.8$. The coloured dashed lines illustrate the respective 68% confidence levels. The coloured solid vertical lines denote the input values given by the best-fit Arnaud models.

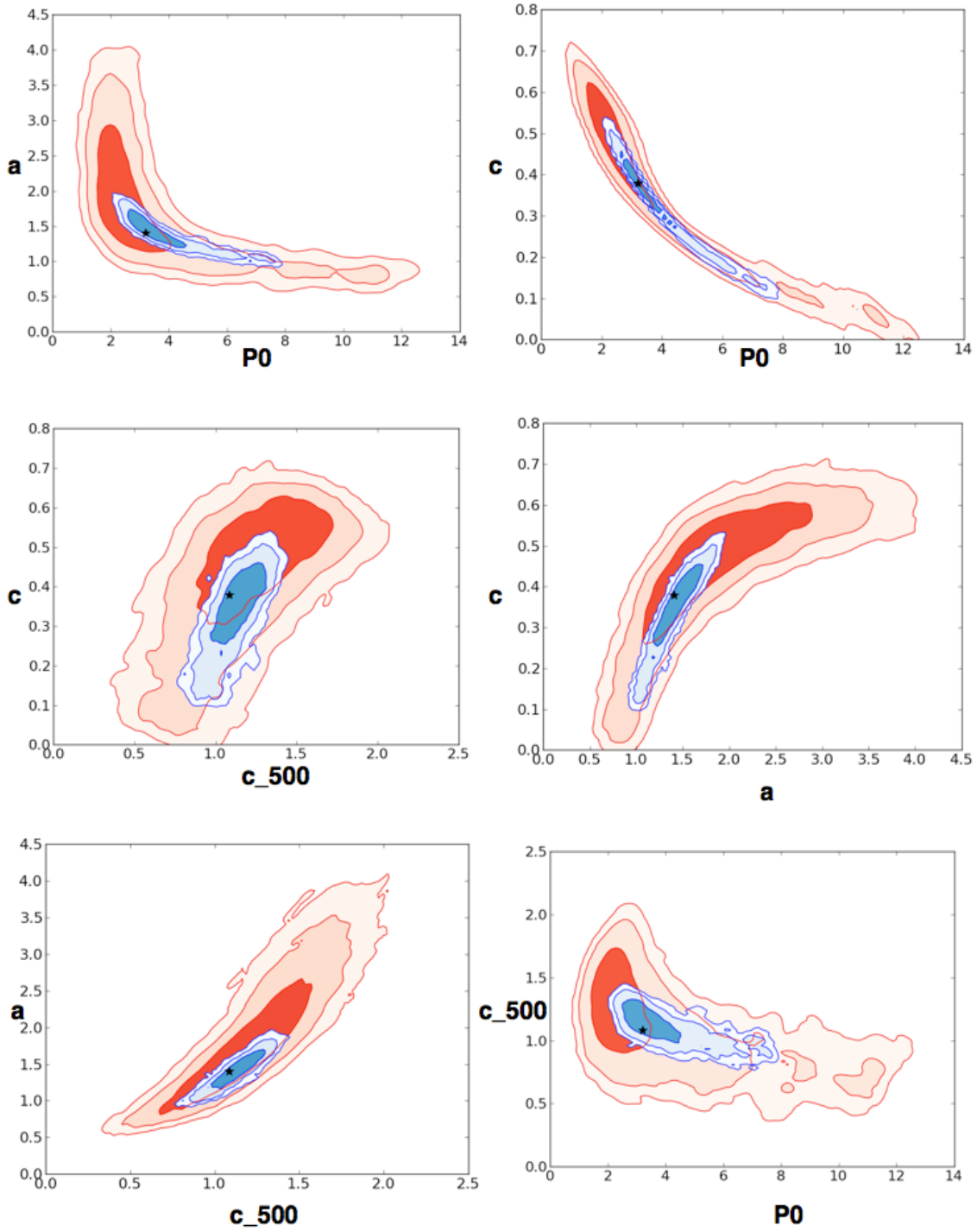

Figure 7.25: The effect of supplementary ALMA/ACA Band 1 (blue) observations for a $M_{500} = 8.0 \times 10^{14} M_{\odot}$ NCC cluster at $z = 0.8$ compared to mere ALMA/ACA Band3 + SZA (red). The contours illustrate the 68.3 %, 95.5 % and 99.7% confidence levels. The expected values are denoted by stars.

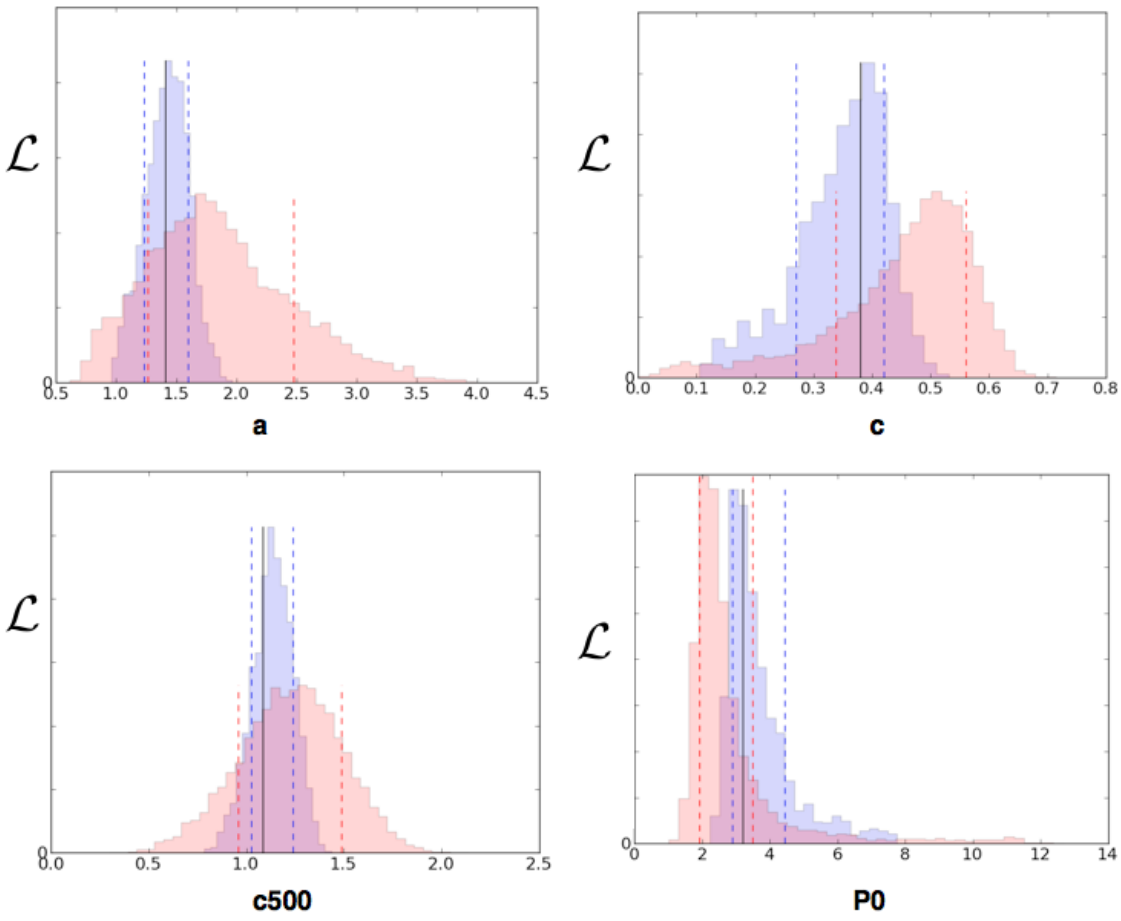

Figure 7.26: Marginal distributions of the sampling parameters for supplementary ALMA/ACA Band 1 mock observations (blue) and ALMA/ACA Band3 + SZA (red) for the NCC cluster case. The dashed lines illustrate the 68% confidence levels. The black vertical line denotes the input values given by the best-fit NCC Arnaud model.

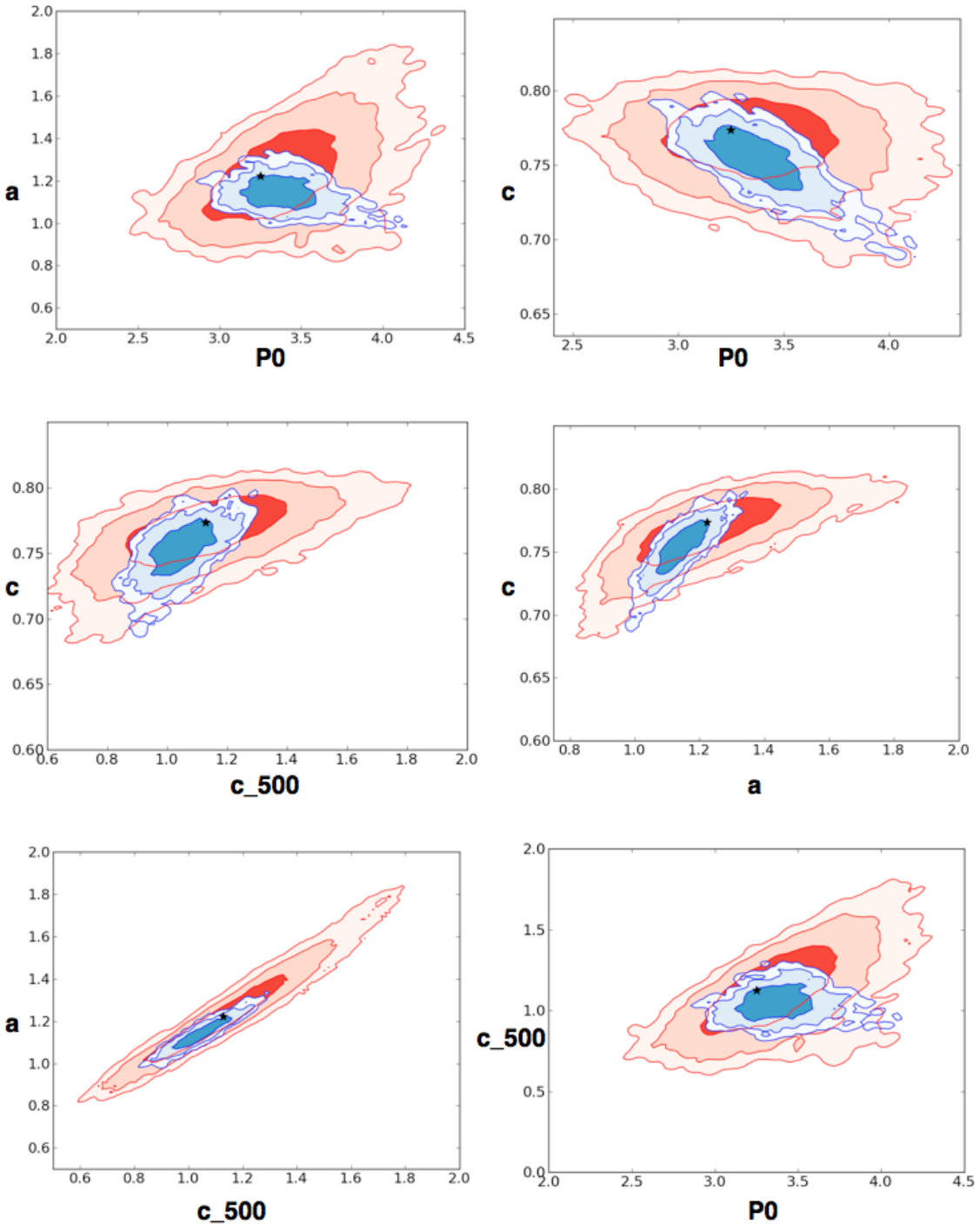

Figure 7.27: The effect of supplementary ALMA/ACA Band 1 (blue) observations for a $M_{500} = 8.0 \times 10^{14} M_{\odot}$ CC cluster at $z = 0.8$ compared to mere ALMA/ACA Band3 + SZA (red). The contours illustrate the 68.3 %, 95.5 % and 99.7% confidence levels. The expected values are denoted by stars.

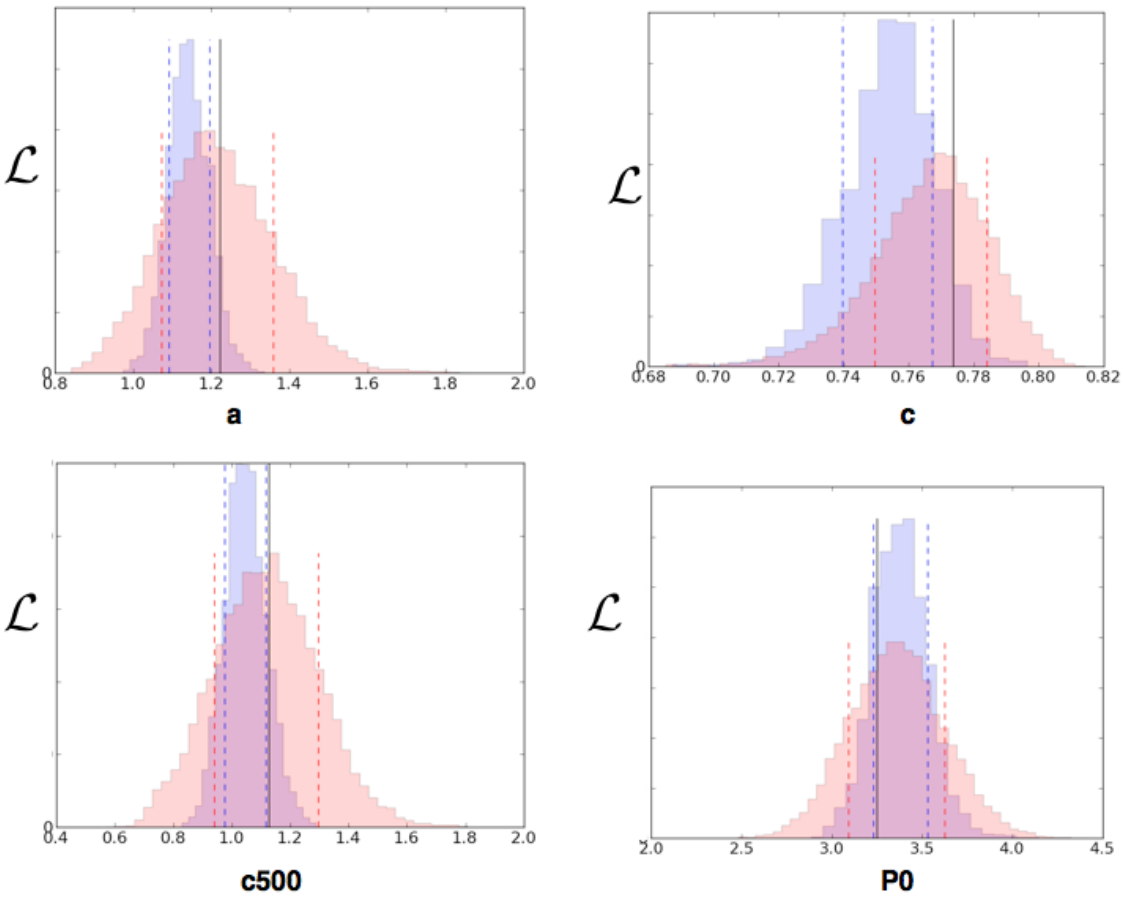

Figure 7.28: Marginal distributions of the sampling parameters for supplementary ALMA/ACA Band 1 mock observations (blue) and ALMA/ACA Band3 + SZA (red) for the CC cluster case. The dashed lines illustrate the 68% confidence levels. The black vertical line denotes the input values given by the best-fit CC Arnaud model.

7.7 A very high redshift galaxy cluster at $z = 1.49$

At redshifts >1.2, the universal Arnaud profile is unlikely to be a realistic and accurate representation of galaxy clusters' median pressure profiles. Hence, the JobRunner by K. Dolag was used to simulate an ALMA 100 GHz observation of such a realistic cluster case [2]. The cluster choice was tailored towards shock detection features at this high redshift.

Out of the 10 cluster high-resolution re-simulations (Dolag et al. 2009), the cluster g51a exhibits a distinct pressure structure at a redshift of 1.49 under csf (weak winds) conditions (Fig. 7.29). It has a mass of $M_{500} = 11.16 \times 10^{14} M_{\odot}$ at $z = 0$ and thus represents a massive cluster.

Simulations were preformed for 3,6 and 9 hrs on-source integration times using ALMA and the corresponding cleaned maps are displayed in Fig. 7.30. The cluster was placed at a declination of -20 deg in order to provide the best-possible uv-coverage, while avoiding pointing directly at the zenith.

It can clearly be seen that ALMA full array Band 3 imaging is ideal for detecting shock structures within the core regions of massive clusters. The tip of the pressure discontinuity, labeled in Fig. 7.29 via the white box, can be recovered via 3, 6 and 9 hrs on-source integration time to a SNR of 17, 28 and 32 respectively. In a real observation, the ACA would need to be included in order to image the more extended scales such as to facilitate shock modeling - an issue that is further discussed in chapter 8.

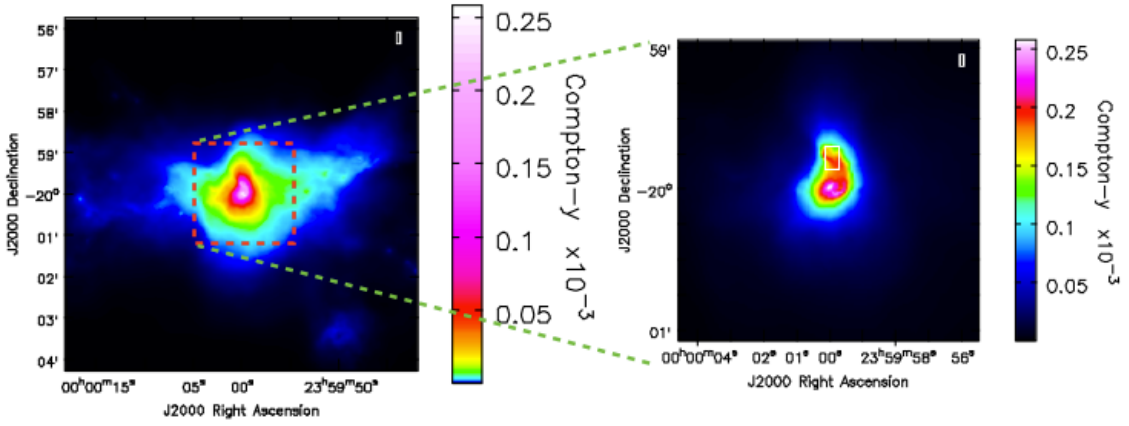

Figure 7.29: The g51a input Compton-y map with a zoomed in image (right) displaying the box (white) in which the SNR is computed for Fig. 7.30

[2] The JobRunner web application was constructed by Laurent Bourges and Gerard Lemson as part of the activities of the German Astrophysical Virtual Observatory.

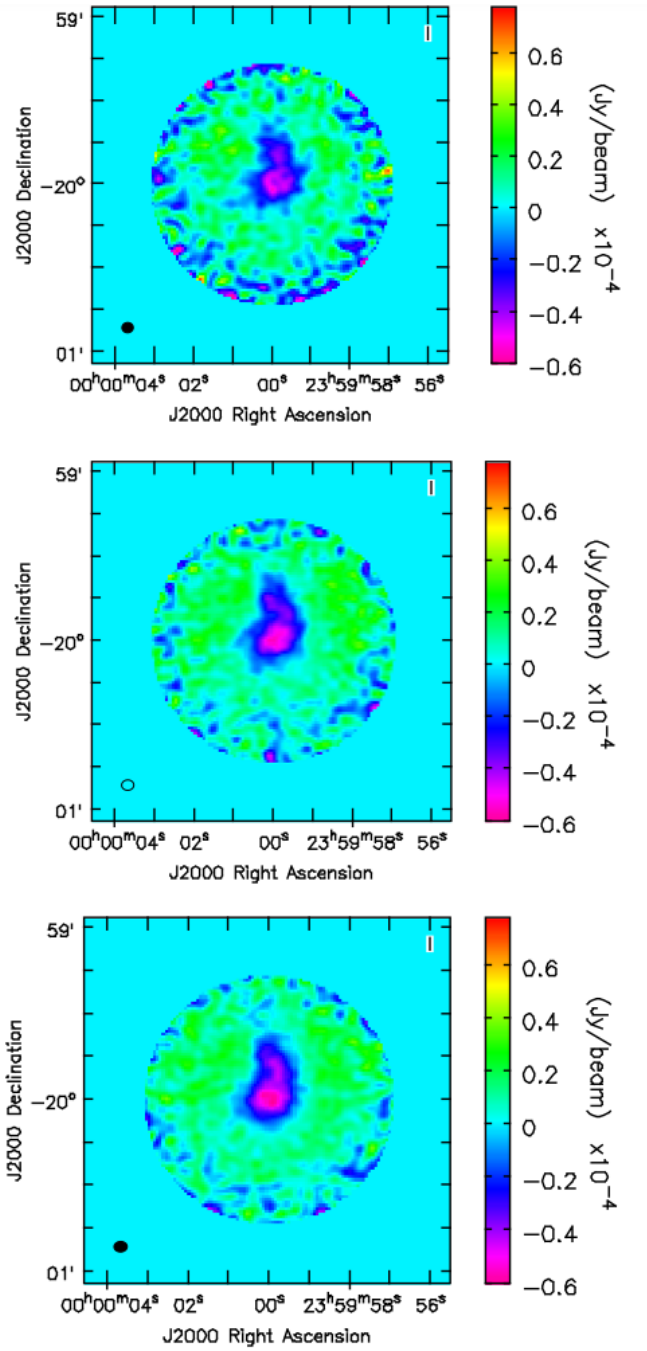

Figure 7.30: ALMA 100 GHz observations for 3 hrs (top), 6 hrs (middle) and 9 hrs (bottom) on-source observation time under realistic noise conditions.

7.8 Future promise for ALMA/ACA/CCAT observations

In light that future CCAT observations will be complemented by high-resolution ALMA/ACA Band 3 observations to obtain SZ images spanning a wide range of angular scales to probe the entire cluster pressure profiles, the uv-coverage is illustrated below in Fig. 7.31.

The lower uv-distance edge of the CCAT mock observations, and thus the maximum recoverable scale, depends on a combination of instrumental noise characteristics, point source removal efficiencies as well as on map coverage.

The spatial extent of significant galaxy cluster mapping would require detailed CCAT simulations taking all the above-mentioned factors into account, which is beyond the scope of this thesis. Hence, the leftmost edge in the uv-plane, and subsequently the maximum spatial scale, merely serves as an indication for CCAT capabilities.

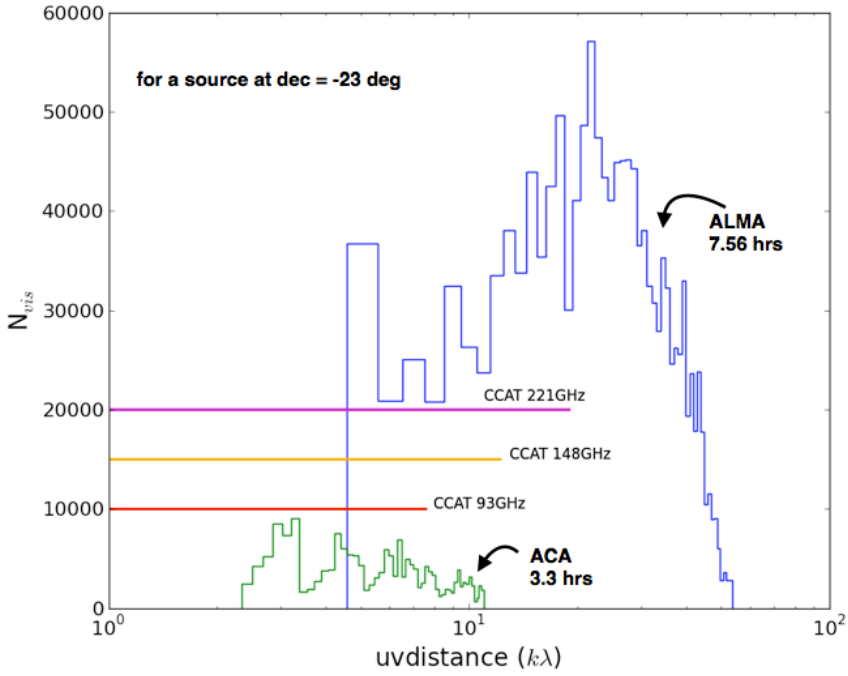

Figure 7.31: The uv-coverage overlap between ALMA/ACA Band 3 and CCAT. Only unflagged visibilities are plotted. The vertical height of the CCAT ranges is arbitrary.

7.9 Conclusion

The reported results have quantitatively illustrated that joint 30 GHz SZA + (ALMA/ACA) Band 3 observations can indeed distinguish different morphological characteristic pressure profiles, denoted by the Arnaud pressure profiles in this analysis, within reasonable on-source integration times at high redshift for the simulations presented in this chapter.

In addition, the 2D-Likelihood parameter spaces as well as the marginalized parameter distributions have been examined for varying mass, redshift and morphology scenarios via a Bayesian MCMC Arnaud profile visibility fitting. The simulation set-ups exploit the complementarity of ALMA/ACA/SZA.

The advantage of having supplementary ALMA/ACA Band 1 information in such investigations has also been illustrated via two separate CC and NCC studies of a high redshift, $z = 0.8$, high-mass $M_{500} = 8.0 \times 10^{14} M_{\odot}$ galaxy cluster. Future reiterations of all simulations with different noise realizations will help to generalize the claims made from the particular test scenarios discussed in this chapter since they will improve the statistical significance of the results.

The suitability of mapping very high redshift galaxy clusters with realistic ALMA Band 3 observation times has been exemplified through mock observations of a cluster stemming from hydrodynamical simulations, which further included pressure discontinuity features - a topic that will be discussed in detail in the following chapter.

In view of future CCAT observations, these investigations shed a positive light on the feasibility of joint CCAT/ALMA/ACA observations that will help to constrain the pressure profiles of clusters over a wide mass and redshift range for a large number of X-ray detected clusters.

Such investigations will greatly contribute to the much needed study of morphologically-induced systematics in the scaling relations as a function of redshift and cluster mass in the near future. It has therefore been illustrated that resolving the structural features in the core regions of clusters is a realistic endeavour for future ALMA/ACA/SZA observations.

Chapter 8

Shocks in galaxy clusters

Galaxy cluster mergers are a direct consequence of hierarchical structure formation scenarios, which constitute the formation of massive halos from the merging processes of smaller mass systems. The collisional signatures as well as the probed astrophysical plasma regimes thus facilitate studies into the nature of dark matter as well as plasma electron-ion equilibration mechanisms.
Joint ALMA/ACA SZ observations are currently opening up a window for studying the intra-cluster medium shock fronts produced in such merger events with an unrivaled combination of high resolution and sensitivity. They are indispensable to current and future X-ray cluster shock front data, since pressure information is needed for disentangling geometric shock dependences.
The 'Bullet Cluster' of galaxies exhibits a textbook example of a bow-shock merger event and is thus a good candidate for a pathfinder experiment study exploiting high-resolution ALMA/ACA SZ. In order to illustrate the feasibility of such observations both, in terms of projected Mach cone mapping as well as in terms of deriving the mean post-shock electron temperature for a given shock geometric model, I present mock ALMA/ACA Cylce 2 simulations, which follow the approach of my submitted ALMA Cycle 2 proposal.

8.1 Motivation for galaxy cluster shock studies

Schocks in the intra-cluster medium represent prominent sites for plasma physics studies as they probe the nature of electron-ion equilibration during energy transfer of the merger's kinetic energy to thermal and non-thermal energy of the plasma (Sarazin 2002). Galaxy cluster shocks can occur in galaxy cluster outskirts due to gas filametary accretion (Plionis et al. 2002), in the central regions caused by AGN outflows (Kirkpatrick et al. 2011) as well as through major merger events.

Both, accretion shocks and small Mach number AGN-induced shocks do not have the necessary density contrast to be detected with current X-ray instruments over a wide redshift range. Not only do galaxy cluster merger shocks offer the opportunity to address potential gas/dark-matter offsets in dissociative mergers, but they also give insight into the attainable shock ICM temperatures. Merger activity is often indicated by wide-scale radio halo emission, whose edges have been shown to coincide with galaxy cluster shock features (Markevitch & Vikhlinin 2007).

From a shock modeling point of view, optimal geometric shock conditions comprise a single merger event that occurs near the plane of the sky since these factors provide the best framework for an accurate determination of the shock Mach number.

Shock fronts are characterized by a pressure jump that can easily be derived from the observed X-ray surface brightness discontinuity in conjunction with high-resolution spectral temperature information at low redshift. The necessary spectral information thus requires high X-ray number counts. The latter is needed in order to distinguish pressure-induced surface brightness discontinuities from so-called cold fronts. Cold fronts do not exhibit such pressure variations as they represent contact discontinuities which, in the case of mergers, often originate from a dense sub-cluster's motion through gas of different entropy (Markevitch & Vikhlinin 2007). In addition, the merger process must be captured in such an evolutionary state that the merger shock front has not moved too far out into the cluster periphery, the n_e^2 dependence of X-ray information hampering the ability to detect discontinuities in these low-density regions with respect to the background noise.

Sunyaev-Zel'dovich observations of shock regions directly probe the line of sight integrated pressure discontinuities in the ICM and thus probe the strength of such shock features directly. It has recently been shown by Korngut et al. (2011) that shock features can indeed be observed through high-resolution, 10", SZ observations with MUSTANG. De-projection capabilities depend significantly on cluster shock geometry. Following Korngut et al. (2011), for a cluster merger event taking place near the plane of the sky, Rankine-Hugoniot shock jump conditions can be applied in conjunction with density and temperature discontinuity information in order to derive the shock Mach number via

$$\mathcal{M} = \left(\frac{2(\rho_2/\rho_1)}{\gamma + 1 - (\rho_2/\rho_1)(\gamma - 1)} \right)^{1/2} \quad , \tag{8.1}$$

and

$$\mathcal{M} = (1/5)^{1/2} \left(8(T_2/T_1) - 7 + \left([8(T_2/T_1) - 7]^2 + 15 \right)^{1/2} \right)^{1/2} \quad , \tag{8.2}$$

where ρ_1 and ρ_2 denote the up- and downstream gas densities and γ is set to 5/3 under the assumption of a non-dominant relativistic sub-population. Sarazin (2002) illustrates how the pressure values at the stagnation point near the cold front edge and in the pre-shock region can be used to find a pressure-based Mach number relevant for Sunyaev-Zel'dovich studies.

Galaxy cluster shock fronts are ideal laboratories for studying astrophysical plasma physics since they give vital insight into the attainable intra-cluster medium (ICM) plasma temperatures during such events. These, in turn, have the potential to constrain the electron heating processes as galaxy clusters collide. As of now, it is uncertain whether electrons are heated instantaneously with the ions, as is suggested by Bullet Cluster observations (Markevitch & Vikhlinin 2007), or whether they equilibrate with the ions on Coulomb collision timescales, thus reaching equilibrium later than the ions, following adiabatic compression (indicated by the merger in Abell 2146, Russel et al. 2012).

The combined effect of cluster mass-redshift evolution and the X-ray observational cosmological dimming factor present a challenge for detecting merger shock density and temperature variations at sufficient angular resolution in high redshift clusters. Sunyaev-Zel'dovich effect measurements, being proportional to the integrated pressure along the line of sight, are useful follow-up probes for pressure variation studies across shock fronts and do not suffer from intrinsic redshift dependence, though the shock front angular size is subject to the angular distance evolution for a given shock geometry, timing and merger scenario.

The approach proposed in this chapter is concerned with the suitability of high-resolution joint ALMA/ACA Sunyaev-Zel'dovich observations for studying the 'Bullet Cluster' of galaxies, whose bow shock structure has already been observed in X-rays by Markevitch et al. (2002, 2007). Even though SZ shock detections will not be able to differentiate between different post-shock temperatures along the cold front/shock front distance, they will however contribute significantly to the study of the average post-shock temperature for a given X-ray density model, under shock geometry assumptions. Alternatively, in case of high quality spectral and spatial galaxy cluster X-ray information being available, these can be used in conjunction with SZ data to constrain the cluster's shock front geometry.

8.2 The Bullet Cluster

The 'Bullet Cluster', at $z = 0.296$, has a textbook example of a merger-induced bow shock structure. It is one of the most extensively studied galaxy clusters in X-ray and weak-lensing studies (Markevitch et al. 2002, Clowe et al. 2006, Bradac et al. 2006) and has recently been mapped with NuSTAR (300ks).

The cluster morphology, being characterized by the displacement of the weak-lensing peaks with respect to the bulk of the baryonic intra-cluster gas (Clowe et al. 2006), originates from a small sub-cluster, the bullet, falling through the main cluster near the plane of the sky (Barrena et al. 2002). This results in a boundary between the hot intra-cluster medium and the bullet core, which has survived ram pressure stripping (Markevitch et al. 2002), giving rise to a cold front at the bullet edge. A shock front propagating away from

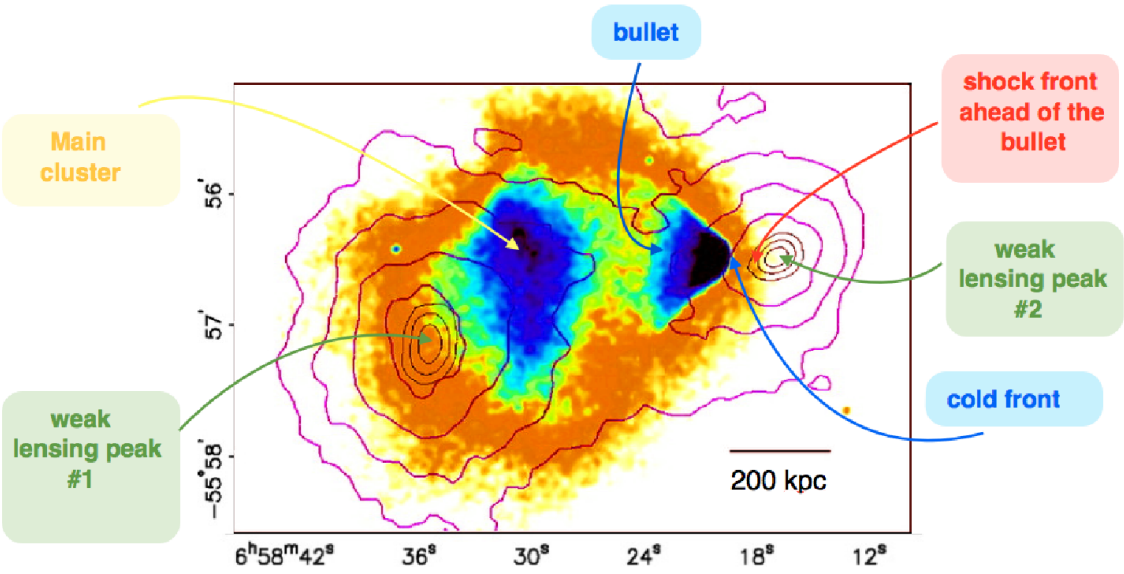

Figure 8.1: The Bullet Cluster Chandra data by Markevitch et al. (2002) with overlayed weak lensing contours. The image is taken from Clowe et al. (2006) and additional annotations of the bullet and bow shock features are shown.

it due to the high collision velocity is clearly visible in X-rays (Fig. 8.1).

Its ideal geometry, the timing of the merger activity and its southern location makes the 'Bullet Cluster' the ideal target for high-resolution Sunyaev-Zel'dovich (SZ) observations with ALMA.

The most compact 34 element 12m ALMA array Cycle 2 configuration in combination with the 9 element 7m antenna ACA array already provide sufficient sensitivity and uv-coverage for current 'Bullet Cluster' observations. The following discussion focuses on the simulation work that lead to the submitted ALMA/ACA cycle 2 proposal (2013.1.01131.S (PI. Burkutean)).

High-resolution ALMA/ACA 100 GHz follow-up observations of the 'Bullet cluster' via the Sunyaev-Zel'dovich effect are motivated by the following three objectives:

- Provide an ALMA/ACA image of the shock front in the Bullet cluster, illustrating the bow shock projected geometry.
- Measure the projected pressure discontinuity across the shock front.
- Derived the shock Mach number from sole SZ data and constrain the associated mean post-shock temperature in conjunction with X-ray information.

The fortunate geometry and the timing of the merger activity in the 'Bullet cluster' are optimal for such analyses. The Bullet sub-cluster was found to be moving through the

main cluster with a velocity of 4500^{+1100}_{-800} km/s (Markevitch et al 2004), as obtained from the X-ray derived shock Mach number of 3.0 ± 0.4. Barrena et al. (2002) were able to show that the line of sight velocity of the sub-cluster is ≈ 600 km/s, supporting that this merger is taking place near the plane of the sky and that it has occurred very recently, roughly 0.1-0.2 Gyrs ago (Markevitch et al. 2002).

The determination of the SZ signal discontinuity will also provide a pressure-derived Mach number estimate, improving the accuracy and precision of the current X-ray density and temperature derived values of 3.0 ± 0.4 (Markevitch et al 2005) and 2.1 ± 1.1 (Markevitch et al. 2002) respectively. The shock Mach number is the most important parameter for the shock-derived dark matter cross-section estimation (Markevitch et al. 2004).

In addition, the available APEX-SZ data (Halverson et al. 2009) recover the SZ signal over 1-6' scales (Fig. 8.2), complementing the proposed 100 GHz ALMA/ACA observations spanning 4-41". The APEX-SZ information will thus help in the modeling of the extended signal that is not re-constructed in the ACA/ ALMA observations.

Immediate objective for real data analysis

The first goal will be to jointly image ALMA/ACA data and thus to confirm the direct detection of the shock front as well as its associated projected pressure discontinuity. Having demonstrated the existence of the bow-shaped pressure discontinuity, one can then perform detailed modeling with joint ALMA/ACA/APEX-SZ + X-ray information in order to obtain a pressure-based Mach number estimate. Current public 500 ks Chandra data allow the projected temperatures to be measured only in two bins near the shock front,

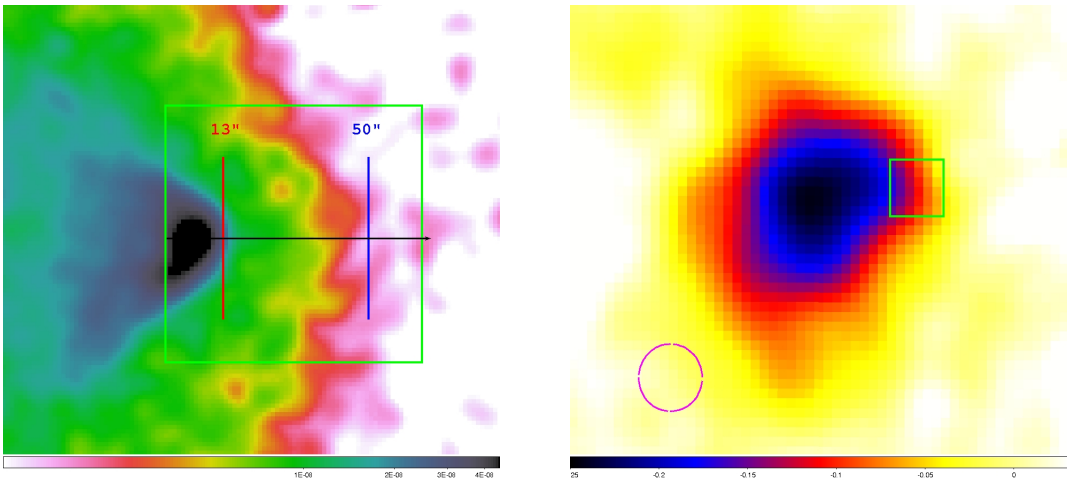

Figure 8.2: Available X-ray and SZ data. *Left:* A stacked X-ray image of the 500 ks Chandra observation by F. Pacaud, illustrating the interesting features of this cluster and the associated spatial scales. Red and blue vertical lines give the cold front and shock front position respectively. *Right:* A reduced map of the Bullet cluster from a 151 GHz APEX-SZ observation by M. Sommer. The APEX-SZ beam is shown in the left corner, the green box has the same dimensions as in the X-ray image.(image credit: F. Pacaud)

giving 27 ± 8 keV and 30 ± 10 keV (Fig. 8.3) (Markevitch et al. 2005). This illustrates that the de-projected temperatures could be as high as 35^{+15}_{-15} - 48^{+15}_{-15} keV (Markevitch et al. 2005) but the errors are very high in this analysis due to the combined effects of modeling uncertainties and the limited ability to measure high temperatures in soft bandpasses with Chandra.

By deprojecting the electron density jump, derived from X-ray observations (Fig. 8.3), and the pressure jump, obtained via joint ALMA/ACA/APEX-SZ observations, with a simplified three-dimensional model (Markevitch et al. 2002) one can compare the derived temperature discontinuity with those from spectroscopic X-ray measurements.

With future NuSTAR publications being expected to provide accurate projected shock temperature measurements, these can be included in the proposed joint ALMA/ACA/ APEX-SZ/Chandra analysis outlined above. NuSTAR 'Bullet cluster' measurements are more sensitive than Chandra observations to the predicted electron post-shock temperatures (T>19 keV).

This will help in quantifying systematic biases arising from simplified geometric assumptions and will put tighter constraints on the possible de-projected shock structure, as well as on the Mach number estimate, than sole current and future X-ray studies will be able to provide. This, in turn, will give tighter constraints on the sub-cluster velocity and on the dark matter collisional cross-section via an independent method to the weak-lensing/X-ray offset test proposed by Markevitch et al. (2004).

8.3 Modelling the Bullet Cluster

Mock interferometric simulations are the best tool to assess the feasibility of future ALMA/ ACA Band 3 observations of the Bullet Cluster shock structure.

The resultant predictions are only as realistic as the assumptions the input model relies on. The following discussion will justify the chosen model parameters while outlining the advantages and disadvantages of the applied modeling approach.

In order to test the technical feasibility of the proposed shock front study, a three-dimensional model of the cluster gas was constructed based on the de-projected density graph in Markevitch et al. (2002), whose respective normalization and slope of the density profile is being shown in Fig. 8.3.

The three-dimensional density of the bullet and the shock region were both modeled with radial power law dependences using the parameters given by Markevitch et al. (2002). This was immersed in a beta model centred on the main cluster. The temperature model was derived from the de-projected temperature graph by Markevitch et al. (2005) in which two spectra very close to the shock front were extracted and the temperature model beyond the cluster shock was taken into account (Fig. 8.3). In the modeling instant electron equilibration with the ions is assumed, the electron temperature being uniform across the cold front to shock front de-projected distance.

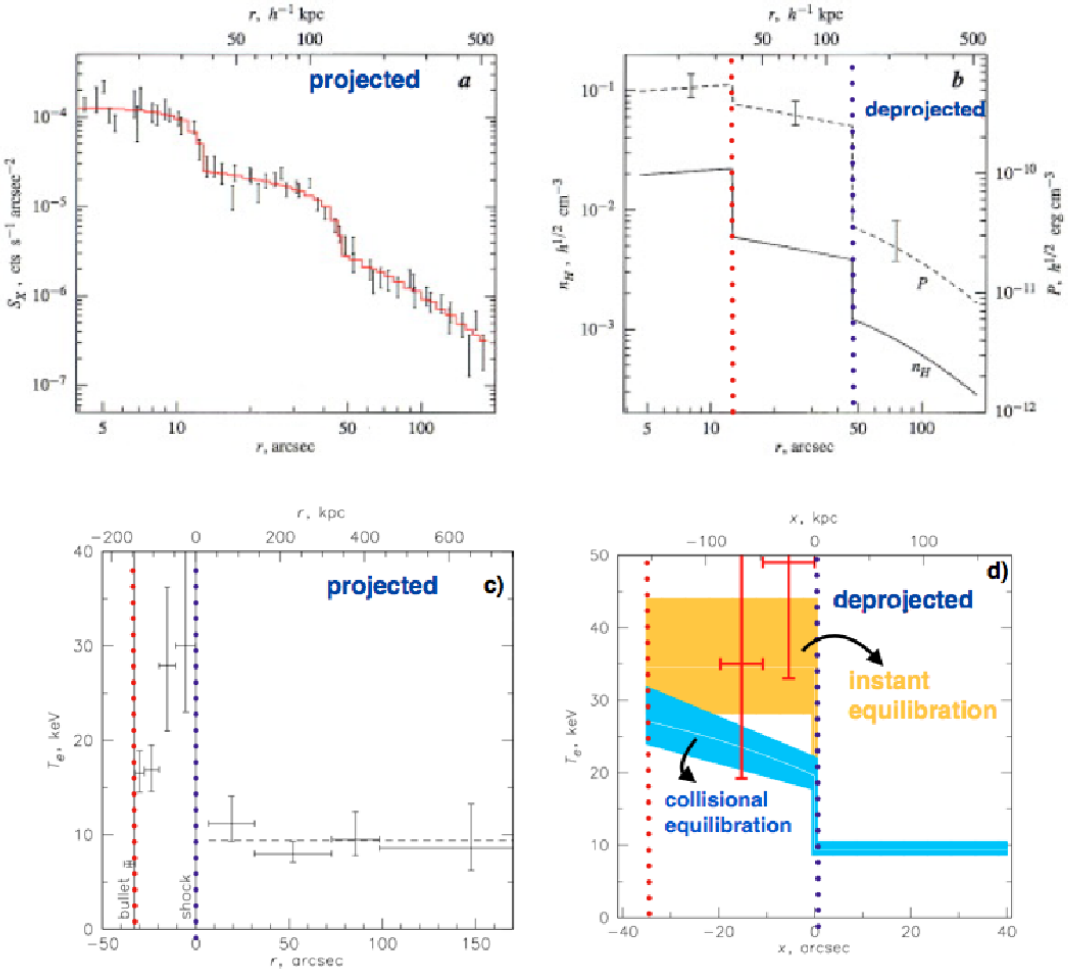

Figure 8.3: Results by Markevitch et al. (2002, 2005) and the resultant parametric model. *a)* Surface brightness profile (Markevitch et al. 2002). *b)* De-projected density profile as a function of distance from the centre of the Bullet sub-cluster by Markevitch et al. (2002). Red and blue vertical lines give the cold front and shock front position respectively. *c)* Projected temperature model by Markevitch et al. (2005). *d)* De-projected temperature profile from Markevitch (2010), centred on the centre of curvature of the shock front, showing the model predictions from instantaneous shock heating versus the adiabatic compression model.

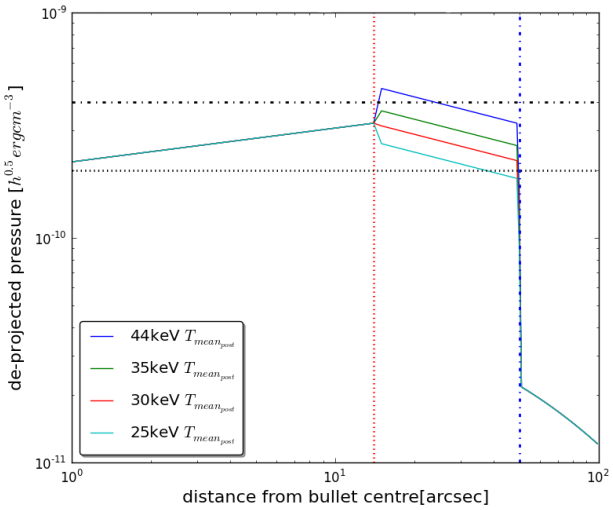

Figure 8.4: De-projected pressure profile from Markevitch et al. (2002) assuming mean de-projected temperatures as in Fig. 8.3. The blue vertical lines give the cold front and shock front position respectively. Horizontal lines show the temperature range estimates from the non-de-projected temperature profile.

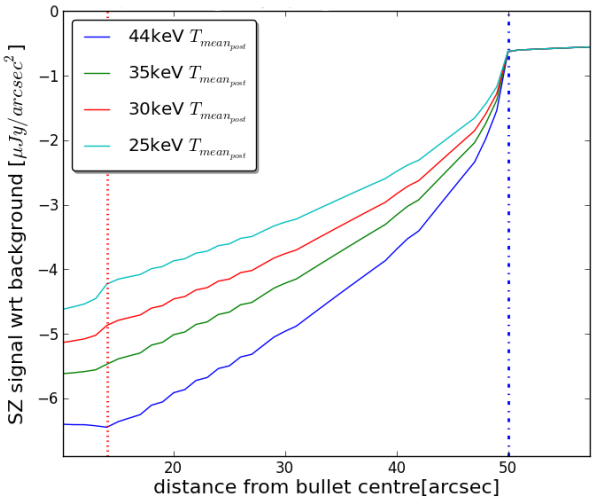

Figure 8.5: A radial cut through the projected Sunyaev-Zel'dovich signal being proportional to the pressure model in Fig. 8.4 and its subsequent integration along the line of sight. Red and blue vertical lines give the cold front and shock front position respectively.

Having obtained a three-dimensional pressure model (Fig. 8.4), it was then integrated along the line of sight in order to obtain the projected Sunyaev-Zel'dovich input map (Fig. 8.5). Relativistic corrections to the SZ effect were also taken into account (Itoh et al. 1998). Another phenomenological model, the 'small shock' model with a smaller cold front to shock front de-projected distance of 20" was also modeled using the same observational set-up to illustrate ALMA/ACA's ability to map the bow shock geometry, which can clearly be differentiated from the Markevitch et al. (2002) model case (Fig. 8.6).

The SZ jump in the adopted model is higher than that derived in Yamada et al. (2012). Yamada et al. (2012) take as the model a two-temperature hydrodynamic simulation from Akahori & Yoshikawa et al. (2012). In this paper the amount of cooling added to the simulation has been shown to affect the width between the shock front and the contact discontinuity (the edge of the bullet) alongside with numerical smearing effects. This may lead to an underestimate of that width by a factor of 1.8/1.4 for the excluded/included numerically smeared region when comparing their X-ray predicted surface brightness profile to that in Markevitch et al. (2002). In simulating the 'Bullet Cluster' a hydrodynamical simulation approach should nevertheless be preferred as it offers greater flexibility in terms of multi-component ICM temperature and shock structure modeling. For instance, Yamada et al. (2012) leave out two cooler bins in the shock region caused by residual cold gas, which is not part of the shock front. In the hereby adopted model, this region is included by always referring to a mean post-shock temperature averaged over all spectral X-ray bins in the shock front. Since hydrodynamical simulations were not available during the course of this thesis, the parametric shock modeling by Markevitch et al. (2002), which is directly based on X-ray data, was assumed and a range of different mean post-shock temperatures were explored. The maximum scale of the model, 36", fits well within the maximum observable scale with the ACA at 100 GHz of 44".

8.4 Bullet cluster ALMA/ACA cycle 2 mock observations

The Sunyaev-Zel'dovich models were simulated for different mean post-shock temperatures, ranging from 25-44 keV in order to explore a realistic mean post-shock temperature range. ALMA C34-1 and ACA cycle 2 configurations were used, giving angular resolutions of 4.3" (ALMA) and 18.5" (ACA) at a central frequency of 100 GHz, 15 GHz total bandwidth and single pointing for 3 hrs (ALMA) and 6 hrs (ACA) on-source integration time. For the spectral set-up, Band 3 observations at an LO1 frequency of 100 GHz were chosen, using the largest 1.875 GHz bandwidth per baseband as the Sunyaev-Zel'dovich spectral signature is known and one requires continuum observations. The configurations were chosen such that the shock width of 36" is covered at 4" resolution, which allows for the tip of the bow shock arc to be imaged (Fig. 8.6) together with the APEX-SZ data (1-6'). The observation times and their associated 100 GHz sensitivities of 8.0μJy/beam (ALMA) and 65.0μJy/beam (ACA) were selected such that the relevant mean post-shock electron temperature ranges (25-44 keV) can be probed with ALMA at sufficient significance (Fig. 8.6), which is motivated by the need for a required margin given the geometric assumptions and uncertainties in the de-projected density model by Markevitch et al. (2002).

In estimating the SNR across the shock front, the SZ signal was averaged in the cleaned simulated ALMA/ACA feathered map over the post and pre-shock regions within the 41"

maximum recoverable region. For the chosen instrumental set-up, the projected SZ discontinuity can be imaged to SNRs of 8 and 15 for the 25 and 44keV mean post-shock temperatures respectively (Fig. 8.6).

In order to stress ALMA/ACA's ability to map the projected pressure bow shock geometry up to 41" scales, Markevitch's model was compared to a 'small shock' model which is characterized by a 20", rather than a 36", de-projected cold front/shock front distance, giving rise to a bow shock pressure arc with a smaller curvature radius. When comparing the cleaned feathered noisy ALMA/ACA maps of Markevitch's model (Fig. 8.6) with the 'small shock model' (Fig. 8.6), it is evident that different bow shock geometries can indeed be distinguished using the proposed observational set-up of a single pointing study including the ACA.

One factor which may limit the detection of the Sunyaev-Zel'dovich signal is the presence of point sources which may 'fill in' the SZ decrement. Rex et al. (2010) and Johansson et al. (2010) investigated the point source SEDs behind the bullet cluster. The sources that lie within 1'-3' of the shock front (Rex et al. 2010) are HLS10, HLS11 and HLS16 with 100 GHz fluxes of 16.7 ± 1.4 mJy, 7.4 ± 1.1 mJy and 25.3 ± 1.3 mJy. These can however be modeled and removed in the visibility plane using the long baselines, as was done in the MS0451 analysis. In addition, radio halos may also come into play at the shock front where electrons are accelerated. The radio halo in the Bullet cluster has been studied by Liang et al. (2000) and they derived a spectral index of -1.2, which suggests that, at 100 GHz, this effect is negligible.

The simulations in Fig. 8.6 take into account the estimated noise level from the ALMA Sensitivity calculator, thus supporting the configuration, time/sensitivity, pointing and correlator set-ups. The feathered 44keV model ALMA/ACA Band 3 simulation with the APEX-SZ cleaned map is illustrated in Fig. 8.7. The information gained by the interferometric data in the shock front imaging is clearly seen by the sharp discontinuity in the combined map. The submitted Cylce 2 proposal therefore asked for a total observation time of 14.87 hrs (with overheads) with 3 hrs ALMA and 6 hrs on-source ACA integration times for ALMA cycle 2 to reach a sensitivity of 8μJy/beam for the ALMA array. The proposal was 'well received by the panel' but it was lower in rank than another cluster shock front proposal and the latter got allocated the observing time.

8.5 Conclusion

The presented mock shock structure simulation studies thus demonstrate the ability of joint ALMA/ACA Band 3 observations, even in their early array Cycle 2 configurations, to map the bow shock structure in the 'Bullet Cluster' of galaxies. The strength of the pressure discontinuity as well as its dependence on the mean post shock electron temperatures has been shown through mock simulations. In addition, the advantage of combining ALMA/ACA Band 3 interferometric and bolomter single-dish data has been demonstrated via a combination of the APEX-SZ cleaned map and the feathered ALMA/ACA Band 3 mock simulation study. The adopted shock front model is parametrically simplified and one may consider extending the above simulation study to a full hydrodynamical simulation approach for the 'Bullet Cluster' of galaxies.

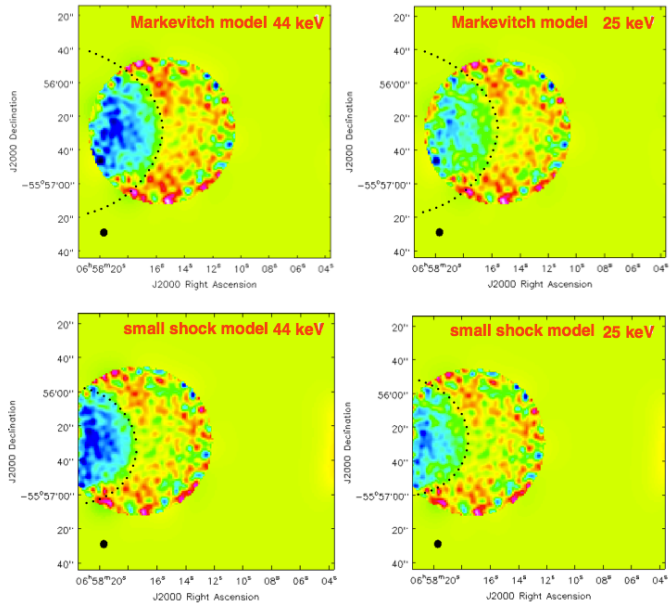

Figure 8.6: Mock simulation study. *Top*: A joint ALMA/ACA simulation (3h ALMA and 6 h ACA integration time) for the 44keV and 25keV models based on Markevitch et al. (2002). *Bottom*: A shock model with a cold/shock front de-projected distance of 20" to illustrated ALMA/ACA's ability to accurately map the bow shock morphology. The simulations are all on the same colour scale ranging from -1.3e-4 to 1.0e-4 Jy/beam. The dotted lines illustrate the bow shock structure.

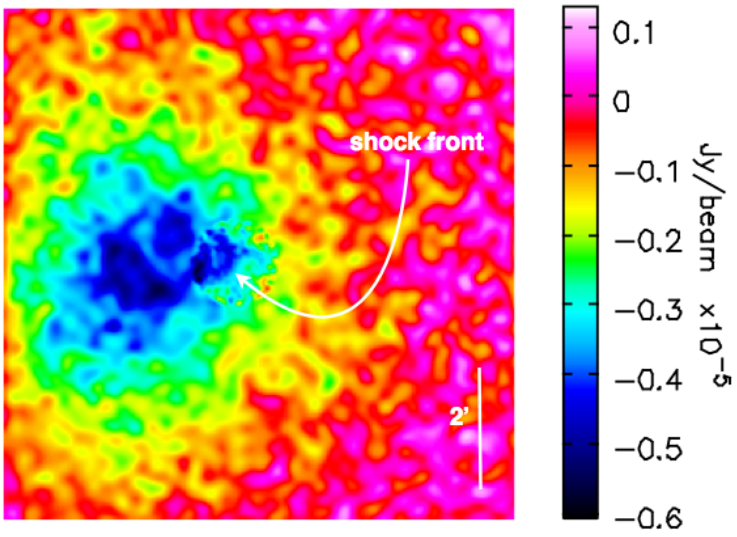

Figure 8.7: The feathered ALMA/ACA 100 GHz simulated map (44 keV model) with the APEX-SZ cleaned image.

Chapter 9

Project extensions - future developments

Having established how interferometric and bolometer single-dish Sunyaev-Zel'dovich measurements on MS0451 can provide complementary information on its projected pressure profile under the assumptions of spherical symmetry for β and GNFW-models or the projected elliptical shape in the plane of the sky, a logical extension of this approach is epitomized via cluster triaxiality.
As discussed in Chapter 3, the determination of a cluster's triaxiality requires multi-wavelength information.
X-ray data are readily available for MS0451, as are archival data suitable for weak lensing studies in conjunction with published values from a triaxial fitting strong lensing approach. Hence, the future application of my Sunyaev-Zel'dovich MS0451 galaxy cluster project will involve multi-wavelength modeling, for which I have already coded a simulation framework presented in this chapter. In addition, the calibration steps of a preliminary X-ray analysis are outlined.
Having established the workings and merits of my MS0451 SZ-fitting, a further natural extension lies in the design of a multi-cluster follow-up program that tests the cross-calibration between APEX-SZ/CARMA for multiple clusters.
A CARMA archive search showed that several cluster datasets have become public during the final months of this thesis. I also present a successful CARMA/APEX-SZ collaboration proposal on selected clusters for which I undertook the planning and writing. My planned span and scope of future analyses on these available SZA/CARMA-observed clusters is outlined at the end of this chapter.

9.1 MS0451 - a triaxial analysis

Having examined ways to study the role of galaxy cluster morphology-dependent structure via high-resolution mock observations in chapter 7, it still remains to be discussed to what extent departures from spherical symmetry affect our mass inference. This topic has developed into an active area of research in the past few years, motivated by mismatches between mutli-wavelength mass estimates (Morandi et al. 2010, Sereno et al. 2011).

The galaxy cluster MS0451 has specifically been chosen so as to facilitate a study into cluster triaxiality owing to the availability of multi-wavelength observations. One necessitates both, the data reduction of the X-ray/weak and strong lensing data as well as a theoretical framework which supplies the input models for the triaxial study with which to compare the data.

In this section, I will present the triaxial code under development to yield gas density and temperature profiles under the assumption of hydrostatic equilibrium for a given triaxial dark matter density shape and projection. It is based on the works by Lee & Suto (2003) whose notation and approach will be followed below. For a given triaxial dark matter halo, one can express its density profile as,

$$\rho(R) = \frac{\delta_c \rho_c(z)}{(R/R_0)^{\gamma}(1+(R/R_0)^{(3-\gamma)}} \quad , \tag{9.1}$$

where the radius, R, is given by

$$R^2 = a^2\left(\frac{x^2}{a^2}+\frac{y^2}{b^2}+\frac{z^2}{c^2}\right), \qquad a \geq b \geq c \quad . \tag{9.2}$$

Since one wants to link the DM density profile to its potential and thus to the gas pressure, assuming hydrostatic equilibrium, one can solve the expression by Binney & Tremaine (2008) to obtain an expression for the gravitational potential

$$\Phi(\mathbf{r}) = -\pi G\left(\frac{bc}{a}\right)\int_0^{\infty}\frac{[\psi(\infty)-\psi(m)]}{\sqrt{(\tau+a^2)(\tau+b^2)(\tau+c^2)}}\mathrm{d}\tau \quad , \tag{9.3}$$

with

$$\psi(m) = 2\int_0^m \rho(R)\, R\mathrm{d}R \tag{9.4}$$

and

$$m^2 = a^2\left(\frac{x^2}{a^2+\tau}+\frac{y^2}{b^2+\tau}+\frac{z^2}{c^2+\tau}\right) \quad . \tag{9.5}$$

Lee & Suto (2003) derive an ellipsoidal approximation to the subsequent potential equipotential surfaces, which, using the X-ray shape theorem, Eq. 2.28, implies that the isodensity and isobaric surfaces coincide with these under hydrostatic equilibrium conditions. This is illustrated in Fig. 9.1, which shows the gas and dark matter isodensity surfaces at a radial distance of 1.2 R_0 and demonstrate that the gas distribution is more circular than the dark matter distribution. In addition, weak lensing analyses infering the projected total mass, will also be affected by sphericity assumptions when studying triaxial halos. Fig. 9.1 illustrates a simulated convergence map with the associated noiseless shear profile for a spherical cluster which can easily be generalized to triaxial cluster projections and noisy galaxy cluster shear estimates.

Both, the ICM triaxial projected gas profiles as well as the presented weak lensing convergence and noiseless shear simulation code lay the frameworks for future applications to the galaxy cluster MS0451.

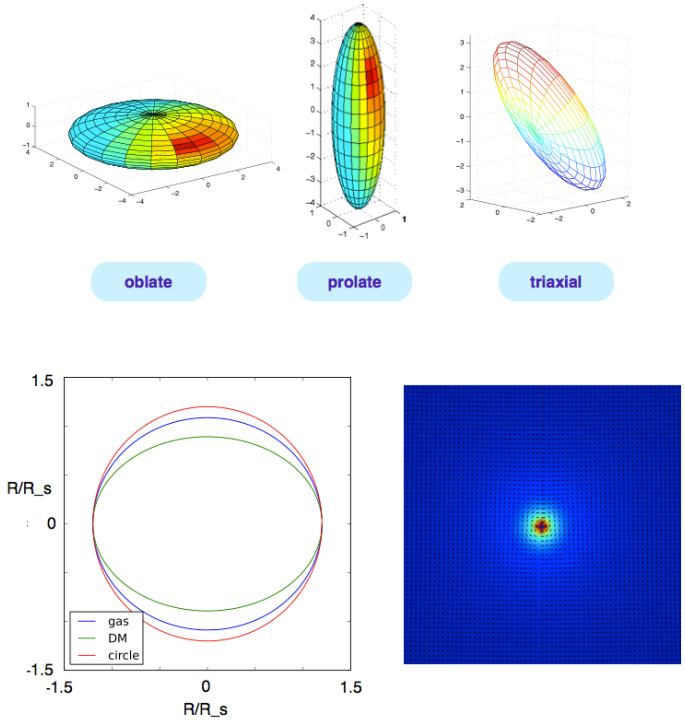

Figure 9.1: The triaxial simulation framework. *Top*: An illustration of possible 3D dark matter density morphologies of galaxy clusters. *Bottom left:* The dark matter and gas iso-density surfaces at a radius of 1.2 R_0 (R_0 being denoted by R_s in the figure), following the approach of Lee & Suto (2003). *Bottom right:* A preliminary output of the weak lensing simulation code showing the noiseless shear on top of the convergence map.

On the data side, a preliminary X-ray data reduction was performed on Chandra MS0451 observations (ID 902), Fig. 9.2a. The CIAO software *chandra-repro* task was applied to the event 1 files, which includes corrections via destreaking and updates the bad pixel

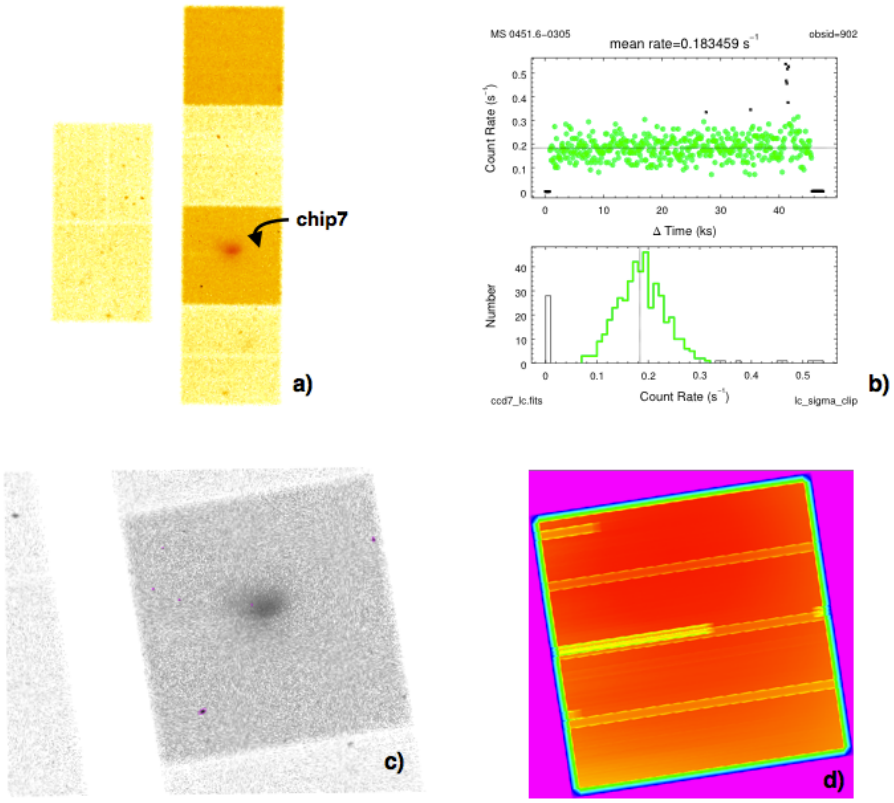

Figure 9.2: Preliminary Chandra X-ray reduction of MS0451. *a)* A view of the Chandra chips. Chip 7 contains the cluster information. b) Light curve examination outputs and subsequent σ clipping. c) Chip 7 with point sources denoted by purple contours and detected via *vtpdetect* . d) Exposure correction.

filters (Chandra reduction manual). The lightcurve was examined, Fig. 9.2b, in order to check for flares and good time intervals (GTIs) were determined, decreasing the exposure time from 44.19 ks to 43.40 ks. The background files were obtained via *acis-bkgrnd-lookup*, changed to contain the correct pointing information and repojected via *reproject-events*. An exposure map was also generated. Point sources were detected and removed via *vtpdetect*, re-adjusting the scale to also detect faint sources. The point sources in the MS0451 field reported by Molnar et al. (2002) were all detected in my reduction pipeline. The next steps in this analysis will be the generation of a surface brightness profile as well as spectrum extraction, which are planned to be linked to the already coded theoretical framework described above.

9.2 SZA archival clusters

Archival data that have recently become available, allow for the extension of the previously presented MS0451 project to multiple clusters, facilitating the study of a range of clusters with the developed techniques in the future. Below, I outline the archival cluster properties with particular regard to the potential for possible scientific investigations that stem from them.

RXCJ1023: This galaxy cluster, also known as Zw3146, is a cool-core galaxy cluster (Edge et al. 1994) at a redshift of $z = 0.291$. The fact that there are both, 30 and 90 GHz data available makes it a promising candidate for exploring the pressure profile in the core region of this cluster (depending on the quality of the 90 GHz data). Having had a look at the track comments, there are several issues which might require a large flagging fraction of the data (Bonamente et al. 2012 only report a rather short integration time on this cluster). Baldi et al. (2007) have reduced Chandra data on this cluster confirming its cool-core nature and also showing a metallicity gradient. This was further analysed by Rafferty et al. (2007). The cluster is also in the APEX-SZ collaboration's point source follow-up program.
Next steps: This cluster lends itself very well to a joint 30GHz/90GHz SZA + APEX-SZ + Planck analysis which can then be compared with X-ray and weak-lensing (WL) data.

MACSJ1931: This cluster is part of the CLASH sample. It has been studied by Ehlert et al. (2011) and was shown to have one of the strongest cool-cores with hints of cool-core disruption. X-ray cavities through AGN feedback have also been observed. The 30 GHz data is observed over a time period of 9 days whereas the 90 GHz data is observed over 2 months. Depending on the quality of the 90 GHz data, some modeling of the potential point source flux variability could be done. In line with RXCJ1023, this cluster could therefore be used for a detailed cool-core study. **Next steps:** This cluster lends itself very well to a joint 30GHz/90GHz SZA + APEX-SZ + Planck analysis, given that the point source can be modeled and removed using the long baselines. This can then be compared with X-ray and WL data.

RXCJ1206: This cluster has an elliptical elongated shape in SZ and X-rays. Umetsu et al. (2012), have recently reported a very detailed weak and strong lensing analysis of this cluster. They find a large projected mass ellipticity and compare their lensing mass estimates to X-ray and SZ Bolocam data. The X-ray emission is elongated within the central arcminute and Bolocam elliptical fits have also been done. **Next steps:** Even though a large multi-wavelength analysis has already been performed on this cluster, it is a great opportunity for a twin project to the MS0451 case. Ellipticity fits between the Bolocam data and the APEX-SZ data can be compared and may shed some light on the suitability of the APEX-SZ (BOA/MATLAB) point source transfer function as opposed to the iterative Bolocam pipeline approach.

A1835: There are only 90 GHz data available. This cluster exhibits diffuse halo emission (Murgia et al. 2009). A weak lensing analysis has been reported by Clowe et al. (2002). Recent Suzaku observations by Ichikawa et al. (2013) suggest deviations from hydrostatic equilibrium.

A1689: This is a very well studied galaxy cluster at a redshift of $z = 0.183$. Recent studies (Sereno et al. 2012, Sereno & Umetsu 2011, Morandi et al. 2011) have focussed on triaxiality in this cluster. Information from SZ has already been used by Morandi et al. (2011). The data quality of the 30 GHz data will be crucial in examining whether our APEX-SZ data can add significantly to a similar triaxial analysis with APEX-SZ.

A2204: Only 90 GHz data are available, such that the full extent of a possible analysis is dependent on the data quality.

RXCJ1347: This cluster was recently studied by Plagge et al. (2013) who reported a detection of pressure sub-structure. Besides the 90 GHz SZA data reported in Table 9.1, there is also 16.8 hrs of 100 GHz E-array data from an old APEX-SZ proposal. In addition, comissioning 30 GHz data are available, whose quality still needs to be examined, as well as 33.2 hrs of 90 GHz E-array and 3.5 hrs of CARMA D-array data. **Next steps:** I have already started the reduction on the old APEX-SZ proposal data. Instead of doing a cleaned component fitting as in Plagge et al. (2013), one might consider combining the cleaned APEX-SZ map with the interferometric data or doing a direct model fitting in the visibility plane.

Table 9.1: Interferometric archival data

cluster name	redshift	declination (J2000)	BOA obstime (hrs)	obstime SZA 30 (hrs)	obstime SZA 90 (hrs)
RXCJ1023	0.291	+04:11:10	15.4	25.0	60.1
MACSJ1931	0.352	-26:35:006	9.4	24.9	41.9
RXCJ1206	0.4414	-08:48:22	14.8	54.7	−−
A1689	0.183	-01:20:17	17.9	18.8	−−
A1835	0.253	02:51:32	12.5	−−	22.9
A2204	0.152	+05:34:43	20.3	−−	22.5
RXCJ1347	0.451	-11:45:12	10.2	−−	25.7

9.3 SZA collaboration proposal

Three clusters, that had previously been observed with SZA but whose results were not public in the previous year are of particular interest to the APEX-SZ collaboration. I undertook the planning and writing of a collaboration proposal on these clusters, which was submitted and accepted in October 2013.

Table 9.2: Accepted Collaboration proposal

cluster name	redshift	declination	BOA obstime	obstime SZA 30	obstime SZA 90
		(J2000)	(hrs)	(hrs)	(hrs)
RXCJ2014.8	0.161	-24:30:30	10.1	14.8	−−
RXCJ2243.3	0.44	-09:35:18	7.1	11.5	−−
RXCJ0956.4	0.17	-10:04:12	10.7	−−	44.6 (SL), 76.6 (SH)

Two of the APEX-SZ clusters of interest were in the CARMA/SZA archive, having recently been observed with 30 GHz SZA: RXCJ2014 and RXCJ2243 (project c1009). RXCJ2014 is a non-detection in our APEX-SZ sample. This is most likely caused by a strong NVSS point source at the centre of the cluster, with a reported flux of 229.2 mJy at 1.4 GHz. The long baseline information of the 30 GHz SZA data will allow the spectral index of the source to be determined. The effect of potential source flux time variability means that such an investigation would be limited to verifying that, at the SZA time of observation, the positive point source flux could cancel the SZ decrement at 150 GHz. The 30 GHz RXCJ2014 SZA data would help to explain the APEX-SZ non-detection, allowing us to better understand our scaling relations (Bender et al. submitted 2014).

RXCJ2243 is a significant detection in our APEX-SZ data. From the experience gained with MS0451 30 GHz SZA data, the APEX-SZ information on RXCJ2243 can be combined with the 30 GHz SZA visibilities in a joint parametric fit to put tighter constraints on the shape of the cluster SZ signal. In addition, a comparison between a sole interferometric and a single-dish/interferometric combination can reveal systematic errors from the necessarily simplifying assumptions underlying each analysis. Just as MS0451, RXCJ2243 has an elliptical projected X-ray shape and our weak lensing follow-up makes it an interesting candidate for a multi-wavelength study.

The relevance and importance of the MS0451 project was thus illustrated in the preceeding section in terms of its potential for future applications to released CARMA/SZA archival data in conjunction with a newly accepted collaboration proposal. The developed visibilitiy fitting code can be incorporated into the coded triaxial fitting framework, allowing for a wide-ranging individual cluster study across the APEX-SZ sample within the SZA declination range.

The aforementioned planned project extension to archival clusters relies on an ad hoc selection of galaxy clusters. A supplementary well-selected sample could constitute a full APEX-SZ follow-up study with SZA at 30 GHz.

9.4 Conclusion

In this thesis, it has thereby been quantitatively illustrated that high-resolution Sunyaev-Zel'dovich measurements contribute constructively to the study of galaxy clusters. Not only can they provide the essential small-scale Sunyaev-Zel'dovich structural information in galaxy cluster shock fronts necessary for pressure-based merger shock analyses, but the currently attainable combination of high sensitivity and angular resolution in the ALMA array also enables the study of the core regions of clusters over a wide redshift range.

With single-dish SZ surveys providing an ever more detailed picture of galaxy clusters up to angular resolutions of $\approx 1'$, the need to combine interferometric and bolometer single-dish data will become ever more imminent. The developed interferometer/sd combination GUI addresses this issue by providing an interactive feathering method to the CASA software - the prime software analysis package for ALMA/ACA observations.

The developed study on the galaxy cluster MS0451 can be extended to a whole sample in the future, stressing the wide application of the developed methods in this thesis. In addition, the potential for multi-frequency investigations has also been outlined in the form of the presented simulation framework.

The developed Bayesian Markov Chain Monte Carlo parametric visibility fitting approach has quantitatively shown that the shape of cluster pressure profiles can be probed with joint ALMA/ACA/SZA observations, presenting a promising frontier in SZ galaxy cluster future research, placing it at the forefront of high-resolution cluster studies at high redshift in terms of pressure-based analyses.

Chapter 10

Appendix

APPENDIX A

The Single Dish/Interferometer combination GUI is written in python such that in can easily be run within the CASA software.

It currently takes an interferometric and a single dish map as inputs and assumes the combination to be made on the central pixel.

A single-dish (SD)/interferometer (INTF) flux scale conversion factor is also incorporated alongside with beam scaling. The weighting widget allows for the exploration of different weighting factors of the de-convolved interferometric and single dish images.

The explored weighting options include:

- Down-weighting of SD data at large spatial scales using a gaussian taper
- Down-weighting of INTF data at large spatial scales using a gaussian taper.
- Hybrid weighting of the SD map
- Hybrid weighting of the INTF map

The different weights can be examined via 'TEST' buttons.
This allows for the resultant combined images to be examined before finalization via the 'FINAL' button.

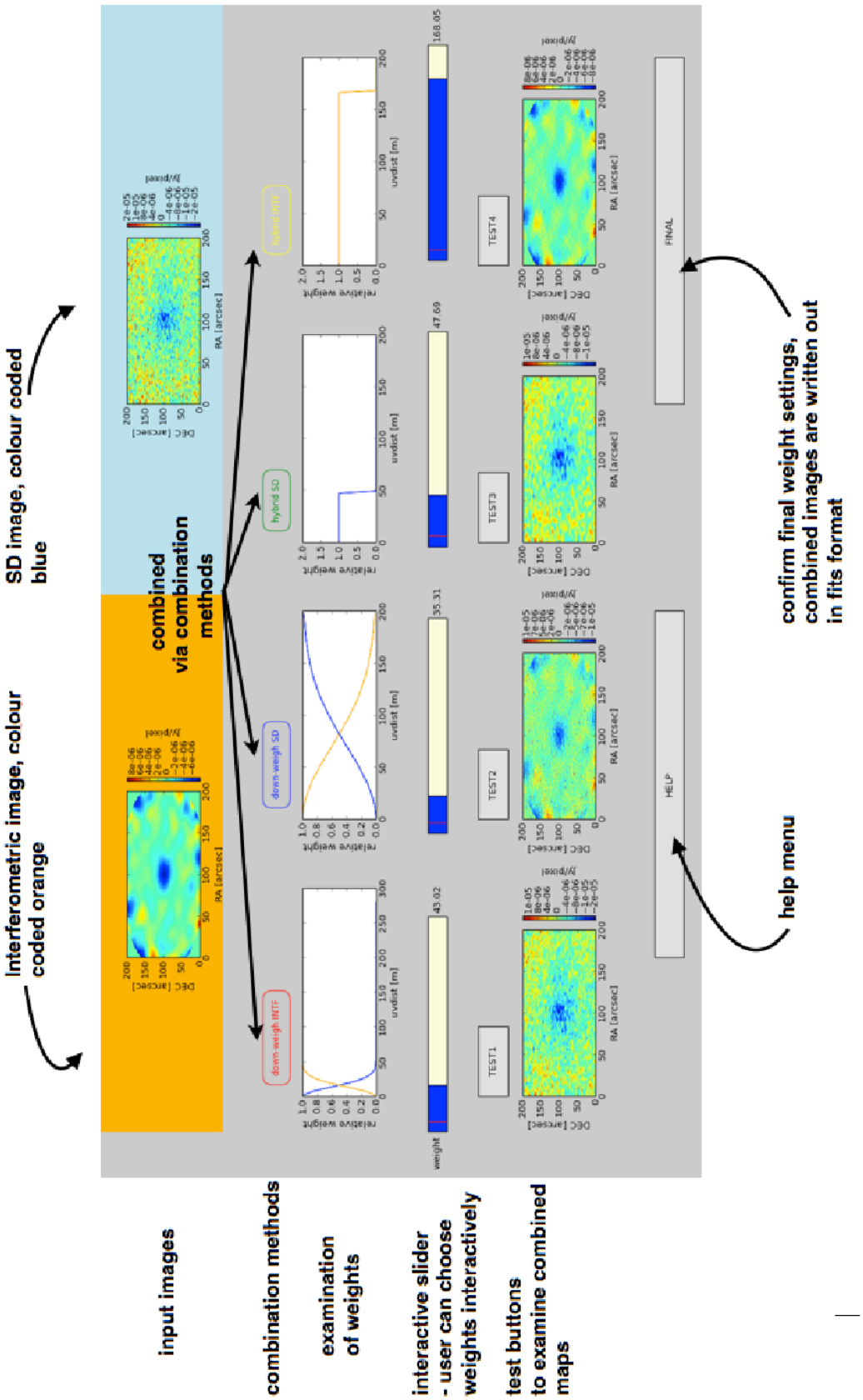

Figure 10.1: The INTF/SD combination GUI outlining the interactive features.

APPENDIX B

The image galleries for the individual ALMA/ACA/SZA mock observations are presented in the following appendix.

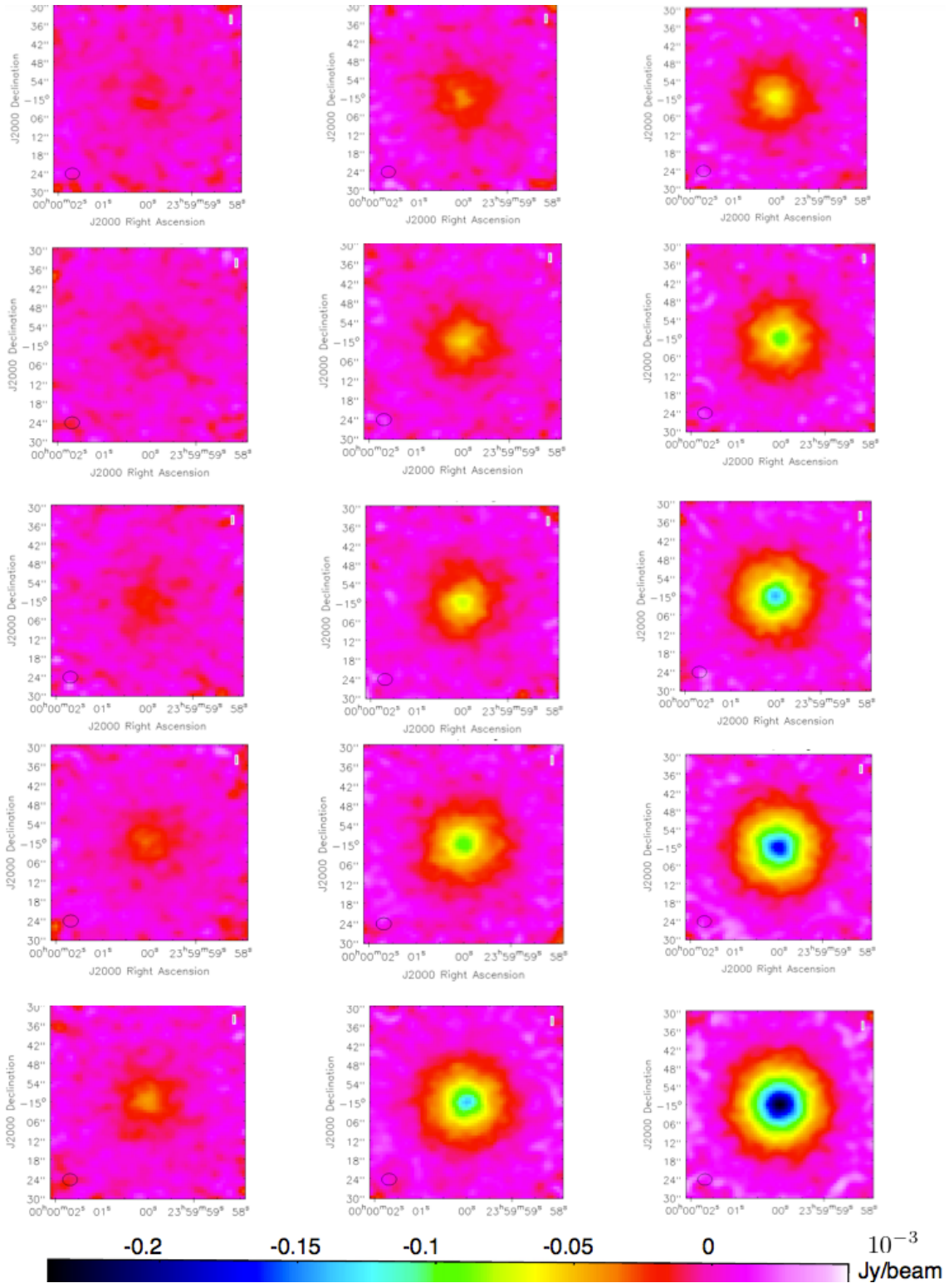

Figure 10.2: Image gallery of ALMA 100 GHz mock observations for the cool-core Arnaud pressure profile. The columns correspond to the M_{500} masses $2.0 \times 10^{14} M_{\odot}$, $5.0 \times 10^{14} M_{\odot}$ and $8.0 \times 10^{14} M_{\odot}$ (left to right). The rows correspond to redshifts 0.2, 0.4, 0.6, 0.8, 1.0 and 1.2 (from top to bottom).

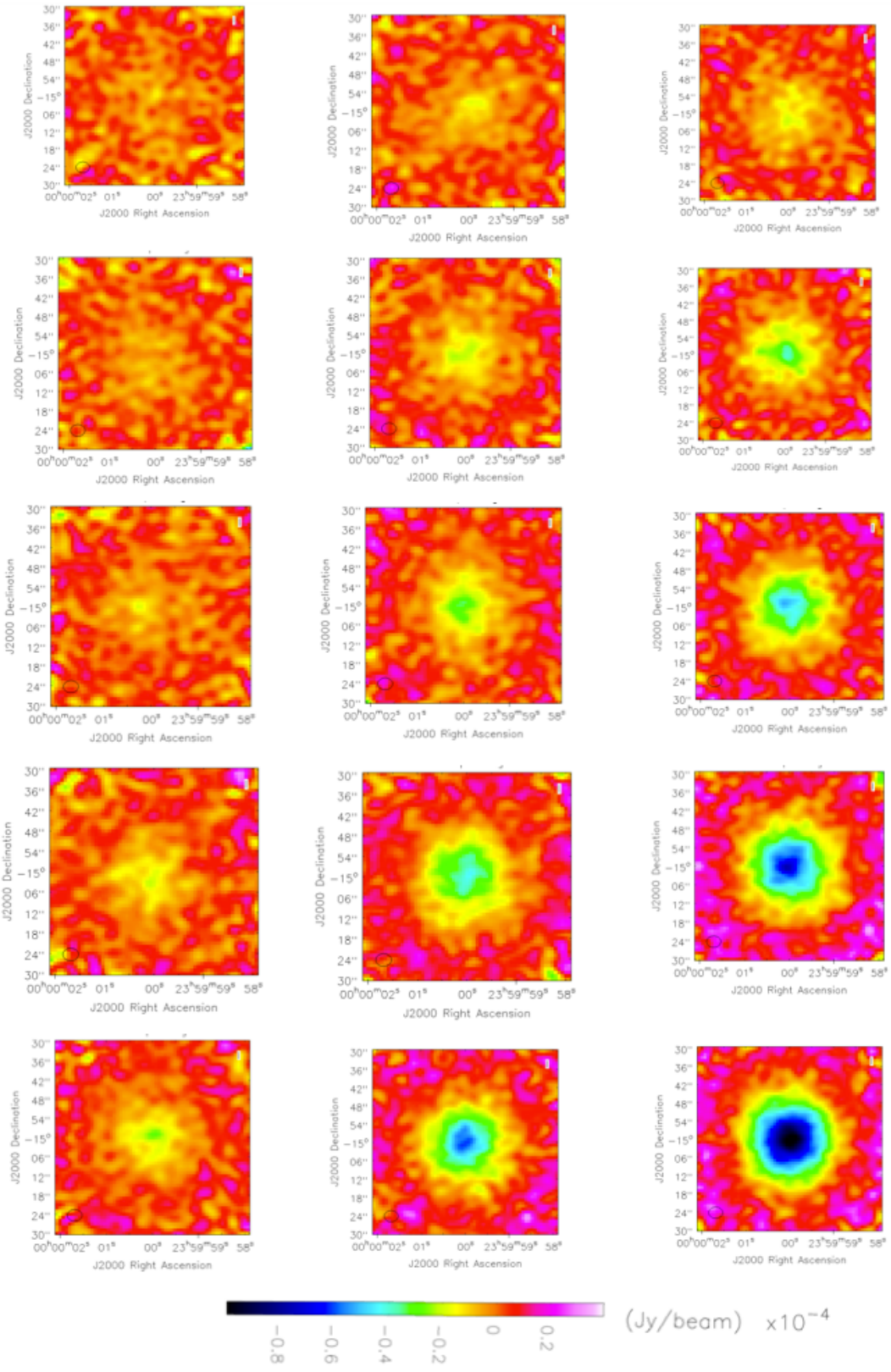

Figure 10.3: Image gallery of ALMA 100 GHz mock observations for the universal Arnaud pressure profile. The columns correspond to the M_{500} masses $2.0 \times 10^{14} M_{\odot}$, $5.0 \times 10^{14} M_{\odot}$ and $8.0 \times 10^{14} M_{\odot}$ (left to right). The rows correspond to redshifts 0.2, 0.4, 0.6, 0.8, 1.0 and 1.2 (from top to bottom).

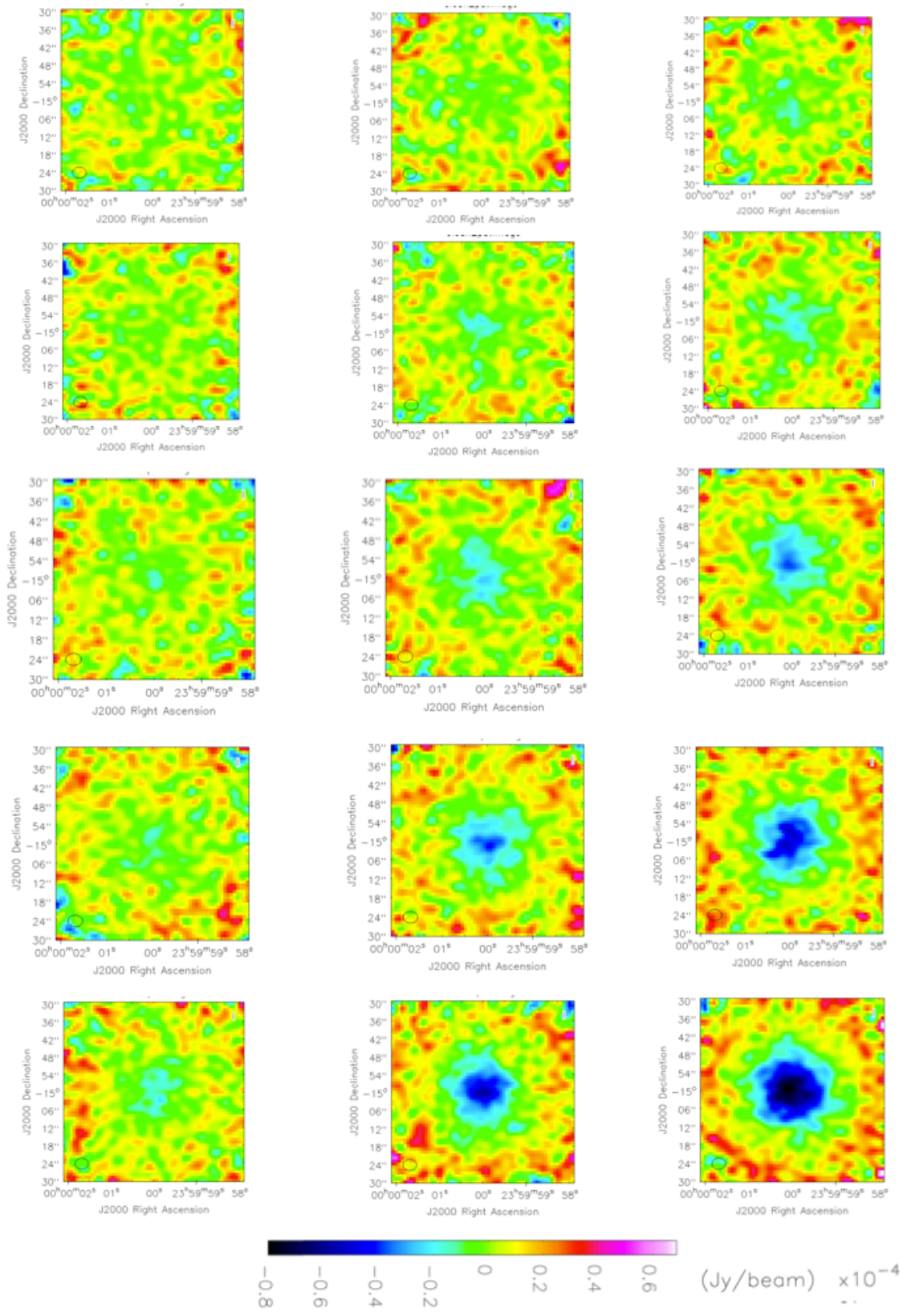

Figure 10.4: Image gallery of ALMA 100 GHz mock observations for the non-cool core Arnaud pressure profile. The columns correspond to the M_{500} masses $2.0 \times 10^{14} M_{\odot}$, $5.0 \times 10^{14} M_{\odot}$ and $8.0 \times 10^{14} M_{\odot}$ (left to right). The rows correspond to redshifts 0.2, 0.4, 0.6, 0.8, 1.0 and 1.2 (from top to bottom).

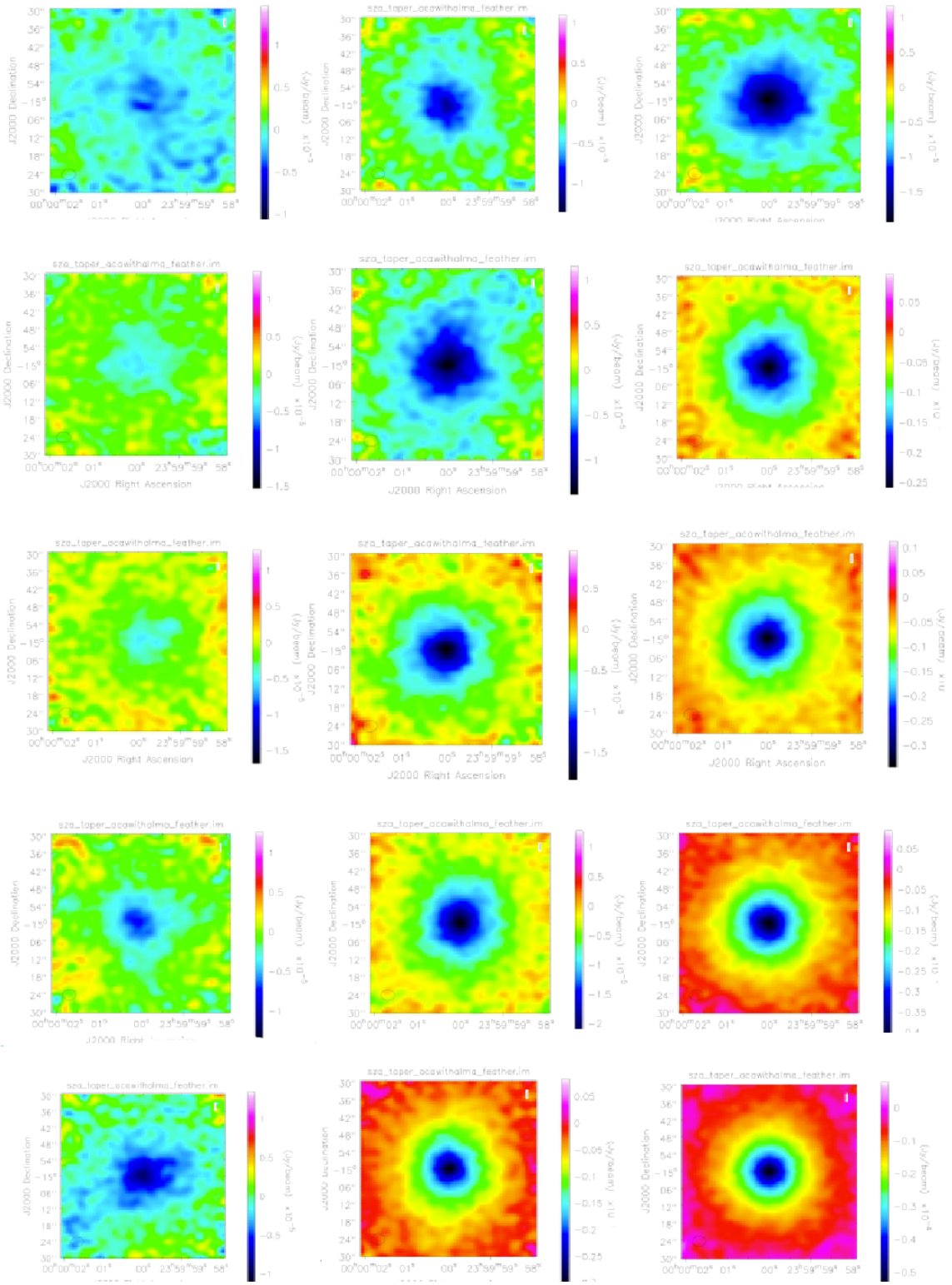

Figure 10.5: Image gallery of ALMA/ACA (Band3)/SZA mock observations for the cool core Arnaud pressure profile. The columns correspond to the M_{500} masses $2.0 \times 10^{14} M_{\odot}$, $5.0 \times 10^{14} M_{\odot}$ and $8.0 \times 10^{14} M_{\odot}$ (left to right). The rows correspond to redshifts 0.2, 0.4, 0.6, 0.8, 1.0 and 1.2 (from top to bottom).

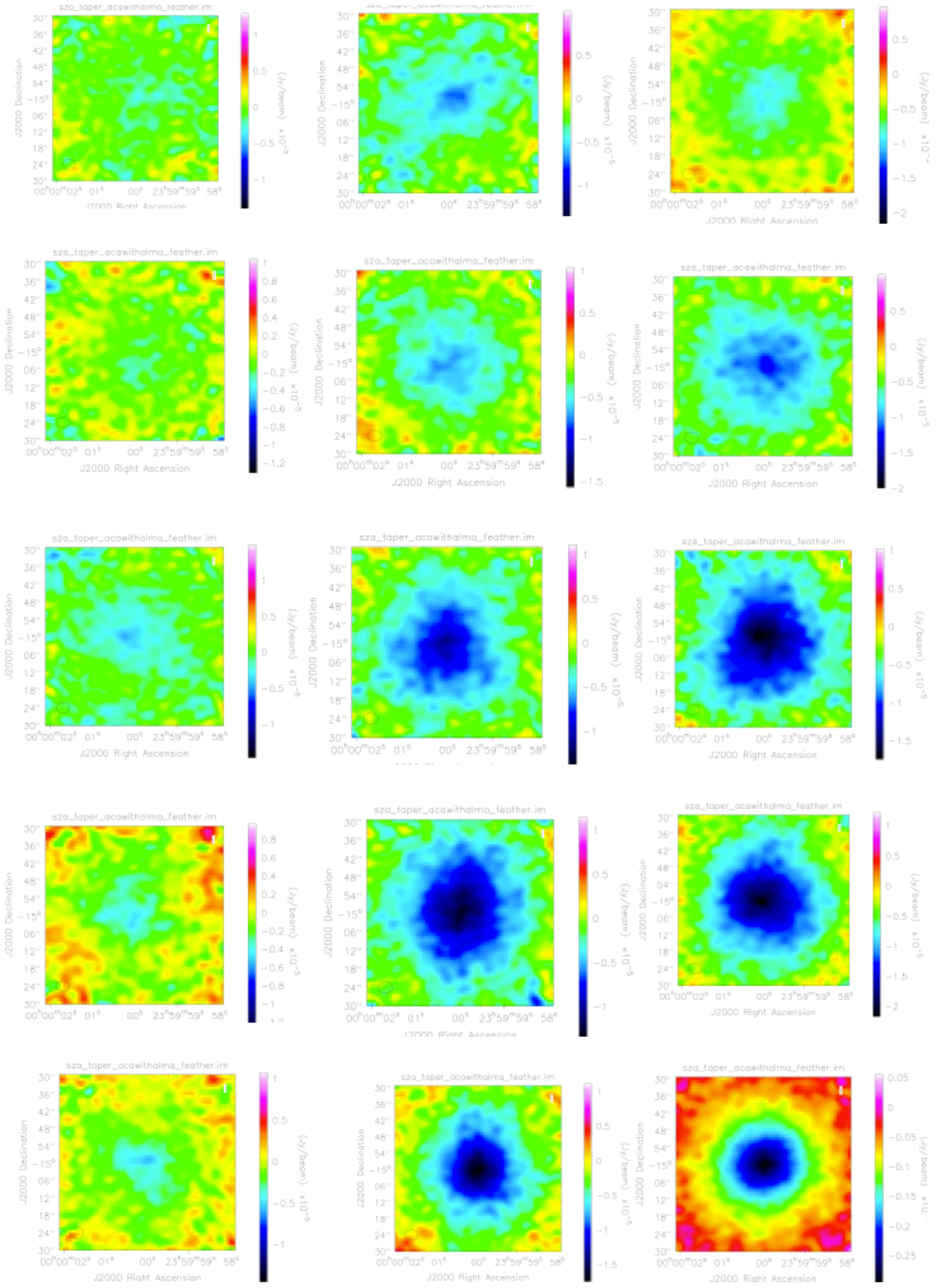

Figure 10.6: Image gallery of ALMA/ACA (Band3)/SZA mock observations for the universal Arnaud pressure profile. The columns correspond to the M_{500} masses $2.0 \times 10^{14} M_{\odot}$, $5.0 \times 10^{14} M_{\odot}$ and $8.0 \times 10^{14} M_{\odot}$ (left to right). The rows correspond to redshifts 0.2, 0.4, 0.6, 0.8, 1.0 and 1.2 (from top to bottom).

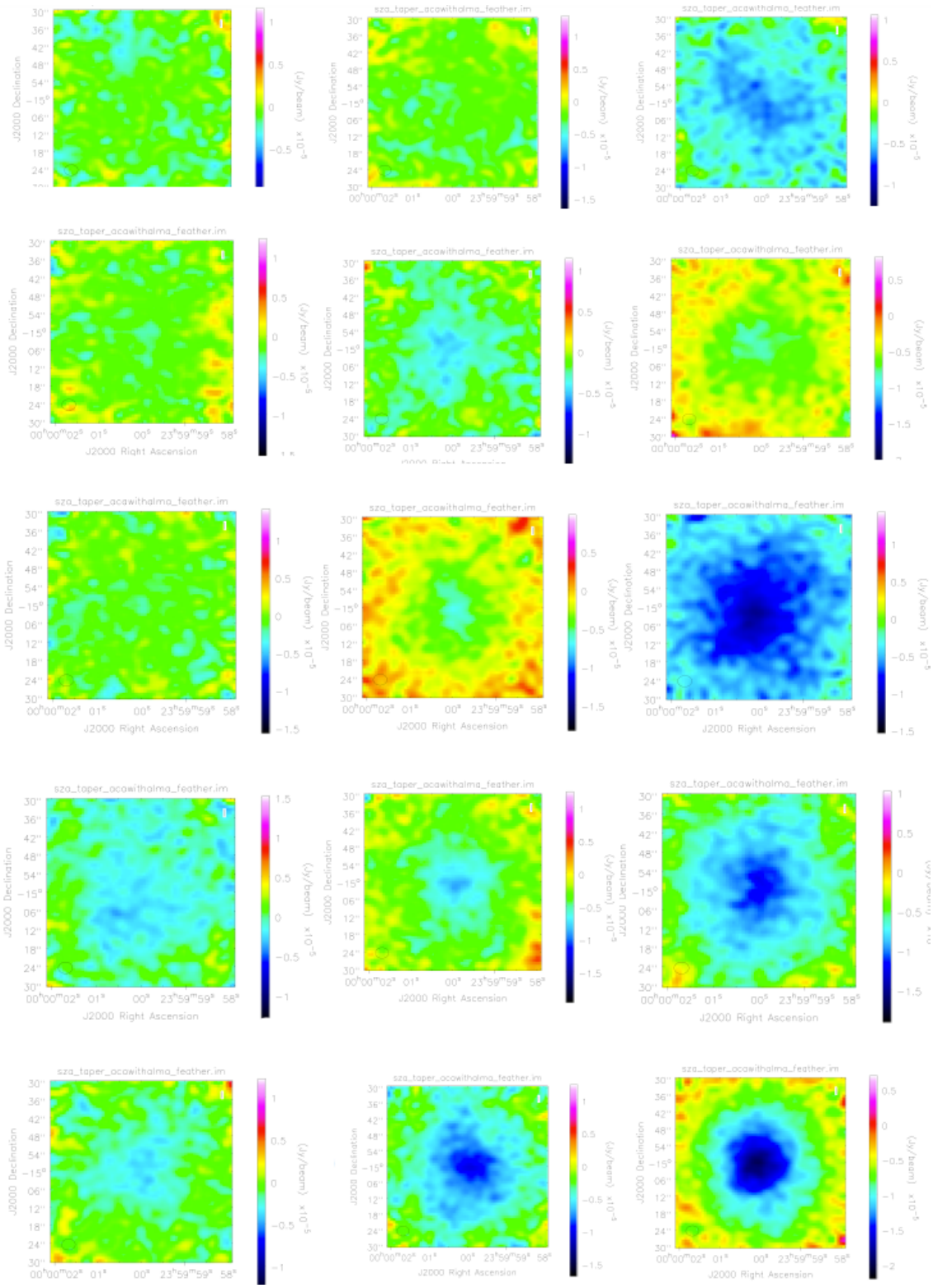

Figure 10.7: Image gallery of ALMA/ACA (Band3)/SZA mock observations for the non-cool core Arnaud pressure profile. The columns correspond to the M_{500} masses $2.0 \times 10^{14} M_{\odot}$, $5.0 \times 10^{14} M_{\odot}$ and $8.0 \times 10^{14} M_{\odot}$ (left to right). The rows correspond to redshifts 0.2, 0.4, 0.6, 0.8, 1.0 and 1.2 (from top to bottom).

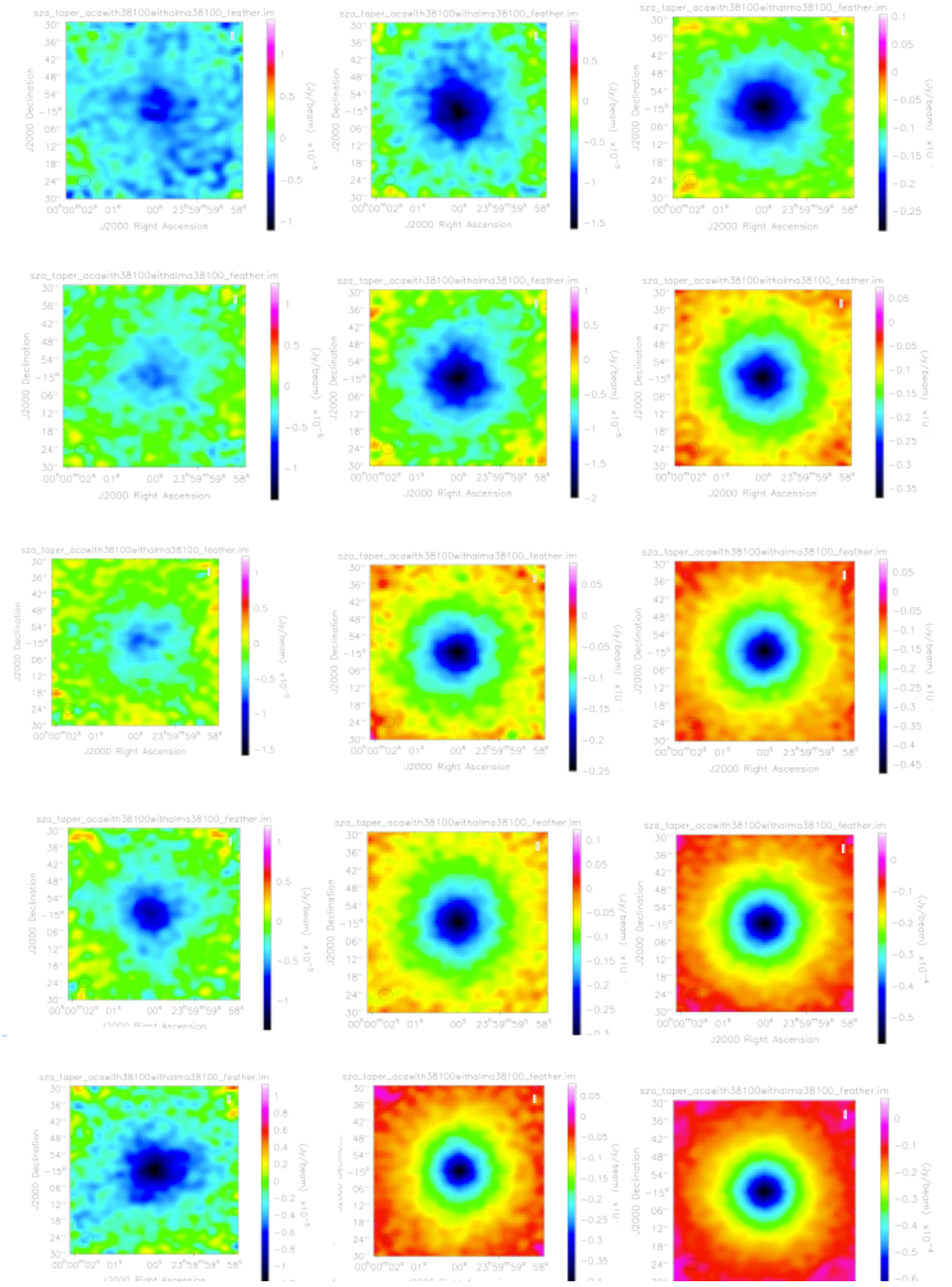

Figure 10.8: Image gallery of ALMA/ACA (Band 3 + 1)/SZA mock observations for the cool core Arnaud pressure profile. The columns correspond to the M_{500} masses $2.0 \times 10^{14} M_{\odot}$, $5.0 \times 10^{14} M_{\odot}$ and $8.0 \times 10^{14} M_{\odot}$ (left to right). The rows correspond to redshifts 0.2, 0.4, 0.6, 0.8, 1.0 and 1.2 (from top to bottom).

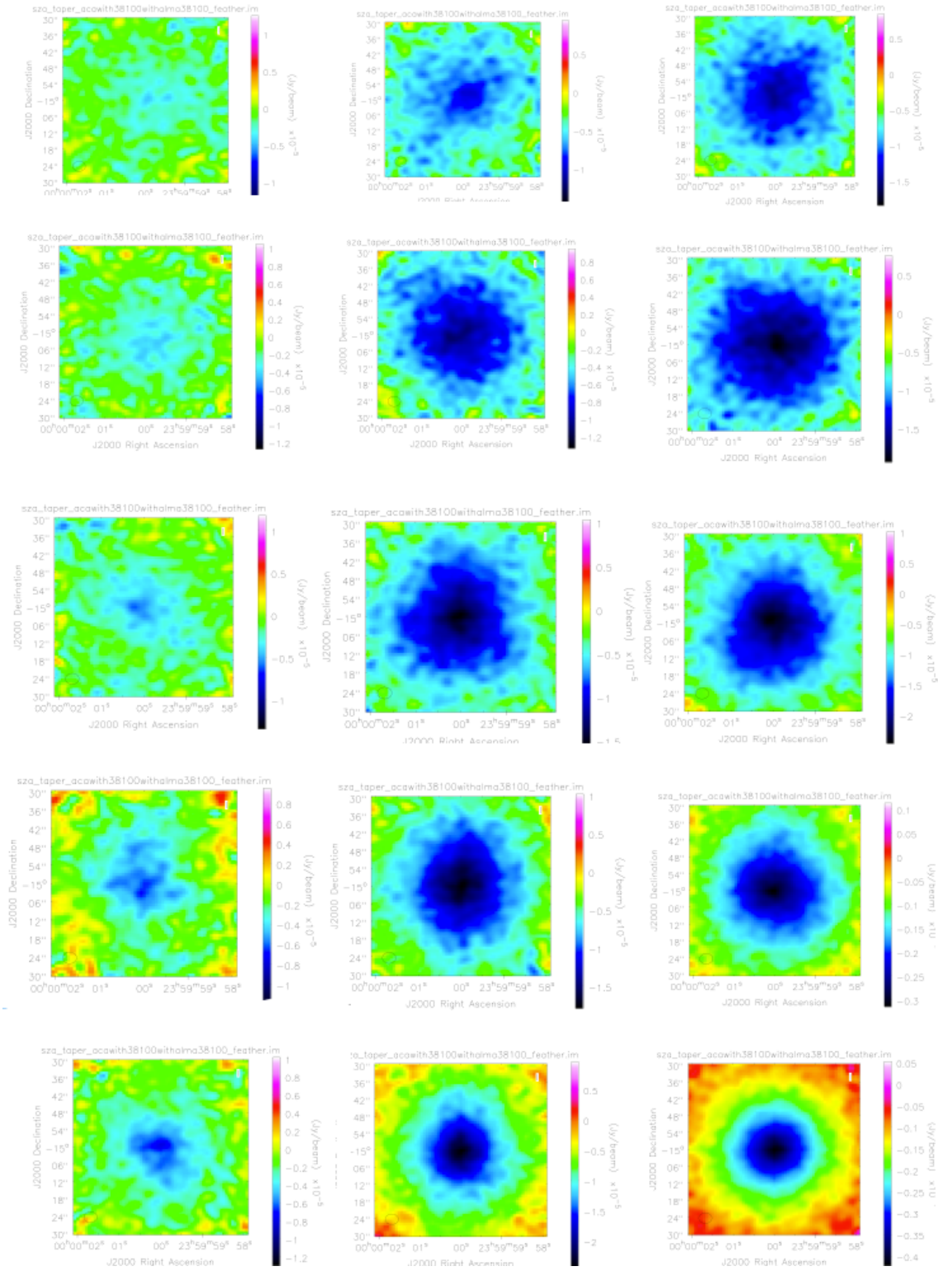

Figure 10.9: Image gallery of ALMA/ACA (Band 3 + 1)/SZA mock observations for the universal Arnaud pressure profile. The columns correspond to the M_{500} masses $2.0 \times 10^{14} M_{\odot}$, $5.0 \times 10^{14} M_{\odot}$ and $8.0 \times 10^{14} M_{\odot}$ (left to right). The rows correspond to redshifts 0.2, 0.4, 0.6, 0.8, 1.0 and 1.2 (from top to bottom).

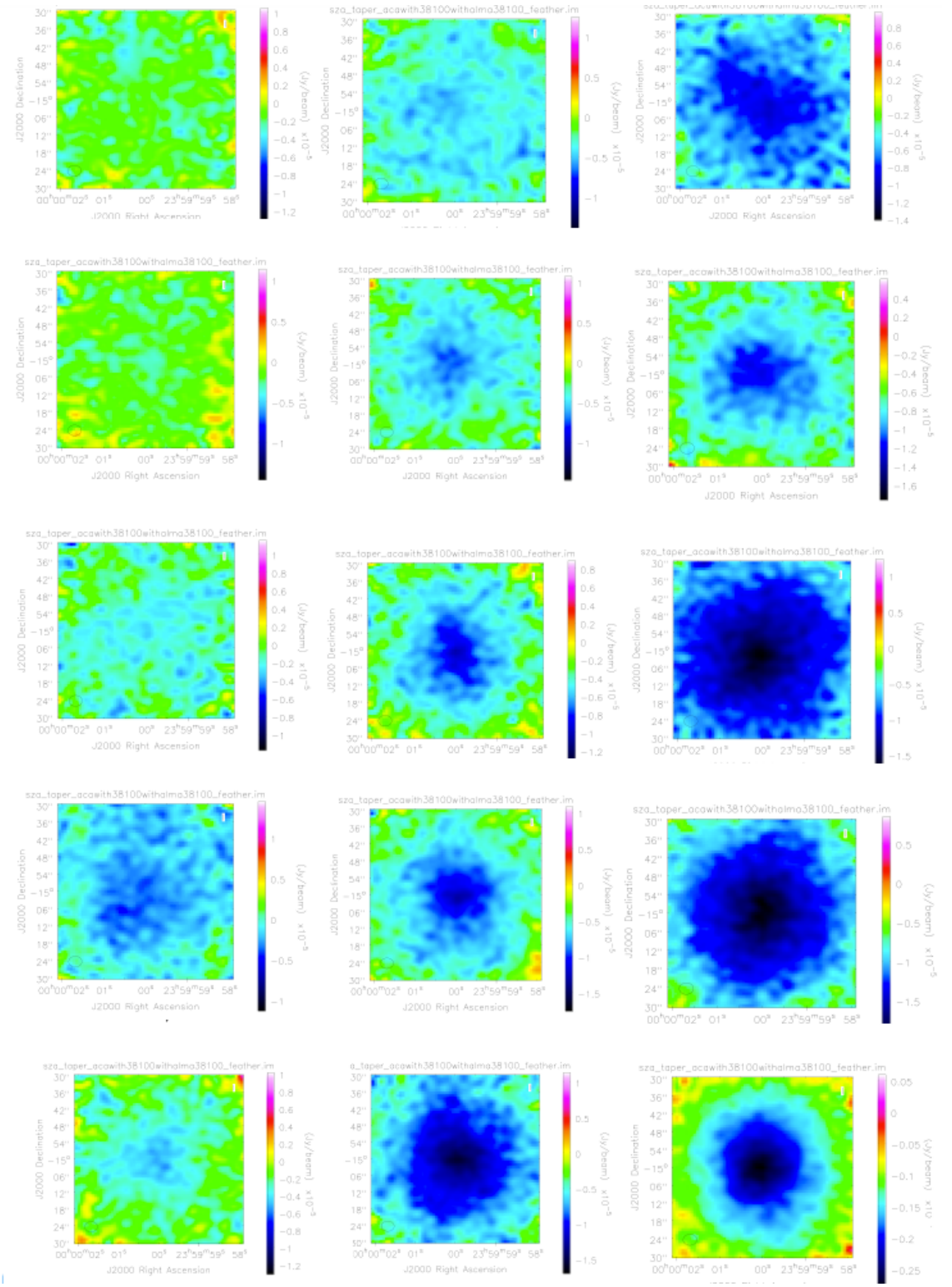

Figure 10.10: Image gallery of ALMA/ACA (Band 3+ 1)/SZA mock observations for the non-cool core Arnaud pressure profile. The columns correspond to the M_{500} masses $2.0 \times 10^{14} M_{\odot}$, $5.0 \times 10^{14} M_{\odot}$ and $8.0 \times 10^{14} M_{\odot}$ (left to right). The rows correspond to redshifts 0.2, 0.4 , 0.6, 0.8, 1.0 and 1.2 (from top to bottom).

Bibliography

Abazajian, K. N., Adelman-McCarthy, J. K., Agüeros, M. A., et al. 2009, ApJS, 182, 543

Ackermann, M., Ajello, M., Albert, A., et al. 2013, Phys. Rev. D, 88, 082002

Akahori, T. & Yoshikawa, K. 2012, PASJ, 64, 12

Allen, S. W., Mantz, A. B., Morris, R. G., et al. 2013, ArXiv e-prints:1307.8152

Allen, S. W., Rapetti, D. A., Schmidt, R. W., et al. 2008, MNRAS, 383, 879

Amendola, L., Appleby, S., Bacon, D., et al. 2013, Living Reviews in Relativity, 16, 6

Anderson, L., Aubourg, E., Bailey, S., et al. 2013, ArXiv e-prints: 1303.4666

Andersson, K., Peterson, J. R., Madejski, G., & Goobar, A. 2009, ApJ, 696, 1029

Applegate, D. E., von der Linden, A., Kelly, P. L., et al. 2012, ArXiv e-prints:1208.0605

Arnaud, M., Pratt, G. W., Piffaretti, R., et al. 2010, A&A, 517, A92

Atwood, W. B., Abdo, A. A., Ackermann, M., et al. 2009, ApJ, 697, 1071

Baldi, A., Ettori, S., Mazzotta, P., Tozzi, P., & Borgani, S. 2007, ApJ, 666, 835

Barrena, R., Biviano, A., Ramella, M., Falco, E. E., & Seitz, S. 2002, A&A, 386, 816

Barrientos, F., Gladders, M., Yee, H., et al. 2003, The Messenger, 112, 40

Bartelmann, M. 2010, ArXiv e-prints:1010.3829

Bartelmann, M. & Schneider, P. 2001, Phys. Rep., 340, 291

Basu, K., Zhang, Y.-Y., Sommer, M. W., et al. 2010, A&A, 519, A29

Battaglia, N., Bond, J. R., Pfrommer, C., & Sievers, J. L. 2012a, ApJ, 758, 74

Battaglia, N., Bond, J. R., Pfrommer, C., & Sievers, J. L. 2012b, ApJ, 758, 75

Baumann. 2012, TASI Lectures on Inflation, ArXiv e-prints:0907.5424v2

Becker, M. R. & Kravtsov, A. V. 2011, ApJ, 740, 25

Becker, M. R., McKay, T. A., Koester, B., et al. 2007, ApJ, 669, 905

Bender, A. N. 2011, PhD thesis, University of Colorado at Boulder

Bender, A. N., Kennedy, J., Ade, P. A. R., et al. 2014, ArXiv e-prints: 1404.7103

BICEP2 Collaboration, Ade, P. A. R., Aikin, R. W., et al. 2014, ArXiv e-prints:1403.3985

Binney, J. & Tremaine, S. 2008, Galactic Dynamics: Second Edition (Princeton University Press)

Birkinshaw, M. 1999, Phys. Rep., 310, 97

Blanton, E. L., Gregg, M. D., Helfand, D. J., Becker, R. H., & White, R. L. 2003, AJ, 125, 1635

Böhringer, H. & Werner, N. 2010, A&A Rev., 18, 127

Bonafede, A., Feretti, L., Murgia, M., et al. 2010, in ISKAF2010 Science Meeting

Bonamente, M., Hasler, N., Bulbul, E., et al. 2012, New Journal of Physics, 14, 025010

Bonamente, M., Joy, M. K., Carlstrom, J. E., Reese, E. D., & LaRoque, S. J. 2004, ApJ, 614, 56

Bonamente, M., Joy, M. K., LaRoque, S. J., et al. 2006, ApJ, 647, 25

Borgani, S., Governato, F., Wadsley, J., et al. 2002, MNRAS, 336, 409

Bradac, M., Clowe, D., Gonzalez, A., et al. 2006, in Bulletin of the American Astronomical Society, Vol. 38, American Astronomical Society Meeting Abstracts, 955

Brodwin, M., Gonzalez, A. H., Stanford, S. A., et al. 2012, ApJ, 753, 162

Brunetti, G. 2012, ArXiv e-prints: 1201.0268

Brunetti, G., Blasi, P., Reimer, O., et al. 2012, MNRAS, 426, 956

Buote, D. A. & Canizares, C. R. 1994, ApJ, 427, 86

Buote, D. A. & Tsai, J. C. 1995a, ApJ, 452, 522

Buote, D. A. & Tsai, J. C. 1995b, ApJ, 439, 29

Carlstrom, J. E., Holder, G. P., & Reese, E. D. 2002, ARA&A, 40, 643

Castro-Rodriguéz, N., Arnaboldi, M., Aguerri, J. A. L., et al. 2009, A&A, 507, 621

Cavaliere, A. & Fusco-Femiano, R. 1976, A&A, 49, 137

Cavaliere, A., Lapi, A., & Fusco-Femiano, R. 2011, A&A, 525, A110

CCAT-collaboration. 2013, CCAT Project Scientific Memo Series: Cosmology with CCAT

Challinor, A. & Lasenby, A. 1998, ApJ, 499, 1

Chaudhuri, A., Nath, B. B., & Majumdar, S. 2012, ApJ, 759, 87

Churazov, E., Forman, W., Jones, C., & Böhringer, H. 2003, ApJ, 590, 225

Clowe, D., Bradač, M., Gonzalez, A. H., et al. 2006, ApJ, 648, L109

Clowe, D., Gonzalez, A., & Markevitch, M. 2004, ApJ, 604, 596

Clowe, D. & Schneider, P. 2002, A&A, 395, 385

Clowes, R. G., Harris, K. A., Raghunathan, S., et al. 2013, MNRAS, 429, 2910

Cohn, J. D. & White, M. 2005, Astroparticle Physics, 24, 316

Comerford, J. M., Meneghetti, M., Bartelmann, M., & Schirmer, M. 2006, ApJ, 642, 39

Condon, J. J., Cotton, W. D., Greisen, E. W., et al. 1998, AJ, 115, 1693

Consortium, A., :, Schammel, M. P., et al. 2012, ArXiv e-prints

Corless, V. L., King, L. J., & Clowe, D. 2009, MNRAS, 393, 1235

Croom, S. M., Boyle, B. J., Shanks, T., et al. 2005, MNRAS, 356, 415

Das, S., Louis, T., Nolta, M. R., et al. 2013, ArXiv e-prints:1301.1037

Davis, M., Efstathiou, G., Frenk, C. S., & White, S. D. M. 1985, ApJ, 292, 371

Dawson. 2012, et al. Discovery of a Galaxy Cluster Merger in Unexplored Merger Phase-space American Astronomical Society Meeting Abstracts

de Hoon, A., Lamer, G., Schwope, A., et al. 2013, A&A, 551, A8

de Pater, I., Romani, P. N., & Atreya, S. K. 1991, Icarus, 91, 220

Dermer, C. D. 1986, A&A, 157, 223

Dimopoulos, K. 2011, Journal of Physics Conference Series, 283, 012010

d'Inverno, R. 2007, Introducing Einstein's Relativity (Oxford University Press)

Dobbs, M., Halverson, N. W., Ade, P. A. R., et al. 2006, New Astronomy Reviews, Volume 50, Issue 11-12, 50, 960

Dolag, K., Borgani, S., Murante, G., & Springel, V. 2009, MNRAS, 399, 497

Dolag, K., Jubelgas, M., Springel, V., Borgani, S., & Rasia, E. 2004, ApJ, 606, L97

Dolag, K., Meneghetti, M., Moscardini, L., Rasia, E., & Bonaldi, A. 2006, MNRAS, 370, 656

Dolag, K., Vazza, F., Brunetti, G., & Tormen, G. 2005, MNRAS, 364, 753

Donahue, M. 1996, ApJ, 468, 79

Donahue, M., Gaskin, J. A., Patel, S. K., et al. 2003, ApJ, 598, 190

Donnert, J. M. F. 2013, ArXiv e-prints: 1306.3101

Duffy, A. R., Schaye, J., Kay, S. T., & Dalla Vecchia, C. 2008, MNRAS, 390, L64

Dunkley, J., Komatsu, E., Nolta, M. R., et al. 2009, ApJS, 180, 306

Eckert, D., Ettori, S., Molendi, S., Vazza, F., & Paltani, S. 2013a, A&A, 551, A23

Eckert, D., Molendi, S., Vazza, F., Ettori, S., & Paltani, S. 2013b, A&A, 551, A22

Edge, A. C., Fabian, A. C., Allen, S. W., et al. 1994, MNRAS, 270, L1

Ehlert, S., Allen, S. W., von der Linden, A., et al. 2011, MNRAS, 411, 1641

Einasto, J. 1965, Trudy Astrofizicheskogo Instituta Alma-Ata, 5, 87

Enßlin, T., Pfrommer, C., Miniati, F., & Subramanian, K. 2011, A&A, 527, A99

Enßlin, T. A. & Brüggen, M. 2002, MNRAS, 331, 1011

Ettori, S. 2013, MNRAS, 435, 1265

Ettori, S., Morandi, A., Tozzi, P., et al. 2009, A&A, 501, 61

EUCLID. 2011, ESA: Mapping the geometry of the dark Universe

Fabian, A. C. 1994, ARA&A, 32, 277

Fabian, A. C. & Sanders, J. S. 2009, in American Institute of Physics Conference Series, Vol. 1201, American Institute of Physics Conference Series, ed. S. Heinz & E. Wilcots, 275–281

Fabian, A. C., Sanders, J. S., Allen, S. W., et al. 2011, MNRAS, 418, 2154

Fabian, A. C., Sanders, J. S., Allen, S. W., et al. 2003, MNRAS, 344, L43

Fabjan, D., Borgani, S., Tornatore, L., et al. 2010, MNRAS, 401, 1670

Ferrari, C., van Bemmel, I., Bonafede, A., et al. 2012, in SF2A-2012: Proceedings of the Annual meeting of the French Society of Astronomy and Astrophysics, ed. S. Boissier, P. de Laverny, N. Nardetto, R. Samadi, D. Valls-Gabaud, & H. Wozniak, 677–680

Floor, S. N., Melott, A. L., & Motl, P. M. 2004, ApJ, 611, 153

Foley, R. J., Andersson, K., Bazin, G., et al. 2011, ApJ, 731, 86

Giacintucci, S., Markevitch, M., Brunetti, G., Cassano, R., & Venturi, T. 2011, A&A, 525, L10

Giodini, S., Lovisari, L., Pointecouteau, E., et al. 2013, Space Sci. Rev., 177, 247

Gladders, M. D. & Yee, H. K. C. 2005, ApJS, 157, 1

Gobat, R., Daddi, E., Onodera, M., et al. 2011, A&A, 526, A133

Gruen, D., Seitz, S., Kosyra, R., et al. 2013, ArXiv e-prints:1310.6744

Halverson, N. W., Lanting, T., Ade, P. A. R., et al. 2009, ApJ, 701, 42

Hashimoto, Y., Henry, J. P., & Boehringer, H. 2008, MNRAS, 390, 1562

Hasler, N., Bulbul, E., Bonamente, M., et al. 2012, ApJ, 748, 113

Hasler, N., Bulbul, E., Bonamente, M., et al. 2009, in Chandra's First Decade of Discovery, ed. S. Wolk, A. Fruscione, & D. Swartz

Hasselfield, M., Hilton, & Marriage, M. 2013, JCAP, 7, 8

Heinz, S., Brüggen, M., Young, A., & Levesque, E. 2006, MNRAS, 373, L65

Hicks, A. K. & Mushotzky, R. 2005, ApJ, 635, L9

Hinshaw, G., Larson, D., Komatsu, E., et al. 2013, ApJS, 208, 19

Hinshaw, G., Weiland, J. L., Hill, R. S., et al. 2009, ApJS, 180, 225

Ho, S., Bahcall, N., & Bode, P. 2006, ApJ, 647, 8

Hobson M.P., G. Efstathiou, A. 2006, General Relativity (Cambridge University Press)

Hoekstra, H., Mahdavi, A., Babul, A., & Bildfell, C. 2012, MNRAS, 427, 1298

Hsu, L.-Y., Ebeling, H., & Richard, J. 2013, MNRAS, 429, 833

Ichikawa, K., Matsushita, K., Okabe, N., et al. 2013, ApJ, 766, 90

Itoh, N., Kohyama, Y., & Nozawa, S. 1998, ApJ, 502, 7

Itoh, N. & Nozawa, S. 2004, A&A, 417, 827

Ivezic, Z., Tyson, J. A., Acosta, E., et al. 2008, ArXiv e-prints:0805.2366

Jeltema, T. E., Canizares, C. R., Bautz, M. W., & Buote, D. A. 2005, ApJ, 624, 606

Johansson, D., Horellou, C., Sommer, M. W., et al. 2010, A&A, 514, A77

Kaiser, N. 1986, MNRAS, 222, 323

Kaiser, N., Squires, G., & Broadhurst, T. 1995, ApJ, 449, 460

Kay, S. T., da Silva, A. C., Aghanim, N., et al. 2007, MNRAS, 377, 317

Keisler, R., Reichardt, C. L., Aird, K. A., et al. 2011, ApJ, 743, 28

Kirkpatrick, C. C., McNamara, B. R., & Cavagnolo, K. W. 2011, ApJ, 731, L23

Klein. 2013, PhD Thesis, Universtity of Bonn

Koda, J., Sawada, T., Wright, M. C. H., et al. 2011, ArXiv e-prints:1102.3060

Korngut, P. M., Dicker, S. R., Reese, E. D., et al. 2011, ApJ, 734, 10

Kowalski, M., Rubin, D., Aldering, G., et al. 2008, ApJ, 686, 749

Krause, E., Pierpaoli, E., Dolag, K., & Borgani, S. 2012, MNRAS, 419, 1766

Kravtsov, A. V., Nagai, D., & Vikhlinin, A. A. 2005, ApJ, 625, 588

Kravtsov, A. V., Vikhlinin, A., & Nagai, D. 2006, ApJ, 650, 128

LaRoque, S. J., Bonamente, M., Carlstrom, J. E., et al. 2006, ApJ, 652, 917

Larson, D., Dunkley, J., Hinshaw, G., et al. 2011, ApJS, 192, 16

Leccardi, A. & Molendi, S. 2008, A&A, 487, 461

Lee, B., Gildemeister, P. A. R., Holmes, A. N., & Lee, A. T. 1998, Appl. Opt. 37, 3391-3397

Lee, J. & Suto, Y. 2003, ApJ, 585, 151

Liang, H., Hunstead, R. W., Birkinshaw, M., & Andreani, P. 2000, ApJ, 544, 686

Limousin, M., Morandi, A., Sereno, M., et al. 2013, Space Sci. Rev., 177, 155

Lin, Y.-T. & Mohr, J. J. 2004, ApJ, 617, 879

Ludlow, A. D., Navarro, J. F., Li, M., et al. 2012, MNRAS, 427, 1322

Lueker, M., Reichardt, C. L., Schaffer, K. K., et al. 2010, ApJ, 719, 1045

Lundgren. 2012, ALMA Technical Handbook Cycle 1

Mahdavi, A., Hoekstra, H., Babul, A., Balam, D. D., & Capak, P. L. 2007a, ApJ, 668, 806

Mahdavi, A., Hoekstra, H., Babul, A., et al. 2013, Astrophys.J., 767, 116

Mahdavi, A., Hoekstra, H., Babul, A., et al. 2007b, ApJ, 664, 162

Mann, A. W. & Ebeling, H. 2012, MNRAS, 420, 2120

Mantz, A., Allen, S. W., Ebeling, H., Rapetti, D., & Drlica-Wagner, A. 2010a, MNRAS, 406, 1773

Mantz, A., Allen, S. W., Rapetti, D., & Ebeling, H. 2010b, MNRAS, 406, 1759

Markevitch, M. 2005 astro-ph/0511345

Markevitch, M. 2006, in ESA Special Publication, Vol. 604, The X-ray Universe 2005, ed. A. Wilson, 723

Markevitch, M. 2010, ArXiv e-prints: 1010.3660

Markevitch, M., Gonzalez, A. H., Clowe, D., et al. 2004, ApJ, 606, 819

Markevitch, M., Gonzalez, A. H., David, L., et al. 2002, ApJ, 567, L27

Markevitch, M. & Vikhlinin, A. 2007, Phys. Rep., 443, 1

Marrone, D. P., Smith, G. P., Okabe, N., et al. 2012, ApJ, 754, 119

Mason, B. S., Dicker, S. R., Korngut, P. M., et al. 2010, ApJ, 716, 739

Mather, J. C., Fixsen, D. J., Shafer, R. A., Mosier, C., & Wilkinson, D. T. 1999, ApJ, 512, 511

Maughan, B. J. 2007, ApJ, 668, 772

Maughan, B. J., Giles, P. A., Randall, S. W., Jones, C., & Forman, W. R. 2012, MNRAS, 421, 1583

Maughan, B. J., Jones, C., Forman, W., & Van Speybroeck, L. 2008, ApJS, 174, 117

Maughan, B. J., Jones, C., Jones, L. R., & Van Speybroeck, L. 2007, ApJ, 659, 1125

McCarthy, I. G., Schaye, J., Bower, R. G., et al. 2011, MNRAS, 412, 1965

McDonald, M., Benson, B. A., Vikhlinin, A., et al. 2013, ApJ, 774, 23

McDonald, M., Veilleux, S., Rupke, D. S. N., Mushotzky, R., & Reynolds, C. 2011, ApJ, 734, 95

Menanteau, F., Hughes, J. P., Sifón, C., et al. 2012, ApJ, 748, 7

Meneghetti, M., Fedeli, C., Zitrin, A., et al. 2011, A&A, 530, A17

Mohr, J. J., O'Shea, B., Evrard, A. E., Bialek, J., & Haiman, Z. 2003, Nuclear Physics B Proceedings Supplements, 124, 63

Molnar, S. M., Hughes, J. P., Donahue, M., & Joy, M. 2002, ApJ, 573, L91

Morandi, A. & Limousin, M. 2012, MNRAS, 421, 3147

Morandi, A., Limousin, M., Rephaeli, Y., et al. 2011a, MNRAS, 416, 2567

Morandi, A., Pedersen, K., & Limousin, M. 2010, ApJ, 713, 491

Morandi, A., Pedersen, K., & Limousin, M. 2011b, ApJ, 729, 37

Morris, R. G. & Fabian, A. C. 2005, MNRAS, 358, 585

Motl, P. M., Hallman, E. J., Burns, J. O., & Norman, M. L. 2005, ApJ, 623, L63

Muchovej, S., Mroczkowski, T., Carlstrom, J. E., et al. 2007, ApJ, 663, 708

Murgia, M., Govoni, F., Markevitch, M., et al. 2009, A&A, 499, 679

Nagai, D., Kravtsov, A. V., & Vikhlinin, A. 2007a, ApJ, 668, 1

Nagai, D., Vikhlinin, A., & Kravtsov, A. V. 2007b, ApJ, 655, 98

Nath, B. B. 2011, Journal of Astrophysics and Astronomy, 32, 545

Navarro, J. F., Frenk, C. S., & White, S. D. M. 1996, ApJ, 462, 563

Navarro, J. F., Hayashi, E., Power, C., et al. 2004, MNRAS, 349, 1039

Navarro, J. F., Ludlow, A., Springel, V., et al. 2010, MNRAS, 402, 21

Niederste-Ostholt, M., Strauss, M. A., Dong, F., Koester, B. P., & McKay, T. A. 2010, MNRAS, 405, 2023

Nord, M. 2009, PhD thesis, Online-Publikationen an deutschen Hochschulen Bonn, Univ., Diss., 2009 URN:urn:nbn:de:hbz:5N-18737

Nord, M., Basu, K., Pacaud, F., et al. 2009, A&A, 506, 623

O'Dea, C. P., Baum, S. A., Privon, G., et al. 2008, ApJ, 681, 1035

Oguri, M., Bayliss, M. B., Dahle, H., et al. 2012, MNRAS, 420, 3213

Oguri, M., Lee, J., & Suto, Y. 2003, ApJ, 599, 7

O'Hara, T. B., Mohr, J. J., Bialek, J. J., & Evrard, A. E. 2006, ApJ, 639, 64

Okabe, N., Smith, G. P., Umetsu, K., Takada, M., & Futamase, T. 2013, ApJ, 769, L35

P., S. 2010, Cosmology lecture notes (Universitaet Bonn)

Papovich, C., Momcheva, I., Willmer, C. N. A., et al. 2010, ApJ, 716, 1503

Percival, W. J., Reid, B. A., Eisenstein, D. J., et al. 2010, MNRAS, 401, 2148

Perlmutter, S., Aldering, G., Goldhaber, G., et al. 1999, ApJ, 517, 565

Peterson, J. R. & Fabian, A. C. 2006, Phys. Rep., 427, 1

Pillepich, A., Porciani, C., & Reiprich, T. H. 2012, MNRAS, 422, 44

Pinzke, A., Pfrommer, C., & Bergström, L. 2009, Physical Review Letters, 103, 181302

Plagge, T., Benson, B. A., Ade, P. A. R., et al. 2010, ApJ, 716, 1118

Plagge, T. J., Marrone, D. P., Abdulla, Z., et al. 2013, ApJ, 770, 112

Planck collaboration, Ade, P. A. R., Aghanim, & et al.Planck 2013 results. XV. CMB power spectra and likelihood. 2013, ArXiv e-prints: 1303.5075

Planck Collaboration, Ade, P. A. R., Aghanim, & et al.Planck 2013 results. XXI. Cosmology with the all-sky Planck Compton parameter y-map. 2013a, ArXiv e-prints: 1303.5081

Planck Collaboration, Ade, P. A. R., Aghanim, N., & et al.Planck 2013 results. XX. Cosmology from Sunyaev-Zeldovich cluster counts. 2013b, ArXiv e-prints: 1303.5080

Planck Collaboration, Ade, P. A. R., Aghanim, N., & et al.Planck 2013 results. XXII. Constraints on inflation . 2013c, ArXiv e-prints: 1303.5082v1

Planck Collaboration, Ade, P. A. R., Aghanim, N., & et al.Planck 2013 results. XXIX. Planck catalogue of Sunyaev-Zeldovich sources. 2013d, ArXiv e-prints: 1303.5089

Planck Collaboration, Ade, P. A. R., Aghanim, N., & et al.Planck 2013 results. XXVIII. The Planck Catalogue of Compact Sources. 2013e, ArXiv e-prints: 1303.5088

Planck Collaboration, Ade, P. A. R., Aghanim, N., & et al.Planck early results. VIII. The all-sky early Sunyaev-Zeldovich cluster samples. 2011a, A&A, 536, A8

Planck Collaboration, Ade, P. A. R., Aghanim, N., & et al.Planck early results. XI. Calibration of the local galaxy cluster Sunyaev-Zeldovich scaling relations. 2011b, A&A, 536, A11

Planck Collaboration, Ade, P. A. R., & Aghanim, N. e. 2013f, A&A, 550, A130

Planck Collaboration, Ade, P. A. R., & et al.Planck 2013 results. XVI. Cosmological parameters. 2013g, ArXiv e-prints: 1303.5076

Planck Collaboration, Ade, P. A. R., & et al.Planck intermediate results. III. The relation between galaxy cluster mass and Sunyaev-Zeldovich signal. 2013h, A&A, 550, A129

Planck Collaboration, Ade, P. A. R., & et al.Planck intermediate results. V. Pressure profiles of galaxy clusters from the Sunyaev-Zeldovich effect. 2013i, A&A, 550, A131

Planck Collaboration, Aghanim, N., & et al.Planck early results. IX. XMM-Newton follow-up for validation of Planck cluster candidates. 2011c, A&A, 536, A9

Planck Collaboration & Aghanim, N. e. 2011, A&A, 536, A10

Planck Collaboration, AMI Collaboration, Ade, P. A. R., Planck intermediate results. II. Comparison of Sunyaev-Zeldovich measurements from Planck and from the Arcminute Microkelvin Imager for 11 galaxy clusters, & et al. 2013j, A&A, 550, A128

Planelles, S., Borgani, S., Dolag, K., et al. 2013, MNRAS, 431, 1487

Plionis, M. & Basilakos, S. 2002, in Astronomical Society of the Pacific Conference Series, Vol. 268, Tracing Cosmic Evolution with Galaxy Clusters, ed. S. Borgani, M. Mezzetti, & R. Valdarnini, 81

Pointcouteau. 2013, Athenaplus-collaboration,The Hot and Energetic Universes: The evolution of galaxy groups and clusters

Poole, G. B., Babul, A., McCarthy, I. G., Sanderson, A. J. R., & Fardal, M. A. 2008, MNRAS, 391, 1163

Poole, G. B., Fardal, M. A., Babul, A., et al. 2006, MNRAS, 373, 881

Pratt, G. W., Arnaud, M., Piffaretti, R., et al. 2010, A&A, 511, A85

Pratt, G. W., Croston, J. H., Arnaud, M., & Böhringer, H. 2009, A&A, 498, 361

Rafferty, D. 2007a, PhD thesis, Ohio University

Rafferty, F. L. 2007b, PhD thesis, Ohio University

Ragozzine, B., Clowe, D., Markevitch, M., Gonzalez, A. H., & Bradač, M. 2012, ApJ, 744, 94

Ragozzine, B. A. & Clowe, D. I. 2012

Rawle, T. D., Edge, A. C., Egami, E., et al. 2012, ApJ, 747, 29

Reese, E. D., Carlstrom, J. E., Joy, M., et al. 2002, ApJ, 581, 53

Reichardt, C. L., Zahn, O., Ade, P. A. R., et al. 2009, ApJ, 701, 1958

Rex, M., Rawle, T. D., Egami, E., et al. 2010, A&A, 518, L13

Ricker, P. M. & Sarazin, C. L. 2001, ApJ, 561, 621

Riess, A. G., Filippenko, A. V., Challis, P., et al. 1998, AJ, 116, 1009

Rosati, P., Borgani, S., & Norman, C. 2002, ARA&A, 40, 539

Rosati, P., Tozzi, P., Gobat, R., et al. 2009, A&A, 508, 583

Russell, H. R., Fabian, A. C., Taylor, G. B., et al. 2012a, MNRAS, 422, 590

Russell, H. R., McNamara, B. R., Sanders, J. S., et al. 2012b, MNRAS, 423, 236

Saliwanchik, B. R., Montroy, T. E., Aird, K. A., et al. 2013, ArXiv e-prints:1312.3015

Sanders, J. S. & Fabian, A. C. 2007, MNRAS, 381, 1381

Sanderson, A. J. R., Edge, A. C., & Smith, G. P. 2009, MNRAS, 398, 1698

Sanderson, A. J. R., Ponman, T. J., & O'Sullivan, E. 2006, MNRAS, 372, 1496

Santos, J. S., Rosati, P., Tozzi, P., et al. 2008, A&A, 483, 35

Sarazin, C. L. 1988, X-ray emission from clusters of galaxies, CUP

Sarazin, C. L. 2002, in Astrophysics and Space Science Library, Vol. 272, Merging Processes in Galaxy Clusters, ed. L. Feretti, I. M. Gioia, & G. Giovannini, 1–38

Sault, B. 2004, Miriad Users Guide

Sault, R. J., Teuben, P. J., & Wright, M. C. H. 1995, in Astronomical Society of the Pacific Conference Series, Vol. 77, Astronomical Data Analysis Software and Systems IV, ed. R. A. Shaw, H. E. Payne, & J. J. E. Hayes, 433

Sayers, J., Czakon, N. G., Mantz, A., et al. 2013a, ApJ, 768, 177

Sayers, J., Golwala, S. R., Ameglio, S., & Pierpaoli, E. 2011, ApJ, 728, 39

Sayers, J., Mroczkowski, T., Zemcov, M., et al. 2013b, ApJ, 778, 52

Scannapieco, E. & Brüggen, M. 2009, in American Institute of Physics Conference Series, Vol. 1201, American Institute of Physics Conference Series, ed. S. Heinz & E. Wilcots, 379–382

Schneider. 2010, Cosmology Lecture Series, University of Bonn

Schneider, P. 2005, ArXiv Astrophysics e-prints:astro-ph/0509252

Schwan, D., Ade, P. A. R., Basu, K., et al. 2011, Review of Scientific Instruments, 82, 091301

Schwan, D., Kneissl, R., Ade, P., et al. 2012, The Messenger, 147, 7

Sereno, M. 2007, MNRAS, 380, 1207

Sereno, M. & Covone, G. 2013, MNRAS, 434, 878

Sereno, M., De Filippis, E., Longo, G., & Bautz, M. W. 2006, ApJ, 645, 170

Sereno, M., Jetzer, P., & Lubini, M. 2010, MNRAS, 403, 2077

Sereno, M. & Umetsu, K. 2011, MNRAS, 416, 3187

Sereno, M. & Zitrin, A. 2012, MNRAS, 419, 3280

Sharp, M. K., Marrone, D. P., Carlstrom, J. E., et al. 2010, Astrophys.J., 713, 82

Shirokoff, E., Reichardt, C. L., Shaw, L., et al. 2011, ApJ, 736, 61

Short, C. J., Thomas, P. A., Young, O. E., et al. 2010, MNRAS, 408, 2213

Simionescu, A., Allen, S. W., Mantz, A., et al. 2011, Science, 331, 1576

Smolčić, V., Schinnerer, E., Finoguenov, A., et al. 2007, ApJS, 172, 295

Song, J., Zenteno, A., Stalder, B., et al. 2012, ApJ, 761, 22

Springel, V., White, S. D. M., Jenkins, A., et al. 2005, Nature, 435, 629

Stalder, B., Ruel, J., Šuhada, R., et al. 2013, ApJ, 763, 93

Stanimirovic, S. 2002, in Astronomical Society of the Pacific Conference Series, Vol. 278, Single-Dish Radio Astronomy: Techniques and Applications, ed. S. Stanimirovic, D. Altschuler, P. Goldsmith, & C. Salter, 375–396

Suzuki, N., Rubin, D., Lidman, C., et al. 2012, ApJ, 746, 85

Taylor, G. B., Carilli, C. L., & Perley, R. A., eds. 1999, Astronomical Society of the Pacific Conference Series, Vol. 180, Synthesis Imaging in Radio Astronomy II

Thompson, A. R., Moran, J. M., & Swenson, Jr., G. W. 2001, Interferometry and Synthesis in Radio Astronomy, 2nd Edition

Tinker, J., Kravtsov, A. V., Klypin, A., et al. 2008, ApJ, 688, 709

Tozzi, P. & Norman, C. 2001, ApJ, 546, 63

Umetsu, K. 2013, ApJ, 769, 13

Umetsu, K., Medezinski, E., Nonino, M., et al. 2012, ApJ, 755, 56

Urban, O., Simionescu, A., Werner, N., et al. 2014, MNRAS, 437, 3939

van Weeren, R. J., Brüggen, M., Röttgering, H. J. A., et al. 2011, A&A, 533, A35

Vazza, F. 2011, MNRAS, 410, 461

Venturi, T., Giacintucci, S., Dallacasa, D., et al. 2013, A&A, 551, A24

Vikhlinin, A., Burenin, R., Forman, W. R., et al. 2007, in Heating versus Cooling in Galaxies and Clusters of Galaxies, ed. H. Böhringer, G. W. Pratt, A. Finoguenov, & P. Schuecker, 48

Vikhlinin, A., Kravtsov, A., Forman, W., et al. 2006, ApJ, 640, 691

Vikhlinin, A., Kravtsov, A. V., Burenin, R. A., et al. 2009, ApJ, 692, 1060

Voit, G. M., Kay, S. T., & Bryan, G. L. 2005, MNRAS, 364, 909

Wechsler, R. H. 2001, PhD thesis, UNIVERSITY OF CALIFORNIA, SANTA CRUZ

Weiland, J. L., Odegard, N., Hill, R. S., et al. 2011, ApJS, 192, 19

Weißmann, A., Böhringer, H., Šuhada, R., & Ameglio, S. 2013, A&A, 549, A19

Westbrook, B., Ade, P. A. R., Bender, A. N., et al. 2009, in American Institute of Physics Conference Series, Vol. 1185, American Institute of Physics Conference Series, ed. B. Young, B. Cabrera, & A. Miller, 363–366

Wik, D. R., Sarazin, C. L., Ricker, P. M., & Randall, S. W. 2008, ApJ, 680, 17

Wright. 2004, SZA location at CARMA site CARMA memo 25

Yamada, K., Kitayama, T., Takakuwa, S., et al. 2012, PASJ, 64, 102

Yoshida, N., Springel, V., White, S. D. M., & Tormen, G. 2000, ApJ, 535, L103

Younger, J. D. & Bryan, G. L. 2007, ApJ, 666, 647

Zeimann, G. R., Stanford, S. A., Brodwin, M., et al. 2012, ApJ, 756, 115

Zhang, Y.-Y., Böhringer, H., Finoguenov, A., et al. 2006, A&A, 456, 55

Zhang, Y.-Y., Okabe, N., Finoguenov, A., et al. 2010, ApJ, 711, 1033

Zwicky, F. 1933, Helvetica Physica Acta, 6, 110

List of Figures

List of Tables

Acknowledgments

First and foremost, I would like to thank my supervisor Prof. Dr. Frank Bertoldi for his advice and encouragement throughout this PhD project. Thank you so much for giving me the tremendous opportunity to be part of the ALMA Regional Center, the European ALMA Imaging Group and the APEX-SZ team, as well as for sending me to numerous great conferences and in supporting my 'International Max Planck Research School' membership. All these factors, in conjunction with your guidance, continued interest and support, have helped me in developing as a scientist.

A big thanks goes to my co-supervisor Dr. Stefanie Mühle, whose interest in my project and always cheerful reassurance have contributed in making this PhD time a truly delightful one. Thank you very much for proof-reading this thesis.

I would also like to thank the whole APEX-SZ collaboration for the useful discussions and for allowing me to explore the bolometer side of Sunyaev-Zel'dovich observations - I have certainly learnt a great deal from all of you throughout these past years. In particular, thank you for your support and great comments in the last CARMA/APEX-SZ collaboration proposal. Thanks to Dr. Martin Sommer and Dr. Kaustuv Basu for explaining APEX-SZ to me when I first arrived in the AIfA. Particular thanks goes to Dr. Martin Sommer for providing the cleaned APEX-SZ images used in this thesis. In addition, I would like to thank Dr. Florian Pacaud for the beautiful Bullet Cluster X-ray images used in the past ALMA proposals. I would also like to thank Dr. Holger Israel for giving me a first insight into weak lensing analysis via his weak lensing tutorial.

I would also like to thank the whole ALMA Regional Center team for supporting me as a member of the ALMA EACIG group as well as a Contact Scientist for ALMA cycle 1. Particular thanks goes to Dr. Stefanie Mühle and Dr. Felipe Alves for always being there to answer questions, no matter how small.

Thanks to Prof. Dr. Ulrich Klein, Prof. Dr. Ian Brock and Prof. Dr. Andreas Bott for joining my thesis committee.

My PhD experience has been greatly enriched by being part of the 'International Max Planck Research School' since the weekly seminars have allowed me to continuously learn about other fields of study from some great fellow students amongst whom I have found many friends. I would also like to thank Aarti, Sameera and Matthias as well as Miriam and the many colleagues and friends in the AIfA for the great time we have shared. Thanks to Dr. Nadya Ben Bekhti for introducing me to the Proseminar and outreach events. I will certainly always remember the first 'Maustag' as being a day of great fun. I would

like to thank Christina Stein-Schmitz, Dr. Emmanouil Angelakis and Dr. Simone Pott for helping in administrative matters throughout my PhD.

A big thanks also goes to all of my teachers, both at school and at university - in unveiling the mysteries of the universe to me you have added a wonderful new component to my life: science.

Thanks also to Anne, Jo and Laura for dragging me away from my desk and ensuring that my violin case did not become too dusty. It is always a true pleasure to practice and perform new pieces with you - music is certainly the best substitute for coffee ...

Mere sentences are not sufficient to value the support and express my deepest gratitude to those dearest to me. I honestly don't know how to thank Michael enough for his frequent travelling back and forth to Frankfurt by plane and for his endless good humour.

My biggest thanks goes to my parents for giving me the freedom to explore. You have always surrounded me with honesty, love and trust - a treasure so big that I could not wish for more. The support received from my most loyal and trusting companion Benny (a dog unique in so many ways, whose innocent wisdom will always turn every day into an adventure) is immeasurable.